



CERN-THESIS-2006-118

Detailed Analysis of Two Particle Correlations in Central Pb-Au Collisions at 158 GeV per Nucleon

Dem Fachbereich Physik
der Technischen Universität Darmstadt

zur Erlangung des Grades
eines Doktors der Naturwissenschaften
(Dr. rer. nat.)

vorgelegte Dissertation von
Dariusz Antończyk
aus Krakau

Darmstadt 2006
(D 17)

Abstract

This thesis presents a two-particle correlation analysis of the fully calibrated high statistics CERES Pb+Au collision data at the top SPS energy, with the emphasis on the pion-proton correlations and the event-plane dependence of the correlation radii. CERES is a dilepton spectrometer at CERN SPS. After the upgrade, which improved the momentum resolution and extended the detector capabilities to hadrons, CERES collected 30 million Pb+Au events at 158 AGeV in the year 2000. A previous Hanbury-Brown-Twiss (HBT) analysis of pion pairs in a subset of these data, together with the results obtained at other beam energies, lead to a new freeze-out criterion [AAA⁺03]. In this work, the detailed transverse momentum and event-plane dependence of the pion correlation radii, as well as the pion-proton correlations, are discussed in the framework of the blast wave model of the expanding fireball.

Furthermore, development of an electron drift velocity gas monitor for the ALICE TPC sub-detector is presented. The new method of the gas composition monitoring is based on the simultaneous measurement of the electron drift velocity and the gas gain and is sensitive to even small variations of the gas mixture composition. Several modifications of the apparatus were performed resulting in the final drift velocity resolution of 0.3 permille.

Zusammenfassung

In der vorliegenden Arbeit untersuchen wir Zweiteilchenkorrelationen und die Abhängigkeit der Korrelationsradien von der Orientierung zur Reaktionsebene in Schwerionenstößen. Eine solche Analyse wird hier zum ersten Mal anhand der vollständig kalibrierten Daten des CERES Detektors zu Pb+Au Kollisionen bei maximaler Strahlenergie am CERN SPS durchgeführt. CERES, ursprünglich als Dileptonenspektrometer konzipiert, verfügt nach der Erweiterung um eine Zeitprojektionskammer über die Möglichkeit Hadronen zu rekonstruieren sowie über verbesserte Impulsauflösung. In der vorliegenden Arbeit untersuchen wir Daten zu 30 Millionen Pb+Au Kollisionen bei 158 AGeV aus dem Jahr 2000. Die kombinierten Ergebnisse einer Hanbury-Brown-Twiss (HBT) Analyse von Pionpaaren aus einer früheren Analyse eines Teils der vorliegenden Daten und Ergebnisse von anderen Strahlenergien resultieren in einem neuen Kriterium für den thermischen freeze-out [AAA⁺03]. In dieser Arbeit diskutieren wir die Systematik der rekonstruierten Pionkorrelationsradien in Abhängigkeit vom Transversalimpuls und der Orientierung relativ zur Stossebene sowie die Pion-Proton-Korrelationen im Rahmen eines "blast wave" Modells des expandierenden Feuerballs.

Ein weiterer Schwerpunkt dieser Arbeit besteht in der Weiterentwicklung einer Apparatur zur Überwachung der Driftgeschwindigkeit in Gasmischungen für die ALICE Zeitprojektionskammer. Zahlreiche Veränderungen zur Verbesserungen der Driftgeschwindigkeitsmessung

wurden vorgenommen um eine Auflösung von 0.3 Promille zu erreichen. Das neue Verfahren zur präzisen Kontrolle der Zusammensetzung der Mischung über die Driftgeschwindigkeit und den Gasverstärkungsfaktor erlaubt es, minimale Abweichungen der Mischungsverhältnisse vom Sollwert nachzuweisen.

Contents

1	Introduction	1
1.1	Strongly Interacting Matter	2
1.2	Heavy Ion Collision Experiments	4
1.2.1	Basics	5
1.2.2	Landau Scenario	7
1.2.3	Bjorken Scenario	8
1.2.4	Observables	9
1.3	Two-particle Interferometry	10
1.3.1	Correlation Function and Source Function	12
1.3.2	Coordinate Systems and Variables	13
1.3.3	Final State Interactions Between Particles	17
1.3.4	Non-identical Particle Correlations	19
2	CERES experiment	21
2.1	Target and Trigger Systems	22
2.2	Silicon Drift Detectors	24
2.3	Ring Imaging Cherenkov Detectors	26
2.4	Time Projection Chamber	26
2.4.1	Gas Properties	29
2.4.2	Readout and Control Systems	30
3	Drift Velocity Monitor for the ALICE TPC	33
3.1	Introduction	33
3.2	Experimental Setup	36
3.3	Gas Monitor Development Studies	39
3.4	Data Acquisition and Analysis	44
3.5	Development of the Read-out Electronics	50
3.6	Results and Discussion	55

4	Analysis of the CERES Data	57
4.1	Run 2000	58
4.2	Production	58
4.3	Data Reduction (step3c)	60
4.4	Momentum Calibration	62
4.5	Energy Loss Calibration	66
4.6	Matching Calibration	68
4.7	Reaction Plane Calibration	71
4.7.1	Determination of the Event Plane	71
4.7.2	Acceptance Corrections	73
4.7.3	Reaction Plane Resolution	74
4.8	Centrality Determination	77
4.8.1	Centrality Calibration	81
4.9	Charged Particle Multiplicity	84
5	Identical Particle Correlation Analysis	89
5.1	Data Selection	89
5.2	Definition of the Correlation Function	94
5.3	Signal and Background Construction	94
5.4	Fitting the Correlation	95
5.5	Coulomb Correction	96
5.6	Transverse Momentum Dependence	99
5.7	Reaction Plane Orientation Dependence	101
6	Non-identical Particle Correlation Analysis	105
6.1	Analysis Variables and Frame	105
6.2	Parameterizing the Asymmetry of the Correlation Peak	108
6.3	Transverse Momentum Dependence	110
7	Monte Carlo	113
7.1	Coulomb Correlation Functions	114
7.2	Momentum Resolution Influence on HBT Radii	115
7.3	Reaction Plane Resolution Influence on HBT Radii	118
7.4	Asymmetry of the Correlation and the Source Displacement	120
8	Discussion of the Results	125
8.1	Transverse Momentum and Centrality Dependence of the HBT Radii	125
8.2	Azimuthally Sensitive HBT Analysis	131
8.3	Pion-Proton Source Displacement	131
8.4	Hydrodynamics and Blast Wave Model Parameterization	137
8.5	Summary	140

CONTENTS

iii

A	step3c – Technical Information	145
B	Non-identical Particle Correlation Functions	150

List of Figures

1.1	Energy density ϵ/T^4 as a function of T/T_c with $n_f = 2, 3$ light quarks as well as two light and one heavier (strange) quarks [KL03]. Arrows depict the energy densities reached in the initial stage of heavy ion collision at the SPS, RHIC, and also for the LHC based on the Bjorken formula (see Eq. 1.19). The arrow parallel to the temperature axis indicate the ideal gas limit.	3
1.2	Phase diagram of hadronic matter [BM00].	4
1.3	Space-time diagram for nucleus-nucleus collision, showing the various stages of the evolution of expanding matter.	5
1.4	Measurement of the separation of two sources, a and b , by correlations of intensities in detectors D1 and D2. L is the distance between an emitting source and detectors, and d is the separation between detectors.	11
1.5	The “out-side-long” coordinate system takes the longitudinal “long” direction along the beam axis. In the transverse plane, the “out” direction is chosen parallel to the transverse component of the pair momentum P_\perp defined as Eq. 1.10, and the “side” direction is perpendicular to the “out” vector.	15
1.6	The origin of the asymmetry in a non-identical particle correlation function. . .	19
2.1	CERES experiment setup used for the measurement of Pb-Au collisions in 2000.	22
2.2	The target system together with Silicon Drift Detectors and part of the trigger system: 1) carbon vacuum beam pipe, 2) PMT housing (BC2), 3) BC2 mirror, 4) 13 Au targets, 5) BC3 mirror, 6) multiplicity counter.	23
2.3	The layout of the trigger and the drift detectors: 1) BC1 mirror, 2) veto scintillator (VC), 3) BC2 mirror, 4) 13 Au targets, 5) BC3 mirror, 6) multiplicity counter (MC), 7,8) silicon drift detectors (SDD).	24
2.4	Operating mode of the silicon drift detectors.	25
2.5	The layout of the interlaced structure of the readout pads used for drift silicon detectors. Each pad is divided into 5 pieces.	25
2.6	Schematic view of the CERES RICH1 detector with a spherical mirror. Produced Cherenkov photons are reflected by a spherical mirror and focused onto the photon detector placed at the focal point of the mirror.	27
2.7	Schematic view of the CERES TPC.	28

2.8	The coordinate system of the TPC.	29
2.9	The layout of the CERES TPC pad plane. One readout channel was connected to four Chevron pads as indicated by the dashed lines. Chevron pads were separated by the ground plane strips in z direction.	31
2.10	The perspective view of the CERES laser system.	32
3.1	Absorption cross-section of CO ₂ and N ₂ as a function of the photon energy [Gar04].	35
3.2	The drift velocity monitor. Right panel: the scheme of GOOFIE (T1, T2 – single-wire cylindrical proportional counters, S1, S2 – α -particles sources); left panel: a photograph with field-defining rings and two trigger detectors mounted along the drift channel.	37
3.3	Top view of the trigger detectors (T) position with respect to the α -particles source (α). The semicircles are plastic holders for both components.	38
3.4	The scheme of the prototype electronic. In the NIM crate the trigger logic was build-up from the discriminator (Disc.) and the logical fan-in fan-out (FI/FO). The flash ADC module (FADC) was sampling incoming signal from the pick-up detector. The latter was supply by the +1.4 kV from the power supply. All slow control parameters e.g. the gas temperature, oxygen contamination, pressure etc. were recording through the multichannel ADC. The CAMAC controller was connected with the PC through the PCI card.	40
3.5	The simulation of electron drift velocity in the Ne-CO ₂ [90-10] and Ne-CO ₂ -N ₂ [90-10-5] gas composition as a function of the electric field performed by the Garfield simulation package.	41
3.6	The energy deposition in the Ne-CO ₂ -N ₂ [90-10-5] gas mixture by the α -particle emitted from an ²⁴¹ Am source as a function of the distance. The comparison between the experimental results (full circle) and the simulations (lines).	42
3.7	The simulation results of previously used pick-up detector. Left panel: the electron drift lines to the three anode wires. Right panel: the multiplication gas factor obtained for layout of anode-cathode wires and the pad cathode.	43
3.8	New design of the pick-up counter. Left top panel: the electric field lines. Left bottom panel: electrons drift line shows a fairly almost uniform electron arrival time. Right panel: the multiplication factor.	44
3.9	The dependences of the gain and the drift velocity as a function of CO ₂ and N ₂ concentration in the ALICE TPC ternary gas mixture.	45
3.10	An example of the pulseheight spectrum accumulated over 2500 events. The blue solid curves are the results of the function fitting 3.4 to each peak.	46
3.11	The time dependence of the drift monitor variable. Top panel: drift velocity as a function of time, the black line is the raw data, and blue line after applying the T/P correction. Middle panel: the gas density. Bottom panel: oxygen contamination.	47

3.12	The time dependence of the pressure and the temperatures.	48
3.13	Correlation between the measured drift velocity and the gas density.	49
3.14	A picture of the new readout board for the GOOFIE monitor together with a short description of the components. The configuration of this board is similar to the front-end electronics of the ALICE TPC.	50
3.15	The block diagram of the new board constructed for the GOOFIE (see text). . .	51
3.16	The data format of the GOOFIE board. The data are organized in 40-bits words ended with the trailer word. The pulseheight spectrum is sampled in bins of 50 ns and each found peak (S) is tagged with two 10-bit words containing time position (T) and number of 10-bit words in the set.	53
3.17	The GOOFIE display application panel.	54
3.18	The corrected drift velocity distribution fitted by Gaussian obtained with the prototype read-out electronics. The derived drift velocity resolution is 0.3 %. .	55
4.1	The reconstructed vertex position along the beam axis after applying the vertex refitting method. The physical position of targets are depicted as horizontal solid lines.	62
4.2	Sketch of the calibration method for small momentum variation. The solid and the dash curves correspond to the nominal and the measured positions of the inverse momentum distribution, respectively. The amount of displacement in the (q/p) -direction is used as an additive correction to $(1/p)$	64
4.3	The position of the minimum in the raw q/p_{comb} distribution as a function of the unit number for six groups of θ_{TPC} track.	64
4.4	Comparison between different methods used to correct the inverse momentum distribution for $\theta \in (0.18, 0.20)$ rad.	65
4.5	Results of the momentum calibration methods. The minimum position of the inverse momentum distribution as a function of unit number for six groups of θ_{TPC} track.	66
4.6	The energy loss as a function of particle momentum from the TPC tracks. The contours represent the pion and proton cuts used in the correlation analysis. . .	67
4.7	The SD-TPC matching distributions. The correlations between $\Delta\theta_{SD-TPC}$ and $\Delta\phi_{SD-TPC}$ are shown in the left top panel. Bottom panels represent projections of two-dimensional SD-TPC matching distribution together with the matching distribution obtained between tracks taken from different events (blue line).	69
4.8	The difference between the SDD and TPC angles vs. ϕ TPC track angle (left plot for ϕ , and right plot for θ). The black points represent the mean position obtained by fitting Gauss distribution to each ϕ_{TPC} slices.	70
4.9	The obtained parameters P0 and P1 describing the momentum dependence of the width of the TPC-SD matching distributions, plotted as a function of θ	71

4.10	Schematic view of a semi-central collision in the center-of-mass frame. The reaction plane is defined by the impact parameter b and the z (beam) axis. The R_p and R_t corresponds to the radius of the projectile and the target nucleus, respectively.	72
4.11	The raw Q_2^Y vs. Q_2^X distribution obtained from the TPC tracks.	73
4.12	The distribution of the reaction plane angle Ψ_2 : raw experimental data – tracks recorded by TPC (RAW), after applying the recentering method, and after dividing the Q components by the widths of the (Q_n^X, Q_n^Y) distribution.	75
4.13	The average value of (Q_n^X, Q_n^Y) obtained for a given unit number, raw data (first and second harmonic).	76
4.14	The recentered average value of (Q_n^X, Q_n^Y) as a function of unit number.	77
4.15	The width of the Q_n^X and Q_n^Y distribution as a function of the unit number.	78
4.16	Left panel: difference between the reaction plane orientation from two sub-events for the most central data bin. The solid line (green) is the Ollitrault fit to the distribution. Right panel: the $\langle \cos [2 (\Psi_2 - \Psi)] \rangle$ obtained from the two different methods is shown as a function of centrality. The resolution of the reaction plane orientation calculated from TPC tracks and from SDD tracks is shown as squares and triangles, respectively. The full symbols correspond to the method proposed in [Oll97] (Met.1), and the open symbols were obtained for the method proposed in [PV98] (Met.2).	79
4.17	Correlations between the three multiplicities in the low intensity minimum bias run.	80
4.18	Multiplicity distributions taken under different running conditions: beam (black) and minimum bias (green) triggers at low beam intensity (runs 1423 and 1424); minimum bias (red) and central (blue) events at high beam intensity (runs 1420 and 1427). The full red histogram represents events taken with the MT (random pulser) trigger during minimum bias run 1424. The solid black histogram represents run 1244: no target, beam trigger, high beam intensity.	82
4.19	Multiplicity distributions from the minimum bias run at low beam intensity (green), normalized to 10^6 beam particles. For comparison, a central run taken at high beam intensity is shown as well (blue).	83
4.20	The edge position of multiplicity distributions as a function of the unit number determined via integration (blue) and via fit (black). The green plot shows the (arbitrarily scaled up) ratio of the two methods.	85
4.21	The calibrated centrality in percent of the geometrical cross section accumulated over all data set. Left panel: correlation between TPC and MC. Middle panel: centrality distribution recorded by MC. Right panel: centrality distribution recorded by the TPC. The solid lines represent the centrality selection used for the two particle correlation analysis presented in this thesis.	86

4.22	Vertex z distribution for the hit pairs from SDD1 and SDD2 in laboratory coordinate system (left) and in the event coordinates (right). The background distribution is depicted as a red line.	86
4.23	Left panel: an example of the extrapolation method for the η between 2.0 to 2.2. Right panel: the charged particle multiplicity as a function of the pseudorapidity for the event centrality integrated from 0 to 5 % of σ_{GEOM} . The raw data is depicted as a black points, the color points correspond to the values extrapolated at $\Delta r = 0$. For comparison, the results of a naive counting SDD tracks are shown as the black dots.	87
4.24	Beam energy dependence of the rapidity density of charge particle.	88
5.1	Left panel: the quality of the track fit in $r(t)$ and $\phi(z)$. The red line represents the cut. Right panel: distribution of the TPC track length: the total number of hits on track (black solid line), the number of fitted hits per track (red dash line). The vertical lines correspond to the cuts applied during the step2 production (dash-dot), and for the particle correlations analysis (solid).	90
5.2	The different topology of pairs in the CERES TPC; a) sailors, b) cowboys. . . .	91
5.3	Two track resolution of the CERES TPC. Number of reconstructed track pairs, normalized to mixed events, $\Delta\phi$ and $\Delta\theta$ for the two pair topologies, sailor (left) and cowboy (right).	92
5.4	The like-sign pion pairs acceptance in the CERES TPC for pairs with relative momentum below 150 MeV/c. The horizontal and the vertical lines represent chosen cuts in the pair transverse momentum and in the pair rapidity, respectively.	93
5.5	One-dimensional distribution of the momentum difference for the like-sign pion pair from the same event (left panel) and from different events (middle panel). The derived correlation function is shown in the right panel.	95
5.6	One-dimensional projection of the three-dimensional correlation function. The fit by Eq. 5.5 is depicted as the blue line, whereas the fit without the Coulomb correction shown by the red line.	97
5.7	The $\pi^-\pi^-$ HBT radii as a function of the pair transverse momentum for different Coulomb correction methods. The HBT radii extracted from the three-dimensional correlation functions by Eq. 5.5 with different Coulomb corrections are shown in the left column. For comparison, the right column presents the HBT radii obtained with the full Coulomb strength. The data were not corrected for the detector resolution. The open red circles represents the uncorrected HBT radii (centrality bin 1-2).	98
5.8	Results of the fit by Eq. 5.5 (blue line) with the parameterization of Coulomb interaction between like-sign particles based on the diluted Gamow factor. The red line shows the fit without Coulomb correction.	99
5.9	The transverse momentum dependence of the raw HBT radii, for $\pi^+\pi^+$ (top) and $\pi^-\pi^-$ (bottom).	100

5.10	Sketch of the analysis method of the reaction plane dependent HBT radii. The space asymmetry in the collision is reflected in the momentum asymmetry of the produced particles depicted as a gray area. Two-pion correlation functions are analyzed separately for 8 bins of the azimuthal angle in respect to the reaction plane.	101
5.11	The reaction plane dependence of the HBT radii and the cross terms integrated over all bins of the pair P_{\perp}	103
6.1	CERES acceptance for pion-proton pairs with the relative pair momentum below 150 MeV/c. The vertical and the horizontal lines represent the bins in the pair rapidity and in the pair transverse momentum, respectively.	106
6.2	An example of the two-dimensional correlation function for π^- - p^+ pairs (left panel). In the right panel the projection on the q_{\parallel} axis with $q_{\perp} \in \{0, 50\}$ MeV/c and the fit by Eq. 8.3 is shown.	107
6.3	Comparison between the two methods (from simulations). Right top panel: one-dimensional correlation functions, left top panel: the one-dimensional projection of two-dimensional correlation function. Left bottom panel: the ratio between C_2^+ and C_2^- correlation functions depicted as a brown star symbols, and the ratio between positive and negative side of the one-dimensional projection depicted as a red circle symbols.	109
6.4	Comparison between the two methods (from experimental data). See Fig. 6.3 for description of the panels.	110
6.5	The source displacement as a function of the pair transverse momentum represented by the asymmetry variable.	111
7.1	The distribution of tracks as a function of the inverse momentum and the θ angle obtained from the simulations.	114
7.2	Coulomb correlation functions for different source sizes.	115
7.3	Comparison between different ways to remove the effect of the finite momentum resolution of detector on the HBT radii (pair P_{\perp} from 1 to 2 GeV/c). . . .	116
7.4	The influence of the finite momentum resolution on the measured $\pi^- - \pi^-$ HBT radii.	117
7.5	The simulation of the reaction plane resolution. The black symbols represent the reaction plane resolution of the CERES experiment.	118
7.6	The influence of the reaction plane resolution on the HBT radii. The solid, dotted, and dash-dotted lines are fits to the three data sets.	120
7.7	Correction factor for the reaction plane angular resolution. The full and the open symbols represent correction factors derived for the $\pi^- \pi^-$ and $\pi^+ \pi^+$ correlation functions respectively.	121
7.8	The momentum resolution influence on the asymmetry of the unlike particles correlation functions.	122

7.9	The asymmetry parameter dependence on the source radii as a function of P_{\perp} .	122
7.10	The asymmetry parameter deviation for different models of particle source emission.	123
7.11	The asymmetry-to-displacement calibration.	124
8.1	Previously obtained HBT radii for the most central events ($<5\%$ $\sigma/\sigma_{\text{GEOM}}$) [A ⁺ 03a] together with the results presented in this work. Both results were corrected for the Coulomb interaction and the detector resolution.	127
8.2	Transverse momentum dependence of the HBT radii corrected for the Coulomb interaction and detector resolution for centrality bin 25-35 %.	127
8.3	Transverse momentum dependence of the HBT radii corrected for the Coulomb interaction and the detector resolution. The top, the middle, and the bottom panel show the radii obtained for the centrality of 0-2.5 %, 2.5-5 %, and 5-7.5 %, respectively.	128
8.4	Transverse momentum dependence of the HBT radii corrected for the Coulomb interaction and the detector resolution. The top, the middle, and the bottom panel show the radii obtained for the centrality of 7.5-10 %, 10-15 %, and 15-25 %, respectively.	129
8.5	The extracted parameters of the emitting source based on the hydrodynamical scenario for three rapidity intervals. All results were obtained for a fixed freeze-out temperature of 120 MeV. Top panel: $Y=1.3-2.3$. Middle panel: $Y=2.3-2.8$. Bottom panel: $Y=1.3-2.8$.	130
8.6	Fourier coefficient of azimuthal oscillations of HBT radii as a function of the event centrality for π^+ and π^- pairs combination (0.0-2.0 GeV/c). The close (open) symbols correspond to the uncorrected (corrected) 2 th -order Fourier coefficient for influence on finite reaction plane resolution. The squared symbols correspond to the results obtained with the different approach of the event mixing background construction (see text).	132
8.7	The two-dimensional HBT correlation functions as a function of the $\phi_{\text{pair}} - \Psi_2$ angle. The z -axis is set to be constant for all bins of $\phi_{\text{pair}} - \Psi_2$ ($0.985 \geq z \geq 1.035$).	133
8.8	The centrality dependence of the source anisotropy measured for different beam energies.	134
8.9	The source displacement ΔR as a function of the pair transverse momentum. The full symbols correspond to asymmetry obtained from the π^+ -p ⁺ (square) and from the π^- -p ⁺ (circle) correlation functions, respectively. The obtained results of the source displacement between (π -p ⁺) from the UrQMD (ver.1.3) are shown as a solid curve (green). The open triangles represent results derived for the unlike pion correlation functions. Fit to the data is based on Eq. 8.4 (see text).	135

8.10	The R_{side} fitted by Eq. 8.4 together with ΔR . Presented radii were integrated over the centrality range (0-25%) and the HBT radii were derive.	136
8.11	The $1-3\sigma$ contours plots of χ^2 , obtained by simultaneous fit of Eq. 8.4 to ΔR and R_{side}	137
8.12	The single transverse momentum spectra [Mar, Rad06] (upper left and middle panel) and results of the elliptic flow [Mil05] analysis from the CERES experiment together with the hydrodynamical predictions (see text).	138
8.13	The HBT radii together with the prediction of the source size based on the hydrodynamical calculations.	139
8.14	The Blast-Wave parameterization of flow and transverse spectra.	141
8.15	The Blast-Wave parameterization of HBT radii.	142
8.16	The Blast-Wave parameterization of pion-proton displacement.	143
B.1	The unlike-charge pion correlation functions.	151
B.2	The π^- - p^+ correlation functions.	152
B.3	The π^+ - p^+ correlation functions.	153

List of Tables

3.1	The plane coefficients used for calculation of the CO ₂ and N ₂ concentration in the ALICE TPC gas mixture.	45
3.2	The list of registers used in the GOOFIE read-out board.	52
4.1	Performance of the step3c production. The two numbers contained in the name denote the version numbers of the step0-2 and the step3 productions, respectively, e.g. prod012.01 means the data were processed with the version 12 of the step0-2 chain, and subsequently with the version 01 of step3.	61
4.2	The charged particle multiplicity $N_{ch}/d\eta$ and the rapidity density of charge particles extrapolated at the midrapidity for different centralities.	88
5.1	The centrality bins used in the analysis. The geometrical cross section for Pb+Au collisions σ_{GEOM} was assumed to be 6.94 b.	91
5.2	P_{\perp} and Y intervals used in the analysis. For each bin the mean P_{\perp} is given. . .	94
6.1	The different p_{\perp} intervals used in the analysis of the non-identical particle correlation together with their mean p_{\perp} values.	107
6.2	The significance of both methods.	110
8.1	The collection of fit results obtained for $T_f = 120$ MeV.	137
8.2	Blast wave fit results.	140
A.1	The list of variables stored in the CSEvent class.	145
A.2	The list of variables stored in the CSTrack class.	146
A.3	The location of the directories used during production of the step3c.	148
A.4	The default name of the calibration files was linked with the names described in the column used file. The filed column correspond to the configuration of the magnetic field in TPC.	149
A.5	The configuration files of the given COOL object used during step3c production. . .	149

Chapter 1

Introduction

Ultra-relativistic heavy ion collisions offer a unique possibility to examine the properties of the strongly interacting matter. The description of such interacting many-body system at high energy densities ϵ is given by the nonperturbative quantum chromodynamics (QCD). For the energy density of $\epsilon \approx 1 \text{ GeV/fm}^3$ the calculations predict a phase transition from a state formed by hadrons to a new state of deconfined quarks and gluons [CP75, Pol78] called the Quark Gluon Plasma (QGP) [Shu78, McL86]. The transition is accompanied by the restoration of the chiral symmetry which is spontaneously broken in the QCD ground state. It is believed that free quarks and gluons existed as the QGP in the Early Universe up to few microseconds after the Big Bang [Oli91]. It has also been suggested that cold and highly compressed QGP may exist in the core of neutron stars [EKO91b, EKO91a]. Understanding of the evolution and properties of the new state of matter created during ultra-relativistic heavy ion collisions would provide a deeper insight into these aspects of cosmology.

Experiments at the Alternating Gradient Synchrotron (AGS), the Super Proton Synchrotron (SPS), and the Relativistic Heavy Ion Collider (RHIC) were and still are looking for signatures of the QGP formation [MAT89, MAT04, MAT06]. It is a challenging task taking into account the diameter of the reaction volume of several fermi and the very short life time of the QGP state, about 5-10 fm/c. Moreover, the signals coming from the QGP are combined with those emitted from the hot hadronic gas phase and thus a combination of various signatures may be needed to conclude whether the quark-gluon plasma was created or not.

The CERES spectrometer was set up at the CERN SPS facility in order to investigate heavy-ion collisions with the focus on the measurement of the low-mass e^+e^- pairs emitted in proton- and ion-induced collisions at ultra-relativistic energies. After upgrade with the Time Projection Chamber the experiment extended its capability to hadronic signatures of the hot and dense matter. This work focuses on the systematic study of the two-particle correlations created during collisions of Pb-Au nuclei at 158 GeV/c per nucleon. The two-particle correlation technique provides access to the information about the space-time geometry and the dynamics

of the collision region and allows to determine the relative emission times or positions of the different particle species.

1.1 Strongly Interacting Matter

The theory of the strong interaction, called quantum chromodynamics (QCD), describes the forces between the colored particles, quarks and gluons. Two remarkable properties of this theory are the *asymptotic freedom* and the *confinement*. The strength of the strong interaction is given by the QCD running coupling constant $\alpha_s(\mathbf{q}^2)$, which depends on the momentum transfer \mathbf{q}

$$\alpha_s(\mathbf{q}^2) = \frac{4\pi}{\left(11 - \frac{2}{3}n_f\right) \ln\left(\frac{\mathbf{q}^2}{\Lambda_{QCD}^2}\right)}, \quad (1.1)$$

where n_f is the number of flavors with mass below $\sqrt{|\mathbf{q}^2|}$ and Λ_{QCD}^2 is the QCD scale parameter introduced in the renormalization process. In the limit of $\alpha_s(\mathbf{q}^2) \rightarrow 0$ the coupling strength between colored particles is vanishing resulting in free quarks and gluons. Expressing the $\alpha_s(\mathbf{q}^2)$ in terms of the coordinate space r , the coupling strength grows like r^2 . Therefore, at large distances the binding between quarks grows giving rise to a strong attractive force confining quarks into hadrons. The quark model introduced by Gell-Mann and Zweig, based on the symmetries and quantum numbers, categorized hundreds of particles states known at that time [GM64]. They postulated that all hadrons are built from smaller constituents called quarks. All hadrons are divided into two groups, called mesons and baryons. Mesons are composed of a quark and anti-quark ($q\bar{q}$) while baryons consist of three quarks (qqq) or ($\bar{q}\bar{q}\bar{q}$). The quarks occur in six *flavors*: u, d, s, c, t, b , have spin $1/2$, and are ruled by the Fermi-Dirac statistics. Since some of the baryons consist of three identical quarks, an additional quantum number was introduced, called *color*, in order to preserve the Pauli principle. There are three different colors a quark can carry, say *red*, *green*, and *blue*. All observed hadrons are colorless (or white) and can be constructed either from *color-anti color* (mesons) or three different *colors* (baryons). Gluons, the *color-charged* field quanta of the strong interaction, can have eight different color states. Therefore, QCD is a gauge theory based on the SU(3) color symmetry group.

Based on the fundamental properties explained above, QCD predicts a transition from a state formed by hadrons to a plasma of deconfined quarks and gluons, at a sufficiently high energy density [CP75, Pol78]. The transition energy density is a few GeV/fm^3 compared with $0.15 \text{ GeV}/\text{fm}^3$ of nuclear matter in its ground state. Lattice QCD calculations predict that such transition should be accompanied by the chiral symmetry restoration which is spontaneously broken at low temperatures [LW74]. Below the critical temperature (T_c) quarks are confined in hadrons with dynamically generated masses of a few hundred MeV. The expectation value of the *quark condensate* $\langle \bar{\psi}\psi \rangle \approx -(235 \text{ MeV})^3$ describes the density of $q\bar{q}$ pairs in the QCD

vacuum and the fact that it is not vanishing is directly related to the chiral symmetry breaking [Kar02]. Lattice QCD calculations show that around the critical temperature the effective masses of quarks are no longer given by the dynamically generated masses but rather by their current masses. In the limit of zero current quark masses the quark condensate is vanishing and chiral symmetry is restored. The results of such calculation are shown in Fig. 1.1. Based on these calculations and on the simple physical intuition one can sketch the phase diagram of strongly interacting matter shown in Fig. 1.2. The hatched band in the temperature vs. baryon chemical potential plane (T, μ_b) there represents a boundary between a gas of hadronic resonances at low energy densities and a QGP phase at high energy densities [BMS02]. The phase transition between QGP and hadronic matter is thought to be of first order at non-vanishing μ_b . However, as $\mu_b \rightarrow 0$ quark masses become significant and a sharp phase transition transforms into a rapid but smooth cross-over. The hadrochemical freezeout points are determined from thermal model analysis [BMSWX96, BMHS99] of heavy ion collision data at SIS, AGS, and SPS energy [Sta99, BM00]. The arrow connection the chemical and the thermal freeze-out curves at the SPS corresponds to isentropic expansion.

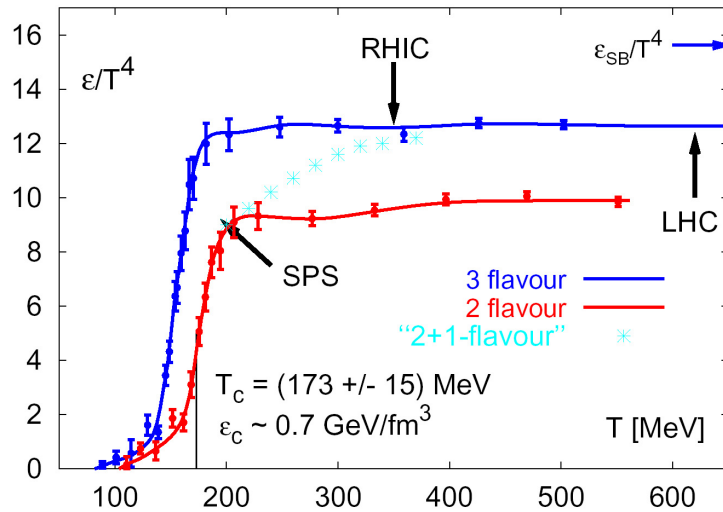


Figure 1.1: Energy density ϵ/T^4 as a function of T/T_c with $n_f = 2, 3$ light quarks as well as two light and one heavier (strange) quarks [KL03]. Arrows depict the energy densities reached in the initial stage of heavy ion collision at the SPS, RHIC, and also for the LHC based on the Bjorken formula (see Eq. 1.19). The arrow parallel to the temperature axis indicate the ideal gas limit.

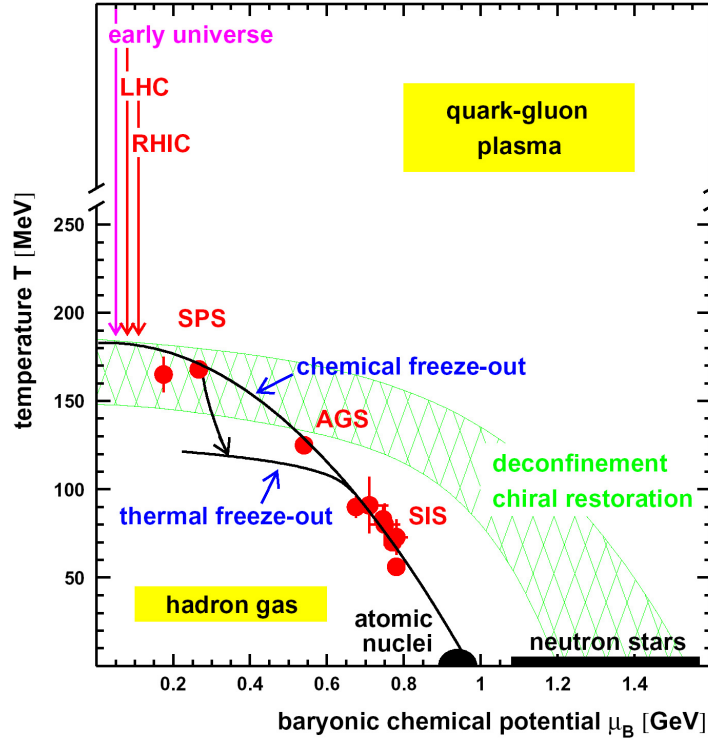


Figure 1.2: Phase diagram of hadronic matter [BM00].

1.2 Heavy Ion Collision Experiments

First heavy ion experiments were performed in the sixties in nuclear emulsions exposed to cosmic-ray nuclei in balloon flights. During that time, first ideas and methods were created to analyze such data which are used still nowadays. In the late sixties, acceleration of heavy ions began. The generation of proton synchrotrons at CERN, Brookhaven, and Protvino at that time reached few hundred MeV/c per nucleon. The accelerators operating nowadays can reach collision energies up to 40 TeV, for the heaviest colliding systems, with a high beam luminosity. That opens a great opportunity to study different colliding systems for various beam energies, and to explore the phase diagram of nuclear matter in hunt for the QGP.

The space-time evolution of an ultrarelativistic heavy ion collision is shown in Fig. 1.3. Due to the Lorentz contraction the colliding nuclei are highly compressed in the beam direction. At the first instants of the collision, called *pre-equilibrium*, the energy deposited in the collision volume is redistributed into other degrees of freedom. After the time $\tau \approx 1$ fm/c (*formation time*) the deposited energy may lead to the formation of the QGP. At this stage one can assume that the system is in thermal equilibrium, and thus the further evolution of the system can be described in terms of hydrodynamical models. The pressure inside the hot and dense medium

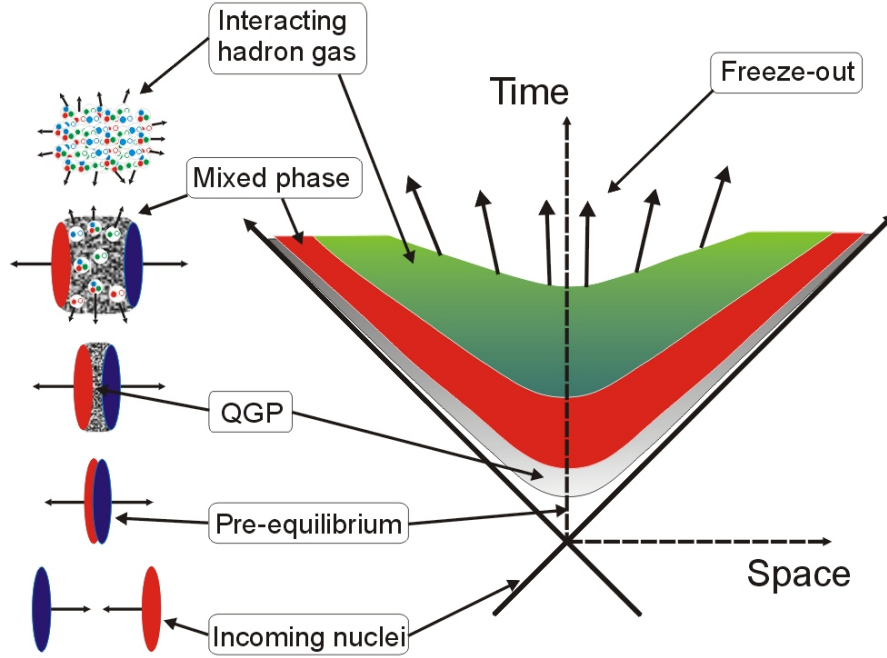


Figure 1.3: Space-time diagram for nucleus-nucleus collision, showing the various stages of the evolution of expanding matter.

leads to an expansion of the system during which its temperature and density are decreasing. If the deconfinement phase transition is of first order the system may go through a *mixed phase* in which the formed hadrons coexist with the deconfined quarks and gluons. Finally, all quarks and gluons condensate into a state of the highly interacting hadron gas which further expands and cools to the point called *chemical freeze-out*, where the last inelastic collisions occur. At this point abundances of all hadrons are fixed and only elastic collisions between particles continue. The final stage where all elastic collisions vanish (*thermal freeze-out*) is reflected in the momenta of the measured particles.

1.2.1 Basics

A particle emitted from an ultrarelativistic nucleus-nucleus collision is commonly described in terms of its transverse momentum p_{\perp} and the rapidity y . The four-momentum vector \mathbf{p} of an emitted particle satisfies the mass-shell constraint $\mathbf{p}^2 = \mathbf{p}^{\mu}\mathbf{p}_{\mu} = m^2$ has only three degrees of freedom. In Cartesian coordinates the particle momentum $\vec{\mathbf{p}}$ can be decomposed in the

longitudinal (p_{\parallel}) and the transverse (p_{\perp}) momentum components. The latter is defined as

$$p_{\perp} = \sqrt{p_x^2 + p_y^2}, \quad (1.2)$$

where p_x and p_y are components perpendicular to the beam direction. The p_{\parallel} component is parallel to the z -axis which coincides with the beam direction. For all presented relations the speed of light c is set to unity. The rapidity variable is defined in terms of the particle energy E and the longitudinal component of the momentum p_{\parallel}

$$y = \frac{1}{2} \ln \left(\frac{E + p_{\parallel}}{E - p_{\parallel}} \right) = \ln \left(\frac{E + p_{\parallel}}{m_{\perp}} \right), \quad (1.3)$$

where $m_{\perp} = \sqrt{m^2 + p_{\perp}^2}$ is the transverse mass with m being the rest mass of particle. In the case of the symmetric system collisions with fixed targets the center-of-mass frame moves with the rapidity $y_{CMS} = 0.5 \cdot y_{beam}$, called therefore mid-rapidity. This leads to the particle rapidity spectrum being symmetric around y_{CMS} and allows to complement the measured particle spectra by reflection. Lorentz transformation between two coordinate frames along the direction of the beam in terms of rapidity has the simple form

$$y_2 = y_1 + y_{12}, \quad (1.4)$$

where $y_{12} = \ln [\gamma_L (1 + \beta_L)]$ depends on the β_L and γ_L values related to the velocity of the moving frame. It is this simple result which gives the rapidity variable its importance as a tool in the analysis of particle production data. The velocity of the particle is given by

$$\beta = \frac{p}{E} = \sqrt{1 - \frac{1}{\gamma^2}}. \quad (1.5)$$

In most experiments angles are measured rather than the three components of \vec{p} . For a particle emitted at a polar angle θ a variable analogous to rapidity, called pseudo-rapidity, can be defined as

$$\eta = -\ln \tan \frac{\theta}{2}. \quad (1.6)$$

Since the mass and the momentum do not enter, this observable is easier to determine. It coincides with rapidity at $p_{\perp} \gg m$. It is useful to rewrite its definition in the form

$$\eta = \frac{1}{2} \ln \left(\frac{p + p_{\parallel}}{p - p_{\parallel}} \right) \quad (1.7)$$

which appears to be almost equivalent to Eq. 1.3. Some useful relations, which provide transformation between $(E, p_{\perp}, p_{\parallel})$ and (m_{\perp}, y) , are

$$\begin{aligned} E &= m_{\perp} \cosh(y), \\ p_{\parallel} &= m_{\perp} \sinh(y) = E \tanh(y) = p \tanh(\eta), \\ y &= \tanh^{-1}(\beta). \end{aligned} \quad (1.8)$$

For the two-particle analysis, the main topic of this dissertation, it is useful to define additional variables like the pair four momentum

$$P = p_1 + p_2 , \quad (1.9)$$

the pair transverse momentum

$$P_\perp = \sqrt{P_x^2 + P_y^2} , \quad (1.10)$$

and the momentum difference

$$q = p_2 - p_1 . \quad (1.11)$$

In the pair center-of-mass frame and for particles with the same masses the length of the spatial component of the four-vector q , (q_x, q_y, q_z) , becomes equal to the Lorentz invariant four-momentum difference

$$q_{inv} = \sqrt{-(q)^2} = \sqrt{-((E_2 - E_1)^2 - (\vec{p}_2 - \vec{p}_1)^2)} . \quad (1.12)$$

1.2.2 Landau Scenario

One of the first description of the space-time evolution of the heavy ion collisions was proposed by Landau in [Lan53]. In this model, the two Lorentz-contracted hadrons or nuclei are completely stopped and the whole energy carried by the participants is transferred into the system with a large energy density (ε) and with the particle production around mid-rapidity. The assumption of the full thermalization of the system in a volume of size $V \approx m_p/\sqrt{E}$, where E is the laboratory energy, justified the use of the classical relativistic hydrodynamics of an ideal (non-viscous and non-heat-conducting) fluid. The energy-momentum tensor $T^{\mu\nu}$ is

$$T^{\mu\nu} = (\varepsilon + p) u^\mu u^\nu - g^{\mu\nu} p , \quad (1.13)$$

where $u^\mu(x)$ is the four-velocity field with $u^2 = u_\mu u^\mu = 1$ and ε, p are the scalar densities of energy and pressure, respectively. The hydrodynamics equations are given by

$$\partial^\mu T_{\mu\nu} = 0 . \quad (1.14)$$

In order to solve these equations an equation of state $\varepsilon = \varepsilon(T, p)$ is required. Landau assumption was based on the equation of state describing the non-interacting gas of photons

$$p = \frac{1}{3} \varepsilon \quad (1.15)$$

which is characteristic of blackbody radiation. Eqs. 1.14 imply that the initial state entropy, which is produced in the process of thermalization, is distributed in the rapidity space with a

Gaussian form, and the width is determined by the initial Lorentz contraction. In addition, the model assumed that the motion of the ideal fluid has to be adiabatic and thus the entropy of the individual regions of the system remains unchanged during the expansion. A straightforward consequence is the multiplicity formula $N = K E^{1/4}$. The energy density of the created system is given by the energy divided by the volume of the reaction zone. However, in the Landau picture, the volume of the system is known only approximately which leads to a large uncertainty in the estimation of the energy density of created matter. This model should be satisfactory up to AGS collisions energies where the nuclear stopping power is quite large. Above these energies the fraction of the longitudinal energy, which is still present after the collision in the nuclei, is about half of the initial one (transparency of the collisions). Compared to the collisions with full stopping, this inherent longitudinal expansion influences the system's evolution and must be considered in the calculations. Such description of the space-time evolution of the colliding system was proposed by Bjorken [Bjo83] and is discussed in the next section.

1.2.3 Bjorken Scenario

The modification of the initial boundary condition of the Landau scenario leads to a different particle production distribution and energy density of the colliding system. The Bjorken scenario assumes that at a sufficiently high energy a plateau in the particle production as a function of the rapidity occurs. The rapidity densities dN/dy are assumed to be independent of rapidity for at least a few units of rapidity around mid-rapidity in $p + p$ and $p + A$ collisions from which it is deduced that the same is true for $A + A$ collisions. Thus, this space-time evolution scenario is a boost-invariance model. At high energy heavy ion collisions, like for the SPS energies, the nucleons can still have enough momentum to proceed forward and move away from the collision zone. Transverse expansion of the source can be neglected in the first approximation, because of the large initial transverse scale of the source as compared to its longitudinal scale. This reduces the situation to a two-dimensional problem in the coordinates z and t . Due to the homogeneity of the source in all frames there is no pressure gradient to change the longitudinal flow, and the velocity of each fluid element stays the same. If it is assumed that, at $t = 0$, right after the two nuclei have collided, the longitudinal extent of the source is negligible, the relation $z = \beta t$ therefore holds at all times $t > 0$. The proper time τ is

$$\tau = \sqrt{t^2 \left(1 - \frac{z^2}{t^2}\right)} = \sqrt{t^2 - z^2} = \frac{t}{\gamma}, \quad (1.16)$$

and the z and t variables are related to the space-time rapidity via

$$\begin{aligned} t &= \tau \cosh(y), \\ z &= \tau \sinh(y), \end{aligned} \quad (1.17)$$

with

$$y = \frac{1}{2} \ln \left(\frac{t+z}{t-z} \right). \quad (1.18)$$

Since the evolution of the system looks the same in all mid-rapidity like frames, the energy density and pressure only depends on τ . This gives rise to hyperbolae of constant energy densities that can be used to distinguish between different phases in the evolution of the collision. The energy density created during collision of nuclei is given by

$$\varepsilon = \frac{\langle E_h \rangle}{\pi R_A^2 \tau_0} \left(\frac{dN_h}{dy} \right)_{y=0}, \quad (1.19)$$

where $\left(\frac{dN_h}{dy} \right)_{y=0}$ is the number of hadrons per unit of rapidity produced at midrapidity, $\langle E_h \rangle$ is the average energy of hadrons, R_A is the nuclear radius, and τ_0 corresponds to the formation time of the medium. The latter was estimated by Bjorken to be $\tau_0 = 1/\Lambda_{QCD} \approx 1 \text{ fm/c}$.

1.2.4 Observables

The deconfinement state of quarks and gluons is believed to occur above certain temperature or/and density of the matter. During ultra-relativistic heavy ion collisions such hot and dense state of matter can be produced for a time of a few fermi units. This short-live QGP state can only be accessed with probes which will carry the information about it after the system hadronizes. Heavy ion experiments detect mostly the charged hadrons which have lost most of the information about the early stages of the collisions through rescattering and collective expansion. On the other hand, the thermalized QGP would emit thermal radiation ($\gamma^* \rightarrow e^+e^-$ or $\mu^+\mu^-$) in form of leptons and real photons produced in quark-anti quark annihilation ($q\bar{q} \rightarrow \gamma g$) and Compton scattering processes ($qg \rightarrow \gamma q$). The photons and leptons interact with matter through the electromagnetic interaction and their mean free path is larger than the size of the system ($\lambda \approx 10^3 \text{ fm}$). Therefore, they contain information of the system at the time of their emission and transport it almost unaffected to the detectors. Theoretical models expect a shift of the ρ peak to lower masses [BR96] or a broadening and slight shift up [RW00] when ρ is immersed in high density hadronic matter. Such process is attributed to pion annihilation $\pi\pi \rightarrow \rho \rightarrow e^+e^-$, thus explaining the enhancement observed in the dilepton mass spectrum in heavy ion collisions. The results of a dilepton analysis, performed on the same experimental data set as used for the two-particle correlations analysis discussed in this dissertation, are presented in [MftCC06].

Another observable related to the early stage of the collision is the anisotropic transverse flow. The anisotropic shape of the overlapping nuclei region created in the non-central collisions causes pressure gradient in the system. The almond shape of the overlapping nuclei has its shorter axis in the reaction plane. Therefore, the transverse velocity and the acceleration is larger in-plane than out-of-plane. Thus, the directions of the outgoing particles are correlated to the orientation of the reaction plane. The dependence on the particle emission azimuthal angle, ϕ , measured with respect to the reaction plane orientation, Ψ , can be expressed as Fourier

series [VZ96]

$$E \frac{d^3 N}{d^3 p} = \frac{1}{2\pi} \frac{d^2 N}{p_t dp_t dy} \left(1 + 2 \sum_{n \geq 1} v_n \cos(n(\phi - \Psi)) \right) \quad (1.20)$$

where $v_n = \langle \cos(n(\phi - \Psi)) \rangle$ are the Fourier coefficients. The first two harmonics ($n=1,2$) describe the directed and the elliptic flow, respectively. Since the flow builds up throughout the evolution of the system, it contains information on both the partonic and the hadronic stage.

Information about the space-time evolution and dynamics of the colliding system accessible through the single momentum spectra and through multiparticle observables are significantly limited in comparison to two-particle momentum distributions. While from the single transverse momentum spectra or from the particle yield analysis the temperature of the freeze-out can be extracted they miss information of the size and the lifetime of the particle emitting source. The only known way to obtain direct experimental information about geometry and dynamics of the reaction zone is through two-particle intensity interferometry. The intensity interferometry provides crucial information for an assessment of theoretical models which try to extract the energy densities of the source from the measured single particle spectra and particle multiplicity density in momentum space. Reliable estimates of the source volume and the energy density are, on the other hand, indispensable for an experimental proof that high energy collisions can successfully generate large volumes of matter with extreme energy density, where a transition into deconfined quark matter might be possible. Therefore, a systematic analysis of the two-particle correlations are of great importance in the search of the QGP. The detailed information concerning the two-particle analysis are presented in following sections as it is the main topic of this dissertation.

1.3 Two-particle Interferometry

The technique of intensity interferometry was introduced by Hanbury-Brown and Twiss to measure angular dimensions of stars [HBT56] and it is after them that this technique is called **HBT**. In the sixties this technique was independently discovered and applied to the subatomic physics as a tool to investigate the space-time evolution of the elementary-particle and nuclear collisions. In the original astrophysics applications of the technique the source was a distant radio-wave emitter while in applications involving the collision of nuclei or particles the source is the reaction region. Experimentally, particles interferometry was first used by Goldhaber, Goldhaber, Lee, and Pais (*GGLP*) [GGLP60] to determine the dimensions of the pion production region in $p\bar{p}$ annihilation. They suggested that the observed enhancement of close pairs of identical pions is a consequence of the Bose-Einstein symmetrization. The interpretation of pion emission in terms of intensity interferometry was pursued more than a decade later by Shuryak [Shu73]. Kopylov and Podgoretskii expressed the HBT effect in terms of the two-particle correlation functions [KP71] and settled the basis of the technique in nuclear

collisions.

In contrast to the conventional amplitude interferometry, where the interference pattern is observed when coherent particles pass through slits, in the intensity interferometry a correlation function ($C_2 = (\langle n_{12} \rangle / \langle n_1 \rangle \langle n_2 \rangle) - 1$) is constructed from the number of counts n_1 and n_2 measured at positions D1 and D2. In Fig. 1.4 the schematic representation of the emissions of two indistinguishable particles observed in detectors is shown. The correlation function is proportional to the intensity of the particle pairs arriving at D1 and D2. The fact that the identical particles cannot be distinguish between themselves imply that the origin of the observed particle correlations is the symmetry (anti-symmetry) of the quantum mechanical wave functions of identical bosons (fermions).

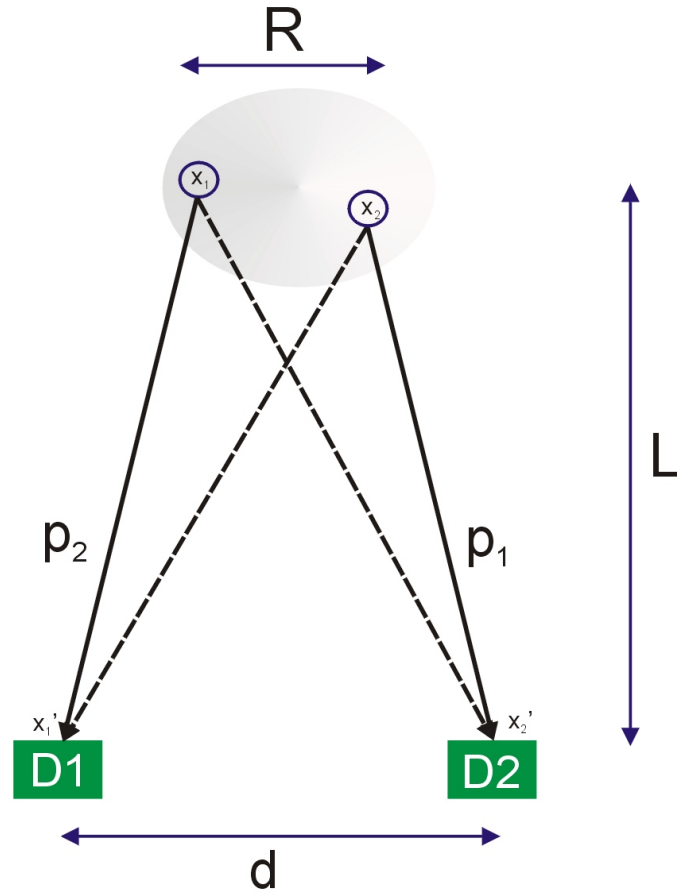


Figure 1.4: Measurement of the separation of two sources, a and b , by correlations of intensities in detectors D1 and D2. L is the distance between an emitting source and detectors, and d is the separation between detectors.

1.3.1 Correlation Function and Source Function

The simplest picture of HBT interferometry, from which it is possible to deduce the fundamental idea, is to consider two distant random points sources of particles, \mathbf{x}_1 and \mathbf{x}_2 , within some generalized source, and a pair of detectors D1 and D2 placed at \mathbf{x}'_1 and \mathbf{x}'_2 , respectively, as depicted in Fig. 1.4. The emitted particles can be represented by plane waves which must be symmetrized (antisymmetrized) according to the Bose-Einstein (Fermi-Dirac) statistics present

$$\Psi = \frac{1}{\sqrt{2}} \left[e^{i(\mathbf{x}'_1 - \mathbf{x}_1) \cdot \mathbf{p}_1} e^{i(\mathbf{x}'_2 - \mathbf{x}_2) \cdot \mathbf{p}_2} \pm e^{i(\mathbf{x}'_1 - \mathbf{x}_2) \cdot \mathbf{p}_1} e^{i(\mathbf{x}'_2 - \mathbf{x}_1) \cdot \mathbf{p}_2} \right]. \quad (1.21)$$

The two measured momenta are denoted as p_1 and p_2 . The probability density of a system of two identical bosons is then given by the square of the plane wave function

$$|\Psi_{1,2}|^2 = |\Psi_{2,1}|^2 = 1 + \cos[(\mathbf{p}_2 - \mathbf{p}_1) \cdot (\mathbf{r}_2 - \mathbf{r}_1)]. \quad (1.22)$$

Then the probability of measuring two particles with momenta p_1 and p_2 in the detectors is given by the integration of the probability density $|\Psi_{1,2}|^2$ over the emission function $S(\mathbf{x}, \mathbf{p})$,

$$P(\mathbf{p}_1, \mathbf{p}_2) = \int S(\mathbf{x}_1, \mathbf{p}_1) S(\mathbf{x}_2, \mathbf{p}_2) |\Psi_{1,2}|^2 d^4\mathbf{x}_1 d^4\mathbf{x}_2, \quad (1.23)$$

while the single particle probability is expressed by

$$P(\mathbf{p}) = \int S(\mathbf{x}, \mathbf{p}) d^4\mathbf{x}. \quad (1.24)$$

Introducing Eq. 1.21 in Eq. 1.23 and assuming that the emission function has a smooth momentum dependence, the two-particle probability can be expressed as

$$P(\mathbf{p}_1, \mathbf{p}_2) = P(\mathbf{p}_1) P(\mathbf{p}_2) \pm \int d^4\mathbf{x} \cos(\mathbf{q} \cdot \mathbf{r}) \cdot \int S\left(\mathbf{R} + \frac{\mathbf{X}}{2}, \mathbf{k}\right) S\left(\mathbf{R} - \frac{\mathbf{X}}{2}, \mathbf{k}\right) d^4\mathbf{X}, \quad (1.25)$$

where $\mathbf{R} = \mathbf{x}_2 - \mathbf{x}_1$, $\mathbf{X} = \frac{1}{2}(\mathbf{x}_1 + \mathbf{x}_2)$, r is relative separation and last term corresponds to the relative distance distribution [WH99]. The correlation function is defined as the two-particle probability (1.24) normalized to the products of single particle probabilities and is equal to

$$C(\mathbf{q}, \mathbf{P}) \approx 1 \pm \frac{|\int d^4x S(x, P) \exp(i\mathbf{q} \cdot \mathbf{x})|^2}{|\int d^4x S(x, P)|^2}. \quad (1.26)$$

The expression takes the plus sign for boson pairs and the minus sign for fermion pairs. The source function $S(\mathbf{x}, \mathbf{P})$ in Eq. 1.26 describes the single particle densities at freeze-out. The source function can be identified with the Wigner transform of the density matrix associated with the classical source amplitudes [Hei96a]. This Wigner density is a quantum mechanical

object defined in phase-space of \mathbf{x} and \mathbf{P} . The integration over phase-space leads to the classical source density in momentum or coordinate space and provides the probability of finding at space-time point \mathbf{x} a source which emits a particle with momentum \mathbf{P} . The simplest approximation of the emission source model is given by space-time Gaussians in its center-of-mass frame

$$S(\mathbf{x}, \mathbf{P}) = f(\mathbf{P}) \exp \left[-\frac{x^2 + y^2}{2R_\perp^2} - \frac{z^2}{2R_\parallel^2} - \frac{(t - t_0)^2}{2(\Delta t)^2} \right]. \quad (1.27)$$

The overview of the different source models can be found in [CNH95].

The space-time saddle point $\bar{\mathbf{x}}(\mathbf{P})$ of the emission function $S(\mathbf{x}, \mathbf{P})$ is defined via four equations [AS95]

$$\frac{\partial}{\partial x_\mu} \ln(S(\mathbf{x}, \mathbf{P}))|_{\bar{\mathbf{x}}} = 0, \quad (1.28)$$

where $\mu = \{0, 1, 2, 3\}$. The saddle point is a point in space-time which has the maximum probability of emitting a particle with momentum \mathbf{P} .

The correlation function between two identical bosons is sensitive to the following physical quantities

- the geometrical extension of the collision region at the time of last hadronic scattering (freeze-out),
- the freeze-out time and particle emission duration,
- the collective velocity of the expanding collision region in the direction parallel and perpendicular to the beam,
- the azimuthal asymmetry of the particle source in collisions with a finite impact parameter collisions.

The experimental two-particle correlation function is constructed from the single- and two-particle cross sections

$$C(\mathbf{p}_1, \mathbf{p}_2) = \sigma_0 \frac{\frac{d^3\sigma}{d^3p_1 d^3p_2}}{\frac{d^3\sigma}{d^3p_1} \frac{d^3\sigma}{d^3p_2}}. \quad (1.29)$$

The details of the procedure are explained in Section 5.2.

1.3.2 Coordinate Systems and Variables

The widely used Gaussian parameterization of the experimental two-particle correlation functions provides a relationship of the corresponding width parameters (HBT radii) with the space-time structure of the source. This relation is based on a quadratic saddle-point approximation

to the true space-time dependence of the emission function and yields

$$S(\mathbf{x}, \mathbf{P}) \approx S(\bar{\mathbf{x}}(\mathbf{P}), \mathbf{P}) \exp \left[-\frac{1}{2} (\mathbf{x} - \bar{\mathbf{x}}(\mathbf{P}))^\mu B_{\mu\nu}(\mathbf{P}) (\mathbf{x} - \bar{\mathbf{x}}(\mathbf{P}))^\nu \right], \quad (1.30)$$

where the symmetric curvature tensor $B_{\mu\nu}$ is given by

$$B_{\mu\nu}(\mathbf{P}) = -\partial_\mu \partial_\nu \ln(S(x, P))|_{\bar{x}}. \quad (1.31)$$

The latter contains, in general, ten independent components, however, only six \mathbf{P} -dependent parameters can be measured by making a Gaussian fit in \mathbf{q} to the measured correlation function, due to the on-shell constraint.

Introducing the following notation of the \mathbf{P} -dependent average of an arbitrary space-time function $\xi(\mathbf{x})$ [CSH95] with the source density $S(\mathbf{x}, \mathbf{P})$

$$\langle \xi \rangle \equiv \langle \xi(\mathbf{x}) \rangle (\mathbf{P}) = \frac{\int d^4\mathbf{x} \xi(\mathbf{x}) S(\mathbf{x}, \mathbf{P})}{\int d^4\mathbf{x} S(\mathbf{x}, \mathbf{P})} \quad (1.32)$$

it is possible to express the correlation function Eq. 1.26 in form

$$C(\mathbf{q}, \mathbf{P}) \approx 1 \pm |\langle \exp(i\mathbf{q} \cdot \mathbf{x}) \rangle (\mathbf{P})|^2. \quad (1.33)$$

The space-time coordinates $(\mathbf{x} - \bar{\mathbf{x}}(\mathbf{P}))^\mu$ in Eq. 1.30 are defined relative to the “effective source center” $\bar{\mathbf{x}}(\mathbf{P})$ for bosons emitted with momentum \mathbf{P} . Furthermore, within the saddle-point approximation Eq. 1.30, the following relations hold

$$\langle \mathbf{x}_\mu \rangle = \bar{\mathbf{x}}_\mu(\mathbf{P}), \quad (1.34)$$

$$(B^{-1})_{\mu\nu}(\mathbf{P}) = \langle \mathbf{x}_\mu \mathbf{x}_\nu \rangle - \langle \mathbf{x}_\mu \rangle \langle \mathbf{x}_\nu \rangle. \quad (1.35)$$

The saddle point is thus the average space-time point from which particle pairs with momentum \mathbf{P} are emitted, and the component of the inverse of the curvature tensor $(B^{-1})_{\mu\nu}(\mathbf{P})$ gives the space-time correlations of the source. The four diagonal elements

$$(B^{-1})_{\mu\mu}(\mathbf{P}) = \langle \mathbf{x}_\mu^2 \rangle - \langle \mathbf{x}_\mu \rangle^2 \quad (1.36)$$

can be understood as the squares of the “lengths of homogeneity” of the source as seen by the pairs with momentum \mathbf{P} [AS95]. Based on the approximations of Eq. 1.26 and Eq. 1.30 the Gaussian form of the correlation function can be written as

$$C(\mathbf{q}, \mathbf{P}) = 1 \pm \exp \left[-\mathbf{q}^\mu \mathbf{q}^\nu (B^{-1})_{\mu\nu}(\mathbf{P}) \right]. \quad (1.37)$$

This involves the smoothness and on-shell approximations which permit to write the space-time variances $(B^{-1})_{\mu\nu}(\mathbf{P})$ as a function of \mathbf{P} only. Different Gaussian parameterizations of Eq. 1.37

exist depending of the choice of the three independent components, the fourth component of \mathbf{q} in Eq. 1.11 is fixed by the requirement that the final state particles are on-shell

$$\mathbf{q} \cdot \mathbf{P} = (p_2^2 - p_1^2) = 0 \Rightarrow q_0 = \frac{\mathbf{P} \cdot \mathbf{q}}{P_0}, \quad (1.38)$$

and thus cannot be studied independently of the other three. The Cartesian parameterization proposed by G.Bertsch and S.Pratt [Ber89, Pra86b] is based on an elimination of the temporal component from Eq. 1.37 via the mass-shell constraint, $q^0 = \beta_\perp q_{out} + \beta_{long} q_{long}$, with $\beta_\perp = |P_\perp/P^0|$ being the velocity of the particle pair transverse to the beam direction while β_{long} is its longitudinal component. The decomposition of the relative momentum three-vector $\vec{\mathbf{q}}$ in the “out-side-long” coordinate system is shown in Fig. 1.5. Therefore, Eq. 1.37 can be expressed by the relation

$$C(\mathbf{q}, \mathbf{P}) = 1 \pm \exp \left[- \sum_{i,j=out,side,long} R_{ij}^2(\mathbf{P}) q^i q^j \right], \quad (1.39)$$

where the six HBT “radius parameters” $R_{ij}^2(\mathbf{P})$ are given as [CSH95, HB95]

$$R_{ij}^2(\mathbf{P}) = \left\langle \left((x - \bar{x}(\mathbf{P}))_i - \beta_i \tilde{t} \right) \left((x - \bar{x}(\mathbf{P}))_j - \beta_j \tilde{t} \right) \right\rangle, \quad i, j = out, side, long, \quad (1.40)$$

through the space-time variances of the source function. In general the correlation function $C(\mathbf{q}, \mathbf{P})$ depends not only on P_\perp and P_{long} but also on the azimuthal orientation Ψ of the

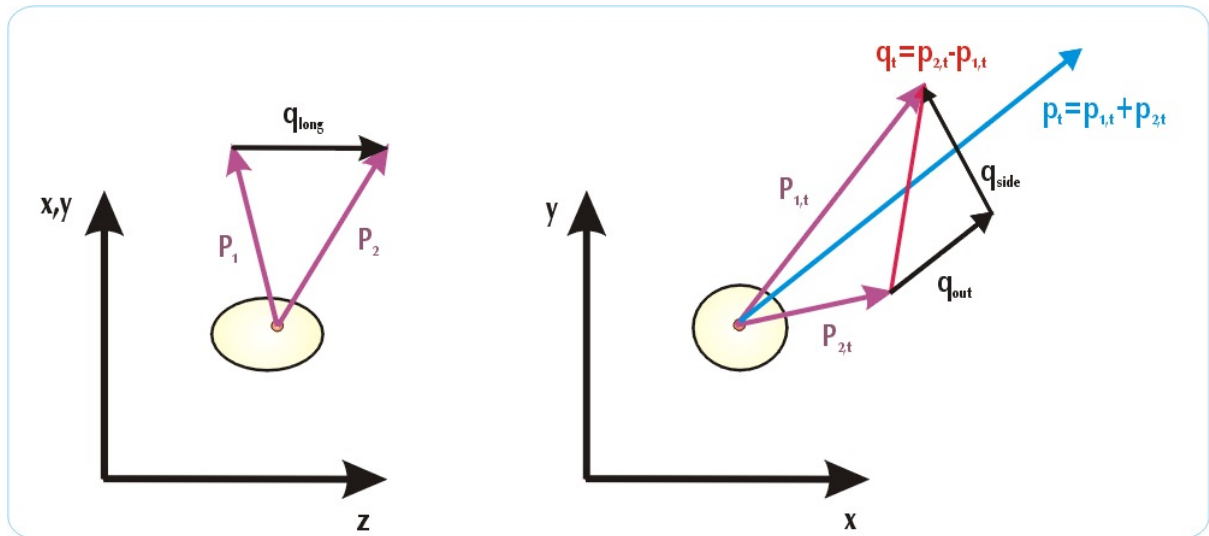


Figure 1.5: The “out-side-long” coordinate system takes the longitudinal “long” direction along the beam axis. In the transverse plane, the “out” direction is chosen parallel to the transverse component of the pair momentum P_\perp defined as Eq. 1.10, and the “side” direction is perpendicular to the “out” vector.

transverse pair momentum with respect to some pair-independent direction in the laboratory system, e.g. relative to the impact parameter \vec{b} .

In the case of the central collisions $|\vec{b}| \rightarrow 0$ the collision region is azimuthally symmetric and the emission function and the $C(\mathbf{q}, \mathbf{P})$ are Ψ -independent. For such a collision the $R_{out,side}^2$ and $R_{out,side}^2$ parameters in Eq. 1.39 vanish and only four independent HBT “radius parameters” remain. Defining $\tilde{x} = \mathbf{x} - \bar{\mathbf{y}}(\mathbf{P})$ it is possible to express the non-vanishing HBT-radius parameters by [CSH95]

$$R_s^2(\mathbf{P}) = \langle \tilde{y}^2 \rangle(\mathbf{P}) , \quad (1.41)$$

$$R_o^2(\mathbf{P}) = \langle (\tilde{x} - \beta_\perp \tilde{t})^2 \rangle(\mathbf{P}) , \quad (1.42)$$

$$R_l^2(\mathbf{P}) = \langle (\tilde{z} - \beta_\parallel \tilde{t})^2 \rangle(\mathbf{P}) , \quad (1.43)$$

$$R_{ol}^2(\mathbf{P}) = \langle (\tilde{x} - \beta_\perp \tilde{t})(\tilde{z} - \beta_\parallel \tilde{t}) \rangle(\mathbf{P}) . \quad (1.44)$$

Another symmetry that may apply to the emission function, is the longitudinal boost-invariance (Bjorken expansion). For such model, near the mid-rapidity, the longitudinal boost-invariance implies a $\tilde{z} \rightarrow -\tilde{z}$, thus in addition to the space-time variances linear in \tilde{y} , now also those linear in \tilde{z} vanish. In the longitudinally comoving system (LCMS), where $\beta_\parallel = 0$, this leads to further simplification

$$R_l^2(\mathbf{P}) = \langle (\tilde{z})^2 \rangle(\mathbf{P}) , \quad (1.45)$$

$$R_{ol}^2(\mathbf{P}) = 0 . \quad (1.46)$$

However, if the azimuthal symmetry of the particle emitting source is broken, then the single particles transverse momentum spectrum depends on the azimuthal direction of the emitted particles. This implies that the two-particles correlation functions should, in general, depend on azimuthal direction Ψ of the pair momentum, as well [VC96, Wie98]. The corresponding Gaussian radius parameters can be written formally in terms of space-time variances which are rotated via \mathcal{D}_Ψ (see Eq. 2.2a in [Wie98]) from the impact parameter fixed to the *out – side – long* coordinate system

$$\begin{aligned} R_{ij}^2(\mathbf{P}) &= \langle ((\mathcal{D}_\Psi \tilde{x})_i - (\mathcal{D}_\Psi \beta)_i \tilde{t}) ((\mathcal{D}_\Psi \tilde{x})_j - (\mathcal{D}_\Psi \beta)_j \tilde{t}) \rangle , \\ (\mathcal{D}_\Psi \beta) &= (\beta_{\perp,0}, \beta_\parallel) . \end{aligned} \quad (1.47)$$

The x, y and z are here given in the impact-parameter fixed system, not the *out – side – long* one. As for the azimuthally symmetric case, the HBT radius parameters show implicit and explicit \mathbf{P} -dependences

$$R_s^2(P_\perp, \Psi, Y) = \langle \tilde{x}^2 \rangle \sin^2 \Psi + \langle \tilde{y}^2 \rangle \cos^2 \Psi - \langle \tilde{x} \tilde{y} \rangle \sin 2\Psi ,$$

$$\begin{aligned}
R_o^2(P_\perp, \Psi, Y) &= \langle \tilde{x}^2 \rangle \cos^2 \Psi + \langle \tilde{y}^2 \rangle \sin^2 \Psi + \beta_\perp^2 \langle \tilde{t}^2 \rangle \\
&\quad - 2\beta_\perp \langle \tilde{t}\tilde{x} \rangle \cos \Psi - 2\beta_\perp \langle \tilde{t}\tilde{y} \rangle \sin \Psi + \langle \tilde{x}\tilde{y} \rangle \sin 2\Psi, \\
R_l^2(P_\perp, \Psi, Y) &= \left\langle \left(\tilde{z} - \beta_\parallel \tilde{t} \right)^2 \right\rangle, \\
R_{os}^2(P_\perp, \Psi, Y) &= \langle \tilde{x}\tilde{y} \rangle \sin 2\Psi + \frac{1}{2} \sin 2\Psi \left(\langle \tilde{y}^2 \rangle - \langle \tilde{x}^2 \rangle \right) \\
&\quad + \beta_\perp \langle \tilde{t}\tilde{x} \rangle \sin \Psi - \beta_\perp \langle \tilde{t}\tilde{y} \rangle \cos \Psi, \\
R_{ol}^2(P_\perp, \Psi, Y) &= \left\langle \left(\tilde{z} - \beta_\parallel \tilde{t} \right) \left(\tilde{x} \cos \Psi + \tilde{y} \sin \Psi - \beta_\perp \tilde{t} \right) \right\rangle, \\
R_{sl}^2(P_\perp, \Psi, Y) &= \left\langle \left(\tilde{z} - \beta_\parallel \tilde{t} \right) \left(\tilde{y} \cos \Psi - \tilde{x} \sin \Psi \right) \right\rangle.
\end{aligned} \tag{1.48}$$

The explicit Ψ -dependence is a purely geometrical consequence of rotating the x -axis from the direction of \vec{b} to the direction of P_\perp .

1.3.3 Final State Interactions Between Particles

For pairs of identical bosons (fermions) the two-particle wave function describing their propagation towards the detector must be symmetrized (antisymmetrized). For boson pairs this results in quantum statistical ‘‘Bose-Einstein correlations’’ between the final state momenta of the two particles. Via the uncertainty relation these momentum space correlations reflect the spatial and temporal structure of the source from which the two particles were emitted. This correspondence forms the basis for Bose-Einstein interferometry in nuclear and particle physics considered in previous sections. In addition to the Bose-Einstein and the Fermi-Dirac effects, the particles, which leave the interaction region, may be subject to mutual strong or Coulomb final state interaction (FSI) and thus cannot be described by plane waves. In the case of charged particles, the mutual Coulomb interaction leads to an enhancement or a suppression of the measured correlation function at small q for unlike-sign and like-sign pairs, respectively. In Section 1.3.4 it is shown that the FSI between different particles species offer supplementary information about properties of the emitting source created in a collisions of heavy ions. The strong FSI through resonances has been discussed based on the wave function formalism, the string model, and within the Wigner function formalism [Wei00]. The two most important effects of hadron resonances are the increase of correlation radius and the lowering of the correlation intercept because of short- and long-lived resonances, respectively. Concerning the strong interactions between pions within a pair it has been argued [Bow88] that the range of strong interactions is smaller (~ 0.2 fm) than the size of the hadronic source and therefore the correlation should be essentially unaffected. The expected source size in the Pb-Au collisions at 158 AGeV is about 6 fm and consequently effects of strong interaction are neglected in this dissertation.

The Coulomb interaction between two particles was considered classically in [BBM96].

Particles of the same (opposite) charge are pushed away from (towards) each other, thus depressing (enhancing) the observed distribution of pairs at small \mathbf{q} . The Coulomb interaction with the rest of the fireball, on the other hand, was shown to be less important. Better insight into the Coulomb induced correlations and, especially, their dependence on the source size, is achieved within the non-relativistic quantum mechanical approach. By reversing the time the particle emission is transformed to particle scattering. By introducing the reduced mass

$$\mu = \frac{m_1 m_2}{m_1 + m_2} . \quad (1.49)$$

the relative motion of the two particles is replaced by a single particle moving in the Coulomb field of the other. The sought Coulomb factor is then equal to the square of the wave function. The Schrödinger equation for the Coulomb wave function reads

$$\left[-\frac{\nabla^2}{2\mu} + V(\vec{r}_2 - \vec{r}_1) \right] \Psi_{coul}(\vec{k}, \vec{r}) = E_p \Psi_{coul}(\vec{k}, \vec{r}) , \quad (1.50)$$

where E_p is the energy of the pair, $V(\vec{r}_2 - \vec{r}_1)$ the Coulomb potential energy, and μ the reduced mass. The general solution of Eq. 1.50 is written in terms of the confluent hypergeometric function F [Mer61, Pra86a]. The wave function Ψ_{coul} squared is

$$\left[\Psi_{coul}(\vec{k}, \vec{r}) \right]^2 = H(\vec{k}, \vec{r}) = G(\eta) \left| e^{i(\vec{r} \cdot \vec{k})} F\left(-i\eta; 1; ik \left(r - \frac{\vec{r} \cdot \vec{k}}{k} \right) \right) \right|^2 , \quad (1.51)$$

where \vec{k} is the asymptotic momentum of a particle in the pair center-of-mass system equal to $\frac{q_{inv}}{2}$. In the limit of the point-like source, $(\vec{r}_2 - \vec{r}_1) \rightarrow 0$, the squared amplitude of the Coulomb wave function reduces to the classical Gamow function [GKW79]

$$G(\eta) = \frac{2\pi\eta}{e^{2\pi\eta} - 1} = |\Gamma(1 + i\eta)|^2 \exp(-\pi\eta) . \quad (1.52)$$

The relative velocity enters through $\eta = 2 Z_1 Z_2 \mu \alpha / q_{inv}$, called Sommerfeld parameter, where α is the fine structure constant and $Z_1 Z_2$ is the product of charges. The Coulomb correlation function is then [Bay98]

$$\frac{C_2^{exp}}{C_2^0} = \int d^3r \rho(\vec{r}) H(\vec{k}, \vec{r}) , \quad (1.53)$$

where $\rho(\vec{r})$ is the source function which describes the probability of emitting a pair of particles with momentum k at relative distance r , and C_2^0 denotes the correlation function in absence of Coulomb field. For actual calculation usually a spherical Gaussian source is used, $\rho(\vec{r}) = \frac{1}{\sqrt{2\pi}^3 R^3} \exp(-\vec{r}^2/2R^2)$. Since \vec{r} represents the relative distance between the two particles a realistic R should be $\sqrt{2}$ times larger than the experimental HBT radius. The Coulomb wave function squared averaged over a spherical Gaussian source is called $F_c(q_{inv})$ and in absence of other sources of correlations may be directly compared to the experimental correlation function.

Apart from the Coulomb interaction between particles in the pair, particles feel the attractive or repulsive interaction, depending on their charge, caused by the positively charged fireball. However, the impact of this effect on the measured $\pi - \pi$ correlation functions was found to be insignificant [ZBB⁺84, Bar99]. The two-particle correlation functions discussed in this work are not corrected for it.

1.3.4 Non-identical Particle Correlations

Correlation functions of non-identical particles contain information on the relative space-time asymmetries in particle emission [LLEN96]. The ones generated mostly by the Coulomb interaction have an exponential-like shape at $\mathbf{q}=0$. The width depends on the average distance squared between the particles at freeze-out, similarly as in the case of identical particle correlations. As was pointed out in [RL04], flow induces a correlation between particles velocities and emission points leading to an effective decrease of measured HBT radii and to different average emission points for particle species with different masses. From this point of view, non-identical correlation can be used as an independent method of flow measurement in heavy ion collisions. The pioneering experimental data analysis of the relative space-time asymmetries in particle emission is presented in [Miš98]. For non-identical particles the generalized momentum difference is defined as

$$\tilde{\mathbf{q}} = \mathbf{q} - \mathbf{P}(\mathbf{q}\mathbf{P})/\mathbf{P}^2, \quad (1.54)$$

where \mathbf{q} is defined by Eq. 1.11, \mathbf{P} is defined by Eq. 1.10, and $\mathbf{q}\mathbf{P} = m_1^2 - m_2^2$. In Fig. 1.6 a simple presentation of the asymmetry mechanism is shown. The origin of the correlation function asymmetry in pion-proton correlations can be understood using this simple sketch. In order to construct correlation function for pair of particles with the different masses one needs to select the fast heavier particle while the lighter should be slow one. Thus one can distinguish two scenarios of the particle correlations, namely, in the first case pions tend to catch up with

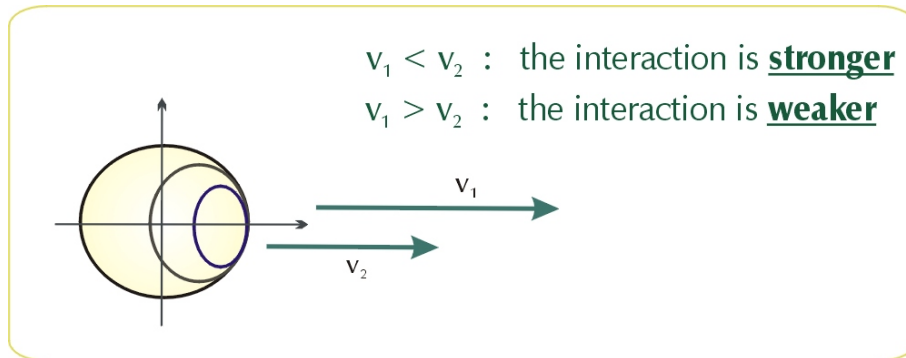


Figure 1.6: The origin of the asymmetry in a non-identical particle correlation function.

protons while in the second case pions tend to move away from protons. The correlations will be stronger in the first case than in the second one, due to longer interaction time between the particles.

Chapter 2

CERES experiment

The CERES (Cherenkov Ring Electron Spectrometer) experiment was operated at the CERN SPS facility and focused on measurement of low-mass e^+e^- pairs emitted in proton- and ion-induced collisions at ultra-relativistic energies. Dileptons and photons are especially attractive probes of QGP since they are produced at all stages of the collision and, in contrast to hadrons, interact mostly electromagnetically. Therefore, they can probe directly the early stage of the collision and carry this information to the detectors. The low-mass dilepton region is governed by the light quark flavors - u , d , and s . In the limit of vanishing quark masses the QCD phase transition is associated with the chiral symmetry restoration which should be manifested in medium modification of the light vector mesons (ρ , ω , ϕ). Here, the ρ meson is of a particular interest because of its short lifetime ($\tau = 1.3$ fm/c) in comparison to the lifetime of the fireball ($\tau = 10$ -50 fm/c). Low mass lepton pairs are produced only with a 10^{-5} fraction relative to pions. The Cherenkov threshold in the RICH (Ring Imaging Cherenkov) detectors was chosen such to distinguish electrons from other charged particles. The material budget used to construct the detector was kept low to minimize the conversion of photons into the secondary e^+e^- pairs.

The spectrometer covers pseudo-rapidity region $2.1 < \eta < 2.65$ and full azimuthal acceptance as well as very broad range of transverse momentum (p_\perp). The initial experimental setup consisted of two RICH detectors providing the electron identification and the measurement of the particle trajectory. The superconducting magnet placed between the RICHes provided an azimuthal symmetric magnetic field. The information about particle charge and momentum was obtained from the deflection angle in the magnetic field between the two RICH detectors. With this configuration different measurements were performed [A⁺95, A⁺98b, A⁺98a]. In order to cope with the high multiplicity environment encountered in collisions induced by lead ions the experimental setup was extended in 1994-95 by two Silicon Drift Counters (SDD) for the vertex reconstruction, the measurement of the energy loss (dE/dx), and coordinates of charged particle tracks with high spatial resolution. In addition, the Multi-Wire Proportional Chamber (MWPC) with a pad readout was located behind the RICH2 mirror. The pad chamber provided an external tracking behind the magnetic field [H⁺ 1] and facilitated the ring

recognition in the RICH2 detector. In 1998, the pad chamber was replaced by the cylindrical Time Projection Chamber (TPC) with radial drift field to enhance the mass resolution for the light vector mesons ρ/ω and ϕ up to $\delta m/m = 2\%$ at $m \approx 1 \text{ GeV}/c^2$. The TPC also extended the experiment's capability to measure the hadronic signatures of the hot and dense matter. The whole CERES experimental setup enabled the exploration of charged particles only. The neutral particles could be accessed by probing the charged products from their decays.

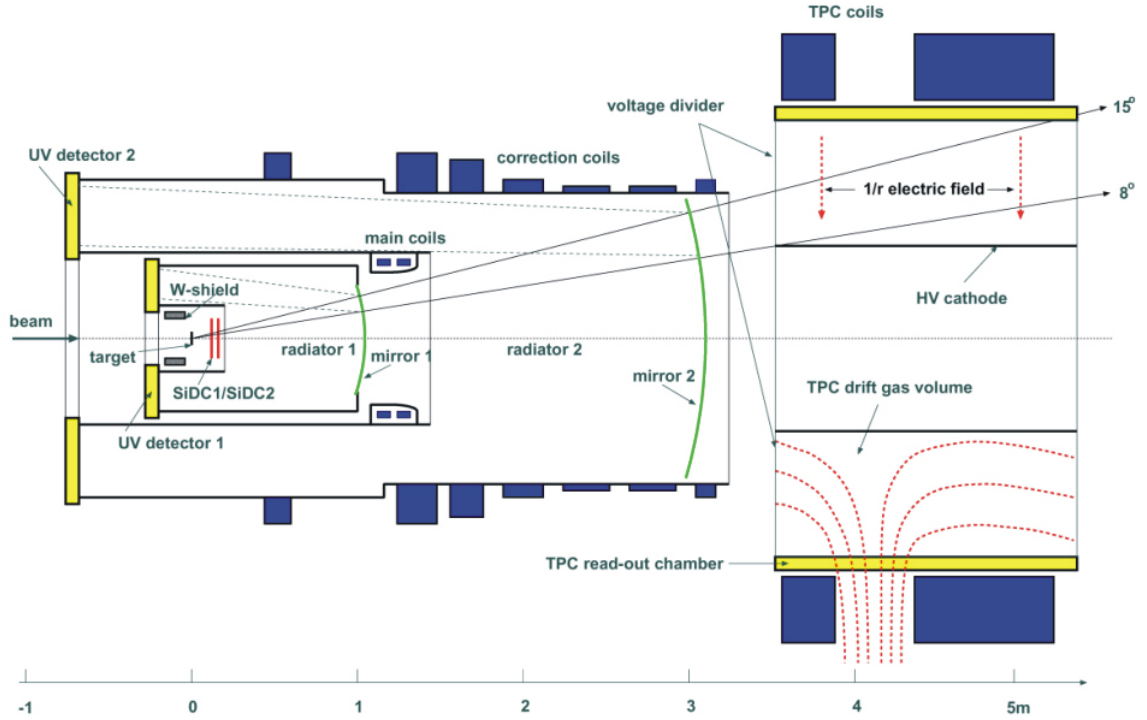


Figure 2.1: CERES experiment setup used for the measurement of Pb-Au collisions in 2000.

In Fig. 2.1 the schematic view of the experimental setup is presented. In 2000 about 33 million Pb-Au collision events at the top SPS beam energy were recorded with this setup. The results presented in this thesis were obtained from analysis of this data set. The CERES experiment was decommissioned in the fall 2003.

2.1 Target and Trigger Systems

During the beam-time in the year 2000 the target system consisted of 13 gold discs of $600 \mu\text{m}$ diameter and $25 \mu\text{m}$ thickness. The distance between the discs was chosen to be 1.98 mm to

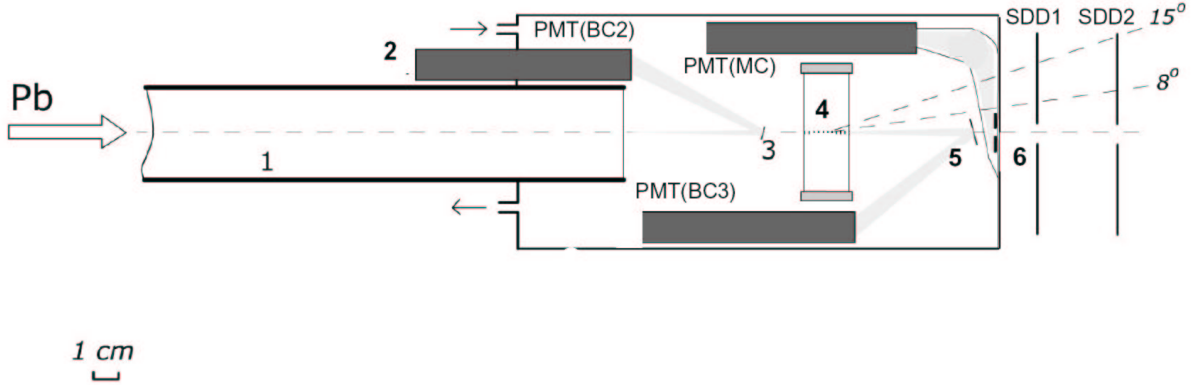


Figure 2.2: The target system together with Silicon Drift Detectors and part of the trigger system: 1) carbon vacuum beam pipe, 2) PMT housing (BC2), 3) BC2 mirror, 4) 13 Au targets, 5) BC3 mirror, 6) multiplicity counter.

minimize the conversion of γ 's into e^+e^- -pairs and the probability of the secondary interaction. The target region and a part of the trigger system are shown in Fig. 2.2. The target is surrounded by a tungsten shield to absorb charged particles scattered backwards which might otherwise hit the RICH UV-detector.

The trigger system was based on gas Cherenkov counters BC1, BC2 and BC3 and scintillator counters MC, MD and Veto. Each gas Cherenkov counter was composed of the $12\ \mu\text{m}$ aluminum-mylar mirror and the photomultiplier (PMT). The Multiplicity Counter (MC) was a plastic scintillator covering $2.3 < \eta < 3.5$ located 79 mm behind the target with reference to its centre. The schematic view of the trigger and silicon drift detectors is shown in Fig. 2.3 (the Veto wall is not shown). Combination of signals from the beam counters was used to define a collision. The logical expression used for triggering on nuclear interactions, called *minimum bias* (mb), is given by

$$T_{mb} = BC1 \times BC2 \times \overline{BC3} \quad (2.1)$$

The direct measurement of the impact parameter is not possible in the experiments. However, based on assumption that collisions with smaller impact parameter will produce more particles, one can use charged particle multiplicity to extract the impact parameter and classify an event. The centrality selection was based on the MC scintillator with the signal proportional to the number of charged particles. The centrality trigger was defined as

$$T_{central} = T_{mb} \times MC \quad (2.2)$$

The MC threshold was set to trigger on the most central collisions of 7% of the geometrical cross section (σ/σ_{geo}). A fraction of the data (3 M) was taken with $\sigma/\sigma_{geo} = 20\%$ and about (0.5 M) of the minimum bias. For further information about implementation of the trigger system we refer to [Miš99].

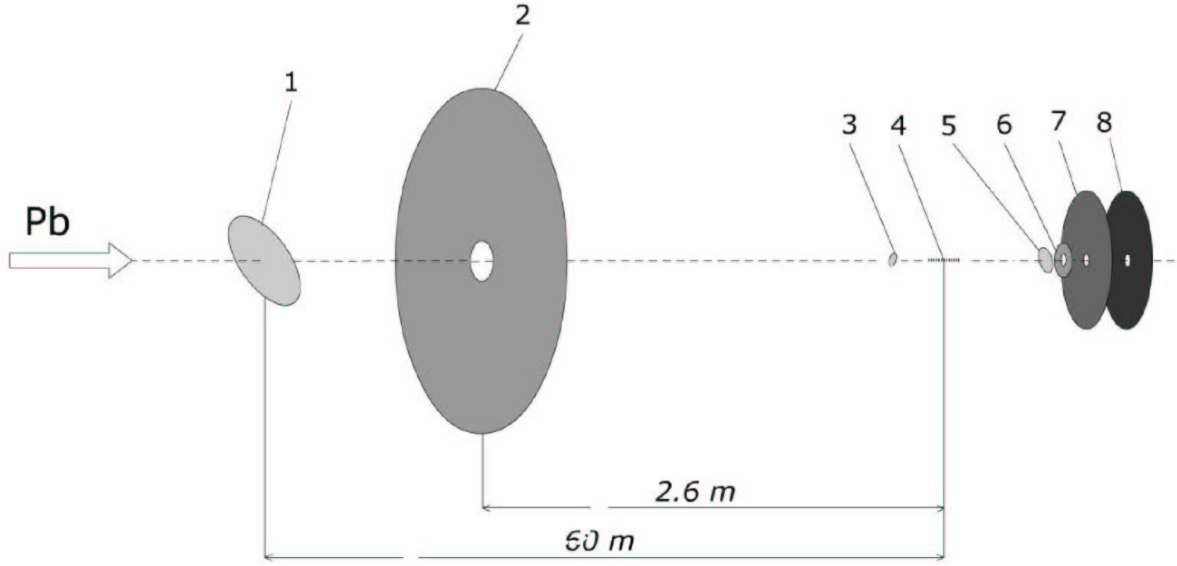


Figure 2.3: The layout of the trigger and the drift detectors: 1) BC1 mirror, 2) veto scintillator (VC), 3) BC2 mirror, 4) 13 Au targets, 5) BC3 mirror, 6) multiplicity counter (MC), 7,8) silicon drift detectors (SDD).

2.2 Silicon Drift Detectors

The determination of the interaction point was based on the two drift silicon detectors (SDD1, SDD2), being located downstream from the target approx. 10 and 14 cm, respectively, as shown in Fig. 2.2. Both detectors are 4 inch silicon wafers covering the full azimuthal acceptance and the pseudo-rapidity region $1.6 < \eta < 3.4$. The thickness of each silicon wafer was $280 \mu\text{m}$.

The working principle of the SDD is shown in Fig. 2.4 [GR84]. The charged particle passing through the silicon wafers creates electron-hole pairs along its trajectory. The drift field created by the field rings of the voltage divider transports the freed electrons towards the outside edge of the silicon wafers where the anode pads are located, while the holes are attracted by the nearest strip of the voltage divider. The shape of the drift field is an asymmetric parabola in the beam direction, this peculiar shape resulting in a uniform detector response. The maximum drift time for a drift field of 700 V/m is approx. $3.8 \mu\text{s}$. Based on the drift time information it is possible to reconstruct the hit position in the radial direction. The readout electronics channels were connected to the 360 anodes radially arranged at the edges of the SDD detectors. The shape of the anode pad is shown in Fig. 2.5. The segmented structure improves the azimuthal resolution by charge sharing between the anodes.

Additionally the silicon drift detectors were used to determine the charged particle density

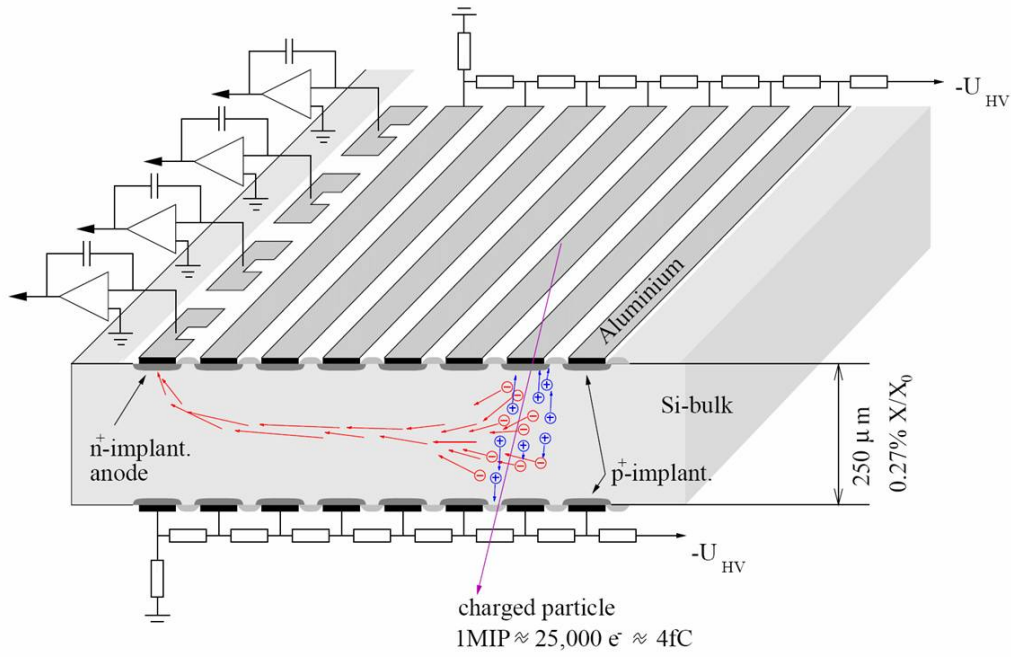


Figure 2.4: Operating mode of the silicon drift detectors.

$dN/d\eta$, and suppress conversion electrons. For more information see [H⁺96, Sl03].

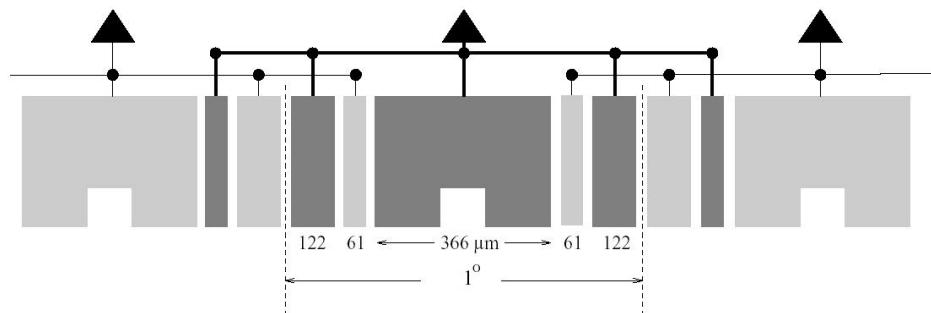


Figure 2.5: The layout of the interlaced structure of the readout pads used for drift silicon detectors. Each pad is divided into 5 pieces.

2.3 Ring Imaging Cherenkov Detectors

Two Ring Imaging Cherenkov detectors played an essential role in the CERES dilepton studies by providing electron identification. The Cherenkov radiation is emitted when a charged particle traverses a medium with refractive index n with a velocity v above the velocity of light c/n in that medium. The threshold condition is given by:

$$\beta_{th} = \frac{v_{th}}{c} \geq \frac{1}{n} . \quad (2.3)$$

The angle of emission increases with the velocity:

$$\theta_c = \arccos \frac{1}{n\beta} , \quad (2.4)$$

and reaches a maximum value for $\beta = 1$. The threshold velocity translates into a threshold energy $E_{th} = \gamma_{th} m_0 c^2$ yielding:

$$\gamma_{th} = \frac{1}{\sqrt{1 - \beta_{th}^2}} = \frac{n}{\sqrt{n^2 - 1}} . \quad (2.5)$$

The number of Cherenkov photons emitted per unit path length dx is given by:

$$\frac{dN}{dx} = 2\pi\alpha z^2 \int \left(1 - \frac{1}{n^2\beta^2}\right) \frac{d\lambda}{\lambda^2} \quad (2.6)$$

for $n(\lambda) > 1$, where z is the electric charge of the passing particle, λ is the wavelength, and α the fine structure constant. The yield of Cherenkov radiation photons is proportional to $1/\lambda^2$, but only for those wavelengths where the refractive index is larger than $1/\beta$.

The CERES RICH detectors were filled with the gas mixture - 94% of Helium and 6% of Methane - at the atmospheric pressure. This choice of the gas mixture as a gas radiator assures that mainly electrons and positrons emit Cherenkov photons due to the high γ threshold ($\gamma_{th} \simeq 32$). This assumption should make RICH detectors almost hadron blind. However, the light hadrons has been recorded in the detectors above certain momentum. Both UV-detectors were filled with the TMAE (Tetrakis-di-Methyl-AminoEthylen) vapor in order to enhance the conversion of incoming photons to electrons via photo-ionization effect. In Fig. 2.6 the operating mode of the RICH1 detector is presented. A complete description of the RICH detectors one will find in [B⁺94, B⁺95]. The information from the RICH detectors were not used for this analysis.

2.4 Time Projection Chamber

The pad chamber was replaced by the Time Projection Chamber in 1998. This upgrade of the CERES experiment extended its detection capability from electrons to all charged particles.

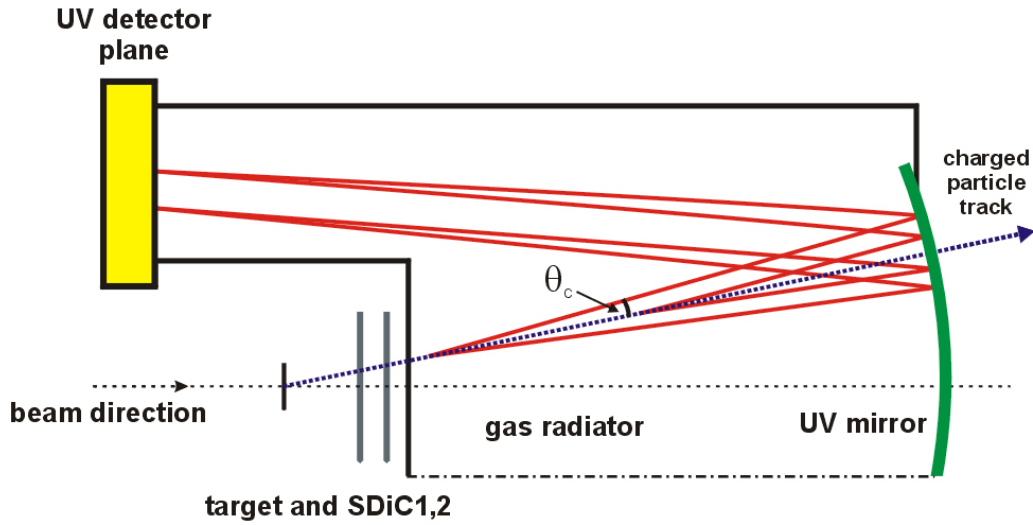


Figure 2.6: Schematic view of the CERES RICH1 detector with a spherical mirror. Produced Cherenkov photons are reflected by a spherical mirror and focused onto the photon detector placed at the focal point of the mirror.

The particle identification was accomplished in the TPC by the measurement of the particle charge, momentum, and energy loss dE/dx .

The Time Projection Chambers provide three-dimensional information about charged particles passing through the active volume of the detector. The capacity of the active volume is limited only by abilities to keep it at the uniform condition. The detector is essentially a large gas-filled cylinder with a high voltage electrode providing an electric drift field. Perpendicular to the drift field, arrays of multi-wire proportional chambers are arranged (read-out chambers). A charged particle passing through the medium produces electron-ion pairs along its path. In the presence of electric drift field liberated electrons drift toward the anode of the read-out chamber. Upon reaching the high field region, close to the anode wire, every electron is quickly accelerated and consequently produces an avalanche. The charge produced in the avalanche induces a signal on cathode pads which is recorded using charged sensitive amplifiers attached to the pad. Two coordinates of the liberated electrons are given by the position of the signal induced on the cathode pads. The third coordinate is given by the drift time of the ionization electrons. Since all ionization electrons created in the sensitive volume of the TPC will drift towards the MWPC, each anode wire over which the particle trajectory crosses will sample that portion of the track. This yields many space points for each track allowing the full reconstruction of the particle trajectory.

The CERES TPC is shown in Fig. 2.7. The azimuthal and polar coverage of the TPC matches the acceptance of the rest of the experimental setup. The drift field was radial and

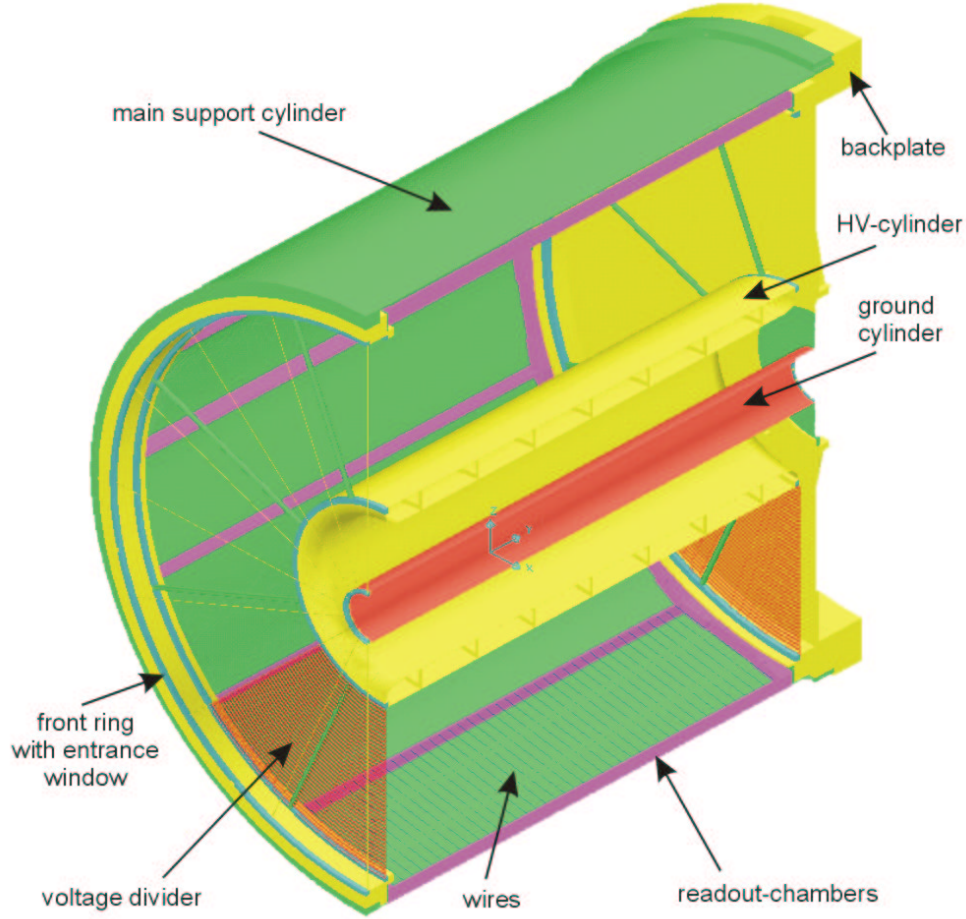


Figure 2.7: Schematic view of the CERES TPC.

the 16 readout chambers were arranged on the outer cylinder ($R=130$ cm), parallel to the beam direction in such a way that they formed a polygonal structure covering the full azimuthal acceptance. Additionally, the TPC was enclosed by the two opposite-polarity solenoidal coils resulting in an inhomogeneous magnetic field. This assured that a particle passing through an active volume of the detector will be deflected predominantly in the azimuthal direction. An active volume of 2 m length was divided into 20 planes providing up to 20 space points per measured track. The inner cylinder of radius of 48.6 cm was at a potential of -30 kV resulting in a $1/r$ dependence of electric field [GM02]. In order to make the electric field uniform in the beam direction both sides of the TPC were closed by 50 μm capton foils with 40 concentric copper rings. The rings were supplied with voltage by two voltage divider chains. The magnetic

field lines for the CERES TPC are indicated in Fig. 2.1 by red dotted lines. The TPC coordinate system is shown in Fig. 2.8. The origin of the coordinate system is in the centre of the SDD1. The z axis corresponds to the beam axis in the experiment. The $x-y$ plane is defined such that the x axis is at the boundary between chamber 15 and 0.

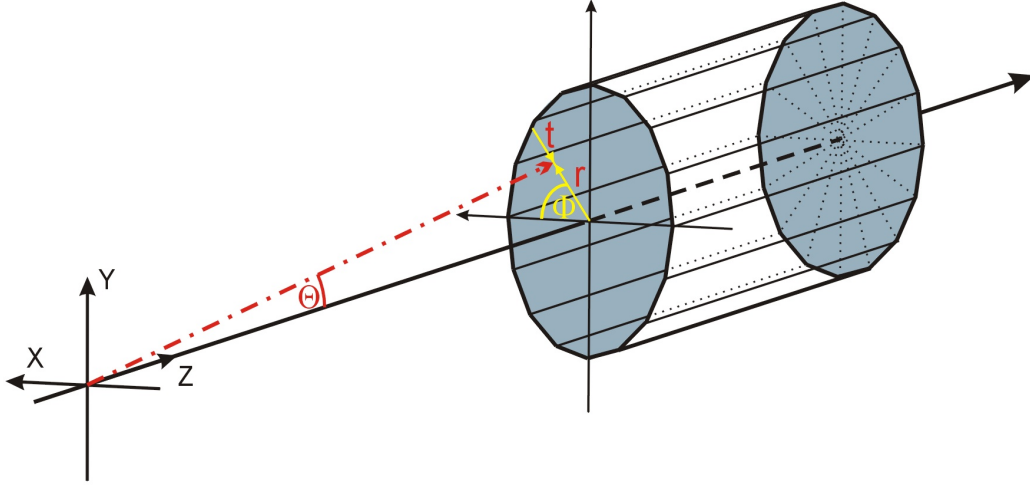


Figure 2.8: The coordinate system of the TPC.

2.4.1 Gas Properties

The choice of the gas mixture used in the proportional chambers is always individually optimized for the given experimental setup, and is governed by several factors: low working voltage, high gain, good proportionality, high rate capability, low diffusion, and low multiple scattering. Two main components of the gas mixture commonly used are a noble gas and so-called quencher. Noble gases are chosen due to the lowest electric field intensities required to form an avalanche. However, the proportional chamber only with the noble gas cannot be operated after the certain gain ($10^3 - 10^4$) due to continuous discharge caused by the high excitation energy of these elements. Excited noble gas atoms formed in the avalanche create high energy photons while they de-excite. Such photons are capable of ionizing the cathode and causing further avalanches. To stabilize the avalanches process some polyatomic gas (quencher) should be added (e.g. CO_2 , CH_4 , $\text{BF}_3 \dots$). These molecules absorb the radiated photons and dissipate this energy through dissociation or elastic collisions.

The motion of charged particles under the influence of electric and magnetic field, \vec{E} and \vec{B} , is described by the drift velocity vector \vec{v}_d , determined by the linear equation [BR94]

$$\frac{\vec{v}_d}{\tau} \frac{e}{m} - [\vec{v}_d \times \vec{B}] = \frac{e}{m} \vec{E}. \quad (2.7)$$

Here m and e are the mass and the electric charge of a particle, and $\tau = m/K$ characterizes the mean time between subsequent collisions of the particle moving through the medium. K describe the frictional force proportional to the drift velocity vector. Solution of this equation reads

$$\vec{v}_d = \frac{e}{m} \tau |\vec{E}| \frac{1}{1 + \omega^2 \tau^2} (\hat{E} + \omega \tau [\hat{E} \times \hat{B}] + \omega^2 \tau^2 (\hat{E} \cdot \hat{B}) \hat{B}) \quad (2.8)$$

where $\omega = (e/m) B$ is the cyclotron frequency of the electron. Here \hat{E} and \hat{B} denotes the unit vectors in the directions of the two fields. The drift direction is governed by the dimensionless parameter $\omega \tau$. The relation between the parameter $\omega \tau$ and the angle between \vec{v}_d and \vec{E} vector is given by

$$\omega \tau = \tan \alpha_L \quad (2.9)$$

where α_L is the Lorentz angle.

The CERES TPC filled with the gas mixture of 80% Ne and 20% of CO₂ [A⁺96a, A⁺96b] was operating at the atmospheric pressure. The gas gain was measured as $8 \cdot 10^3$, resulting in the electronic gain of 46 mV/fC. The drift velocity was varied between 0.7 and 2.4 cm/ μ s with the maximal drift time of about 71 μ s. The relatively large radiation length of Neon gas minimized the effect of the multiple scattering and on the other hand provided enough electron-ion pairs as required by the CERES TPC. The choice of CO₂ as a quencher minimized the effect of the Lorentz angle which was caused by the characteristic arrangement of the magnetic field with respect to the radial electric field. Also, the diffusion of the electrons drifting towards the readout chambers was reduced resulting in an increase of the detector spatial resolution. Gas mixtures using CO₂ as a quencher are very sensitive to the changes of the ambient conditions. Therefore the monitoring of the gas properties has to be performed (see Section 2.4.2).

2.4.2 Readout and Control Systems

The CERES TPC readout system was based on the 16 MWPCs. Each chamber was divided into 20 planes in the beam direction with 48 cathode pads in the azimuthal direction. Three groups of the wires planes, the gating grid, the cathode, and the anode, were mounted in the azimuthal direction above the readout pads. The gating grid wires plane, placed 12 mm above the chamber surface, was responsible for protecting the TPC from ions being produced during the avalanches as well as from free charges being induced apart from the triggered collision. The potential of the gating grid wires was $-70, -210, -70, -210, \dots$ V in the closed state and -140 V during a valid event. The grounded cathode wire plane was placed 6 mm above the readout pads and 3 mm above the anode wires. The anode wires of the diameter of 20 μ m were on positive potential of about 1.3 kV resulting in a gas gain of about 10^4 . The charge induced during the avalanche was collected by the Chevron-shaped pads cathode. The Chevron pad shape (see Fig. 2.9) was selected because of its efficient charge sharing in the azimuthal direction and was optimized to minimize the differential non-linearity [Sch98]. The measurement

of the charge sharing in the azimuthal direction showed that the charge was usually distributed over three pads, with size of $6 \times 10.3 \text{ mm}^2$. The measured pad response function was approximated with a Gaussian function with a standard deviation of 0.5 pads. Each pad was connected

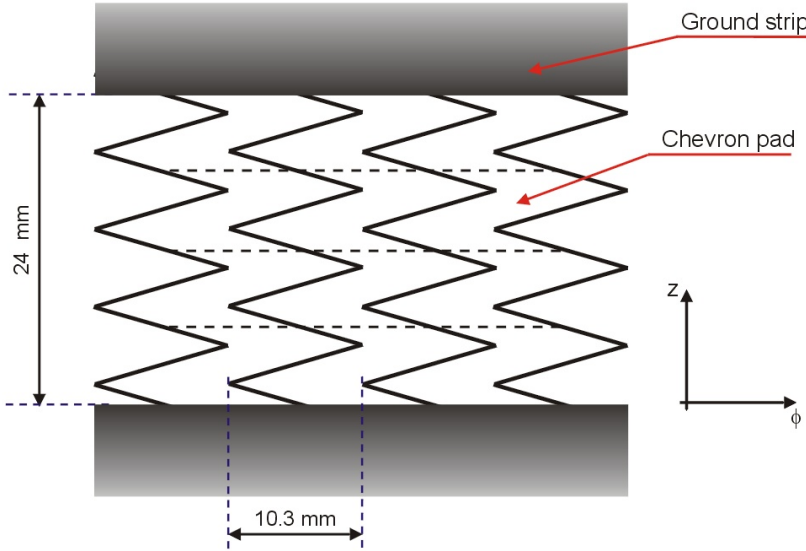


Figure 2.9: The layout of the CERES TPC pad plane. One readout channel was connected to four Chevron pads as indicated by the dashed lines. Chevron pads were separated by the ground plane strips in z direction.

to the charge amplifier and to an 8-bit ADC chip which sampled the analog signal in 256 times bins per channel, resulting in the total 4 million spatial points. For more detailed description of the readout electronic of the CERES TPC see [Til02].

The slow control of the TPC recorded periodically detector working conditions including the gas mixture, the pressure, the drift velocity, the temperature, and the CO_2 contamination. Moreover, in order to keep the drift velocity variation below 0.1% the temperature of the TPC had to be stabilized as accurate as 0.2 K. To monitor the drift velocity in the CERES TPC, a gas monitor detector (**G**as **p**r**O**portional **c**ounter **F**or **d**rifting **E**lectrons – **GOOFIE**) was used. In Chapter 3 the development of the new designed drift velocity monitor is presented. The latter will be implement into the gas system of the ALICE TPC.

In order to understand better the response of the CERES TPC, the laser track as a calibration system has been used. The laser system, based on a Nd:YAG laser, provided a low divergence laser beam with a wavelength of 1064 nm. To induce an ionization in the gas mixture used in the TPC, the wavelength of the laser was reduced to 266 nm. The position of the straight laser tracks was determined with spatial and time accuracy of $200 \mu\text{m}$ and 10 ns respectively. In Fig. 2.10 the perspective view of the TPC calibration system is show. Further information about the CERES TPC laser system can be found in [BMMZ98].

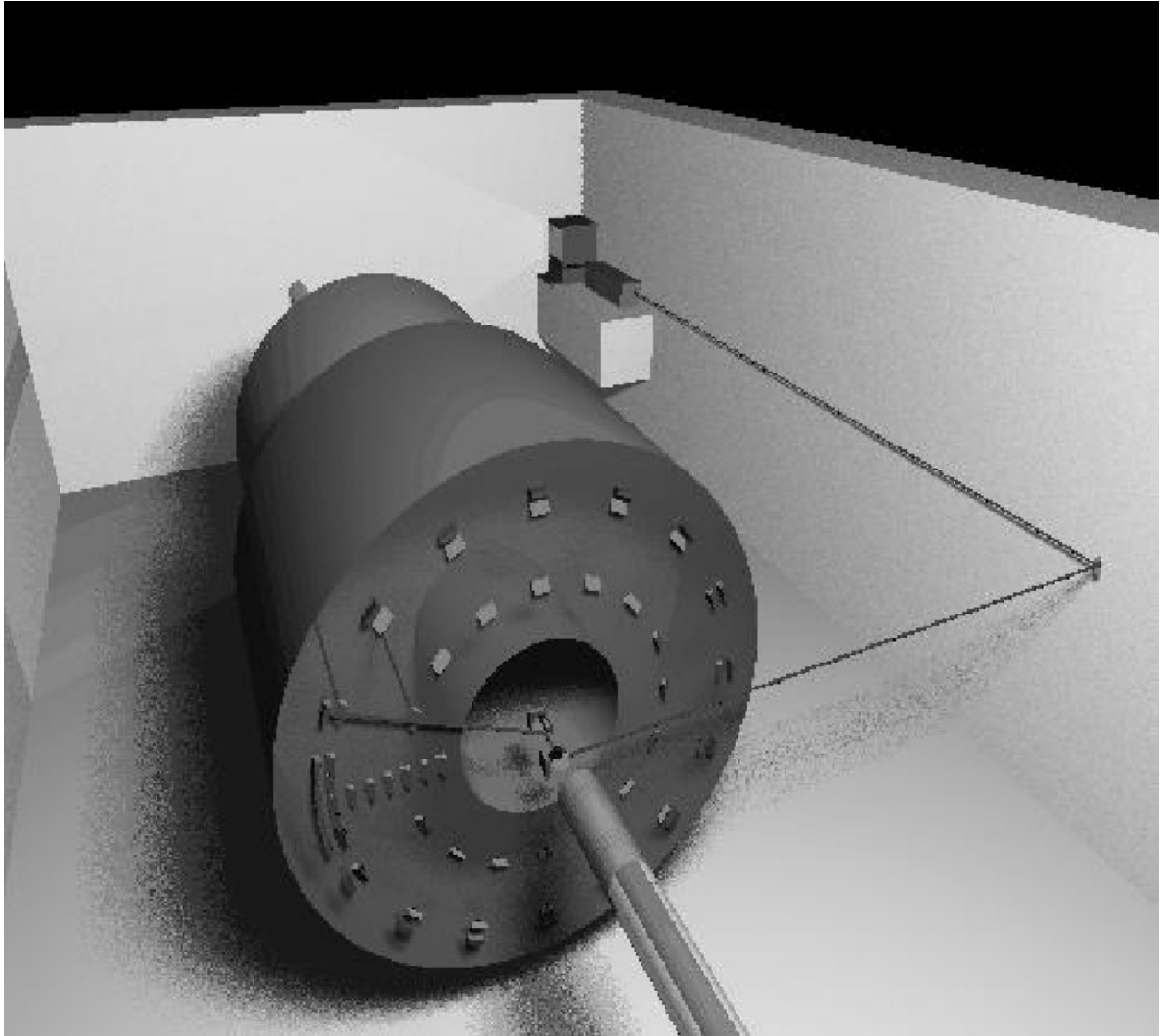


Figure 2.10: The perspective view of the CERES laser system.

Chapter 3

Drift Velocity Monitor for the ALICE TPC

3.1 Introduction

Gaseous detectors (multi-wire proportional chambers, drift chambers and TPCs) among others are nowadays frequently used in many experiments around the world. They provide information about particle tracks being created during collisions between projectile and target particles. The active volume of currently constructed gas detectors reaches values in the order of 10^2 m^3 (for instance the ALICE¹ TPC [TPC01] will have an active volume of 88 m^3). Such a large volume requires a special attention to ensure isotropic conditions as a whole active volume of the detector as well as to provide stable conditions during detector operating. To obtain such conditions a number of controlling systems must be used. Since the gas detectors are very sensitive to the ambient conditions as temperature and pressure, specially those using CO_2 in the gas mixture, they require the online monitoring of the gas properties (gain, drift velocity, composition, etc.). One of the frequently used gas monitoring system is known as GOOFIE [Lip00]. The GOOFIE is traditionally used to monitor the drift velocity in drift chambers (or TPCs). We extend its use to monitor also the gain (in order to determine the ternary gas composition).

The ALICE experiment is located at the **L**arge **H**adron **C**ollider (LHC) [Pot96] optimized for the study of heavy-ion collisions, at a center-of-mass energy of 5.5 TeV per nucleon pair. Such collision energy allows one to study properties of strongly interacting matter into a radically new energy region, previously reached only in the interactions of the highest energy cosmic rays. All parameters relevant to the formation of the QGP, as the energy density, the size and the lifetime of the system, will be increased by large factors, more than an order of

¹A Large Ion Collider Experiment

magnitude in comparison with previous accelerator experiments. The initial temperatures will largely exceed the calculated critical temperature for QGP formation which allow one to study, in detail, nonperturbative aspects of QCD such as the deconfinement and the chiral symmetry restoration. Moreover, it will be possible to exploit a wider set of relevant observables (see Section 1.2.4) as compared to previous experiments, thus substantially enhancing the understanding of the properties of the quark-gluon plasma. The hard probes, which are sensitive to the nature of the medium at the earliest stages of the collision, will be explored at higher energy and higher luminosities. In addition, the expected very high multiplicity, several thousands of charged particles per pseudorapidity unit, will allow to measure a large number of observables on an event-by-event basis as the impact parameter, the multiplicity, the particle composition and the spectra, as well as the correlation function between different particles species. Therefore single event analysis, and in particular the study of non-statistical fluctuations associated to the critical phenomena, can be effectively performed at the LHC.

The choice of the gas mixture of the TPC depends on the specific requirements of the experimental setup as it was already mentioned in Section 2.4.1. Therefore, after detailed research [Gar04, Vee03] the Ne-CO₂-N₂ [90-10-5] gas mixture was chosen for the ALICE TPC. The expected high multiplicity ($dN/dy = 8000$ at the time of the design) and the required momentum resolution ($dp/p=1\%$ at the multiple scattering limit) ruled out the use of argon as a noble gas because of its low ions mobility in comparison with Ne⁺. The CO₂ was the only gas that fulfilled all requirements and restrictions assumed for the quencher in ALICE TPC. Any quencher based on the hydrocarbon was unacceptable due to the high doses expected at the anode wire for the lifetime of the experiment (11 mC/cm), the modern safety regulations and the production of thermal neutrons. Performed ageing test with the P10 gas mixture on a full size prototype readout chamber has shown dramatic gain degradation equivalent to 1-2 years of ALICE operation. The small amount of nitrogen was added to the gas mixture to minimize the risk of breakdown in the form of self-sustained glow discharges. The absorption cross-section of N₂ explains the substantial quenching improvement in the neon-based mixture. Fig. 3.1 presents the photon absorption cross-section of both CO₂ and N₂ as a function of the photon energy. The main excited state of neon (16.8 eV) can be de-excited by the ionization mechanism based on the process $A + B^* \rightarrow A^+ + B + e^-$ (Penning effect). The rather low absorption cross-section of CO₂ at this energy is not able to quench all excited atoms resulting in delocalised new avalanches or induced field emissions from the cathode surface. Therefore, N₂ as an additional component of the gas mixture reduces sufficiently such effect and moreover, the drift velocity does not nearly change. Ideally, the gas composition should be preserved during the time operation of the detector. However, this is not always the case in the real experiment. Due to some imperfections in the chambers or/and the field cage the air can enter into the active volume of the detector. The well known main components of the air, N₂ and O₂ (approx. 78 % and 21 %), will slowly accumulate in the gas mixture. The purification system based on activated copper can easily remove the oxygen molecules from the active volume of the detector, however, it will not affect the nitrogen. Moreover, the CO₂ filling the containment vessels can

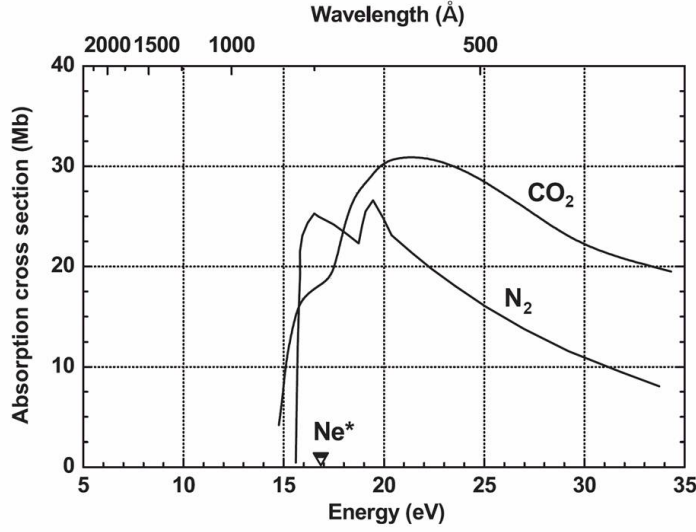


Figure 3.1: Absorption cross-section of CO_2 and N_2 as a function of the photon energy [Gar04].

mix with the TPC gas composition too. Therefore, the monitoring of the gas composition as well as the gas properties will be an integral part of the ALICE TPC slow control system. This task will be entrusted to the GOOFIE which will monitor the drift velocity together with the gas gain and from them the gas composition will be derived (see Section 3.3).

In the presence of an electric field \vec{E} , the electrons and ions freed by radiation move along the field lines towards anode and cathode respectively. This acceleration is interrupted by collisions with the gas molecules that limit the maximum average velocity. The latter can be attained by the charge along the field direction. Attained average velocity is known as the drift velocity of the charge and is superimposed upon its normal random movement. The drift speed of the ions is slow, compared to their thermal velocities, while, for electrons it can be much higher since they are much lighter. Eq. 2.8, for the case when the electric field vector \vec{E} is along the drift vector \vec{v}_d , is simplified to the form

$$\vec{v}_d = \frac{e}{m} \tau \vec{E} \quad (3.1)$$

where $(e/m)\tau$ defines the scalar mobility μ of electron-ion pairs. For a given gas mixture the drift velocity is a function of the electric field, the temperature and the pressure. For ideal gases, in which the moving charges remain in thermal equilibrium, the mobility can be shown to be related to the diffusion constant by $D/\mu = kT/e$ [PS75]. This is the result of a classical reasoning and it is known as the Einstein relation.

3.2 Experimental Setup

The goal of this research was to develop a gas monitor which will be able to determine a drift velocity for the ALICE TPC with a relative resolution in the order of 10^{-4} . The first attempts concentrated on the development of a drift velocity monitor were performed at GSI². Further development was performed at the Max-Planck-Institut für Physik in München for the STAR FTPC³ [Mor01]. Based on the STAR FTPC gas monitor, development studies were made to achieve the required resolution and to assure stable operation under the unprecedented electric field of 400 V/cm which is enforced by the ALICE TPC. The GOOFIE is operating with a Ne-CO₂-N₂ [90-10-5] gas mixture as for the ALICE TPC [Gar04]. The experimental setup tests were performed at GSI.

The approach, used in this device to measure the drift velocity v_d in a gas, is given by the equation

$$v_d = \frac{\Delta l_d}{\Delta t_d} \quad (3.2)$$

where Δl_d is a known distance between two radiation sources ionizing the gas and Δt_d is a time difference in drift of electrons. The practical realization of such measurement is shown in Fig. 3.2 and is based on the measurement of the difference in drift time of electrons produced in the gas by alpha-particle tracks, at two known distances from a so-called pick-up detector. The electrons released in the gas drift down to the pickup-up detector through a constant field drift channel defined by equally spaced ring electrodes. The two single-wire cylindrical proportional counters depicted as T1 and T2 (far and near respectively) in Fig. 3.2 provide a trigger signal. The α -particles are emitted from an Americium source $^{241}_{95}\text{Am}$ with activity of 90 kBq. Both sources (S1, S2) are placed in front of the detector at well defined distances (see Fig. 3.3). These distances were calculated and measured to account for the Bragg peak produced by the α -particle in our gas. The pulseheight spectrum in the pick-up is recorded as a function of time. The pick-up detector consists of anode and cathode wires planes which are placed parallel above a cathode pad. The cathode wires are at ground potential, preserving the high \vec{E} field induced by the anode wires from entering the active drift volume of the monitor. The nominal operation voltage for the anode wires is approximately 1.4 kV. The cathode pad, of size $9.0 \times 16.8 \text{ mm}^2$, collects the signal induced during an avalanche. A newly designed pick-up detector is described in detail in Section 3.3. The voltage of the anode wire and the cathode tube of trigger counters is provided from the nearest drift field electrodes. This prevents from formations of a strong fields near the counters, and simultaneously limits the field distortions in the drift channel. Therefore, the trigger signal induced on the cathode is read through a 1.5 nF capacitor in order to decouple the read-out electronics from the high voltage of the field cage. Moreover the drifting electrons can be snatched by the field of the anode wire of the

²Gesellschaft für Schwerionenforschung mbH, Darmstadt, Germany

³Solenoidal Tracker At RHIC Forward TPC

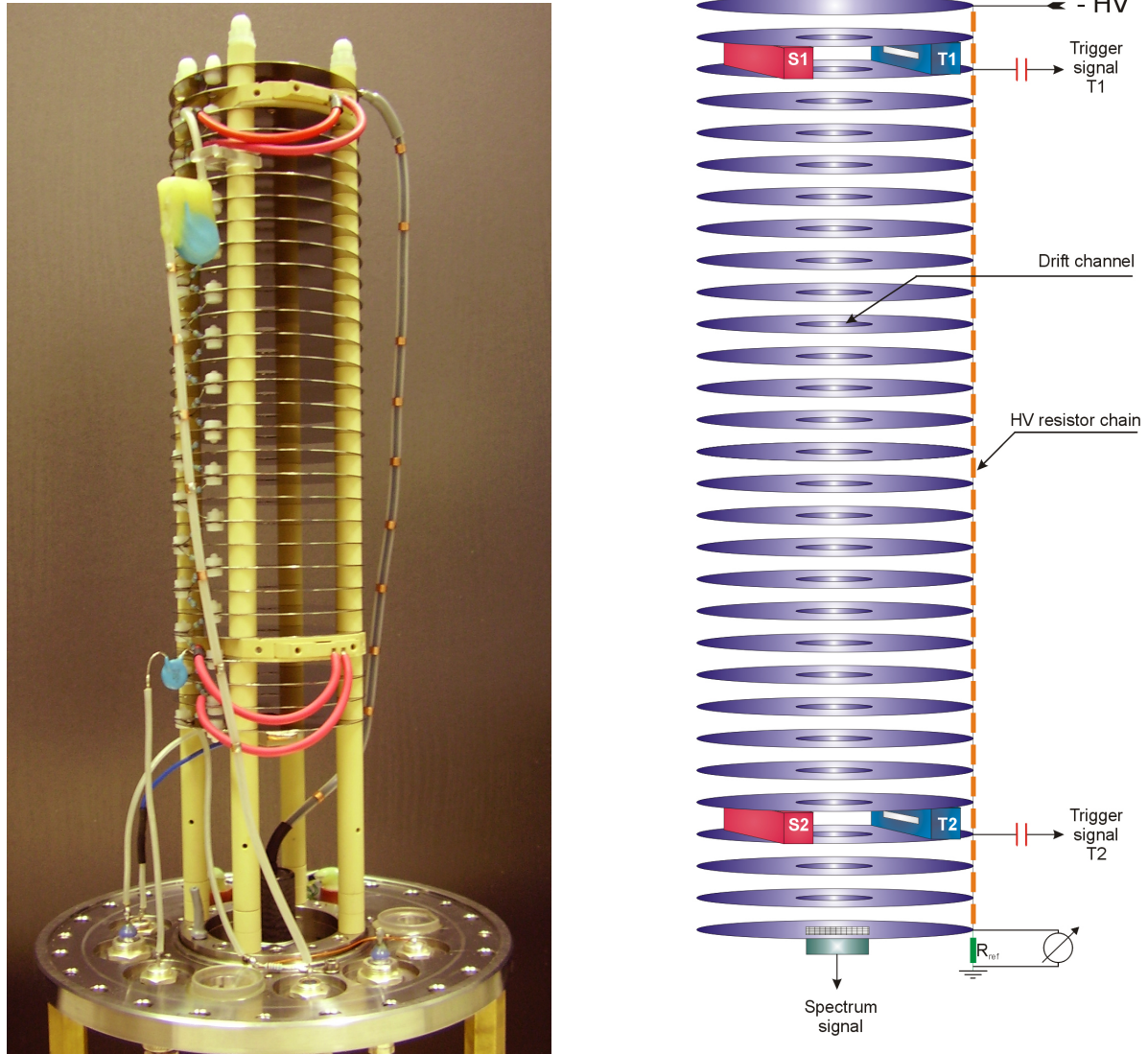


Figure 3.2: The drift velocity monitor. Right panel: the scheme of GOOFIE (T1, T2 – single-wire cylindrical proportional counters, S1, S2 – α -particles sources); left panel: a photograph with field-defining rings and two trigger detectors mounted along the drift channel.

trigger detectors. To minimize this effect, a wire-mesh has been mounted on the entrance of the counter.

The field cage is composed of 30 parallel stainless steel plates (width 0.5 mm) separated by 8.0 mm from each other. The 28 plates with a hole of $\varnothing 10$ mm in the centre provides a drift channel for freed electrons and ions. The negative high voltage is distributed between plates

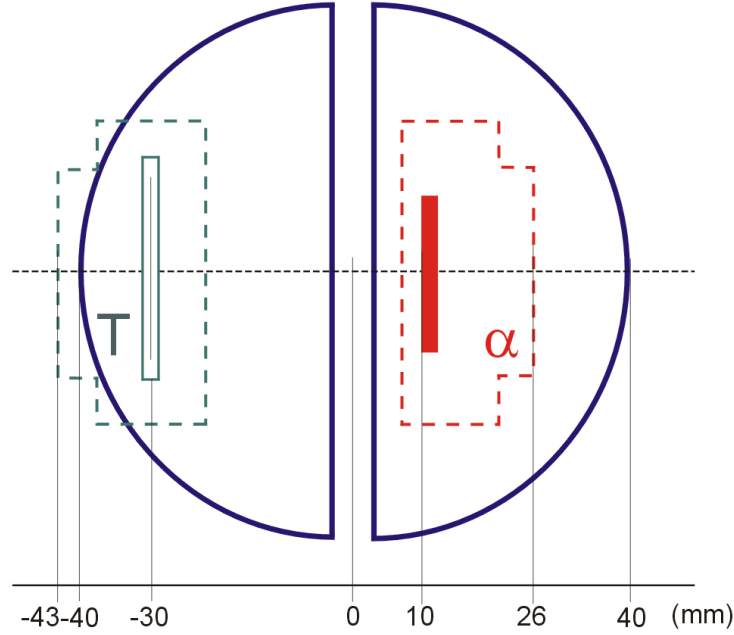


Figure 3.3: Top view of the trigger detectors (T) position with respect to the α -particles source (α). The semicircles are plastic holders for both components.

through 29 resistors. Each resistor of $2.75 \pm 0.003 \text{ M}\Omega$ is connected to the two plates via nylon screws. The field cage is inserted in a stainless steel tube which contains the inlet and outlet for the gas mixture flow and a water-cooling. The distance between the wall of the tube and the field rings electrodes is 31.5 mm, to avoid high voltage breakdowns as well as to minimize the amount of a gas in the vessel. In order to better understand the origin of the discharges which occurred in the drift monitor, viewing ports ($\varnothing 10 \text{ mm}$, $\varnothing 12 \text{ mm}$) were mounted on the main flange. The field cage is supplied with the negative high voltage of approximately -10 kV by a Heinzinger power supply PNC 20000-3 neg. The disadvantage of this power supply was that it has a significant noise due to the alternating current (AC) component remaining in the supplying voltage. Since the trigger counters are connected directly to the resistor chain of the drift monitor it was necessary to minimize AC component by introducing an external passive RC filter ($R=1.1 \text{ M}\Omega$, $C=1 \text{ nF}$). Additionally, the ability to monitor the gas temperature was increased by embedding inside the vessel two PT-100 temperature sensors at the beginning and at the end of the field cage. The sensor signals were then extracted through feedthroughs at the main flange. The **Modular Converters for Regulation Systems (MCR)** modules were used to convert the temperature measured by the PT-100 sensors into standardized electrical analog signals. The module provided a small current for the sensor (approx. 1 mA). The resulting voltage drop was amplified in the module and converted into a signal proportional to the temperature. For linerization of the resistance characteristics, the measured signal was

subsequently fed back to the input. For calibration purposes, both signals were recorded using a sampling ADC CAMAC module (LeCroy LG8252).

The results presented in Section 3.4 were obtained with the prototype read-out electronics shown in Fig. 3.4. The preamplifier-shaper cards depicted as A^{Far} , A^{Near} and $A^{Pick-up}$ were previously used as a read-out system for the CERES GOOFIE (see Section 2.4.2). The trigger logic (the discriminator and the logic fan-in fan-out (LeCroy, LRS429)) based on NIM⁴ modules provided a trigger signal for FADC module. The latter stored the pulseheight spectrum from pick-up detector. The FADC unit is a CAMAC⁵ module [Leo94] for high speed analog sampling applications. One FADC unit enables every 10 ns sampling and storing of 1024, 6 bit wide, samples into the building random access memory. For our chosen gas composition the average electron drift velocity at 400 V/cm is equal to 2.6 cm/ μ s, as shown in Fig. 3.5. This results in an average electron drift time for electrons induced by the α -particle emitted from S1 source to the pick-up detector of approximately 9 μ s. Thus, the sampling time and the storage memory of FADC module as well as the new read-out board described in Section 3.5 allows to perform the acquisition of the pick-up spectrum.

3.3 Gas Monitor Development Studies

The required drift velocity resolution of 10^{-4} by the ALICE TPC forced a further development for the gas monitors. Previously designed GOOFIE at the Max-Planck-Institut in München for the STAR collaboration does not allow for stable operation at 400 V/cm. The required electric field strength is obtained at -9860 V taking into account the monitor field cage length. The highest reached voltage within this configuration is approx. -7 kV before continuous discharge occurs. In order to better understand the origin of such behavior simulations of the GOOFIE layout were performed based on the Garfield [Vee98] application. They confirm the hypothesis that the high potential difference between the far counter and the field cage plates causes the discharges. One of the proposed solutions was to connect the anode wire and cathode tube to the nearest drift field, in order to prevent the formation of strong fields near the counters as it was described in Section 3.2. After this modification it was possible to run the GOOFIE monitor under an electric field of 400 V/cm with the electron drift length Δl_d approx. 20.4 cm. The only disadvantage of the applied solution is that the induced signal has to be decoupled from the high voltage of the field cage. Therefore the trigger signal is read through a capacitor. To avoid the discharges between the wires of the capacitor it was necessary to protect them by a layer of glue as shown in Fig. 3.2 (left panel). Moreover, the signal cable was equipped with copper rings in order to protect it from spurious discharges along the insulating surface. The same solution was applied to the HV cable increasing significantly the stability of the monitor. In order to increase the GOOFIE ability to monitor the gas temperature, which can directly improve the

⁴Nuclear Instrument Module

⁵ Computer Aided Measurement And Control

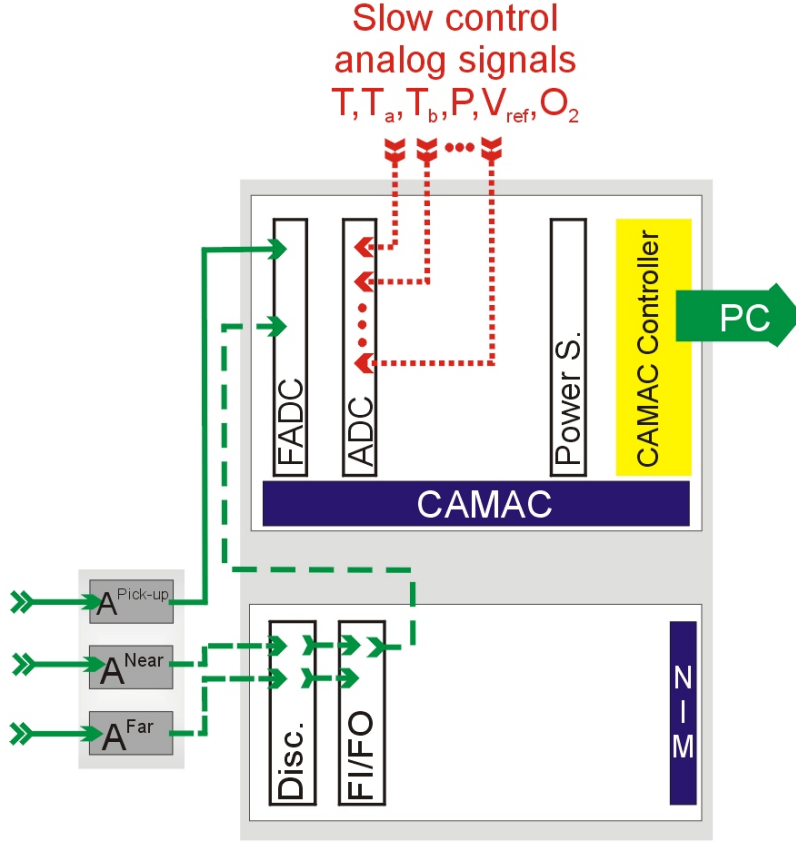


Figure 3.4: The scheme of the prototype electronic. In the NIM crate the trigger logic was build-up from the discriminator (Disc.) and the logical fan-in fan-out (FI/FO). The flash ADC module (FADC) was sampling incoming signal from the pick-up detector. The latter was supplied by the +1.4 kV from the power supply. All slow control parameters e.g. the gas temperature, oxygen contamination, pressure etc. were recording through the multichannel ADC. The CAMAC controller was connected with the PC through the PCI card.

drift velocity resolution (see Section 3.4), two PT-100 sensors were inserted into the active volume of the detector. In addition to these modifications, wire-meshes were mounted on the entrance of the trigger counters (see Section 3.2).

When a charged particle travels through matter, it ionizes the medium and deposits a dose along its path [WW02]. A peak occurs because the interaction cross section increases as the charged particle's energy decreases. The maximum of this dose is called the Bragg Peak; it occurs shortly before the particle stops due to total energy lost. Therefore, the trigger counter should be placed shortly before the Bragg peak in order to maximize its efficiency. The measurement was performed using the prototype TRD ALICE [A⁺03b] chamber with 8 pads read-

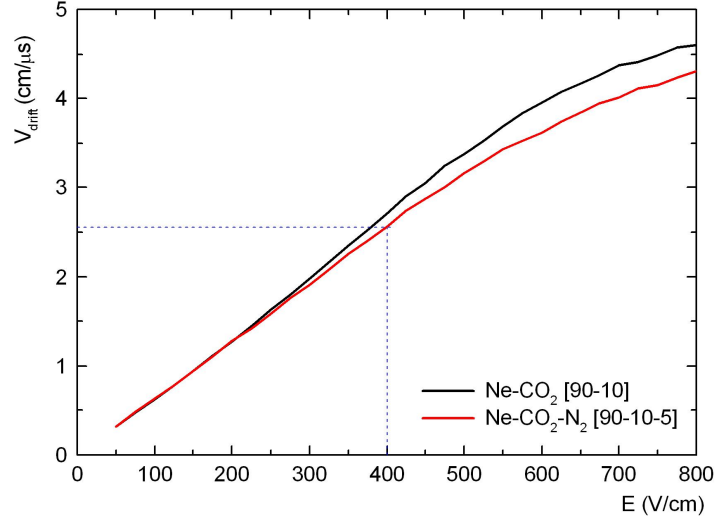


Figure 3.5: The simulation of electron drift velocity in the Ne-CO₂ [90-10] and Ne-CO₂-N₂ [90-10-5] gas composition as a function of the electric field performed by the Garfield simulation package.

out. The uncollimated $^{241}_{95}\text{Am}$ source was located perpendicular to the read-out pads. The energy deposited by α -particles was recorded for each pad using one read-out channel. Therefore, the accuracy of the measurement was folded with the width of a single pad. Additionally to the measurement, numerical calculations of the energy loss by helium nucleus of energy 5480 keV in our gas mixture were performed using the SRIM application [Zie98]. In Fig. 3.6 the ionization as a function of the α -particles range in the Ne-CO₂-N₂ [90-10-5] gas mixture is shown. The data points represent the measured value, and the lines are the simulated values arbitrarily normalized. In order to account for the charge sharing between pads which depends on the electrode geometry, the simulated data were folded with the pad response function (PRF) [GL79, Mat88] of the detector. The discrepancy between the measurement and the simulation was due to the fact that α -particles source was not collimated. Qualitatively, both methods are in agreement concerning the Bragg peak determination. The optimum separation distance was found to be 40 mm.

Previously used pick-up detector had not an uniform gain distribution (see Fig. 3.7), whereas the electric fields created by the anode wires affects significantly the drift field channel of electrons, thus smearing the arrival time of the drifting electrons. Therefore, based on the simulation performed with the Garfield software, a new pick-up detector was designed [Gar]. In Fig. 3.8 the layout of the detector together with the electric field and the electron drift lines, as well as the gas multiplication factor are shown. The new pick-up detector is composed of

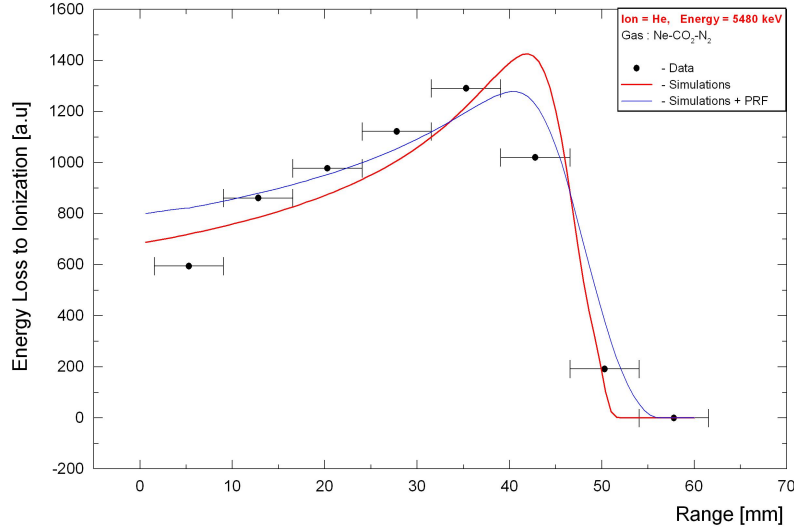


Figure 3.6: The energy deposition in the Ne-CO₂-N₂ [90-10-5] gas mixture by the α -particle emitted from an $^{241}_{95}\text{Am}$ source as a function of the distance. The comparison between the experimental results (full circle) and the simulations (lines).

two planes of wires, anode and cathode, and one cathode pad where induced signal is recorded. The distance between the anode and the cathode wires plane is 2.75 mm, and between cathode pad and anode wires plane is 1.7 mm. The anode wires plane is divided into three groups, one in the center with wires of $\varnothing 0.25 \mu\text{m}$, and remaining two at the edge with wires of $\varnothing 0.75 \mu\text{m}$. The pitch between wires within the group is 1 mm, and between groups is 1.25 mm. Such arrangement of the anode wires significantly increases the uniformity of the gain and the electron arrival time in comparison with the old pick-up detector. Moreover, the disturbance of the electron drift field, caused by an electric field induced by anode wires of the pick-up detector, is significantly reduced by increased number of cathode wires. In order to reduce the charge accumulated on the external surface of the pick-up detector (the charge is accumulated close to the mounting points of the anode wires being covered by a layer of glue) the copper strips were attached to it and connected to the ground. This eliminates discharges which occurred sometimes in the GOOFIE monitor. Other origin of discharges was connected to the poor curing of the glue that was used to protect the tips of anode wires in the pick-up detector. Furthermore, similar problem - extended curing period of the glue - was recognized during the production stage of the ALICE TRD chambers[Gar]. These discharges, of frequency 14 μHz , were observed through the viewing ports installed in the main flange.

The drift velocity and the gas gain depends directly on the gas composition. Therefore,

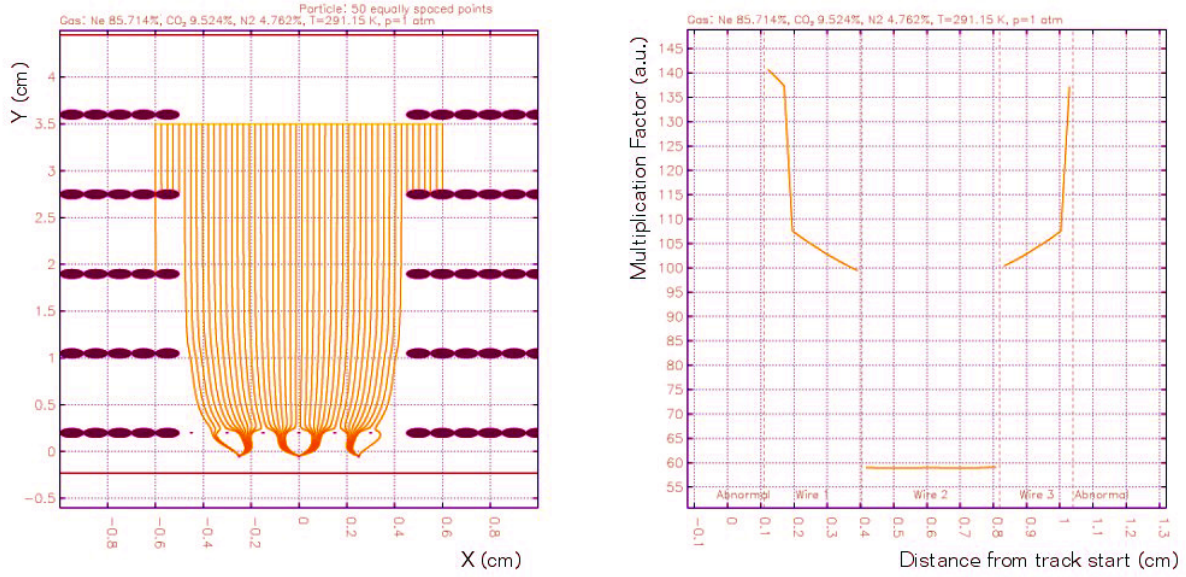


Figure 3.7: The simulation results of previously used pick-up detector. Left panel: the electron drift lines to the three anode wires. Right panel: the multiplication gas factor obtained for layout of anode-cathode wires and the pad cathode.

in order to monitor the gas mixture in the ALICE TPC, the gain and the drift velocity were simulated for a different content of the CO_2 and N_2 . The simulations performed by the Maxwell [Bia99] and the Garfield applications provided for our gas mixture two-dimensional tables of the drift velocity v_d and the gas gain G , respectively, as a function of CO_2 and N_2 concentration (see Fig. 3.9). The GOOFIE monitor provides both input values, the drift velocity and the gain, therefore after normalization with respect to the initial values of ($\text{CO}_2=10\%$ and $\text{N}_2=5\%$) it is achievable to calculate the gas composition by solving a set of linear equations

$$\begin{aligned} v_d(\text{CO}_2(\%), \text{N}_2(\%)) &= A \cdot \text{CO}_2(\%) + B \cdot \text{N}_2(\%) + C, \\ G(\text{CO}_2(\%), \text{N}_2(\%)) &= D \cdot \text{CO}_2(\%) + E \cdot \text{N}_2(\%) + F \end{aligned} \quad (3.3)$$

where, $\text{CO}_2(\%)$ and $\text{N}_2(\%)$, are contents of the carbon dioxide and the nitrogen in the gas mixture respectively. The parameters (A-F) correspond to the plane coefficients obtained by fitting the simulated two-dimensional tables which were normalized for the drift velocity and the gain to initial values. In the table 3.1 the obtained fit parameters from the normalized the drift velocity and gas gain tables are shown. Moreover, the measured variables, v_d and G , also depend on the gas density, thus both of them need to be corrected for.

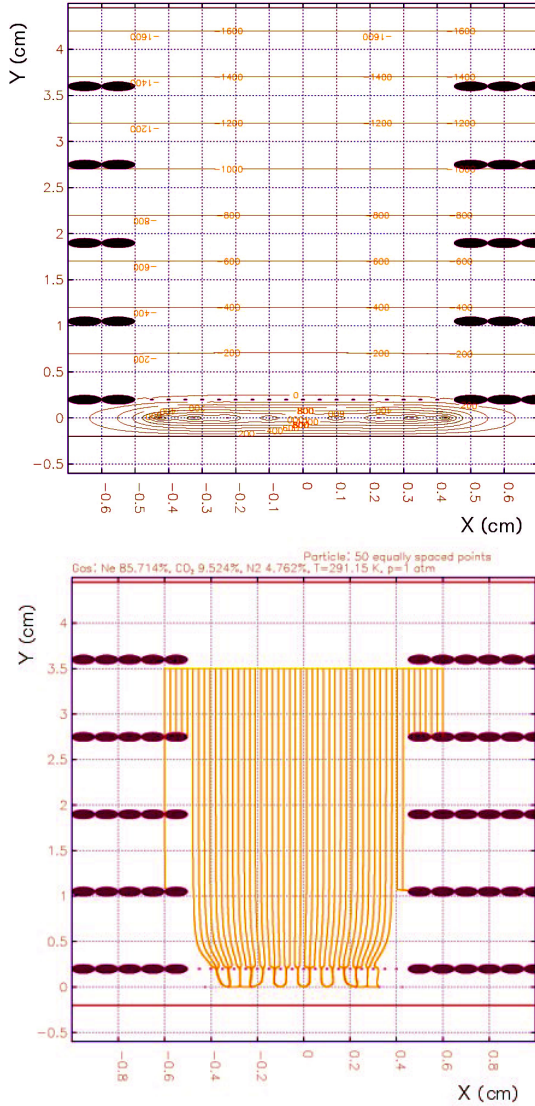


Figure 3.8: New design of the pick-up counter. Left top panel: the electric field lines. Left bottom panel: electrons drift line shows a fairly almost uniform electron arrival time. Right panel: the multiplication factor.

3.4 Data Acquisition and Analysis

After implementing all modifications explained in Section 3.3, several runs of the detector response were performed. The data acquisition and an online monitoring was based on the LabView application running under Windows. During approximately 20 minutes the pulse-height spectrum from the pick-up detector was accumulated over 2500 events recorded by the FADC (see Fig. 3.10). The slow control variables (the gas temperature inside and at the gas outlet, the ambient pressure, the oxygen contamination, and the electric field of the drift channel) were averaged over this time and stored together with the accumulated spectrum of the pick-up on ASCII file. Such file was used as an input for the offline data analysis. Moreover,

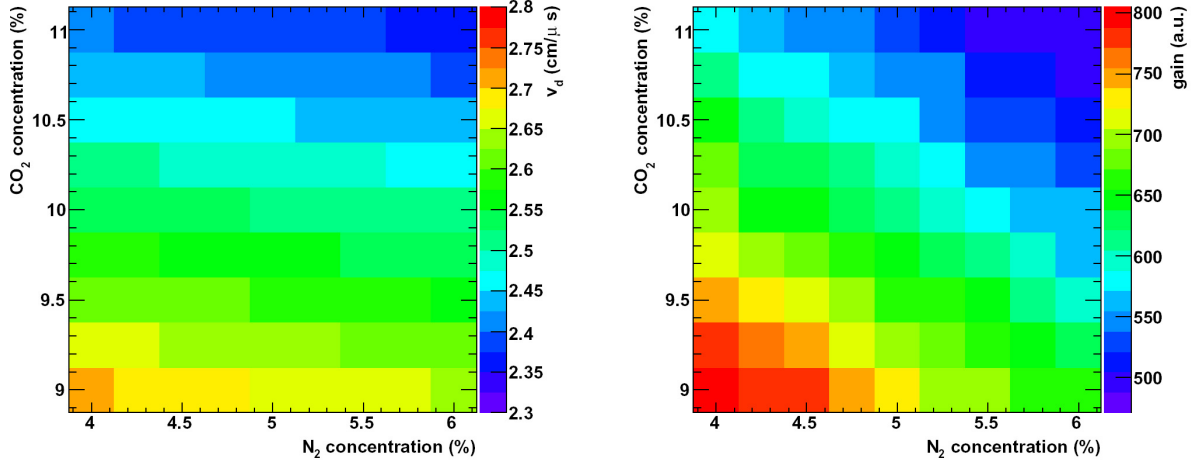


Figure 3.9: The dependences of the gain and the drift velocity as a function of CO₂ and N₂ concentration in the ALICE TPC ternary gas mixture.

parameter	value	error
A	-5.657×10^{-2}	1.72×10^{-1}
B	-9.012×10^{-3}	1.72×10^{-1}
C	1.615	1.93
D	-1.667×10^{-1}	1.73×10^{-1}
E	-1.102×10^{-1}	1.73×10^{-1}
F	3.238	1.96

Table 3.1: The plane coefficients used for calculation of the CO₂ and N₂ concentration in the ALICE TPC gas mixture.

the online application extracts the drift velocity and the gas gain from the accumulated pick-up spectrum by fitting a Gauss distributions to the peaks coming from the near and far source. The obtained values were plotted together with the slow control variables as a function of the production time. The results presented in this section were obtained with a premixed gas in order to avoid, at this stage, any possible fluctuation in the gas composition. The drift velocity is extracted from the position of the peaks in time corresponding to the signals triggered from either the near and the far detectors. Each peak, accumulated over about 2500 events, is fitted with the function

$$f(t) = f_0 + A \cdot \exp \left\{ - \exp \left(- \left(\frac{t - t_{MPV}}{w} \right) \right) - \left(\frac{t - t_{MPV}}{w} \right) + 1 \right\} \quad (3.4)$$

where, f_0 is an offset, t is the time, t_{MPV} is the peak position, and w is the peak width.

An example of the fit results to the pulseheight spectrum, integrated over 2500 events, is shown in Fig. 3.10. Also, the areas under the peaks of the integrated pulseheight spectrum are

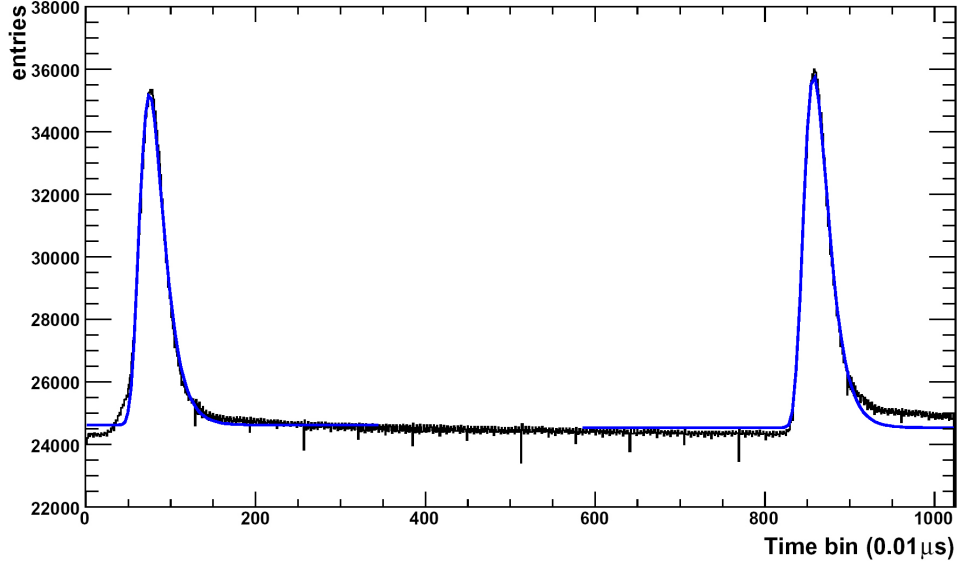


Figure 3.10: An example of the pulseheight spectrum accumulated over 2500 events. The blue solid curves are the results of the function fitting 3.4 to each peak.

extracted from the fit functions by integrating the time bins in a reasonable range around the peak position. The results obtained are normalized to the number of events which contribute into these peaks. These values, which are proportional to the gas gain, together with the drift velocity and slow control information are stored for each accumulated spectrum in a file. This file is then used as an input for the display application. The time dependence of the drift velocity, the gas density, and the oxygen contamination in the gas mixture are shown in Fig. 3.11. The steep increase in the measured drift velocity at the beginning is correlated with the temperature stabilization of the HV resistor chain (see Fig. 3.12), and partially caused by the high oxygen level at this stage. Therefore, this data subset was neglected for the calculation of the GOOFIE monitor resolution.

The influence of the pressure and the temperature changes on the drift velocity and the gas gain has to be corrected for before any analysis of the gas composition is performed. The ability to eliminate such influence is directly connected with the resolution of the gas monitor. Therefore, the accurate monitoring of the ambient condition is one of the crucial issues for the GOOFIE monitor. Assuming the precise knowledge of those variables, the drift velocity can be corrected following

$$v_{d,corr} = v_{d,raw} - P1 \left(\frac{T}{P} - \left\langle \frac{T}{P} \right\rangle \right) \quad (3.5)$$

where, $v_{d,raw}$ is the measured drift velocity, T/P is the gas density at the time of the measurement, $\langle T/P \rangle$ corresponds to the average value of the gas density (calculated over the whole time), and the $P1$ parameter is the slope of the linear function fitted to the correlation shown

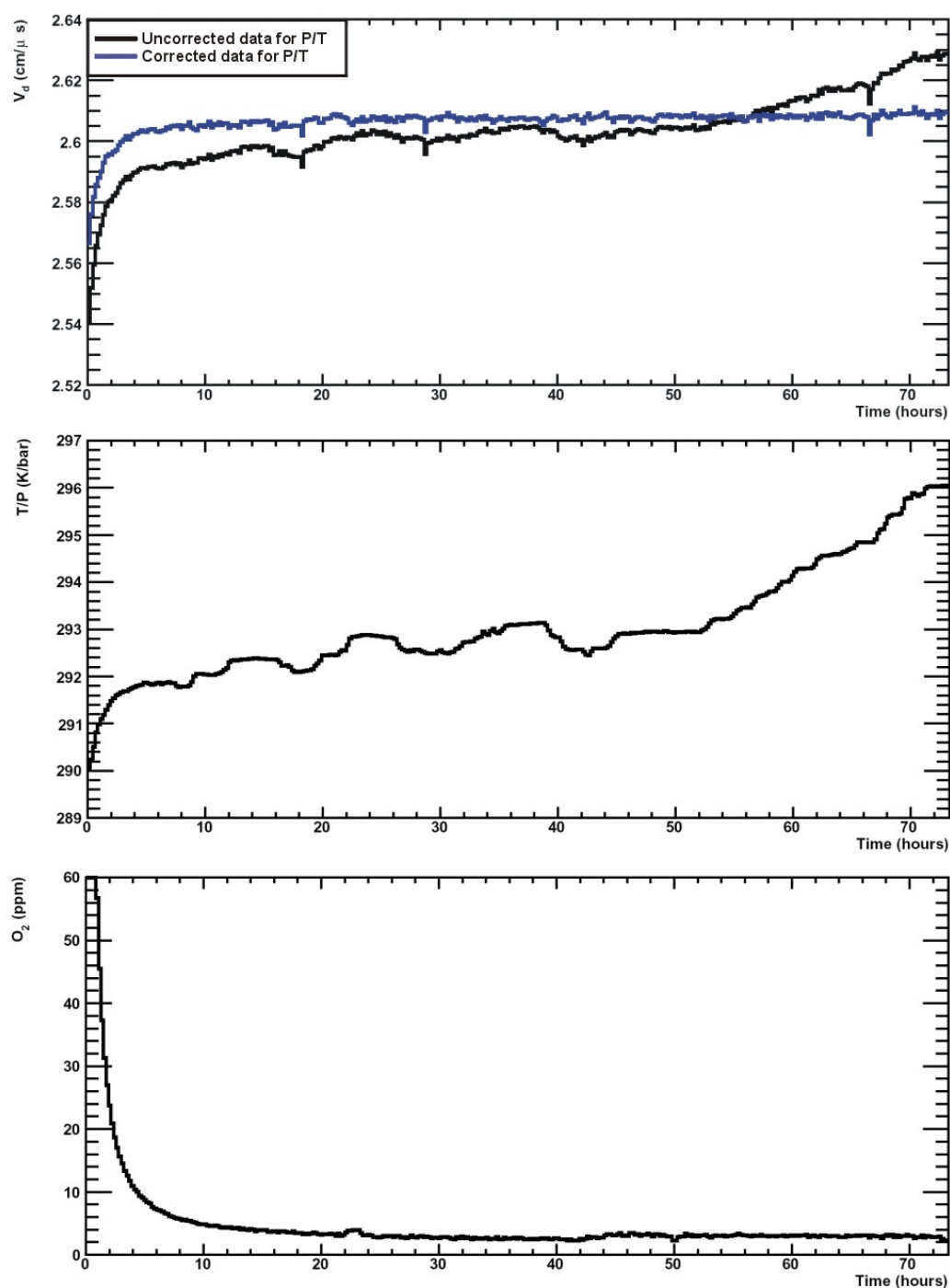


Figure 3.11: The time dependence of the drift monitor variable. Top panel: drift velocity as a function of time, the black line is the raw data, and blue line after applying the T/P correction. Middle panel: the gas density. Bottom panel: oxygen contamination.

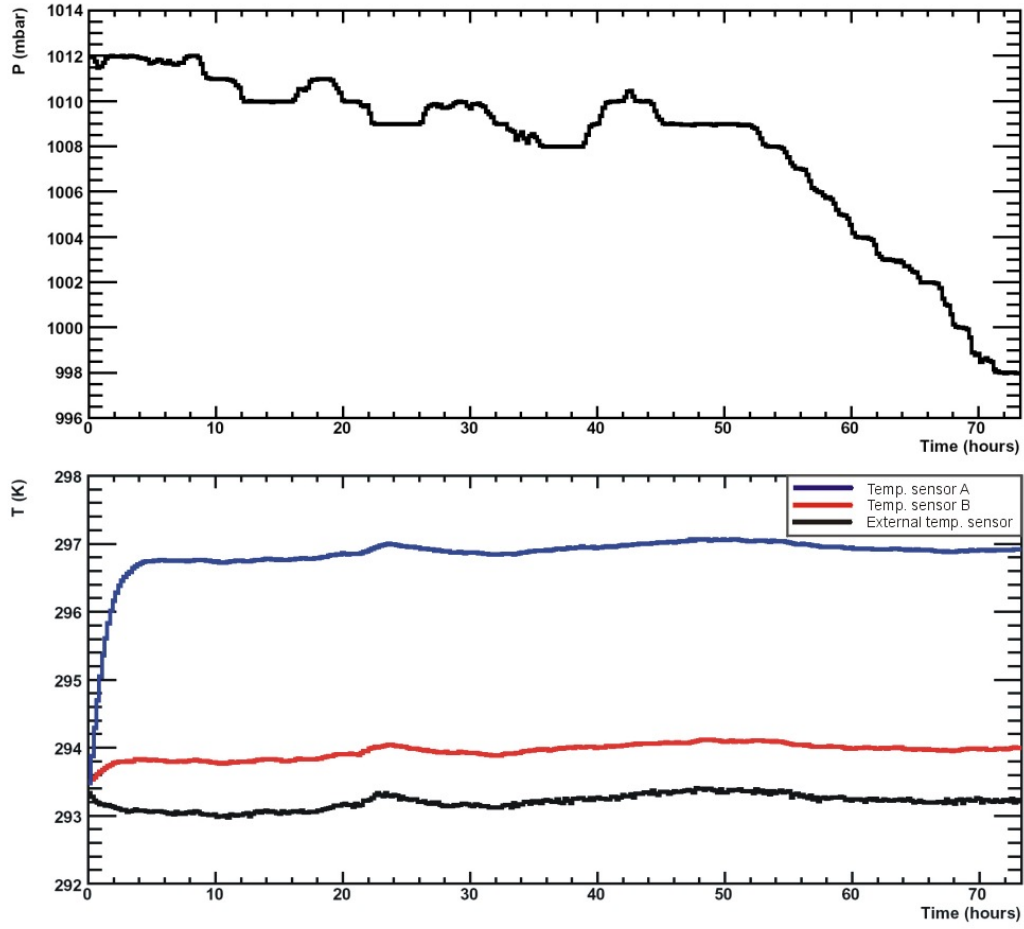


Figure 3.12: The time dependence of the pressure and the temperatures.

in Fig. 3.13. In a similar manner, the gas gain can be corrected for the T/P changes. The corrected drift velocity values are shown in Fig. 3.11 (top panel) as a blue solid curve.

A subsequent offline event-by-event analysis was also performed. This allows to investigate the following aspects

- number of events per integrated pulseheight spectrum,
- different method for the extraction of peak parameters,
- gain dependence of the gas composition,
- gas density influence on the drift velocity resolution.

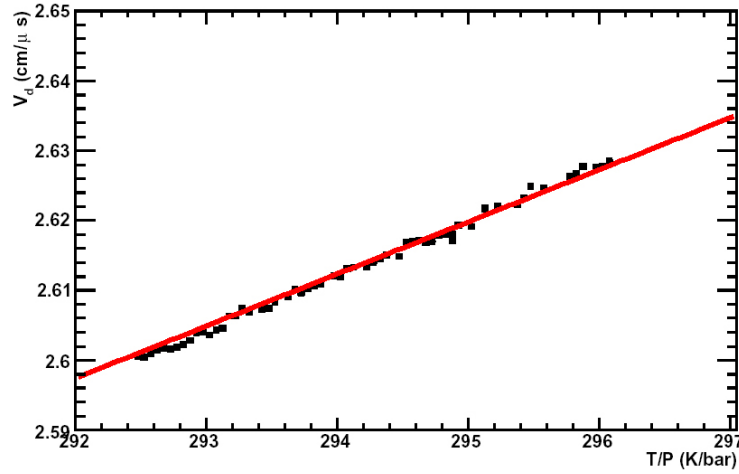


Figure 3.13: Correlation between the measured drift velocity and the gas density.

For each event the pulseheight spectrum was recorded together with the slow control information and stored in an ASCII file. Such solution is not optimized but allows one to record each individual event without significant changes in the online LabView [Ins] application. In this fashion approximately 300 thousand of events were recorded. However, to perform an efficient analysis the data set was first translated into ROOT data format [BR]. Within this framework an analysis data chain was implemented what allowed to study the different peak extraction methods, to merge different numbers of events, and to perform the drift velocity and the gas gain analysis for different events cuts. The results of this analysis answered only partially the questions mentioned above. The optimal number of integrated events was found to be about 2500 as the compromise between the statistical deviations and the ambient conditions changes. Two additional methods of the peak position extraction were also performed. The first is based on the position of the time bin with maximal amplitude, whereas in the second method each individual peak is fitted with Eq. 3.4. The extracted peak positions from the pulseheight spectra are averaged over 2500 events and the mean value is thus obtained. At this stage the different quality cuts can be applied too. From the data set prepared in this manner the drift velocity and the gas gain is extracted and stored in additional ROOT file. These files are used as an input for the offline display application. The qualitative comparison of the results from the different method of the peak extraction analysis showed that the event-by-event peak fitting procedure is a most suitable method for drift velocity analysis. However, in order to quantitatively distinguish between the different methods of peak extraction as well as to understand better the gain variation further analysis has to be accomplished. Therefore, the event-by-event analysis of the GOOFIE data was performed with the newly designed read-out electronics and the redesigned data acquisition chain (see Section 3.5).

3.5 Development of the Read-out Electronics

The prototype electronics used during the monitor response study was a collection of NIM and the CAMAC modules. In order to minimize the read-out electronics of the GOOFIE a new read-out board was developed at CERN EP/ED department [Mus05, Jun05]. In Fig. 3.14 the picture of the new read-out electronics is shown. The GOOFIE monitor provides two trigger signals and the pulseheight spectrum from the pick-up, therefore the board contains three identical input channels that process the analog signals through the electronics chain shown in Fig. 3.15. Access to the information stored on the board is through a USB port. The board is supplied by two DC power supplies that deliver +5 volts for analog and digital circuit respectively. It uses the front-end ALICE TPC read-out components: the **PreAmpShaperAmplifier (PASA)** and the **ALICE TPC Read Out (ALTRO)** chips to process the analog signal. The PASA is a charge sensitive amplifier followed by a semi-Gaussian pulse shaper which has a conversion gain of 12 mV/fC with an output dynamic range of 2 V. The produced pulse has a rise time of 120 ns and a shaping time (FWHM) of about 200 ns. After the PASA, a 10-bit ADC integrated

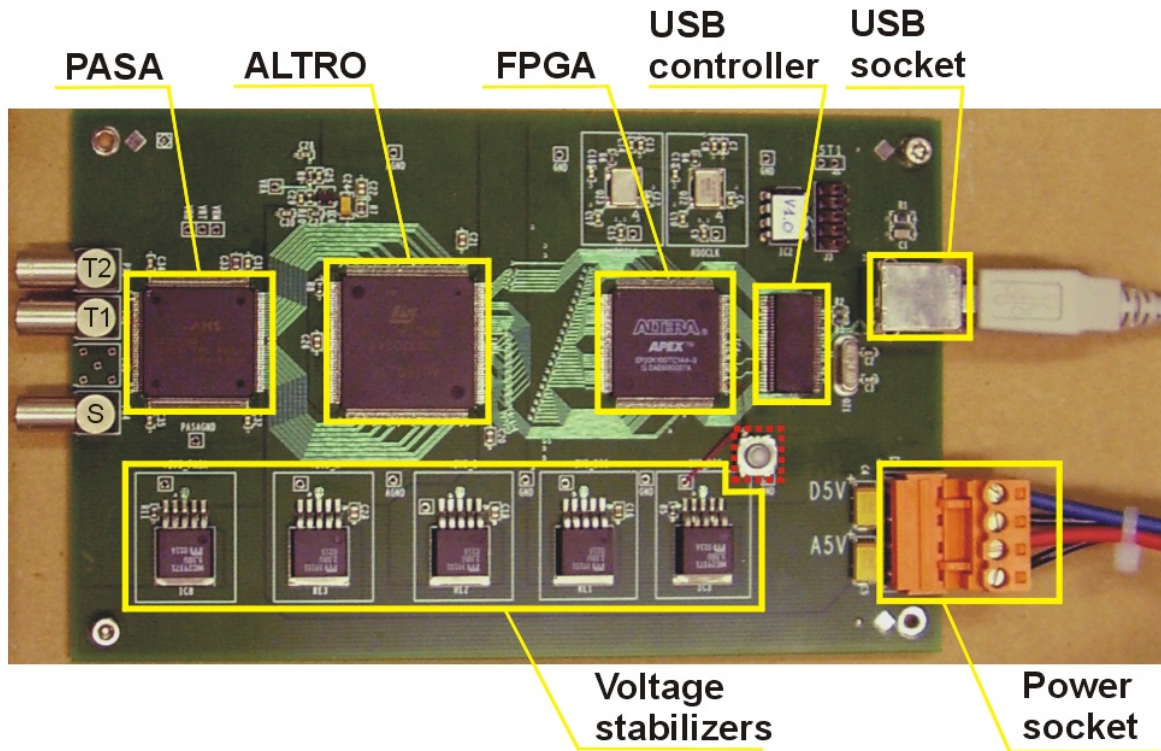


Figure 3.14: A picture of the new readout board for the GOOFIE monitor together with a short description of the components. The configuration of this board is similar to the front-end electronics of the ALICE TPC.

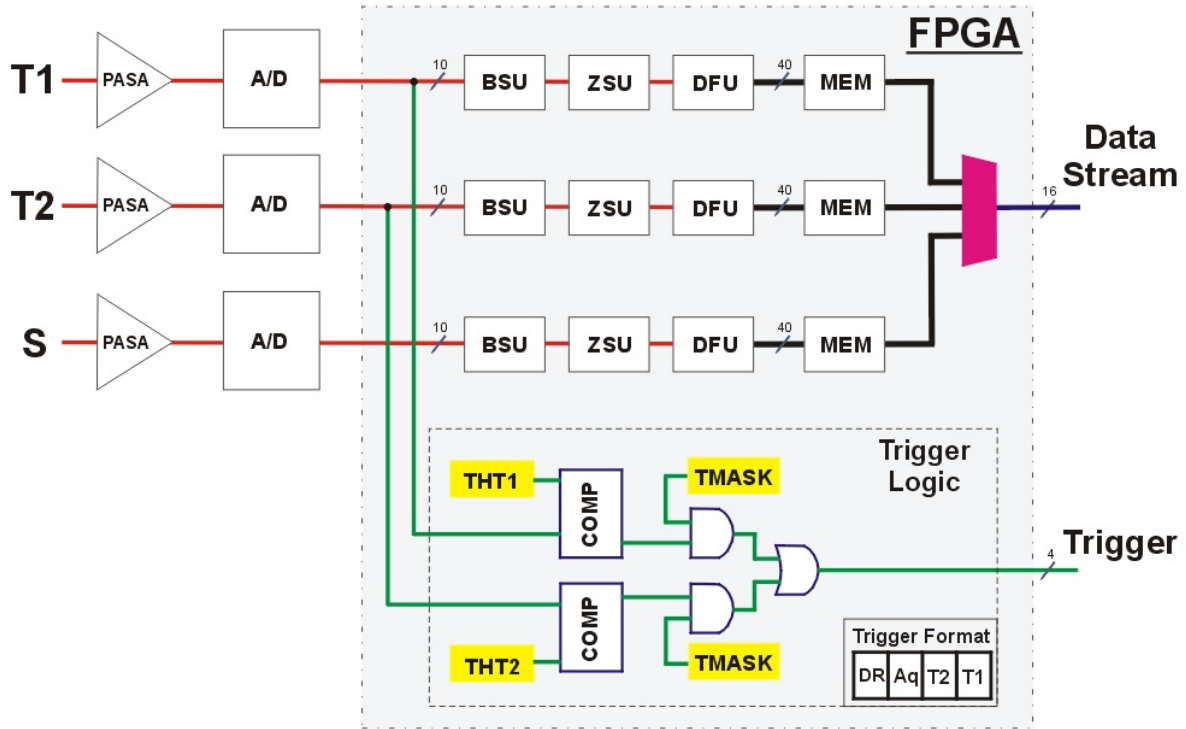


Figure 3.15: The block diagram of the new board constructed for the GOOFIE (see text).

into the ALTRO chip provides the analogue to digital conversion [CE02]. The digital signal is sent to the FPGA where processing chain units of the ALTRO chip were implemented together with the trigger logic. Originally the ALTRO provides all algorithms necessary for the signal processing (tail cancellation, base line restoration, zero suppression, etc.). First, the signal is corrected for the long-term components of the pulseheight spectrum and then the baseline is restored (BSU). In the next step, the zero suppression (ZSU) and the data forming (DFU) are performed. After a trigger occurrence the signal is stored in the memory unit (MEM). The BSU allows to remove systematic effects from measured signal by subtraction of the spurious ones. In order to perform such operation the pattern (pedestal) memory is used. Every time the chip starts an acquisition, the values stored in pedestal memory are subtracted from the measured signal, thus removing systematic perturbations. It is foreseen to use this unit to remove entirely the noise originating from the power supply. Also a fixed value ($ZSPED$) can be subtracted from the incoming signal. A test mode allows to monitor the pattern in the memory. The choice between different modes is selected through the board register $BSLCT$ described in table 3.2. After the BSU the data reduction based on the zero suppression method is performed in the ZSU. In order to distinguish between the pulse from the noise a fixed threshold is applied ($ZSTHD$). All samples below this level are rejected, while a sample above the threshold is

Register	Description	Range
BSLCT	Pedestal subtraction modes, signal - fix value (fpd), pedestal memory (pmem) - fpd, signal - pmem	0, 3, 5
ZSPED	Fix pedestal value	0-512
ZSCTL	Zero suppression mode	(see text)
ZSTHD	Zero suppression threshold	0-512
PRTRG	Pre/Post trigger sample	0-9
NSEVT	Maximum number of samples	500
TMASK	Trigger mask; only trigger from T1, only trigger from T2, or both	1, 2, 3
TATHD	Trigger threshold for channel T1 (THT1)	0-512
TBTHD	Trigger threshold for channel T2 (THT2)	0-512
TRGEV	Trigger information	(see text)
ACTCH	Not used	

Table 3.2: The list of registers used in the GOOFIE read-out board.

considered as a start of the pulse. Additionally, the glitch filter was introduced to check for a consecutive number of samples above threshold in order to confirm the existence of a real pulse. The so-called `seq-mask` can vary from 1 to 3 samples per cluster. In order to keep enough information for further extraction, the complete pulse shape must be recorded. Therefore, a sequence of samples (pre-samples) before the signal overcome the threshold and a sequences of samples (post-samples) after the signal returns below the threshold are also recorded. The number of pre-samples and the number of post-samples can vary independently in the range between 0 and 4. The mode of the glitch filter and pre-samples, post-samples is controlled by a 7 bit register called `ZSCTL`. The bits 6-5 corresponds to `seq-mask`, 4-2 are responsible for post-samples and remaining two for pre-samples. After the zero suppression unit, each found pulse has to be tagged with a time stamp. Otherwise the timing information would be lost by removal of a variable number of samples between accepted pulses. Besides that, in order to distinguish the sample data from the time data an extra word is needed. The latter represents the number of words in the set. Such procedure is performed by the **Data Format Unit (DFU)**. Moreover, the 10-bit words of the data pulses, the time stamp and the number of words in the set are packed in 40-bit words. A trailer completes the data packet, which is the last 40-bit word of the data structure and is composed of the total number of 10-bit words and the channel address. In Fig. 3.16 the back linked data block is shown. The recorded data block is stored in the local memory (MEM) in the FPGA. When a trigger occurs the data is sent, in 16 bits words, to the USB controller and further to the PC through the standard USB 2.0 protocol.

The trigger information is obtained from channels T1 and T2 which are connected to the trigger counters in the GOOFIE. Induced signals in the counters are processed through the trigger logic implemented in the FPGA chip as depicted in Fig. 3.15. The trigger logic permits

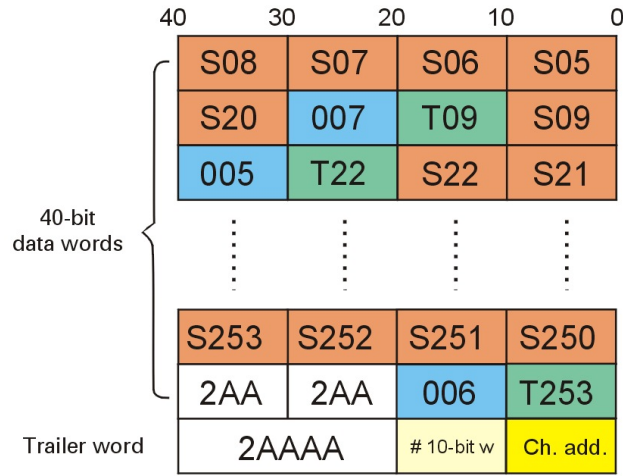


Figure 3.16: The data format of the GOOFIE board. The data are organized in 40-bits words ended with the trailer word. The pulseheight spectrum is sampled in bins of 50 ns and each found peak (S) is tagged with two 10-bit words containing time position (T) and number of 10-bit words in the set.

to set an individual threshold for each trigger channel (THT1, THT2). Moreover, it allows to select a channel which will serve as a trigger signal by register TMASK (see table 3.2). The format of the trigger is a four-bit word containing the information about the origin of the trigger (bit 1-0), the data acquisition (bit 3) as well as the information whether the data is ready to be read from the board (bit 4).

The information exchange with the board is through the USB port, therefore a specific USB driver is required for any operating system. It was possible, after some modifications, to use the USB driver originally designed for the RCU of the ALICE TPC [G⁺05], working under the Linux operating system. The modifications were performed at CERN PH-ESS division [Joo05]. Since the driver provided only a low level of functionality it was necessary to design an additional framework in order to perform the data analysis efficiently. The basic objectives of this framework were

- automatic initialization and termination of the connection with the board,
- access to the registers and pedestal memory,
- unpacking of the data,
- recording and displaying of the pulseheight spectrum for all channels,
- data acquisition,

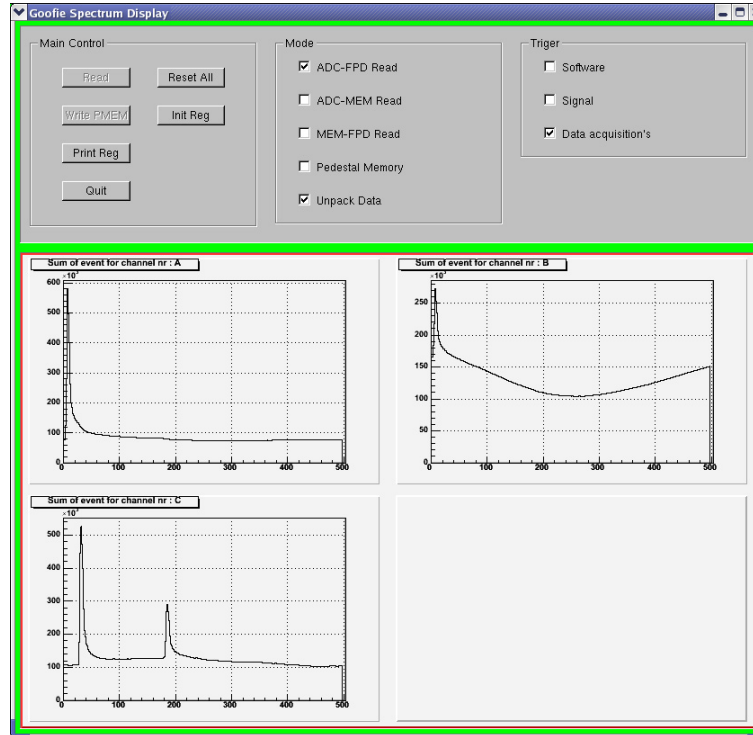


Figure 3.17: The GOOFIE display application panel.

- additional functionality for tests.

This has been implemented in the C++ programming language. The tasks were divided between four main classes. Three of them represent a group of code which can be implemented into any framework in order to process the data exchange with the board, e.g. the GOOFIE DIM server which is foreseen to be a part of the implementation into the DCS of the ALICE TPC. The last class provides a graphic interface for visualization of the incoming data. It is based on ROOT GUI classes and was implemented in order to better understand the new read-out board of GOOFIE monitor. In Fig. 3.17 the display panel is shown together with the pulseheight spectra, integrated over 2500 events, derived from triggers (channels A and B) and pick-up (channel C) detectors of the GOOFIE read-out board. The newly designed framework allows to collect individual events in an efficient way, thus opening a broad flexibility for detailed data analysis. Several runs were performed with the new read-out system and the designed framework. The results of one example are presented in [Her06]. During this run the premixed gas composition was used in order to compare the drift velocity resolution with previous results. The monitoring of the slow control variables was performed by the LabView application under the Windows operation system. The off-line analysis of this data set were performed in a similar manner as the raw data analysis obtained with the prototype electronics (see Section 3.4). Moreover, the gas composition analysis performed on the subset of these data shows irrefutably that the

GOOFIE monitor is sensitive to changes in the gas composition.

3.6 Results and Discussion

With all modifications explained in Section 3.3 being implemented, the GOOFIE gas monitor can be operated under the unprecedented high electric field of 400 V/cm, as in the ALICE TPC. The monitor resolution can be calculated as the ratio between the width of the drift velocity distribution and the mean peak position assuming a Gaussian shape. The drift velocity distribution obtained with the prototype read-out electronics together with the Gaussian fit is shown in Fig. 3.18. The obtained drift velocity resolution of 3×10^{-4} is close to required one (10^{-4}) but still above it. In order to improve the resolution of the monitor an active cooling system is foreseen to be implemented in the final version. Moreover, it can be possible to minimize the data acquisition time, now about 25 minutes per point, by modifications of the trigger counters. The results of the data collected with newly designed read-out electronics presented in Section 3.5 confirmed that the method of measurement the gas composition in the ternary mixture of the ALICE TPC with the GOOFIE monitor is efficient and sensitive to the small variation of the individual components of the mixture. Slightly worse resolution of 0.5 ‰ obtained for this setup can be attributed to the longer time of the data acquisition process, caused by the stronger influence of the baseline fluctuation seen by the far trigger. Moreover,

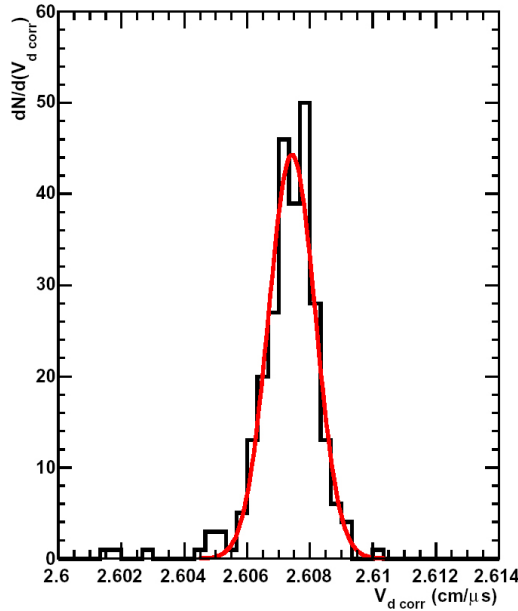


Figure 3.18: The corrected drift velocity distribution fitted by Gaussian obtained with the prototype read-out electronics. The derived drift velocity resolution is 0.3 ‰.

a pulseheight spectrum from the pick-up detector is sampled with a larger time intervals than the previous read-out electronics. Also, the peak shape of the obtained pickup spectrum differ from the previously used parameterization. Therefore, the elimination of the background induced by the high voltage power supply from the signal distributions, better monitoring and controlling of the detector temperature and decreasing the acquisition time should results in a better monitor resolution.

Chapter 4

Analysis of the CERES Data

The present high energy physics experiments are complex systems consisting of many subdetectors. Extracting meaningful numbers from the subdetectors and direct using them for any kind of physical analysis is a tedious task. Before any physics analysis can be performed, the raw data have to be converted to more convenient data format. During this process, called `production`, the compressed raw data is decompressed and the ADC values are transformed into detector hits. At this stage usually the calibrations of the recorded data can be performed. The data are corrected for effects like environmental changes, imperfections of the detectors, gas composition, beam fluctuation, etc. Afterwards hits are grouped into tracks, and are fitted to extract the momentum information. After this step information for physics analysis becomes available. The CERES `production` chain can be presented as follows

- `step0` – first scan of the raw data, determination of the positions and widths of peaks in TDC and ADC spectra
- `step1` – second scan of the raw data, collecting calibrations information
- `step2` – third scan of the raw data, application of the calibration and data reduction
- `step3` – scan of the `step2` output data, further calibrations and data reduction.

The C++ COOL (Ceres **O**bject **O**riented package **L**ibrary) was an integral part of the CERES data analysis chain. Since the COOL package is a very complex and has a sophisticated structure, this framework was not suitable for the efficient physical analysis. In order to facilitate and speed up experiment analysis, a new data format and the essential analysis framework has been designed (see Section 4.3). The first three steps of the analysis were performed in the COOL framework. The output format of `step3c` was designed to minimize the data volume for the subsequent physics analysis.

The `step3` production and all the calibrations described in this section were performed as a part of this thesis work.

4.1 Run 2000

In 2000 the CERES experiment collected a sample of about $33 \cdot 10^6$ Pb-Au collision events at 158 GeV per nucleon. Majority of this data sample was recorded triggering on the most central 7 % of σ_{GEOM} ; additionally, approx. $3 \cdot 10^6$ events with 20 % of σ_{GEOM} and about $0.5 \cdot 10^6$ events with minimum bias trigger were taken. For the calibration purposes, short runs were recorded with the laser tracks, lowered beam intensity, without the target, and without magnetic field. The complete list of the runs taken in the year 2000 can be found in [Miš00]. The SPS accelerator provided ions beam as 4 s bursts every 19,2 s with typical beam intensity of 10^6 ions per burst. Each recorded file corresponded to one burst. The recorded data was stored at the CERN Advanced **STOR**age Manager – CASTOR [B⁺05]. The $\sim 10^5$ bursts were organized in groups (units) of ~ 200 to facilitate calibrations. One calibration unit, thus, corresponds to about 1 hour of data taking.

4.2 Production

The `step0` to `step2` were combined into the large scale `production` of the CERES raw data set [Yur06]. It was performed at the Batch Farm of the CERN Computing Center and took approx. 2 months. During this stage the raw data collected from each detector was unpacked in order to recover the original time sequence of the signals. Such unpacked data, together with the information about the detector calibration stored in the **Start Of Run** – SOR file, was used to fill the lists of the pixels for a given subdetector with the amplitudes and time information.

In the presented analysis of the two particle correlations mainly information from TPC was used, therefore only for this subdetector the short description of the data reconstruction chain is presented. More detailed information about the data reconstruction for all subdetectors can be found in [Yur06, Lud06].

The total number of the spatial pixels in TPC is close to 4 millions. Such large number of pixels taking into account the number of event recorded by the CERES experiment, requires a fast and an accurate algorithm for the track reconstruction. To accomplish this goal the task was organized in the three following steps

- **TPC Hit Finding** – A hit is defined as a local maximum of the amplitude for a given pad and a given time bin. To identify a local maximum the pad and the time coordinates of the pixels were stored in the two-dimensional array and afterward scanned in azimuthal and then in radial direction. The criteria applied during this scan allow to suppress artificial peaks originating from the noise fluctuations. In the case of the amplitude values equal over an odd number of pixels – a middle one is chosen, whereas for an even number of pixels – the amplitude value of the neighboring pixels is used and a pixel with a

neighbor having bigger amplitude is chosen as a local maximum. The signal induced by the particle is usually shared by three pads (see Section 2.4.2) which correspond to 3 pixels in pad direction and approx. 5 in the time direction. Therefore, in order to calculate the position of a hit a center of gravity in ϕ and time direction is derived in a frame of 3 pads \times 5 time-bins around a local maximum called a hit-area. To cope with the overlapping hit-areas each pixel in a frame is weighted with the sum of the adjacent local maximum amplitudes. The hits derived in the pad-time coordinates are transformed to the Cartesian coordinate system with the help of a lookup table which absorb the whole transport process of the charge clusters in the electric and magnetic fields inside the TPC.

- **TPC Track Finding** – Reconstructed hits are combined into the tracks. The maximum number of hits per tracks is given by the number of TPC planes (20). The minimum of 6 hits was required in order to reduced the numbers of artificial tracks. The procedure to find a track is based on the so-called candidate hit with a z -position around the centre of the TPC. Afterwards, from the four subsequent planes (2 upstream and 2 downstream) the four hits closest to the candidate hit are chosen and next all five hits are combined and the sign of the track's curvature in ϕ direction is found. This information is used to define a ϕ window in which further hits are searched. In the next step a linear extrapolation is used to find another hit position in ϕ direction and the procedure is repeated until no more further hits are found. Subsequently, a second order polynomial fit with the Tukey weights [MT87] is used to find the hits omitted during the first iteration. In the case of the soft tracks, which are of a great importance for the dilepton analysis, even more sophisticated algorithms were applied [Yur06].
- **TPC Track Fitting** – Information about the kinematical properties of the reconstructed tracks are accessible only with the help of a Monte-Carlo simulations. Due to an inhomogeneous magnetic field of the CERES TPC analytical description of the particle trajectory was not possible. Thus, a collection of reference tracks generated with the magnetic field map is used for the momentum calculation. The reference tables used for the track fit in the $\phi - z$ and $r - z$ planes were generated using the GEANT simulation [B⁺87] of the CERES experimental setup. The generated hits were stored for a classes of the track inverse momentum, polar angle, and azimuthal angle. For each reconstructed track a straight line in the $r - z$ plane was fitted and then an azimuthal deflection of the track was derived from the fit of two different functions with 2 or 3 parameters. The two-parameters function assumed that the track has an origin at the vertex and provides the radial offset and the inverse momentum of the track, whereas the three-parameters fit additionally takes into account the multiple scattering. Since the low momentum tracks are much more affected by the multiple scattering the three-parameter fit better describes their momentum. For tracks with the momentum larger than approx. 4 (GeV/c) the two-parameters fit has a better resolution due to the additional vertex constraint. In order to take advantage of both parameterizations a weighted combination is provided. Due to

the multiple scattering in the RICH2 mirror and the magnetic field generated by the TPC coils an incoming particle can be distorted before it will reach the TPC active volume. Therefore, the track orientation was an extrapolation to the RICH2 mirror position.

The tracks reconstructed in this manner, after further calibrations explained in the following sections, were used for the two particle correlations analysis.

Monitoring of the quality of the reconstructed data was an integral part of the `production` chain. The monitoring of the `step2` data was accomplished by histogramming the most important variables and fitting them in order to extract the quality parameters. The monitored quantities were organized in five groups

- Trigger – information about the event and the slow control parameters
- Silicon Detector – monitoring of the silicon drift detectors
- RICH Detector – performance of the RICH detectors
- TPC – information about reconstructed hits and tracks from TPC
- Correlations – matching characteristics between subdetectors, etc.

For each unit three groups of 10 bursts, selected from the beginning, middle, and the end, were monitored. The obtained quality parameters were visualized using *cermon* application [Ant04b]. The results could be plotted vs. the data taking time or vs. the data analysis time, thus helping to track the origin of changes in data quality.

4.3 Data Reduction (step3c)

The output data volume of `step2`, explained in Section 4.2, was still too large for an efficient physics analysis and thus further data reduction was required. This was achieved in `step3c` which stored only those variables which were needed for physics analysis. The output of this step was stored in ROOT tree format (Appendix A). The information from each stored event was divided into two main classes, the event (`CSEvent`) and the track (`CSTrack`). The `CSEvent` class contained the information which allows to characterize the event like the collision vertex, the multiplicity, the production time, the trigger properties, and the reaction plane orientation, as well as the array of tracks recorded by all the subdetectors. Each `CSTrack` contained a TPC track segment and the information from the closes tracks of the remaining subdetectors. Closes tracks were found based on the opening angle calculation. Only for the SDD non-vertex tracks a custom matching algorithm was used [Lud06].

production name	average cpu time per event (sec)	total number of produced events 10^6	total size in (TB)
prod012_01	2.2	21.6	0.90
prod013_00	2.2	7.9	0.34

Table 4.1: Performance of the step3c production. The two numbers contained in the name denote the version numbers of the step0-2 and the step3 productions, respectively, e.g. prod012_01 means the data were processed with the version 12 of the step0-2 chain, and subsequently with the version 01 of step3.

The step3c was performed at the CERN Batch Farm and took approx. 2 weeks. All production components were implemented using C/C++ programming languages. Table 4.1 shows the performance of the step3c. The available data set was divided into groups of five units. For each such group a file with the setup information was created. The production chain was using these files as an input and processing the files as follow

- transferring the step2 output files from the CASTOR tapes to the pool via Remote File I/O (RFIO) protocol,
- executing one batch job for each ten step2 ROOT files,
- storing the reduced events in the new step3c ROOT file,
- collecting a trigger information from the step2 ROOT files for the centrality calibration (see Section 4.8) purpose,
- storing a momentum calibration information,
- grouping ten step3c ROOT files into one tar file in order to avoid an overloading of the CASTOR system with a high number of the small size files,
- transferring a tar file to the CASTOR tapes,
- copying the output of the momentum calibration files on the AFS volume.

Prior to the data reduction the event vertex refitting procedure and TPC tracks refitting were performed. The event vertex refitting procedure was used for final tuning of the vertex position. In the step2 it was already clearly visible that the reconstructed vertex positions were not in agreement with the physical position of the 13 gold discs. Therefore, in the step3c the event vertex refitting procedure was implemented. In this procedure the radius of the reconstructed hits was recalculated using the correction values. The obtained hits were combined into tracks and from them the new event vertex was calculated. In Fig. 4.1 the distribution of the reconstructed vertex positions is shown. Thirteen gold discs were well resolved along the

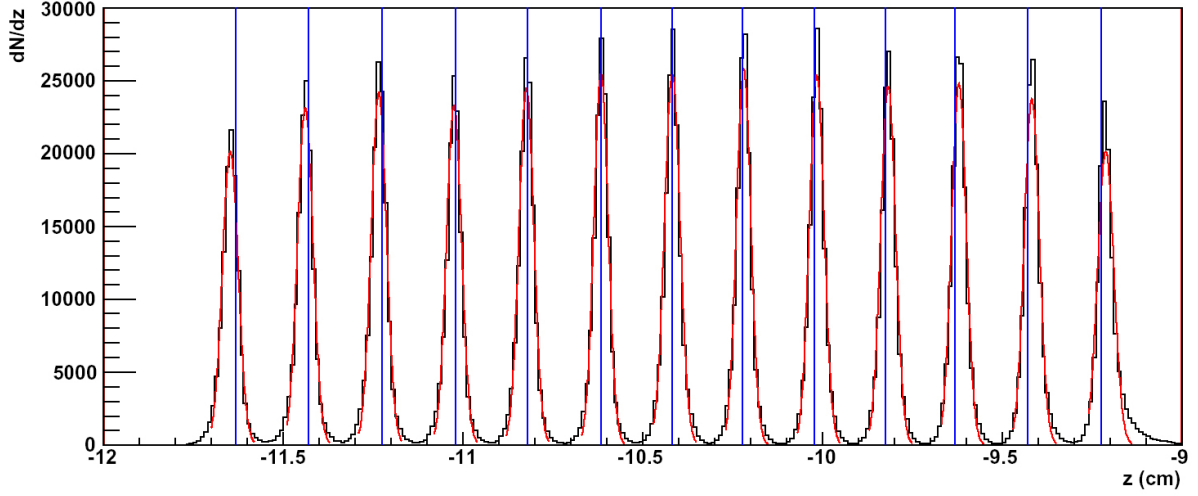


Figure 4.1: The reconstructed vertex position along the beam axis after applying the vertex refitting method. The physical position of targets are depicted as horizontal solid lines.

beam direction with a resolution of approx. $210.0 \mu\text{m}$. On the other hand, in order to improve the momentum resolution, the position of TPC hits was calibrated using the high momentum π tracks. This procedure was implemented in the `step3c` and called TPC tracks refitting. Also, trigger information (scalars) were collected in order to properly calibrate the centrality of the collision (see Section 4.8). The data quality was monitored, similar like for `step2`, by histogramming the most important variables separately for each data unit. The access to the monitoring information was provided through the *cermon* application [Ant04a] from the GSI Linux environment.

4.4 Momentum Calibration

The momentum resolution of the TPC is determined by the spatial hit resolution, the number of reconstructed hits on tracks, and the multiple scattering in the active volume. In order to estimate quantitatively the momentum resolution of the CERES TPC, a full tracking simulation was performed [Yur06]. The differences between the original and the reconstructed momenta defined the momentum resolution as the standard deviation of the derived distribution. The track fitting algorithm allows to use the two- and three- parameterizations of the track curvature. The two-parameter fit (p_2) yields optimal results for high momentum tracks, while the three-parameter fit (p_3) describes better low momentum tracks. A combination of both fitting methods was used for best momentum resolution over the whole momentum range. The

relation between the combined momentum track p_{comb} and p_2, p_3 is given by

$$p_{comb} = \frac{(p_2/\sigma_2^2) + (p_3/\sigma_3^2)}{(1/\sigma_2^2) + (1/\sigma_3^2)}, \quad (4.1)$$

where σ_2 , and σ_3 are the relative momentum resolutions of a given momenta obtained for the two- and three-parameter fit, respectively. The momentum resolution obtained with the final calibration is

$$\frac{\Delta p}{p} = 2\% \oplus 1\% \cdot p/\text{GeV} \quad (4.2)$$

resulting in $\Delta m/m = 0.038$ for the ϕ meson.

The absolute measured value of a particle momentum can vary during the data taking period. It is caused by the fluctuation in the electric and the magnetic field, the change in the gas composition, the temperature, and in the ambient pressure. Calibrations applied to account for these effects in some cases are not sufficient to remove them entirely. This leads to smearing of the reconstructed momentum. Assuming the equal abundances of positively and negatively charged particles and the infinite spatial and temporal resolution of the detector, the distribution of the charge over momentum (q/p) should be centered at zero. The residual miscalibration, discussed above, can manifest itself as a shift of the q/p distribution, as depicted in Fig. 4.2. Therefore, further calibrations of the reconstructed momentum have to be performed. A convenient particle choice for this purpose are pions, due to similar multiplicities of π^+ and π^- . The nominal minimum position of the q/p distribution was found by comparing the reconstructed masses of Λ^- and $\bar{\Lambda}$ -hyperons in the data as a function of momentum. The systematic variation of the q/p minimum position was quantitatively parameterized by

$$F(q/p) = F(0) + P1 \cdot (q/p - q/p_{min.pos.})^2 + P2 \cdot (q/p - q/p_{min.pos.})^4, \quad (4.3)$$

where $F(0)$ is an offset of the q/p minimum position ($q/p_{min.pos.}$), $P1$ and $P2$ are the slopes of the q/p distribution. In Fig. 4.3 the position of the minimum of the raw q/p_{comb} distributions, obtained for pions sample identified via the energy loss vs. momentum in the CERES TPC, are shown as a function of the unit number. The difference between the nominal value and the one extracted from the fit is used to correct remaining deviations in the reconstructed momentum.

The calibration was done in the three major steps. In the first step, the necessary information was collected during the data reduction process (`step3c`) for each calibration unit. Based on the information from RICH detectors the high momentum pions were identified by the ring radius and afterwards matched with the remaining SDD-TPC tracks. The momenta of the found pion tracks were stored in two-dimensional histograms of $n(q/p, \phi_{TPC})$ for a given bin of polar angle (θ_{TPC}). This allows to account for the geometrical effects and the limited knowledge about \vec{B} and \vec{E} fields. The optimum bins were found to be 43.5 mrad for the azimuthal angle and 20 mrad in the polar angle. The recorded two-dimensional histograms were merged in three groups of subsamples: for positive \vec{B} field at the beginning of the beam

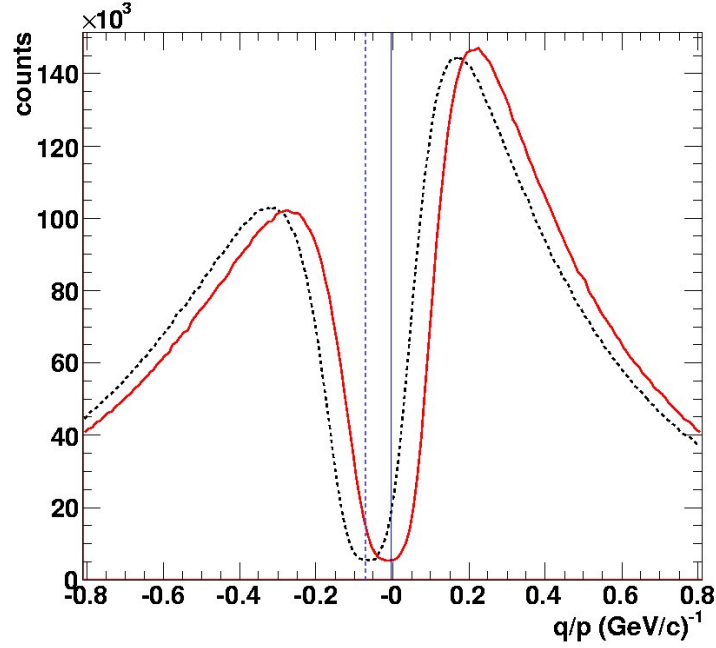


Figure 4.2: Sketch of the calibration method for small momentum variation. The solid and the dash curves correspond to the nominal and the measured positions of the inverse momentum distribution, respectively. The amount of displacement in the (q/p) -direction is used as an additive correction to $(1/p)$.

time, negative \vec{B} field, and positive \vec{B} field at the end of the beam time. The correction factors

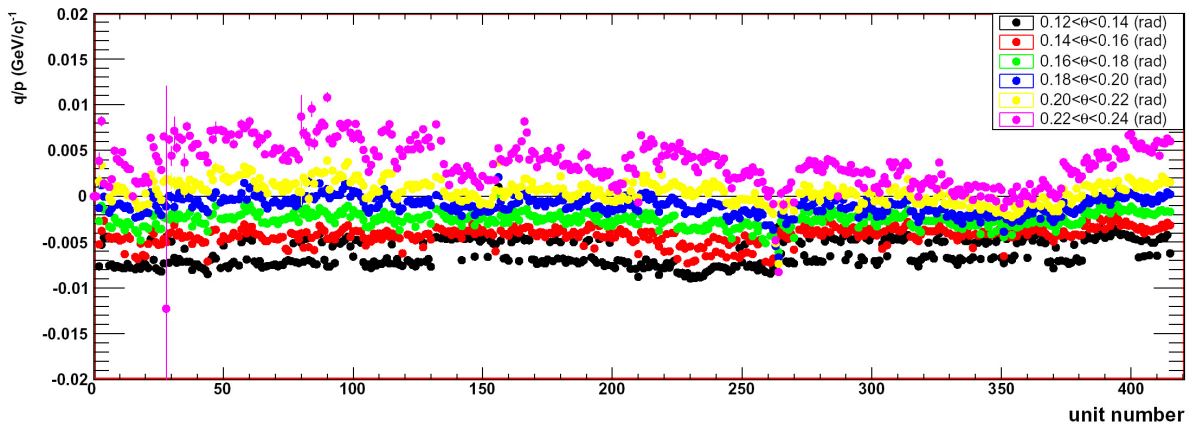


Figure 4.3: The position of the minimum in the raw q/p_{comb} distribution as a function of the unit number for six groups of θ_{TPC} track.

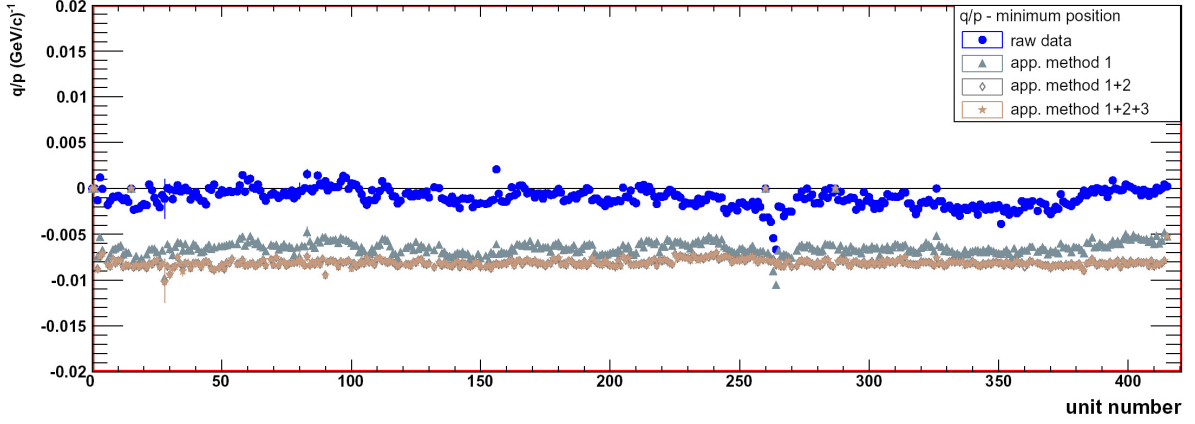


Figure 4.4: Comparison between different methods used to correct the inverse momentum distribution for $\theta \in (0.18, 0.20)$ rad.

$\Delta(1/p_{2,3})(\theta, \phi)$ were extracted from the fit function (Eq. 4.3). Moreover, from $n(q/p, \phi_{TPC})$ histograms, integrated over the ϕ_{TPC} and θ_{TPC} , the minimum position of $\Delta(1/p_2)(unit)$ and $\Delta(1/p_3)(unit)$ for each calibration unit was extracted as well as the average values ($\overline{\Delta(1/p_2)}$, and $\overline{\Delta(1/p_3)}$) for all available statistics were obtained. The combination of these values results in a correction factor given by

$$\Delta(1/p_n)_{method1} = \Delta(1/p_n)(0) \cdot B + \left[\Delta(1/p_n)(\theta, \phi) - \overline{\Delta(1/p_n)} + \Delta(1/p_n)(unit) \right], \quad (4.4)$$

where $n=2,3$ correspond to the two- or three-parameters fit method, $\Delta(1/p_n)(0)$ is a shift obtained from Monte Carlo simulations and B is a sign of the applied magnetic field in the TPC. In Fig. 4.4 the results of the correction (full triangle) together with the uncorrected data (full circle) are shown. Subsequently, the last two corrections were performed on the pion subsamples identified via an energy loss vs. momentum in the TPC. This allows to increase significantly statistics, but to diminish the purity of the pions samples. Number of pions selected in this manner allows to study the q/p minimum position as a function of θ_{TPC} integrated over an azimuthal angle for each calibration unit separately. Obtained correction factors are given by

$$\Delta(1/p_n)_{method2} = B \cdot \left[\Delta(1/p_n)(\theta, unit) - \overline{\Delta(1/p_n)(\theta, unit)} \right], \quad (4.5)$$

where $\overline{\Delta(1/p_n)(\theta, unit)}$ is the average value integrated over the calibration units and the θ angles. The latter were combined with the one calculated from the so-called “method 1” ($\Delta(1/p_n)_{method1}$) and subtracted from the measured inverse momentum of the track (see Fig. 4.4 (open diamond)). Finally, a last correction is determined in even finer entities of 10 bursts, but integrated over ϕ and θ , so-called “method 3”. The corrected values of the inverse momentum can be expressed as follow

$$(q/p_n)_{corr} = (q/p_n) - \{ \Delta(1/p_n)_{method1} + \Delta(1/p_n)_{method2} + \Delta(1/p_n)(10\ burst) - B \cdot \overline{\Delta(1/p_n)(10\ burst)} \}. \quad (4.6)$$

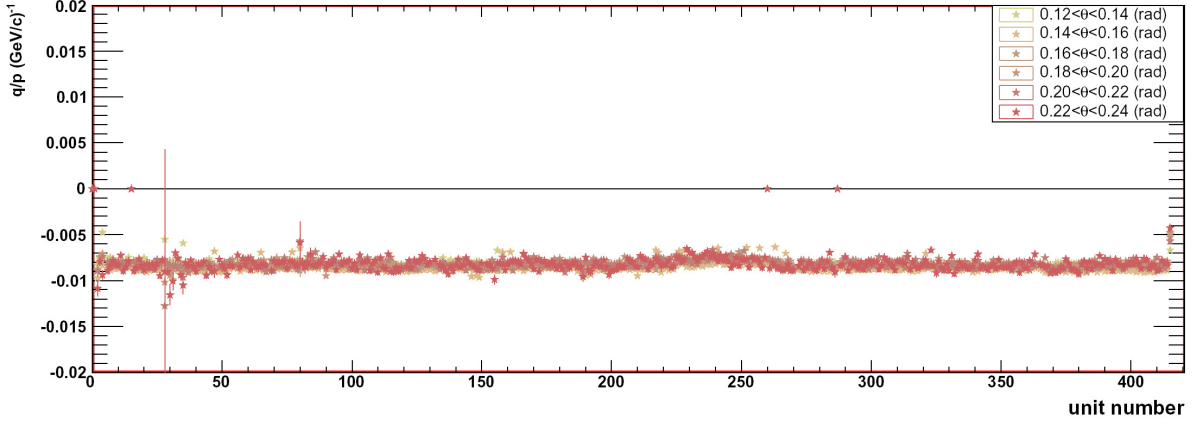


Figure 4.5: Results of the momentum calibration methods. The minimum position of the inverse momentum distribution as a function of unit number for six groups of θ_{TPC} track.

The minimum positions of the fully calibrated q/p distributions as a function of the unit number are shown in Fig. 4.5.

4.5 Energy Loss Calibration

The energy loss of charged particles in the medium occurs mainly via ionization. The mean rate of the energy loss is well described in terms of the Bethe-Bloch equation [WW02] which can be parameterized by

$$\frac{dE}{dx} \approx \frac{A}{\beta^2} \cdot \left(B + C \cdot \ln(\beta^2 \gamma^2) - D \cdot \beta^2 - \frac{\delta}{2} \right), \quad (4.7)$$

in case of the CERES TPC data. The $A - D$ parameters were found based on the analysis of the clear sample of electrons and pions identified through the RICH detectors ($A=13.2$, $B=15.05$, $C=1.08$, $D=4.0$). The last term in the Eq. 4.7 corresponds to the density effect. The latter reduces the relativistic rise from $\sim \ln \gamma^2$ to $\sim \ln \gamma$ at high γ and can be parameterized by [SP71]

$$\begin{aligned} \frac{\delta}{2} &= 4.606 \cdot X + C + a \cdot (X_1 - X)^m & (X_0 < X < X_1), \\ \frac{\delta}{2} &= 4.606 \cdot X + C & (X > X_1). \end{aligned} \quad (4.8)$$

In these formulas δ is expressed as a function of X , defined by $X = \log_{10}(\beta\gamma)$, where the term $4.606 \cdot X$ is simply $2 \ln(\beta\gamma)$. The parameters X_0 and X_1 are particular values of X , such that

$\delta=0$ for $X < X_0$ and for $X > X_1$ δ reaches its asymptotic form. All parameters in Eqs. 4.8 depend on the medium and can be found in literature. For particular composition of the CERES TPC gas mixture the density effect parameters were set to $C = -11.73$, $a = 0.31$, $m = 2.96$, $X_0 = 2.11$, and $X_1 = 4.0$. Since the dE/dx distribution has a long Landau tail, it is common to use in an experiment a truncated mean to characterize the energy loss of a particle. The CERES TPC provided up to 20 samples per measured track (see Section 2.4). The distribution of the truncated mean energy loss as a function of the particles momentum is shown in Fig. 4.6. The contours depicted in Fig. 4.6 follow the parameterization explained above and are used to select protons and pions for two particle correlation analysis presented in the following chapters. The TPC dE/dx resolution depends on the number of hits; the average resolution is 10 % [Yur06]. In addition to the unit-by-unit calibration of dE/dx accomplished during the data production, a finer granulated calibration was performed on the output of the `step3c`. Monitoring of the dE/dx pion peak position for a given range of the particle momentum was performed for every 10 bursts. The correction factor chosen such as to bring the mean dE/dx of pions to its nominal value, was applied to each measurement within the 10 bursts. As the fluctuations of the dE/dx pion peak position as a function of time are rather small the influence of this calibration on the

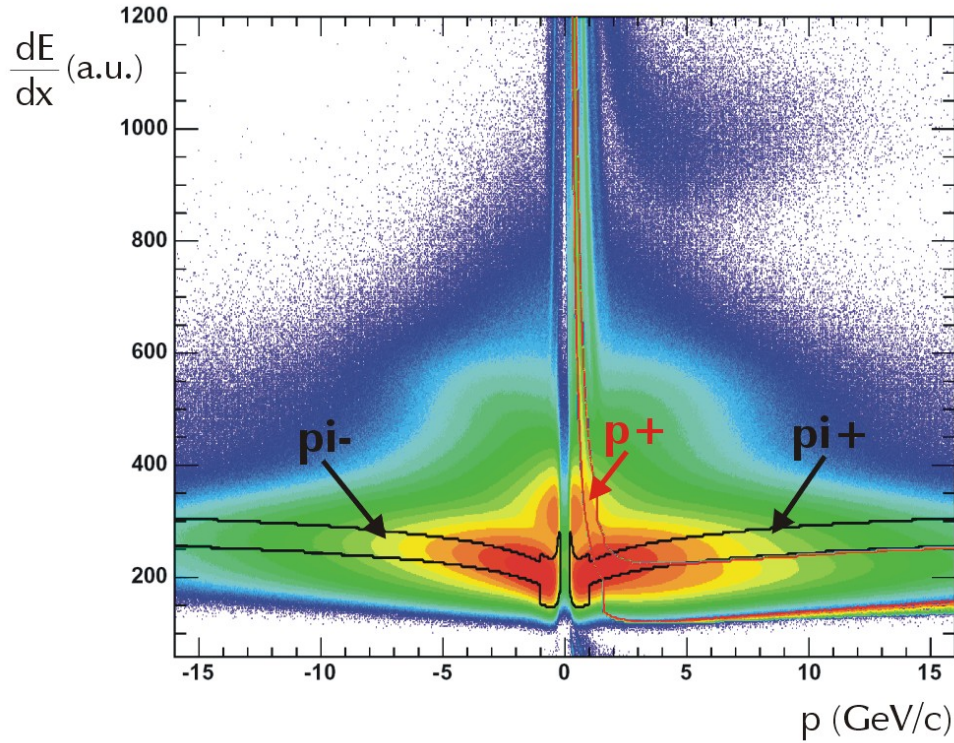


Figure 4.6: The energy loss as a function of particle momentum from the TPC tracks. The contours represent the pion and proton cuts used in the correlation analysis.

obtained resolution is not very significant.

4.6 Matching Calibration

In the CERES experiment the position of particles was measured mainly by the SDD and the TPC. Each of these subdetectors reconstructed tracks from hits induced by particles moving through its active volume. Therefore, in order to obtain complete paths of particles created during the collision, tracks from the SDD and the TPC were combined to TCP-SDD tracks based on the calculation of the opening angles ($\Delta\theta$, $\Delta\phi$). The latter was calculated for each combination of tracks recorded by subdetectors, and a pair with the minimum opening angle was chosen as the best candidate for the TCP-SDD track. In order to account for the geometrical effects in the subdetectors and the different track reconstruction efficiency the matching distribution $n(\Delta\theta, \Delta\phi)$ was calculated for each unit separately in bins of

- inverse momentum (7),
- azimuthal angle (48),
- polar angle (7),
- numbers of anodes per reconstructed hit in SDD (2).

The hit resolution of the SDD depends on the number of anodes on which the induced signal was recorded. Thus, the first of the bin represents the SDD tracks which were reconstructed from the multi-anode hits in both silicon detectors only, and the second bin describes the rest. The obtained distributions were projected on $\Delta\theta$ and $\Delta\phi$ axis, respectively, and fitted by one-dimensional Gaussian to extract the mean position of the peak. The correction factors, derived for each unit, represent a deviation of the mean positions of the matching distribution from zero. In Fig. 4.7 an example of two-dimensional distribution of the opening angle (top left panel) together with the projections on $\Delta\phi$ (bottom left panel) and $\Delta\theta$ (bottom right panel) axis, for a sample of reconstructed track with inverse momenta $-0.7 < 1/p < -0.4$ (GeV/c)⁻¹, polar angle between 0.16 and 0.18 radians, and azimuthal angle from -0.52 to -0.39 radians, are shown. The influence of the uncorrelated matching between TPC and SDD tracks on the extracted mean position was studied by subtracting background distribution from the signal distribution. The background matching distribution was obtained by choosing the TPC and SDD track from different events and finding the best candidate for the TCP-SDD track, similar as for tracks originating from the same event. An example of the derived background distributions (blue histogram) normalized to the tails of the signal distributions (green histogram) is shown in the two bottom panels in Fig. 4.7. The mean position of the background-free matching distribution does not differ significantly from the raw matching distribution, therefore, the background subtraction was neglected in this calibration step. In addition to the unit-by-unit calibration, the

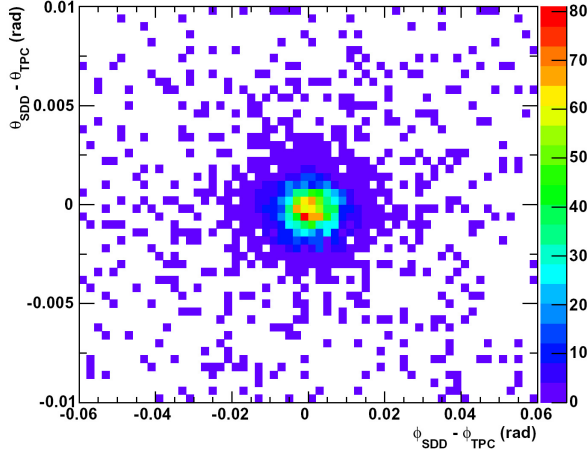
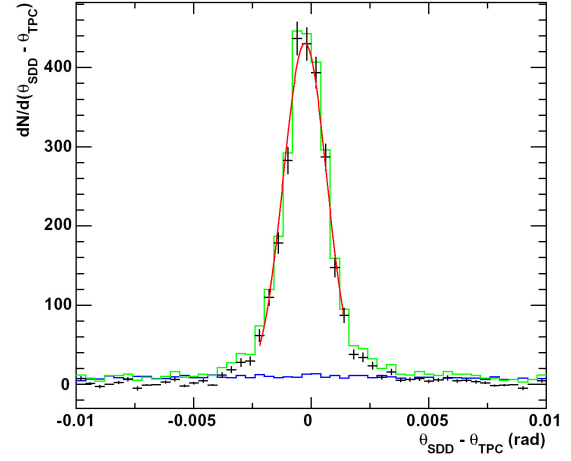
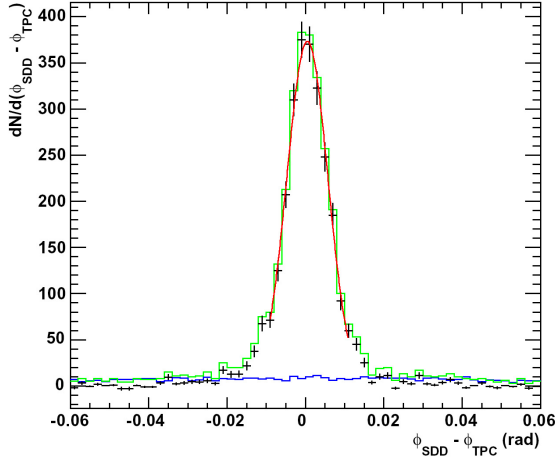


Figure 4.7: The SD-TPC matching distributions. The correlations between $\Delta\theta_{SD-TPC}$ and $\Delta\phi_{SD-TPC}$ are shown in the left top panel. Bottom panels represent projections of two-dimensional SD-TPC matching distribution together with the matching distribution obtained between tracks taken from different events (blue line).



matching distributions were corrected for the deviations in the azimuthal direction originating from the presumably time-independent imperfections in the chamber alignment, dead electronics channels, etc. In Fig. 4.8 example distributions of the $\Delta\phi$ (left panel) and the $\Delta\theta$ (right panel) as a function of the azimuthal angle of the TPC track are shown. The mean position for each ϕ_{TPC} slice was derived by fitting with a Gaussian. The correction was performed in the 7 bins of the polar angle and in two classes of the anode number per hit recorded in the SDD. The narrow bins allow to solve the fine structures of the distortions in the azimuthal angle. The data set was integrated over the positive and negative magnetic field units. Two calibration maps were obtained to recenter the $\Delta\phi$ and the $\Delta\theta$ at zero for given ϕ value.

The quality of the TCP-SDD tracks directly depends on the spatial resolution of the detectors and on the multiple scattering in the material. For tracks with high enough momentum the matching quality depends only on the spatial resolution, whereas, for the low momentum tracks the matching quality is deteriorated due to the multiple Coulomb scattering in the detector ma-

terial. The multiple Coulomb scattering is approximated by the deflection angle [LD91, E+04]

$$\Theta_0 = \frac{13.6 \text{ MeV}}{\beta c p} z \sqrt{\frac{L}{X_0}} \left\{ 1 + 0.038 \ln \left(\frac{L}{X_0} \right) \right\} \quad (4.9)$$

where X_0 is the radiation length of the medium, L is the thickness of the medium, p , $c\beta$, and z are the momentum, the velocity, and the charge of the incident particle, respectively. The matching quality is reflected in the width of the opening angle distributions ($\Delta\theta$, $\Delta\phi$), which has been studied under the different conditions (p , θ_{TPC} , number of anodes per hit in the SDD). The width of the matching distribution was parameterized as a function of the inverse momentum ($1/p$) by

$$\Delta\theta = \sqrt{P0_{\Delta\theta}^2 + \left(\frac{P1_{\Delta\theta}}{p} \right)^2} \quad (4.10)$$

where $P0_{\Delta\theta}$ corresponds to the angular detector resolution, and $P1_{\Delta\theta}$ stands for the contribution from the multiple Coulomb scattering. For the $\Delta\phi$ distributions a similar parameterization was performed. After implementing the corrections explained above the $n(\Delta\theta, \Delta\phi)$ distributions integrated over azimuthal angle and the data units were produced for bins of the track θ angle and the inverse momentum. The background distributions were subtracted from the signal distributions. The $\Delta\theta$ and the $\Delta\phi$ projections were fitted with a Gaussian in order to extract the width and the mean position for each the θ angle and the inverse momentum bin. The derived widths were plotted as function of the inverse momentum and fitted for each θ slice by the Eq. 4.10. The fit coefficients obtained for three classes of the SDD hit configurations (Fig. 4.9) were parameterized by

$$P_n(\theta_{TPC}) = \frac{1}{A + B \cdot \theta_{TPC} + C \cdot \theta_{TPC}^2 + D \cdot \theta_{TPC}^4 + E \cdot \theta_{TPC}^6}. \quad (4.11)$$

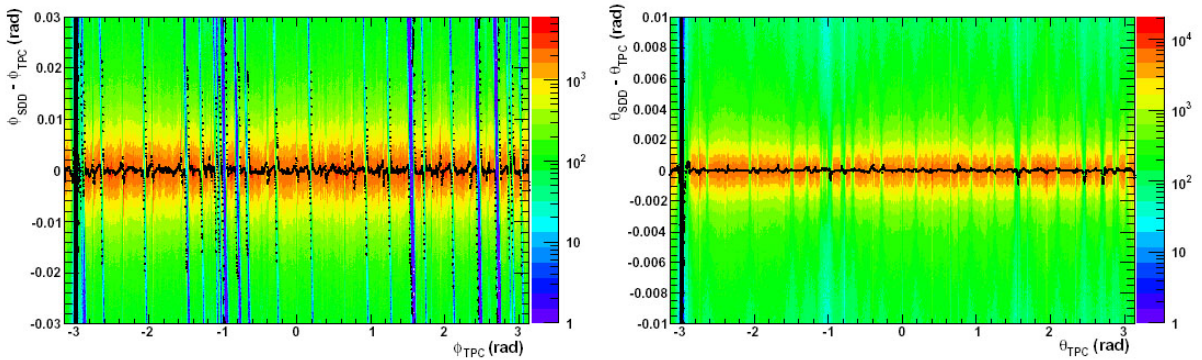


Figure 4.8: The difference between the SDD and TPC angles vs. ϕ TPC track angle (left plot for ϕ , and right plot for θ). The black points represent the mean position obtained by fitting Gauss distribution to each ϕ_{TPC} slices.

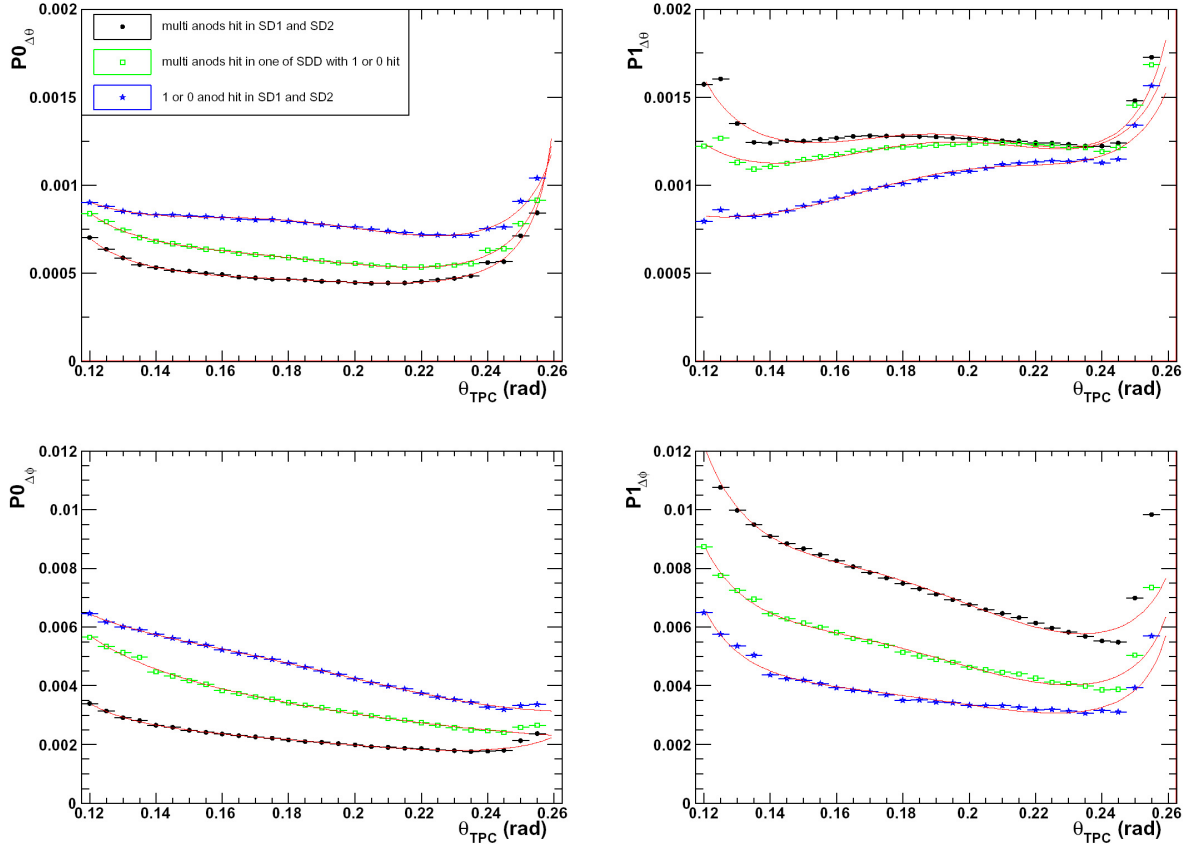


Figure 4.9: The obtained parameters $P0$ and $P1$ describing the momentum dependence of the width of the TPC-SD matching distributions, plotted as a function of θ .

4.7 Reaction Plane Calibration

The distance between the trajectories of two colliding nuclei is called the impact parameter $|\vec{b}|$ and is an important parameter of a nucleus-nucleus collisions. Fig. 4.10 depicts schematically a collision of two nuclei in the center-of-mass system. Using information about the impact parameter and defining the beam axis to be the z axis, the reaction (event) plane is characterized by the angle Ψ_n between the \vec{b} and the x axis. In the limit of central collisions, $|\vec{b}| \rightarrow 0$, the reaction plane cannot be defined.

4.7.1 Determination of the Event Plane

The information about the impact parameter \vec{b} in experiments can be accessed only indirectly (see Section 4.8). The orientation of the reaction plane can be reconstructed from the collision

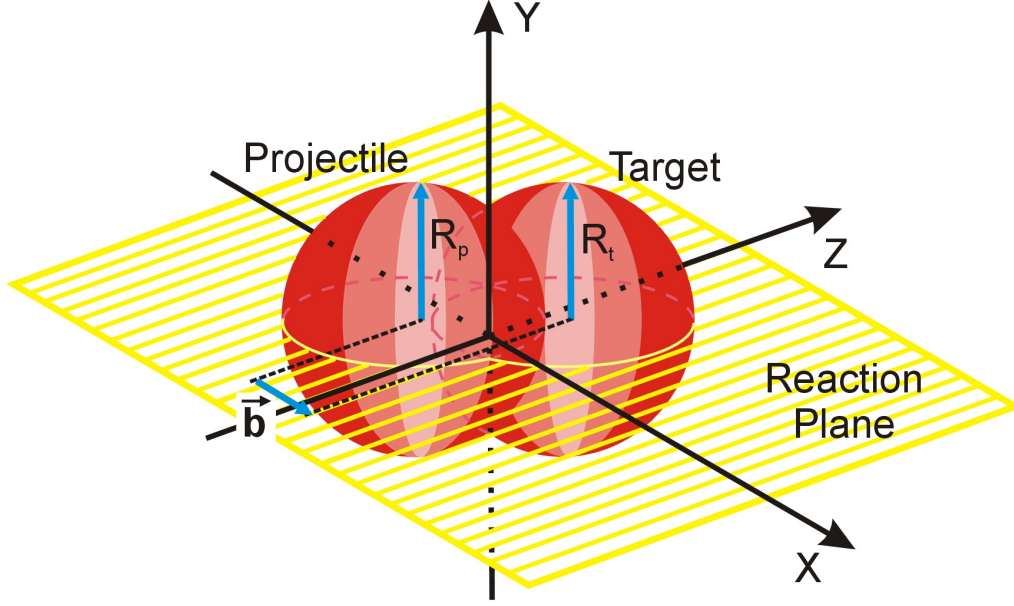


Figure 4.10: Schematic view of a semi-central collision in the center-of-mass frame. The reaction plane is defined by the impact parameter b and the z (beam) axis. The R_p and R_t corresponds to the radius of the projectile and the target nucleus, respectively.

products. In the CERES experiment, the reaction plane is reconstructed based on the azimuthal distribution of charged particles emitted around midrapidity [Oll95, VZ96]. The method uses the anisotropic flow itself to determine the event plane which means that the event plane can be determined independently for each harmonic (n) of the anisotropic flow. For each event the reaction plane vector \vec{Q}_n is defined by the equation:

$$\vec{Q}_n = (Q_n^X, Q_n^Y) = \frac{1}{N} \sum_{i=1}^N w_i \exp(in\phi_i) \quad (4.12)$$

where N is the total particle multiplicity and ϕ_i is the azimuthal angle of the i -th particle. The weights w_i are chosen to optimize the reaction plane resolution. Usually the weights for the odd and even harmonic planes are different. One can weight each particle with its rapidity in case of the first harmonic or with the transverse momentum in case of the second harmonic, as it was done in the presented analysis. In Fig. 4.11 an example two-dimensional distribution of the reaction plane vector \vec{Q}_2 is shown. For a given n -th harmonic, the orientation of the reaction plane can be derived from the relation

$$\Psi_n = \frac{1}{n} \arctan \left(\frac{Q_n^Y}{Q_n^X} \right). \quad (4.13)$$

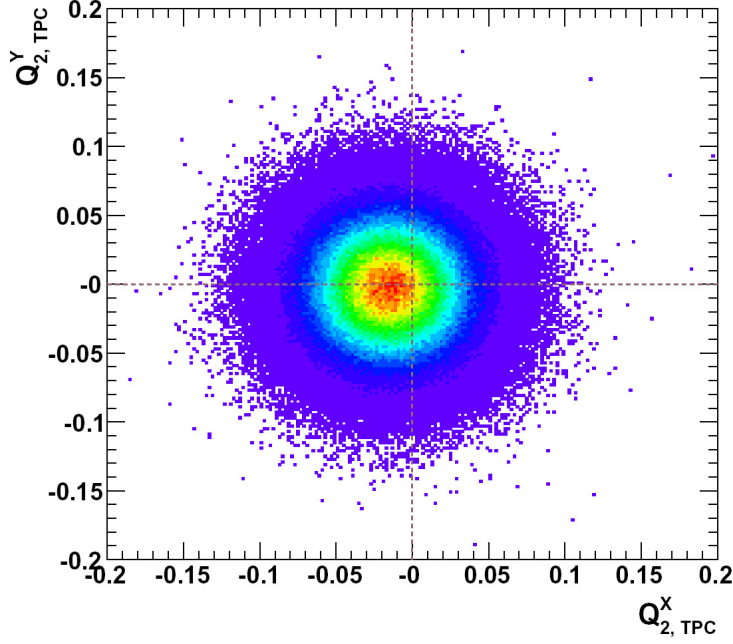


Figure 4.11: The raw Q_2^Y vs. Q_2^X distribution obtained from the TPC tracks.

In order to suppress fake tracks and decay products of long lived resonances in the calculation of the Q_n^X and Q_n^Y the matching between TPC and SDD was required to be better than 5σ . Furthermore, the following quality cuts were applied for each track

- $0.125 \leq \theta_{TPC} \leq 0.235$ (fiducial acceptance)
- $\chi_{phi}^2 \leq 4.0$ and $\chi_{rad}^2 \leq 3.0$ (χ^2 of the track fit)
- $N_{FH} \geq 10$ (number of fitted hits on the TPC track)
- $0.025 \text{ GeV}/c \leq p_{\perp} \leq 4.0 \text{ GeV}/c$ (p_{\perp} range).

The reaction plane angle Ψ_n determined from the n -th harmonic is in the range between $-\pi/n$ and π/n . For analysis of the HBT radii dependence on the reaction plane orientation presented in this work the second Fourier coefficients derived from the TPC tracks were used to calculate the event plane.

4.7.2 Acceptance Corrections

The distribution of the azimuthal angle of the reaction plane, $dN/d\Psi_n$, is isotropic since the orientation of the impact parameter is random in the collision of heavy-ions. The reaction

plane distribution measured in the experiment, on the other hand, is not always uniform (see Fig.4.12). The particle distribution becomes azimuthally anisotropic mostly due to the finite acceptance of the detector and fluctuation of the beam position in respect to the experimental setup. Before the information about the reaction plane orientation can be further used, methods to remove the effects of anisotropy have to be applied. In the simplest approach, the distribution of (Q_n^X, Q_n^Y) is recentred [B⁺97] by subtracting the $(\langle Q_n^X \rangle, \langle Q_n^Y \rangle)$ values previously averaged over groups of events (for each unit such corrections were found). This method allows to remove effectively the first harmonic from the distribution of Ψ_n . In Fig. 4.13, the two plots represent the correction factor $(\langle Q_n^X \rangle, \langle Q_n^Y \rangle)$ obtained for the particle track recorded by the TPC. The two plots in Fig. 4.14 show the result of the recentering method. After applying this correction, the raw distribution of the reaction plane angle becomes as shown in the middle panel of Fig. 4.12. Further correction has to be applied to remove the remaining anisotropy. The next step uses the width of the (Q_n^X, Q_n^Y) distribution to remove the second harmonic from the distribution of Ψ_n . The Q_n^X and Q_n^Y widths as a function of the unit number are shown in Fig. 4.15. With both corrections, the components (Q_n^X, Q_n^Y) of the reaction plane vector \vec{Q}_n become

$$\begin{aligned} Q_{n,cor}^X &= \frac{Q_n^X - \langle Q_n^X \rangle}{\sigma(Q_n^X)}, \\ Q_{n,cor}^Y &= \frac{Q_n^Y - \langle Q_n^Y \rangle}{\sigma(Q_n^Y)}. \end{aligned} \quad (4.14)$$

The reaction plane orientation angle, Ψ_n , is then calculated from equation 4.13 using $Q_{n,cor}^X$ and $Q_{n,cor}^Y$. Its distribution is reasonably flat (Fig. 4.12, right panel).

4.7.3 Reaction Plane Resolution

In the experiment, the reconstructed reaction plane angle, Ψ_n , differs in general from the true reaction plane orientation Ψ by a finite angle $\Delta\Psi = \Psi_n - \Psi$. This is caused by the finite number of detected particles, detector coverage and resolution, and finite-number fluctuations. Quantitatively, the knowledge about these differences is of great importance for analysis of the azimuthal anisotropy like the flow or the HBT vs. reaction plane. Different methods were proposed to account for this effect in measured observables [OI97, PV98]. Expressing azimuthal distribution as Fourier series (see Eq. 1.20) and averaging over many events, assuming that Ψ and $\Delta\Psi$ are statistically independent, it is possible to obtain a relation between the reconstructed and true Fourier coefficients

$$\langle \cos(n\Psi_n) \rangle = \langle \cos(n\Psi) \rangle \langle \cos(n\Delta\Psi) \rangle. \quad (4.15)$$

The resolution of the reconstructed reaction plane is often expressed in terms of a correction factor $\cos(n\Delta\Psi)$. Following [OI97] the distribution of the azimuthal angle deviation $\Delta\Psi$ can

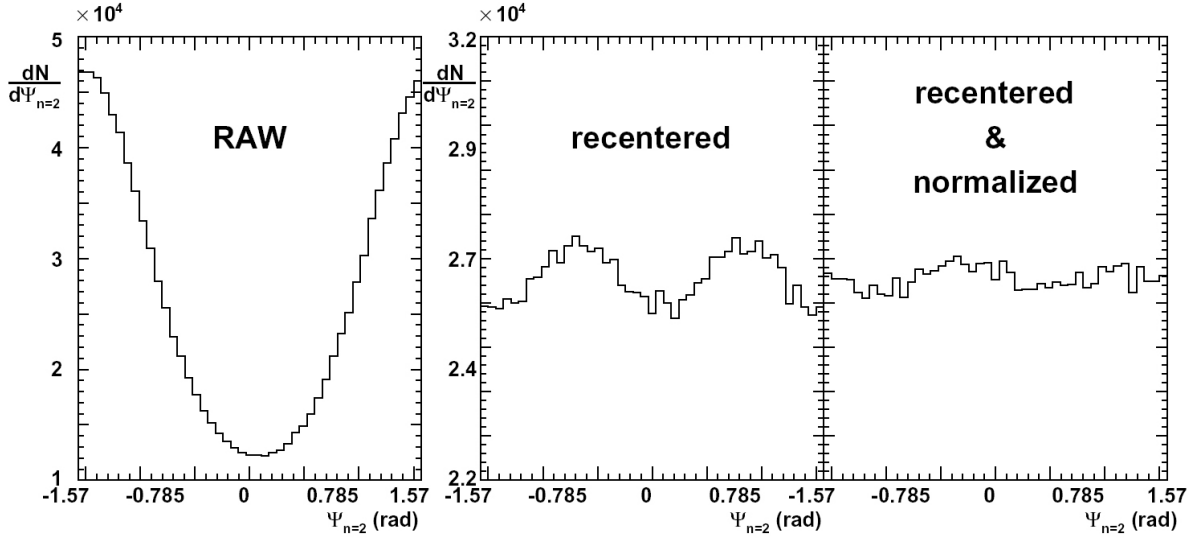


Figure 4.12: The distribution of the reaction plane angle Ψ_2 : raw experimental data – tracks recorded by TPC (RAW), after applying the recentering method, and after dividing the Q components by the widths of the (Q_n^X, Q_n^Y) distribution.

be expressed in terms of a real parameter χ , which measures the accuracy of the reaction plane determination

$$\frac{dN}{d\Delta\Psi} = \frac{1}{\pi} \exp(-\chi^2) \left\{ 1 + z\sqrt{\pi} [1 + \text{erf}(z)] \exp(z^2) \right\} \quad (4.16)$$

where $z = \chi \cos(\Delta\Psi)$ and $\text{erf}(z)$ is the error function. The Fourier coefficients can be obtained by integrating Eq. 6 in [Oll97] first over $\Delta\Psi$ and then over Q

$$\langle \cos(n\Delta\Psi) \rangle = \frac{\sqrt{\pi}}{2} \chi \exp(-\chi^2/2) \left[I_{\frac{n-1}{2}} \left(\frac{\chi^2}{2} \right) + I_{\frac{n+1}{2}} \left(\frac{\chi^2}{2} \right) \right] \quad (4.17)$$

where I_k is the modified Bessel function of order k . The parameter χ can be derived by dividing randomly each event into two (or more) subevents. Consequently, for those subevents the reaction plane angles Ψ_n are reconstructed resulting in $\Psi_{n,SE1}$ and $\Psi_{n,SE2}$. However, since each subevent contains only $N/2$ particles, corresponding χ parameter scales as $\chi_{SE1} = \chi_{SE2} = \chi/\sqrt{2}$. The distribution of the relative angle $\Delta\Psi_R \equiv |\Psi_{SE2} - \Psi_{SE1}|$ can be calculated analytically

$$\frac{dN}{d\Delta\Psi_R} = \frac{\exp(-\chi_{SE1}^2)}{2} \left\{ \frac{2}{\pi} (1 + \chi_{SE1}^2) + z [I_0(z) + L_0(z)] + \chi_{SE1}^2 [I_1(z) + L_1(z)] \right\} \quad (4.18)$$

where $z = \chi_{SE1}^2 \cos(\Delta\Psi_R)$, and L_0, L_1 corresponds to modified Struve functions. The value of χ can be obtained by fitting Eq. 4.18 to the measured distribution of $\Delta\Psi_R$. Therefore,

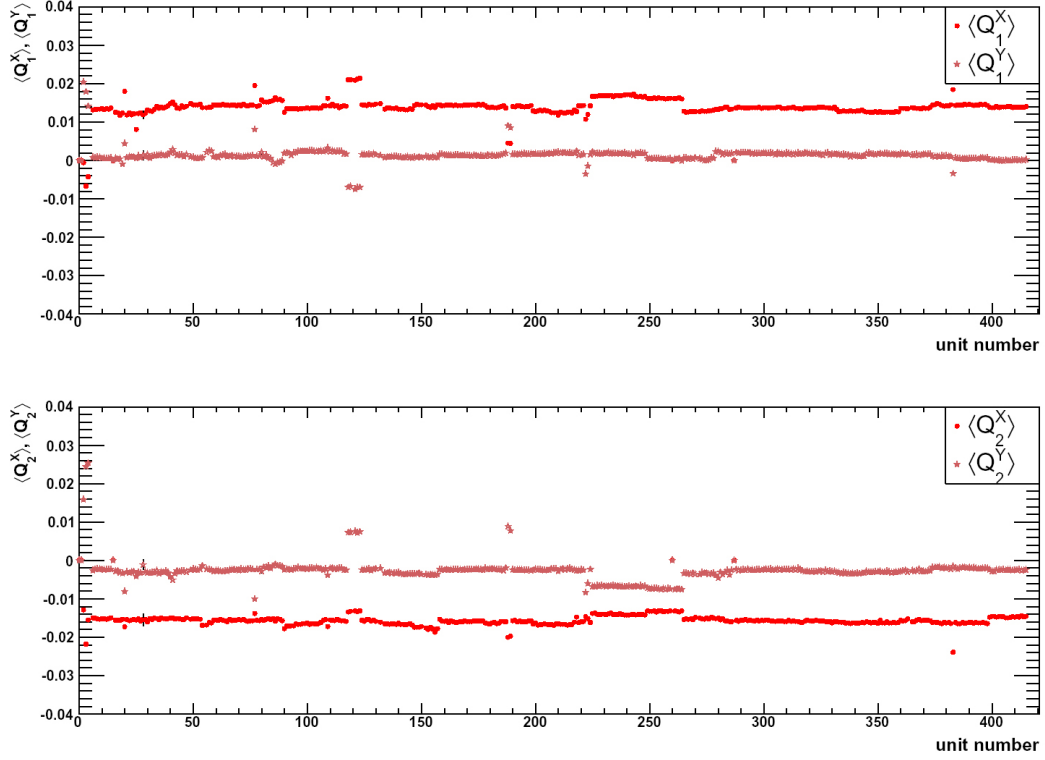


Figure 4.13: The average value of (Q_n^X, Q_n^Y) obtained for a given unit number, raw data (first and second harmonic).

the reaction plane resolution can be expressed in terms of $\langle \cos(n\Delta\Psi) \rangle$ by solving Eq. 4.17. Alternatively, one can obtain the correction factor $\langle \cos(n\Delta\Psi) \rangle$ from the relation [PV98]

$$\langle \cos(n\Delta\Psi) \rangle = \sqrt{2} \langle \cos[n(\Psi_{SE1} - \Psi)] \rangle \quad (4.19)$$

where

$$\langle \cos[n(\Psi_{SE1} - \Psi)] \rangle = \sqrt{\langle \cos[n(\Psi_{SE2} - \Psi_{SE1})] \rangle}. \quad (4.20)$$

The estimation of the reaction plane resolution in CERES experiment was based on both presented method. The particle tracks per each event, recorded by SDD or TPC, were divided into two subsets $SE1$ and $SE2$. For each subset the reaction plane orientation was calculated and the difference $\Psi_{n,SE2} - \Psi_{n,SE1}$ was derived. The obtained difference was accumulated over many events and stored in centrality classes. The reaction plane resolution as a function of the collision centrality is shown in Fig. 4.16.

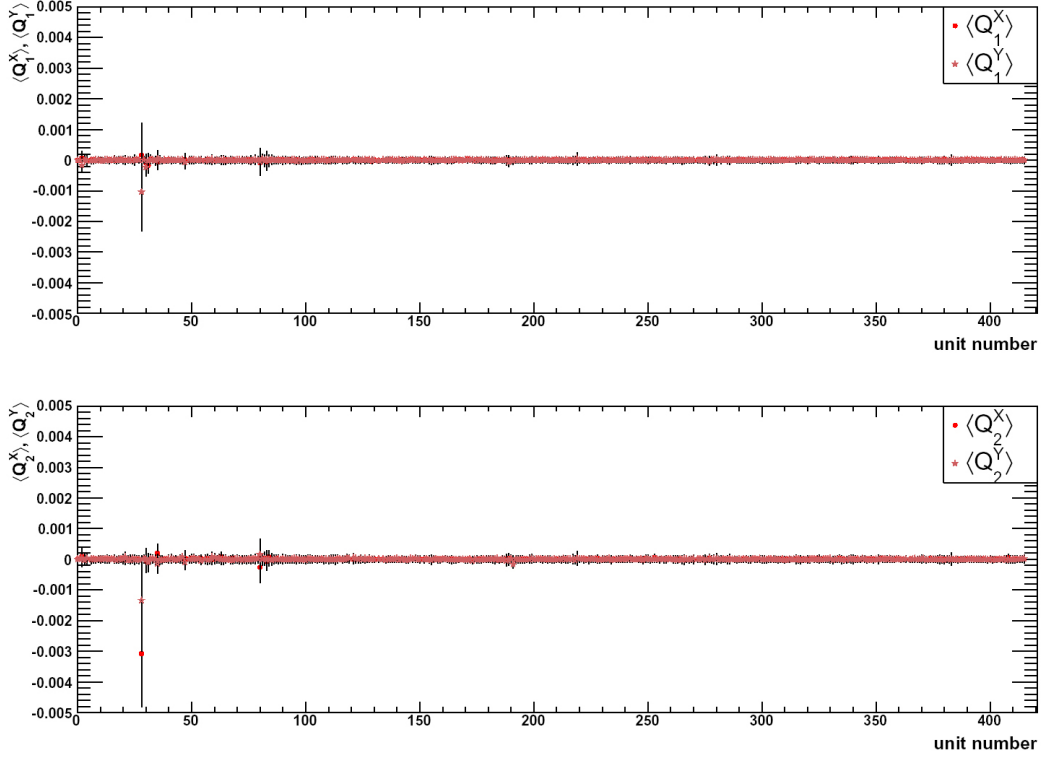


Figure 4.14: The recentered average value of (Q_n^X, Q_n^Y) as a function of unit number.

4.8 Centrality Determination

The nuclear overlap model [EKL89] represents a nucleus-nucleus collision in terms of binary collisions between nucleons. Based on the density distributions within the two colliding nuclei, the number of participating nucleons and of binary NN collisions are expressed as functions of the impact parameter $\vec{b} \equiv \langle \vec{r}_B \rangle - \langle \vec{r}_A \rangle$, and the total geometric cross section is calculated. The nuclear density $n_A(r)$ distribution, defined as the number of nucleons per unit volume, can be approximated by a Woods-Saxon profile

$$n_A(r) = \frac{n_0}{1 + \exp\left(\frac{r-R}{d}\right)}, \quad (4.21)$$

where $n_0 = 0.17 \text{ fm}^{-3}$ is a density of nucleons at the center, $R = (1.12A^{1/3} - 0.86A^{-1/3}) \text{ fm}$ is the half-density radius, and d the surface thickness chosen to be 0.54 fm . The $n_A(r)$ is normalized to the number of nucleons

$$\int d^3r n_A(r) = 4\pi \int_0^\infty r^2 dr n_A(r) = A. \quad (4.22)$$

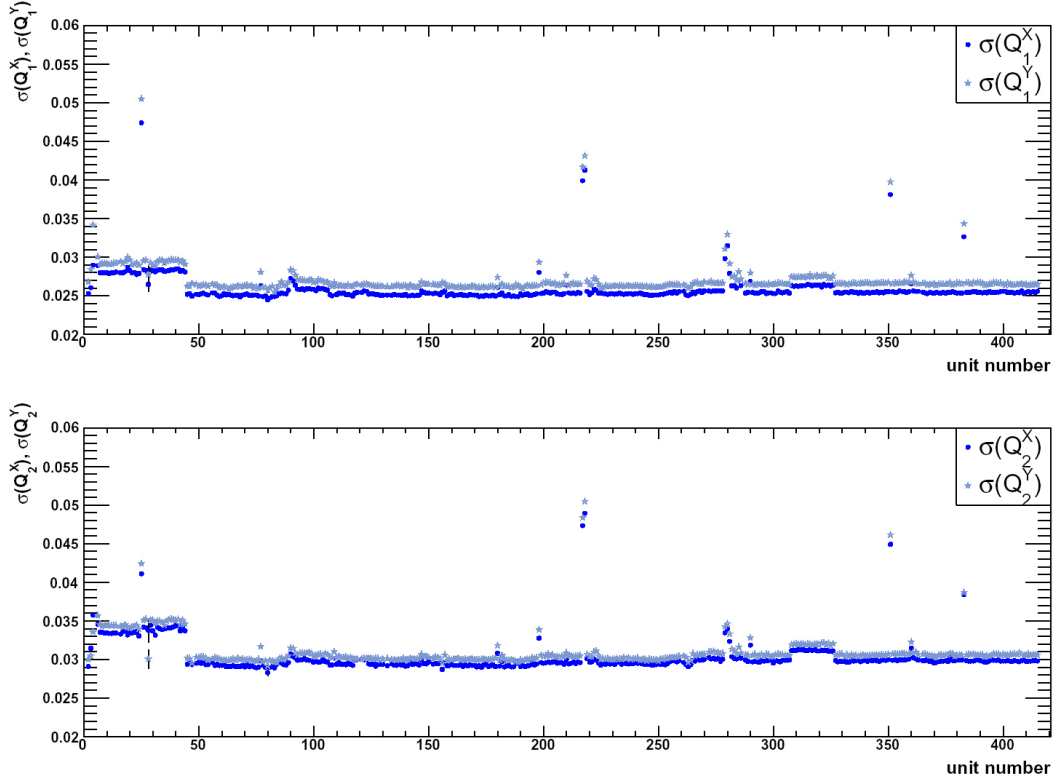


Figure 4.15: The width of the Q_n^X and Q_n^Y distribution as a function of the unit number.

For the following consideration it is convenient to introduce the nuclear thickness function defined as the density distribution integrated along the beam axis z

$$T_A(b) = \int_{-\infty}^{\infty} dz n_A(\sqrt{b^2 + z^2}), \quad (4.23)$$

also normalized to A

$$\int d^2b T_A(b) = A. \quad (4.24)$$

For a given \vec{b} , the overlap function is defined as the product of the thickness functions of the colliding nuclei A and B, integrated over the two transverse dimensions

$$T_{AB}(b) = \int d^2s T_A(\vec{s}) T_b(\vec{s} - \vec{b}), \quad (4.25)$$

where \vec{s} and \vec{b} are perpendicular to the beam direction. The normalization condition for the thickness function is given by

$$\int d^2b T_{AB}(b) = AB. \quad (4.26)$$

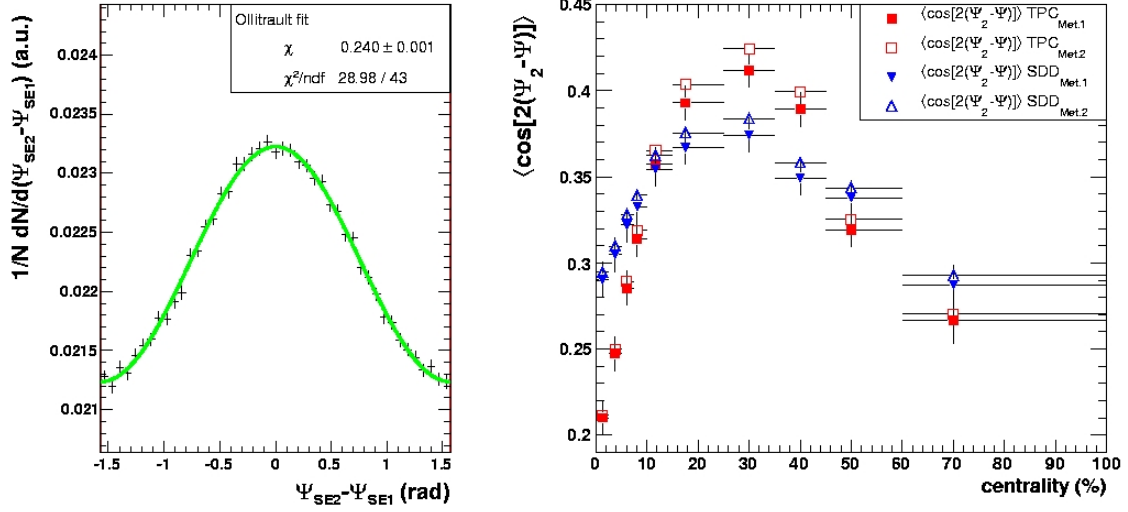


Figure 4.16: Left panel: difference between the reaction plane orientation from two sub-events for the most central data bin. The solid line (green) is the Ollitrault fit to the distribution. Right panel: the $\langle \cos[2(\Psi_2 - \Psi)] \rangle$ obtained from the two different methods is shown as a function of centrality. The resolution of the reaction plane orientation calculated from TPC tracks and from SDD tracks is shown as squares and triangles, respectively. The full symbols correspond to the method proposed in [Oll97] (Met.1), and the open symbols were obtained for the method proposed in [PV98] (Met.2).

The product $T_{AB}(b) \cdot \sigma_{NN}$ can be interpreted as the number of binary NN collisions in A+B collision at given \vec{b} , with σ_{NN} being the total inelastic nucleon-nucleon cross section: $N_{AB}^{coll}(b) = T_{AB}(b) \sigma_{NN}$.

Defining “participants” as the nucleons which have encountered at least one binary collision it is possible to calculate the mean number of participants of an A+B collisions at a given impact parameter via

$$\begin{aligned}
 N_{AB}^{part}(b) = & \int d^2s \, T_A(\vec{s}) \left\{ 1 - \left[1 - \frac{\sigma_{NN} T_B(\vec{s} - \vec{b})}{B} \right]^B \right\} \\
 & + \int d^2s \, T_B(\vec{s}) \left\{ 1 - \left[1 - \frac{\sigma_{NN} T_A(\vec{s} - \vec{b})}{A} \right]^A \right\}. \quad (4.27)
 \end{aligned}$$

The expression in the curly brackets represents a probability of becoming participant.

The total geometric cross section σ_{GEOM} is the cross section for such A+B collisions that at least one binary NN collision occurs. Using a Poisson distribution the σ_{GEOM} can be written

as

$$\sigma_{GEOM} = \int d^2b [1 - \exp(-T_{AB}(b) \sigma_{NN})] . \quad (4.28)$$

The geometrical cross section of Pb+Au at $\sqrt{s_{NN}} = 17.2$ GeV is equal to 6.94 barn (b) derived from the overlap model with a Woods-Saxon nucleus density profile and a binary NN collision cross section of $\sigma_{NN}=30$ mb [Miś04]. Three observables related to the centrality are directly¹ available in the `step3c` output data: the MC amplitude, the track multiplicity in the SDD ($0.10 < \Theta < 0.26$), and the track multiplicity in the TPC ($0.12 < \Theta < 0.24$, $N_H > 13$). In the following, these three variables are called “multiplicities”. The centrality calibration means finding the relation between a multiplicity on one side and the impact parameter, or, equivalent to it but more commonly used, the percentage of geometrical cross section σ_{GEOM} on the other. The calibration was done in two steps, described in Sections 4.8.1. First, a low beam intensity minimum bias run (unit 218, run 1424, bursts 0-201) was used to find the calibration tables for the three multiplicities. The correlations between the three multiplicities in a minimum bias run are presented in Fig. 4.17. Second, the run-by-run variation was checked and factors

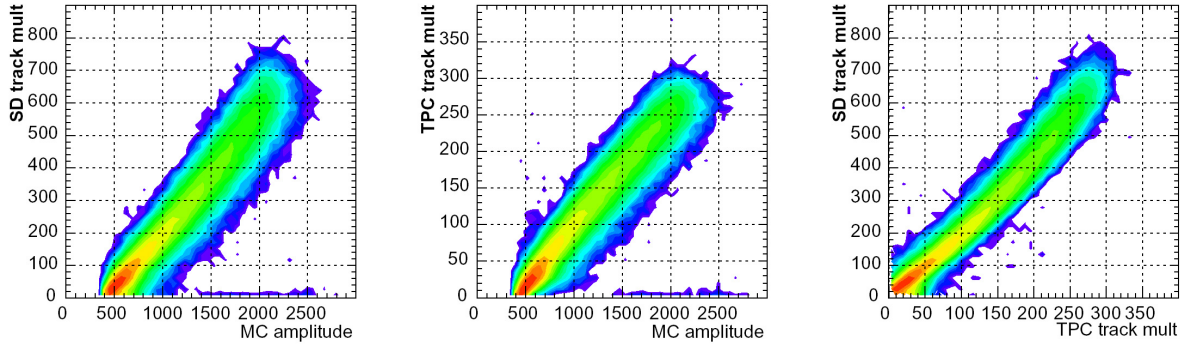


Figure 4.17: Correlations between the three multiplicities in the low intensity minimum bias run.

which allow to scale multiplicities in all runs were found such that the corrected high edge was at the same place as the edge in unit 218. Before performing these two steps, the systematic dependence of the multiplicities on the running conditions was studied. For this, distributions recorded in different runs were normalized to 10^6 incident beam particles. The normalization was performed as follows

$$n_{cent}(m) = \frac{n_{0,cent}(m)}{N_{0,cent}} \cdot \frac{cent}{beam} \cdot 10^6 \quad (4.29)$$

$$n_{minb}(m) = \frac{n_{0,minb}(m)}{N_{0,minb}} \cdot \frac{minb}{beam} \cdot 10^6 \quad (4.30)$$

¹Other variables can be, of course, generated by looping over tracks.

$$n_{beam}(m) = \frac{n_{0,beam}(m)}{N_{0,beam}} \cdot \frac{beam}{beam} \cdot 10^6, \quad (4.31)$$

where $n_0(m)$ and $n(m)$ are the raw and the normalized multiplicity distributions. The *beam*, *minb*, and *cent* are the numbers of beam, minimum bias, and central trigger candidates seen in the scalers (no deadtime); and $N_{0,i}$ is the integral of the $n_{0,i}(m)$ histogram for $i = (beam, minb, cent)$ respectively. This way the DAQ deadtime factor and the losses introduced via event cuts are corrected for, the only assumption being that they do not introduce any centrality bias. The normalized multiplicities obtained with the beam and the minimum bias trigger at low beam intensity together with the data obtained for central and the minimum bias trigger for high intensity beam are shown in Fig. 4.18. The MC amplitude (above ADC pedestal equal to 380) and the TPC multiplicity are roughly proportional. The SDD multiplicity increases with centrality faster than the other two indicating that random hit coincidences are not negligible. Similar increase is visible in Fig. 4.18 (middle panel) for runs taken under the high beam intensity. Moreover, the SDD multiplicity is sensitive to noise as can be seen by the presence of high signals in the run without the target (counting only tracks with a good matching between the two SDD's might give a more reliable track multiplicity). Delta electrons produced by a beam particle passing without a nuclear interaction can be shown by comparing the beam trigger and random pulser trigger events. The bump at TPC multiplicities below 50 might come from interactions in other than gold materials. According to the overlap model the maximum number of participants in Pb+C collision should be 7-8 times lower than in Pb+Au collision at the top SPS energy. This is consistent with the position of the upper edge of the bump.

4.8.1 Centrality Calibration

The minimum bias run 1424 was particularly clean since it was taken with a reduced beam intensity. The number of events n per beam particle can be transformed to cross section σ by multiplying it with 521 barn

$$\sigma = n \cdot \frac{m_{Au}^{mol}}{N_A \rho d} = n \cdot \frac{196.967 \text{ g}}{6.022 \cdot 10^{23} \cdot 19.32 \text{ g/cm}^3 \cdot 325 \mu\text{m}} = n \cdot 521 \text{ b} \quad (4.32)$$

where m_{Au}^{mol} is a molar mass of gold, N_A is the Avogadro number, and ρ and d are the density of gold at 293 K and the thickness of the target ($13.25 \mu\text{m}$), respectively. The normalized distributions from the low intensity minimum bias run, shown in the previous section, are thus multiplied by $521/10^6$ and subsequently integrated from right to left. The integral has the meaning of the cross section for events with the multiplicity above a given value. In Fig. 4.19 the normalized multiplicity distribution together with the ratio of the integrated cross section to the geometrical cross section is shown. The centrality as a function of multiplicities, obtained in this fashion, was saved on ASCII files and used to convert the measured multiplicity to the percentage of the geometrical cross section σ_{GEOM} . Integrating the entire multiplicity range

triggered on in the central run 1427 gives 7.35 %. The events with centralities above the 45 % σ_{GEOM} are contaminated by non-target interactions.

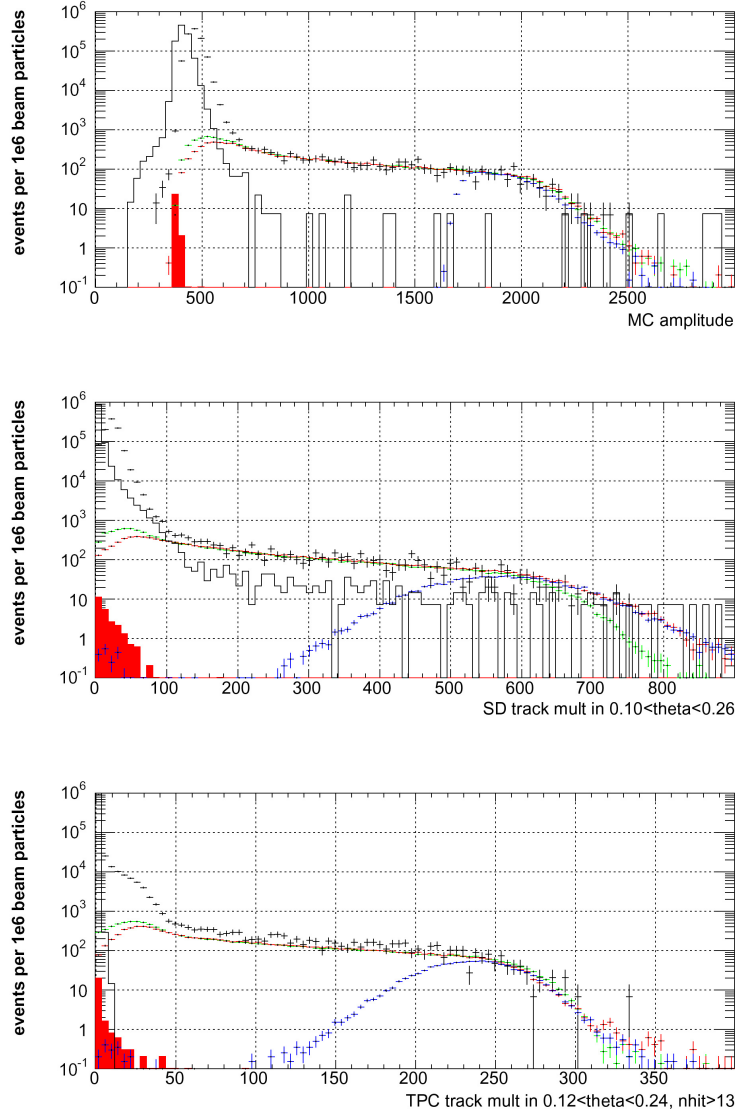


Figure 4.18: Multiplicity distributions taken under different running conditions: beam (black) and minimum bias (green) triggers at low beam intensity (runs 1423 and 1424); minimum bias (red) and central (blue) events at high beam intensity (runs 1420 and 1427). The full red histogram represents events taken with the MT (random pulser) trigger during minimum bias run 1424. The solid black histogram represents run 1244: no target, beam trigger, high beam intensity.

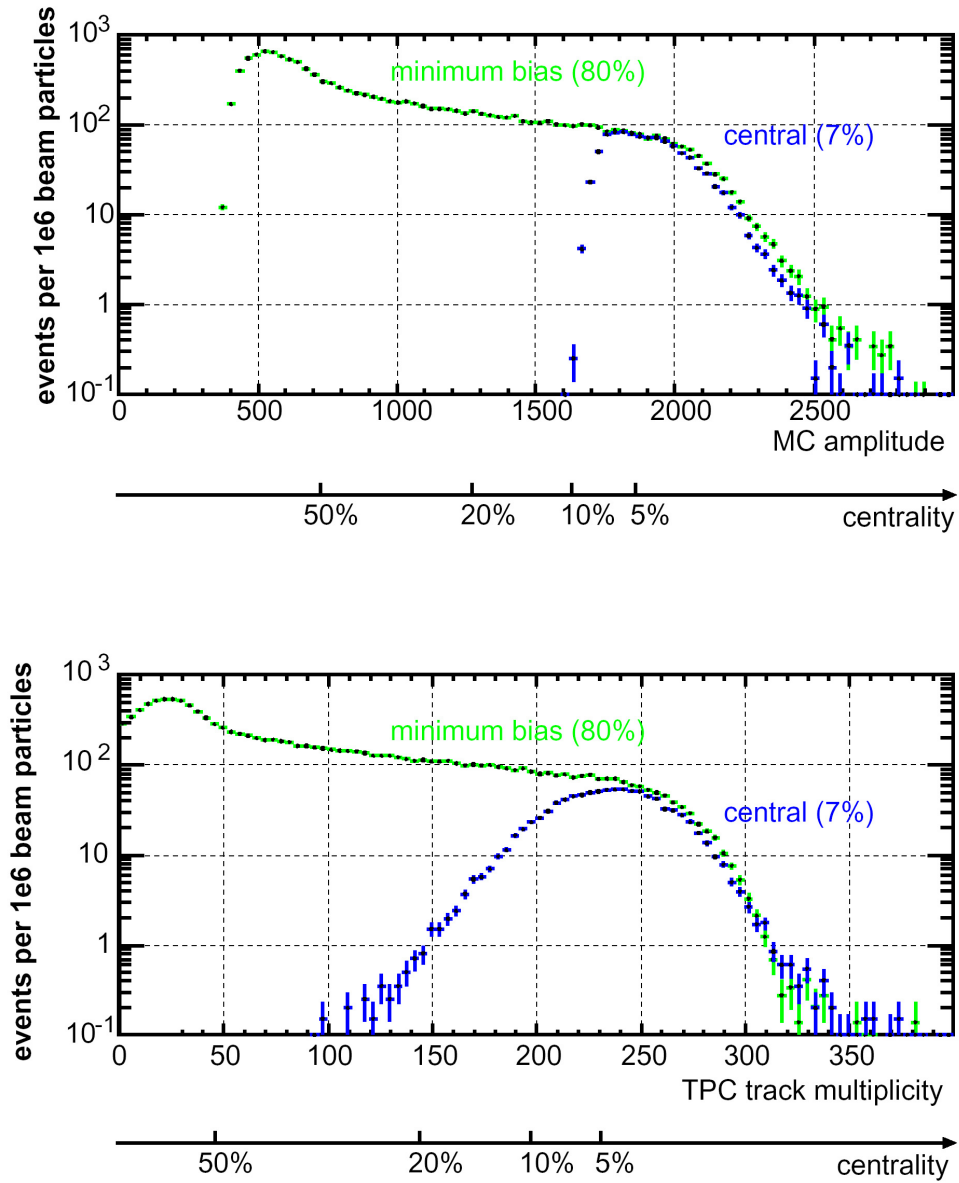


Figure 4.19: Multiplicity distributions from the minimum bias run at low beam intensity (green), normalized to 10^6 beam particles. For comparison, a central run taken at high beam intensity is shown as well (blue).

The position of the upper edge of the multiplicity distributions can vary run-by-run due to various technical reasons. In order to monitor these variations and to correct for them, the edge position was determined in each unit. This was done in two independent ways:

- by finding such a multiplicity value that the number of events with a multiplicity equal or higher than it corresponds to 200 mb,
- by fitting the

$$f(m) = \frac{A}{1 + \exp(\frac{m - E_{pos}}{C})} \quad (4.33)$$

to the multiplicity distribution, and extracting the E_{pos} parameter.

The results of these two methods of the edge determination are shown in Fig. 4.20 as the blue and black points, respectively. The run-by-run variations were 6 % for MC, 5 % for SD, and 9 % for TPC (peak-to-peak). The green plot represents the blue to black ratio; both methods agree within 4 %. Since the fit method seems more reliable and does not seem to introduce any systematic difference between the minimum bias and central runs it was chosen for the centrality calibration for data collected during 2000 run. The distributions of calibrated centrality for the events used for the two particle correlation analysis are shown in the Fig. 4.21. The data were taken with three different triggers. This is best reflected in the centrality distribution recorded by Multiplicity Counter, used for triggering during the run 2000. Ideally the centrality distribution recorded by TPC should follow the MC. The width of the SD and TPC edges can be used as the upper limit on the respective centrality resolutions. The impact parameter b can be calculated from centrality fraction c using the relation

$$\pi b^2 = c \cdot 6.94 \text{ b}. \quad (4.34)$$

4.9 Charged Particle Multiplicity

As described in the previous subsection, the number of detected particle tracks varies with the impact parameter. The absolute multiplicity of charged particles N_{ch} can be determined for events within a reasonably narrow bin of centrality. The minimum bias data (100 bursts of run 1424 from `step2`) recorded during the 2000 run were chosen for this analysis. Out of the two high resolution tracking detectors of CERES, SDD and TPC, the first one is more suitable for this kind of analysis because it allows to select the vertex tracks. In order to minimize an inefficiency of the detector the analysis was restricted to a ϕ -range within

- SDD1 covered $-1.81 < \phi < -1.61$ and $0.40 < \phi < 0.60$ radian,
- SDD2 covered $-1.83 < \phi < -1.58$ and $0.38 < \phi < 0.62$ radian,

where all anodes worked properly. For every combination of SDD1 and SDD2 hits, the track vertex z was calculated using the z -position of the detectors and the r -coordinate of the two hits. The reconstructed z vertex was then shifted to the event coordinate system resulting in a

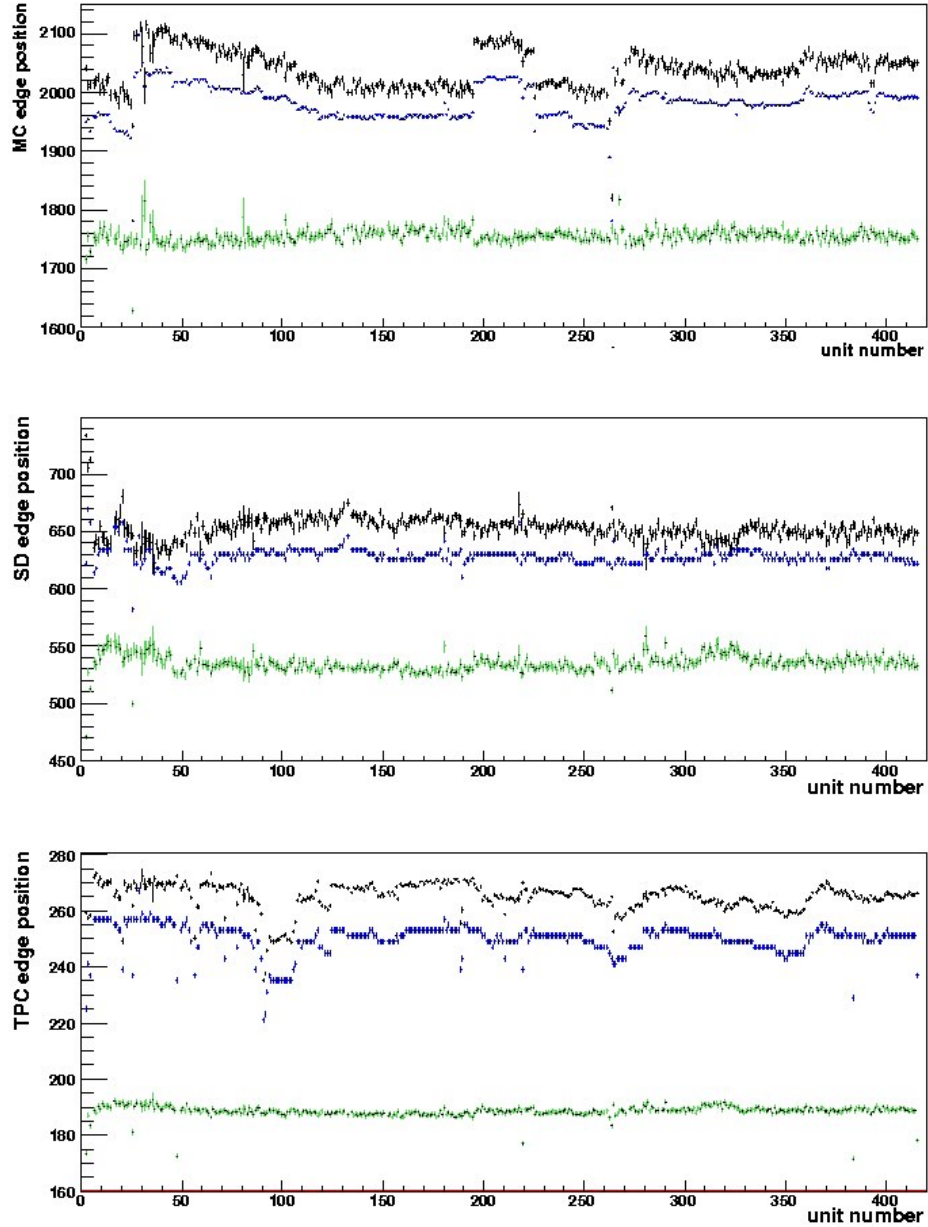


Figure 4.20: The edge position of multiplicity distributions as a function of the unit number determined via integration (blue) and via fit (black). The green plot shows the (arbitrarily scaled up) ratio of the two methods.

narrow peak positioned on a broad background of the random hit combination (see Fig. 4.22). The background subtraction procedure was based on the determination of z vertex position by

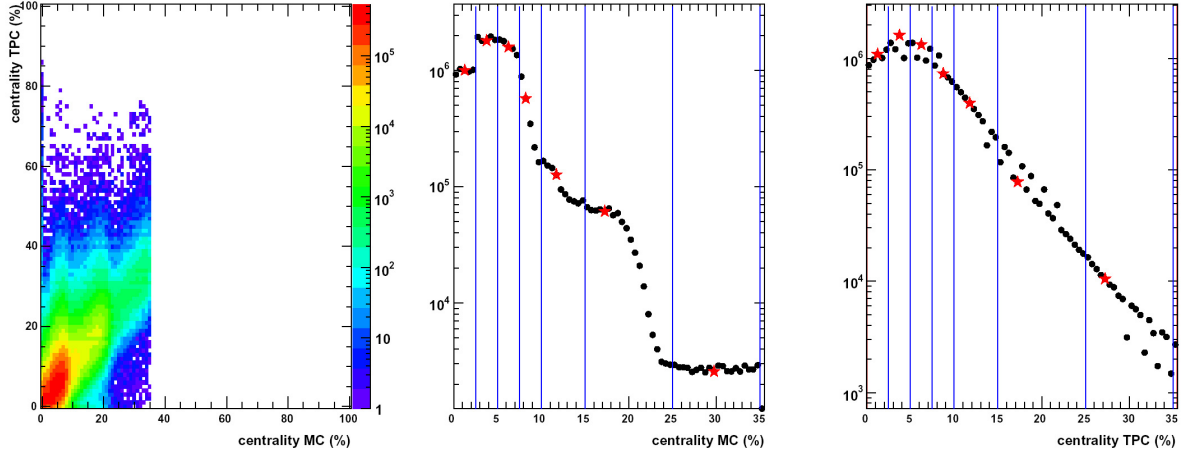


Figure 4.21: The calibrated centrality in percent of the geometrical cross section accumulated over all data set. Left panel: correlation between TPC and MC. Middle panel: centrality distribution recorded by MC. Right panel: centrality distribution recorded by the TPC. The solid lines represent the centrality selection used for the two particle correlation analysis presented in this thesis.

combining hits belonging to different ϕ regions e.g. $-1.81 < \phi < -1.61$ with $0.38 < \phi < 0.62$. The remaining peak was integrated from -1.2 cm to 1.2 cm, yielding the fake-free number of tracks originating from the vertex. This number was divided by the number of events and the ϕ -acceptance factor $\Delta\phi/(2 \cdot \pi) = 0.4/(2 \cdot \pi) = 0.0637$. Such procedure was performed separately in five bins of η covering $2 < \eta < 3$. The obtained $dN_{ch}/d\eta$ still has to be corrected

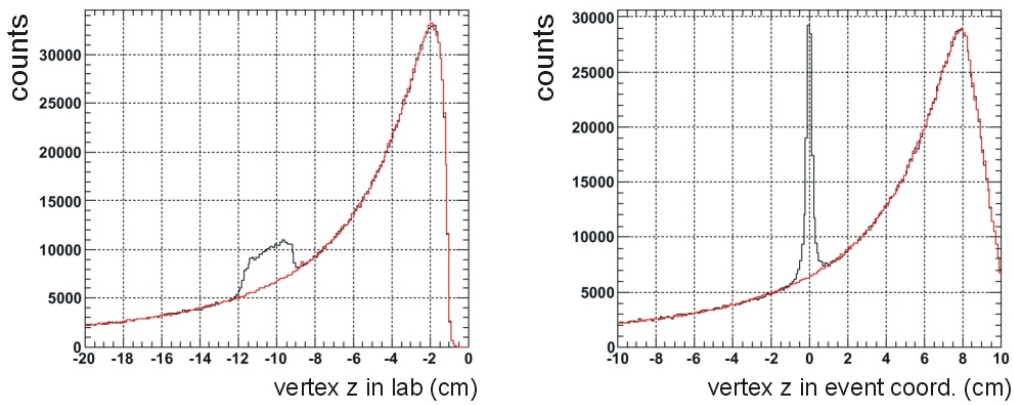


Figure 4.22: Vertex z distribution for the hit pairs from SDD1 and SDD2 in laboratory coordinate system (left) and in the event coordinates (right). The background distribution is depicted as a red line.

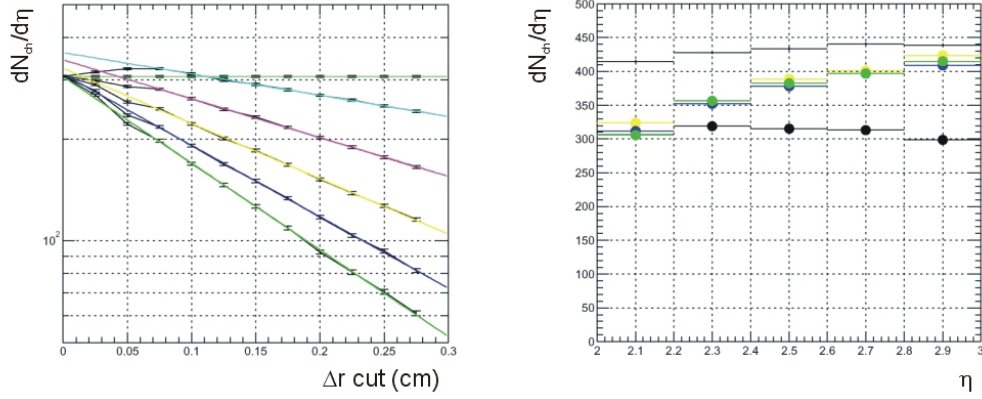


Figure 4.23: Left panel: an example of the extrapolation method for the η between 2.0 to 2.2. Right panel: the charged particle multiplicity as a function of the pseudorapidity for the event centrality integrated from 0 to 5 % of σ_{GEOM} . The raw data is depicted as a black points, the color points correspond to the values extrapolated at $\Delta r = 0$. For comparison, the results of a naive counting SDD tracks are shown as the black dots.

for the two-hit resolution and the δ -electrons coming from the target. The two-hit resolution is responsible for decreasing efficiency for the reconstruction of close tracks. In order to account for this effect, the procedure, described above, was repeated for different values of the two-hit separation cuts Δr and $\Delta\phi$. For a fixed $\Delta\phi$, $dN_{ch}/d\eta$ vs. Δr was fitted by an exponential function in the range $0.07 \text{ cm} < \Delta r < 0.21 \text{ cm}$ and extrapolated to zero (see Fig. 4.23). The extrapolated $dN_{ch}/d\eta(0)$, obtained in this fashion for $\Delta\phi=0.027$, 0.036 , and 0.045 are very similar. For the final result the histograms obtained with $\Delta\phi=0.036$ were used. The δ -electrons were estimated by applying the complete procedure for the beam trigger data (100 bursts of run 1423). The result was 16 electrons on average into the η -interval from 2 to 3. Half of this was then subtracted from the minimum bias run results to account for electrons knocked out of the targets preceding the one in which the interaction occurred.

The resulting $dN/d\eta$ values for different classes of centrality, corrected for the δ -electrons, are listed in Table 4.2. In addition, dN_{ch}/dy was calculated as $1.025 \times dN_{ch}/d\eta$, based on the UrQMD calculations. This result fits the available beam energy systematic (see Fig. 4.24).

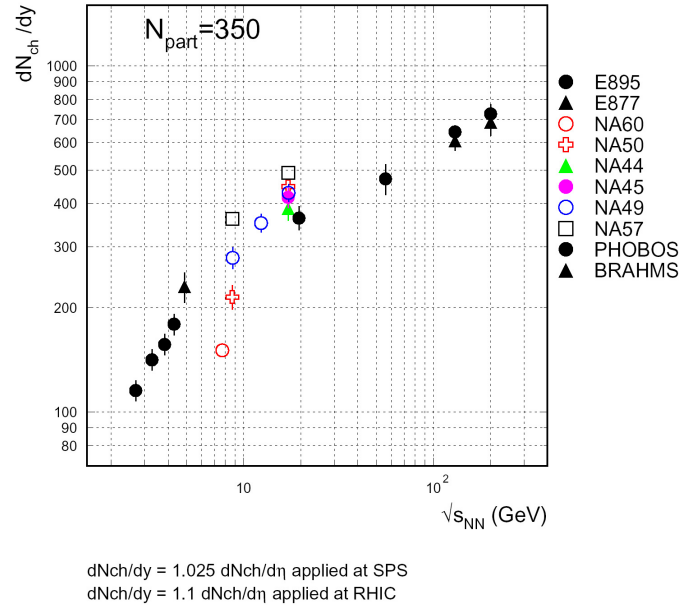


Figure 4.24: Beam energy dependence of the rapidity density of charge particle.

centrality (%)	$dN_{ch}/d\eta(3.1)$	$dN_{ch}/d\eta(2-3)$	$dN_{ch}/d\eta(2.1-2.65)$	$dN_{ch}/dy(2.91)$
0-5	404.4+-4.4	359.3+-2.4	347.2+-2.4	412.5+-4.5
5-10	340.1+-3.8	300.7+-2.1	291.6+-2.1	346.9+-3.9
10-15	278.7+-3.3	253.8+-1.8	246.1+-1.8	284.3+-3.3
15-20	230.5+-2.8	213.6+-1.6	209.0+-1.6	235.1+-2.8
20-25	189.9+-2.4	177.7+-1.4	173.7+-1.4	193.7+-2.5
25-30	157.8+-2.1	145.9+-1.2	144.2+-1.2	161.0+-2.2
30-35	132.2+-1.9	120.5+-1.1	117.7+-1.1	134.9+-1.9
35-40	107.6+-1.7	97.5+-1.0	94.2+-1.0	109.8+-1.8
40-45	89.5+-1.5	78.1+-0.9	75.6+-0.9	91.3+-1.5
45-50	69.9+-1.4	61.2+-0.8	58.8+-0.8	71.3+-1.4
50-55	54.4+-1.2	47.9+-0.7	46.2+-0.7	55.5+-1.2
55-60	43.9+-1.1	38.6+-0.6	37.5+-0.6	44.8+-1.1
60-65	35.2+-1.0	31.0+-0.6	29.9+-0.6	36.0+-1.0
65-70	30.0+-0.9	24.6+-0.5	22.6+-0.5	30.6+-1.0
70-75	23.7+-0.9	18.9+-0.5	17.2+-0.5	24.1+-0.9
75-80	16.1+-0.8	13.0+-0.4	12.0+-0.4	16.4+-0.8
80-85	11.1+-0.8	6.3+-0.4	5.2+-0.4	11.3+-0.8
85-90	329.2+-1215.9	0.4+-0.3	-0.1+-0.3	335.8+-1240.2

Table 4.2: The charged particle multiplicity $N_{ch}/d\eta$ and the rapidity density of charge particles extrapolated at the midrapidity for different centralities.

Chapter 5

Identical Particle Correlation Analysis

High energy heavy-ion collisions produce matter under extreme conditions of temperature and density. While the highest densities are reached in the early stages of the collision, most of the observed particles are hadrons which are emitted rather late in the evolution of the collision. Because of that the measured momentum spectra and correlations contain direct information only about the size, shape, and dynamics of the source at freeze-out. The two-particle Bose-Einstein interferometry is tool to study this information through the measurement of the relative momentum distribution of identical particles pairs. The analysis of three-dimensional correlation functions of like-sign π pairs, performed on the CERES data set, will be presented in this chapter. The Gaussian parameterization of the correlation functions, connecting the theory predictions with the experimental results, was performed in the Cartesian Bertsch-Pratt coordinate system (see Section 1.3.2). The ‘out-side-long’ components of the relative pair momentum four-vector were calculated in the Longitudinally CoMoving System (LCMS) in which the longitudinal component of the pair momentum vanishes.

5.1 Data Selection

The data set recorded in the year 2000 by the CERES experiment, after various calibrations, was used for the two-particle correlation analysis presented in this dissertation. Within this data set only the standard event cuts, namely the trigger event selection and the beam pile-up suppression, were performed. After high quality events were selected, every track used for the two-particle correlation analysis was subject to the following quality cuts:

- small χ^2 of the track fit (Fig. 5.1, left panel),
- at least 12 hits used in the fit (Fig. 5.1, right panel),
- fiducial acceptance cut $0.125 < \theta < 0.240$,

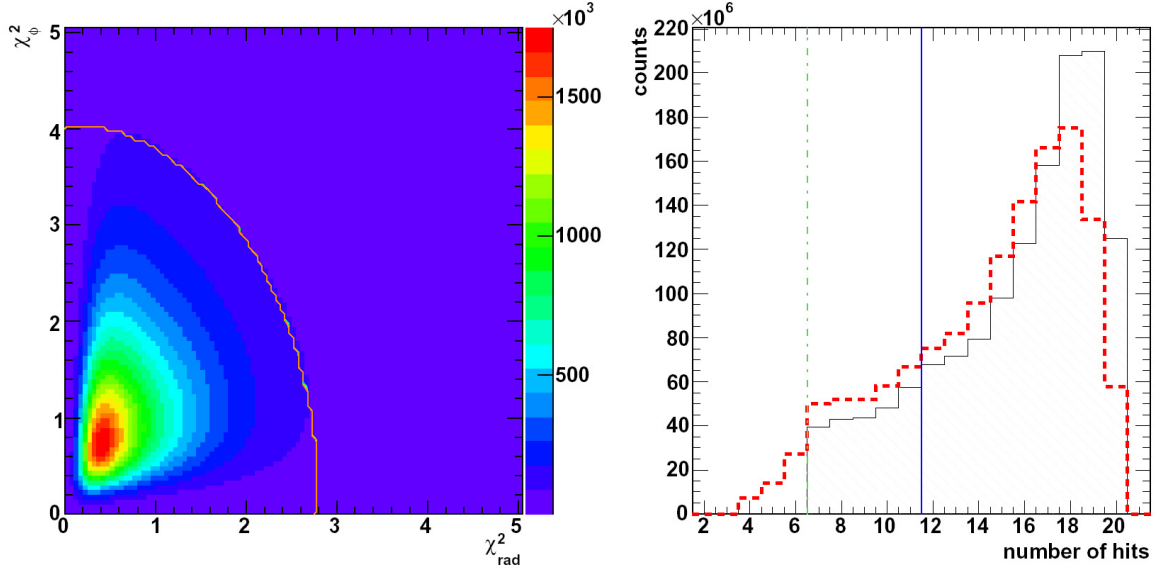


Figure 5.1: Left panel: the quality of the track fit in $r(t)$ and $\phi(z)$. The red line represents the cut. Right panel: distribution of the TPC track length: the total number of hits on track (black solid line), the number of fitted hits per track (red dash line). The vertical lines correspond to the cuts applied during the step2 production (dash-dot), and for the particle correlations analysis (solid).

- particle (pion-proton) identification based on the energy loss dE/dx versus track momentum (contours in Fig. 4.6),
- vertex cut (matching between SDD and TPC better than 2.5σ) to suppress pions from K^0 and Λ^0 decays, as well as the protons coming from Λ^0 decays.

Since the time-space evolution of the colliding system strongly depends on the centrality of the collision the good knowledge of the event centrality is one of the important issues in the HBT interferometry. The relation between the measured event multiplicity and the impact parameter \vec{b} is discussed in Section 4.8. Based on the fully calibrated information from the Multiplicity Counter seven centrality classes were selected for the two-particle correlation analysis. Table 5.1 summarizes the centrality selection.

While the pions from long-lived resonances like Λ^0 and K^0 can be significantly suppressed with a vertex cut the short-live resonances, which decay very close to their production point, could not be removed from the input data. Their most important effect is to lower the intercept of the correlation function ($\lambda < 1$) [CL95, Hei96b, WH97].

The most important cuts in the two-particle analysis are the pair cuts. The finite granularity of the TPC resulted in the decrease of the reconstruction efficiency for very close tracks. Since

bin	$\sigma/\sigma_{\text{GEOM}}(\%)$	$\langle\sigma/\sigma_{\text{GEOM}}\rangle (\%)$	$b_{\min} - b_{\max} \text{ (fm)}$	$\langle N_{\text{part}} \rangle$	$\langle N_{\text{coll}} \rangle$	$\langle \frac{dN_{\text{ch}}}{d\eta} \rangle _{\eta=3.1}$
1	< 2.5	1.28	< 2.4	366	850	428.3
2	2.5 - 5	3.74	2.4 - 3.3	325	781	389.9
3	5 - 7.5	6.10	3.3 - 4.1	298	666	356.2
4	7.5 - 10	8.06	4.1 - 4.7	274	643	330.5
5	10 - 15	11.65	4.7 - 5.8	234	522	288.1
6	15 - 25	17.49	5.8 - 7.4	180	345	230.4
7	25 - 35	29.98	7.4 - 8.8	124	224	142.9

Table 5.1: The centrality bins used in the analysis. The geometrical cross section for Pb+Au collisions σ_{GEOM} was assumed to be 6.94 b.

the track separation is related to the relative momentum between the two particles, and the effect mentioned above does not occur for the mixed pairs (background), the two-particle correlation function is strongly affected. Those pairs, for which the deflection in the magnetic fields brings the particles closer together, suffer more then the others. The two topologies, thus, have to be considered separately (Fig. 5.2). The selection between the so-called sailor and cowboy pairs was based on the condition

$$SC = (Q_1 \cdot Q_2)(Q_2 \cdot p_2 - Q_1 \cdot p_1)(\phi_2 - \phi_1) \quad (5.1)$$

where $p_i = |\vec{p}_i|$, Q_i , and ϕ_i are the momenta, charges, and azimuthal angles of the two particles ($i=1,2$), respectively. The positive and negative value of SC indicates, respectively, the sailor and the cowboy topology. The pairs, for which SC was equal to zero, were rejected. The efficiency, calculated as the ratio between the signal and the background pairs, is presented as a function of $\Delta\theta$ vs. $\Delta\phi$ for different pair transverse momenta in Fig. 5.3. This effect is corrected

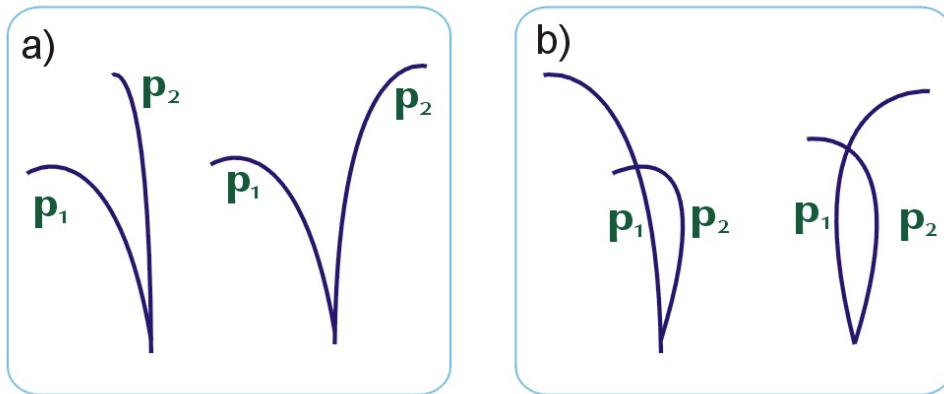


Figure 5.2: The different topology of pairs in the CERES TPC; a) sailors, b) cowboys.

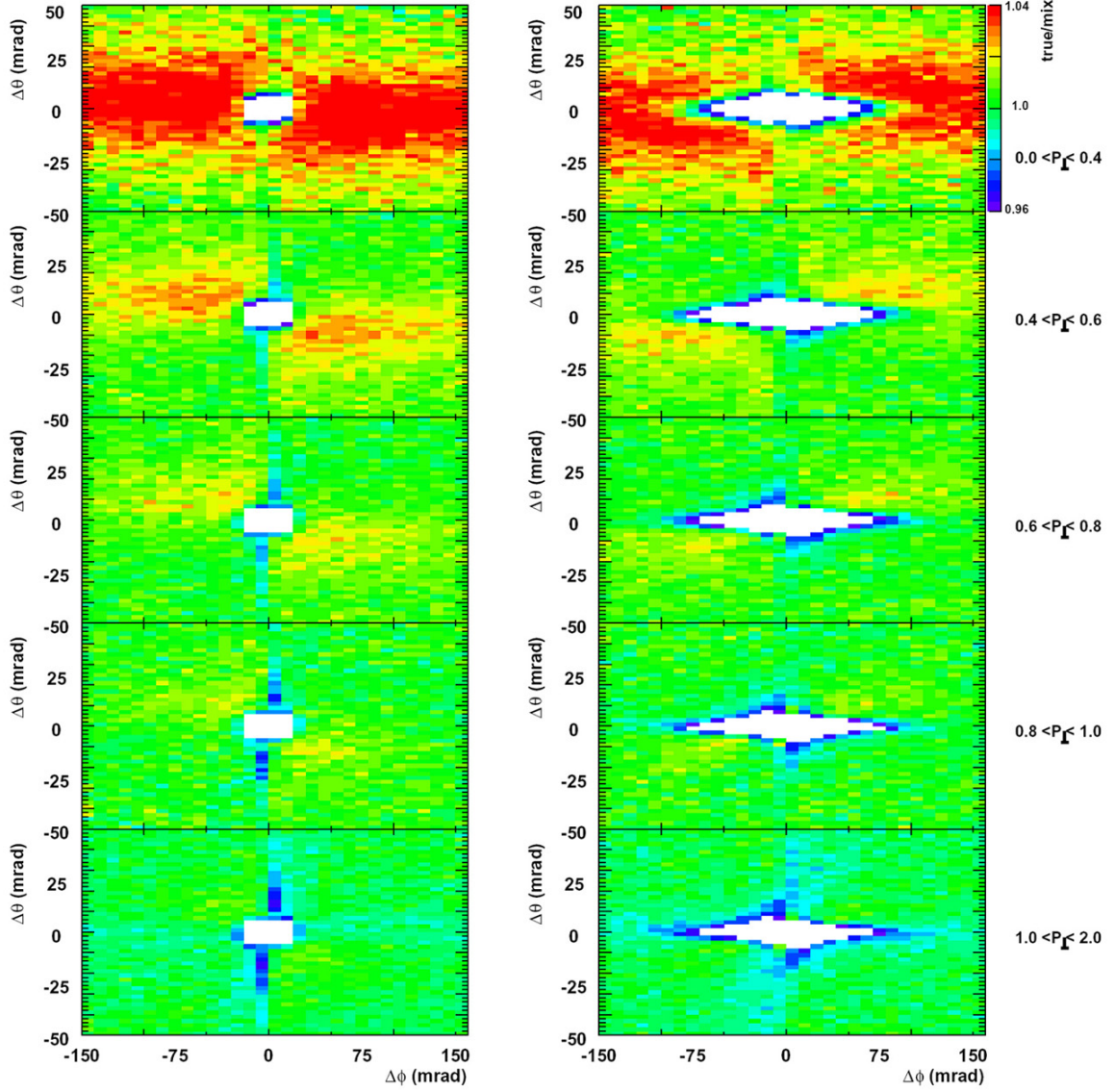


Figure 5.3: Two track resolution of the CERES TPC. Number of reconstructed track pairs, normalized to mixed events, $\Delta\phi$ and $\Delta\theta$ for the two pair topologies, sailor (left) and cowboy (right).

for by requiring a minimum opening angle between the tracks in a pair, both in the signal and in the background. The corresponding two-dimensional cuts were applied separately for a given pair topology, rapidity, and transverse momentum. The P_{\perp} -dependent separation cuts applied for the sailor pairs were varied between 8-9 mrad for $\Delta\theta$ and between 38-45 mrad for $\Delta\phi$. Small fluctuations in the $\Delta\theta$ around $\Delta\phi=5$ mrad were also removed. In the case of cowboy

pairs also so-called cross cuts were applied, however, with the much wider window in the $\Delta\phi$ (90-140 mrad).

Information concerning the dynamics of the relativistic heavy-ion collisions can be derived from the pair momentum dependence of the measured correlations functions. Therefore, the HBT analysis of the like-sign π was performed in eight bins of the transverse pair momentum ($P_{\perp,\pi\pi}$) defined by Eq. 1.10. The CERES experiment for the Pb-Au collision system at 158 GeV/c covered the backward Y region, close to the midrapidity $Y_B/2=2.91$. The results of many theoretical models are usually determined for the midrapidity region, hence the existed data set was divided into two bins of pair rapidity ($Y_{\pi\pi}$) in order to study qualitatively the rapidity dependence of the HBT parameters. In Fig. 5.4 the $n(P_{\perp,\pi\pi}, Y_{\pi\pi})$ distribution of the π pairs with relative pair momentum below 150 MeV/c is shown. The horizontal and vertical lines represent chosen slices of $P_{\perp,\pi\pi}$ and $Y_{\pi\pi}$, respectively. Table 5.2 contains the mean values for each (P_{\perp}, Y) bin which were used for the representation of the HBT parameters vs. P_{\perp} in the following chapter.

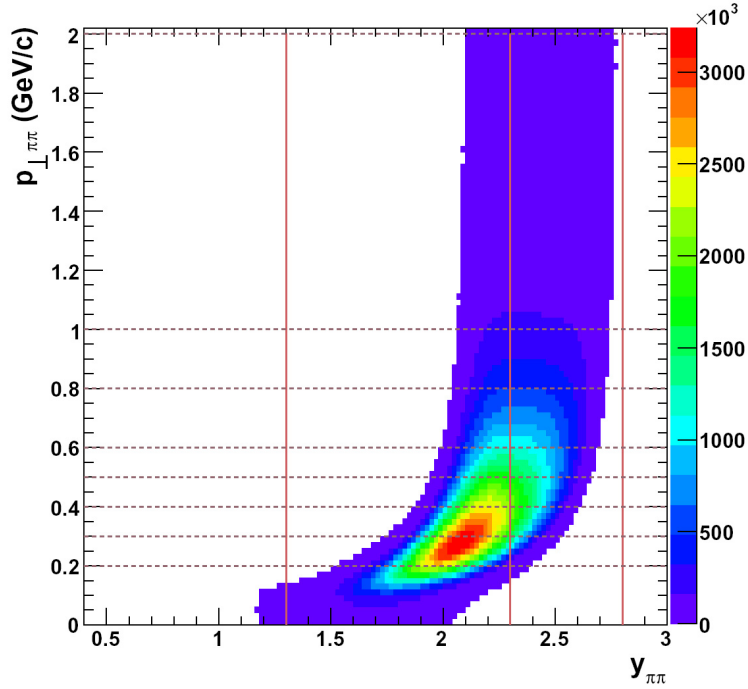


Figure 5.4: The like-sign pion pairs acceptance in the CERES TPC for pairs with relative momentum below 150 MeV/c. The horizontal and the vertical lines represent chosen cuts in the pair transverse momentum and in the pair rapidity, respectively.

pair	$Y_{\pi\pi} / P_{\perp}$ bin	0.0-0.2	0.2-0.3	0.3-0.4	0.4-0.5	0.5-0.6	0.6-0.8	0.8-1.0	1.0-2.0
$\pi^- \pi^-$	1.3-2.3	0.170	0.252	0.343	0.441	0.541	0.668	0.871	1.112
	2.3-2.8	0.190	0.282	0.362	0.452	0.548	0.681	0.876	1.119
$\pi^+ \pi^+$	1.3-2.3	0.169	0.253	0.345	0.443	0.543	0.672	0.873	1.118
	2.3-2.8	0.190	0.283	0.363	0.453	0.549	0.683	0.877	1.127

Table 5.2: P_{\perp} and Y intervals used in the analysis. For each bin the mean P_{\perp} is given.

5.2 Definition of the Correlation Function

Experimentally, the two-particle correlation function for a given pair momentum \mathbf{P} (see Eq. 1.9) and relative momentum \mathbf{q} (see Eq. 1.11) is obtained by dividing the signal distribution $S(\vec{q}, \vec{P})$ by the reference or background distribution $B(\vec{q}, \vec{P})$ which should be ideally similar to the S in all respects except for the presence of femtoscopic correlations

$$C_2(\vec{q}, \vec{P}) = \frac{S(\vec{q}, \vec{P})}{B(\vec{q}, \vec{P})} . \quad (5.2)$$

In Fig. 5.5 an example of the signal and the background π pair distributions and the resulting correlation function is shown. Similarly, the three-dimensional like-sign π correlation functions were obtained using the ‘out-side-long’ components of the relative pair momentum vector calculated in the LCMS frame. Values of the relative momentum obtained in this frame were stored in three-dimensional histograms with a binning of 10 MeV/c for signal and background distributions. In order to correct for the final state Coulomb interaction between particles, an additional three-dimensional histogram of the same binning stored the Lorentz invariant four-momentum difference q_{inv} (see Eq. 1.12). The latter was used during the fit procedure of the correlation function as will be explained in Section 5.5.

5.3 Signal and Background Construction

The cuts, described in Section 5.1, were applied both for the signal and the background pairs. The signal $S(\vec{q}, \vec{P})$ refers to the relative momentum q distribution of two particles coming from the same event. The background distribution $B(\vec{q}, \vec{P})$ was obtained using pairs consisting of particles taken from two different events. Such method of background construction, commonly used in the data analysis of the high energy experiments, is called the event-mixing technique [Kop74]. In order to reduce the statistical uncertainties in the derived correlation functions the background was calculated from four additional events. The latter were chosen as an optimum between the computing time and the reduction of statistical errors. The background distributions should be indistinguishable from the signal distribution in all respects

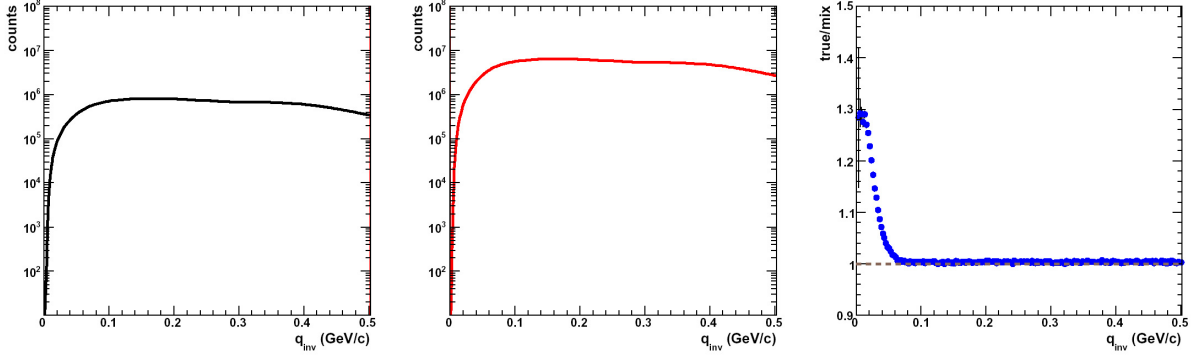


Figure 5.5: One-dimensional distribution of the momentum difference for the like-sign pion pair from the same event (left panel) and from different events (middle panel). The derived correlation function is shown in the right panel.

except for the presence of femtoscopic correlations. Therefore, each event was characterized by its centrality, vertex position, and the reaction plane orientation, and only events with similar properties were used to calculate the background distribution. The events were accumulated in ten bins of centrality. The bin width varied from 2 % $\sigma/\sigma_{\text{GEOM}}$ for the most central collision region to 5 – 20 % $\sigma/\sigma_{\text{GEOM}}$ in the case of more peripheral collisions. Moreover, events were split into eight classes of the reaction plane orientation angle Ψ_2 , and only events coming from the same reaction target were mixed. This prevents the creation of an artificial structure in the correlation functions.

5.4 Fitting the Correlation

The three-dimensional correlation function for the like-sign particles can be parameterized

$$C_2(\vec{q}, \vec{P}) = N \cdot \left\{ 1 + \lambda(\vec{P}) \cdot \exp \left(- \sum_{i,j=1}^3 R_{ij}^2(\vec{P}) q_i q_j \right) \right\}, \quad (5.3)$$

where N is a normalization factor and the correlation strength λ accounts for the long-lived resonances halo of the source distribution. The latter is also influenced by the detector resolution as well as by the misidentification of the particle species. The R_{ij}^2 parameters correspond to the Gaussian source radii derived in the ‘out-long-side’ coordinate system described in Section 1.3.2. The indices i, j run over three of the four components of q indicated as *out*, *long*, *side*.

Fitting the Eq. 5.3 to the derived correlation function based on the least square method and using the square root of the number of counts as an estimator of the error introduces a systematic bias by overestimating the significance of bin with a low number of counts [BC74]. The

maximum likelihood method, on the other hand, is free from this kind of bias. The MINUIT [MIN] package was used to minimize the negative logarithmic likelihood function

$$-2 \log \mathcal{L} (R_{ij}^2) = 2 \sum_b \left[C_2 (R_{ij}^2) N_b - n_b \log (C_2 (R_{ij}^2) N_b) + \log (n_b!) \right], \quad (5.4)$$

where n_b and N_b are the numbers of signals and background pairs in the relative momentum q bin b , and $C_2(R_{ij}^2)$ is the Gaussian parameterization of the correlation function. The last term in Eq. 5.4 does not depend on R_{ij}^2 and, consequently, can be neglected.

The correlation functions have to be corrected for the final state interaction of which the Coulomb interaction between charge particle is the most significant one. Therefore, the fit function was modified in order to account for such effect.

5.5 Coulomb Correction

Apart from Bose-Einstein statistics, correlations between like-sign charge particles occur by the final state interactions. The latter, due to repulsive interaction in the case of the like-sign particles, decrease the correlation strength and influence the width of the correlation function. In order to account for such effects different methods were tried. In the first approach the background distribution of the relative momentum difference was weighted with a correction factor characterizing the Coulomb repulsion. This over-corrects the correlation function since it neglects the fact that pions which come from long lived resonances do not feel Coulomb repulsion. A better method of removing the Coulomb effects from measured correlation functions was first suggested by [Bow91, S⁺98] and then applied for the previous CERES analysis of the two particle correlation presented in [A⁺03a]. The correlation function in this procedure was fitted by

$$C_2(\vec{q}) = N \cdot \left\{ (1 - \lambda) + \lambda \cdot F_c(q_{inv}) \left[1 + \exp \left(- \sum_{i,j=1}^3 R_{ij}^2 q_i q_j \right) \right] \right\}, \quad (5.5)$$

where $F_c(q_{inv})$ is the squared Coulomb wave function described by Eq. 1.51 integrated over the emitting source. In this method the Coulomb term is coupled with λ to avoid the over-correction of the correlation function. The detailed description of deriving $F_c(q_{inv})$ factors for different source size (in steps of 0.5 fm) used in this work is presented in Section 7.1. In Fig. 5.6 an example of one-dimensional projection of the three-dimensional correlation function together with both fits (Eq. 5.3 and Eq. 5.5) is shown. The projections q_{out} , q_{side} , q_{long} of relative momentum vector decomposed in the Bertsch-Pratt coordinate system were produced for each component with an interval of $|q| < 40$ MeV/c in the other two directions. The difference between two fits reflects a Coulomb correction to the correlation function.

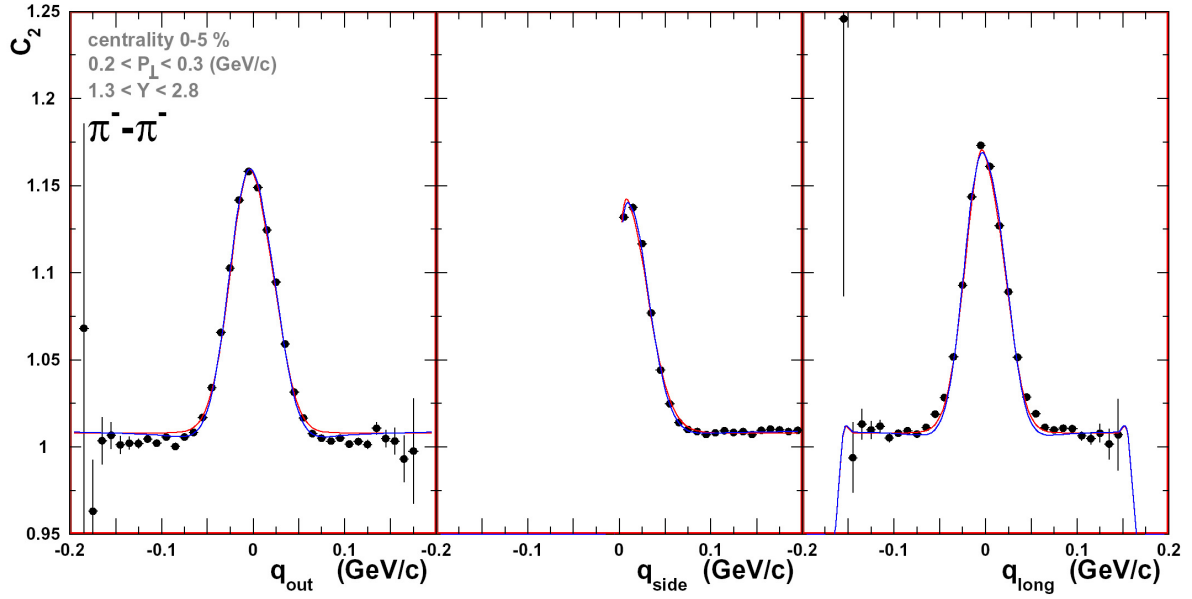


Figure 5.6: One-dimensional projection of the three-dimensional correlation function. The fit by Eq. 5.5 is depicted as the blue line, whereas the fit without the Coulomb correction shown by the red line.

The usually applied Gamow correction describes the square of the relative Coulomb wave-function of a particle pair at zero separation in the configuration space and thus does not take into account the finite source size. The effect of Gamow correction applied in its full strength or reduced by λ on the $\pi^-\pi^-$ correlation radii is shown as open triangles in the right and left column of Fig. 5.7, respectively. The results obtained with the finite-source Coulomb correction, calculated by averaging the squared Coulomb wave function over a Gaussian source distribution with $\sigma_x = \sigma_y = \sigma_z = 3$ fm and $\sigma_t = 0$ fm/c, are shown as full stars. The last method of Coulomb correction, depicted in Fig. 5.7 as full circle, consistently takes into account the actual size of the measured emitting source. The HBT radii dependence on the pair transverse momentum causes an under- or over-estimation of Coulomb interaction effects on the measured correlation functions when a constant source size Coulomb correction function is used for all P_\perp 's. Therefore, the measured one-dimensional HBT correlation function was used as an estimator of the emitting source size for a given P_\perp bin. The one-dimensional function, similarly to the three-dimensional one, was fitted by

$$C_2(\vec{q}) = N \cdot \left\{ (1 - \lambda) + \lambda \cdot F_c(q_{inv}) \left[1 + \exp(-R^2 q^2) \right] \right\}, \quad (5.6)$$

where R reflects its size. The fit was done iteratively with the value of R , obtained from one iteration, used for the Coulomb correction in the next one. In first iteration the Coulomb correction factor was set to unity. The Coulomb correction factor obtained in such a way is

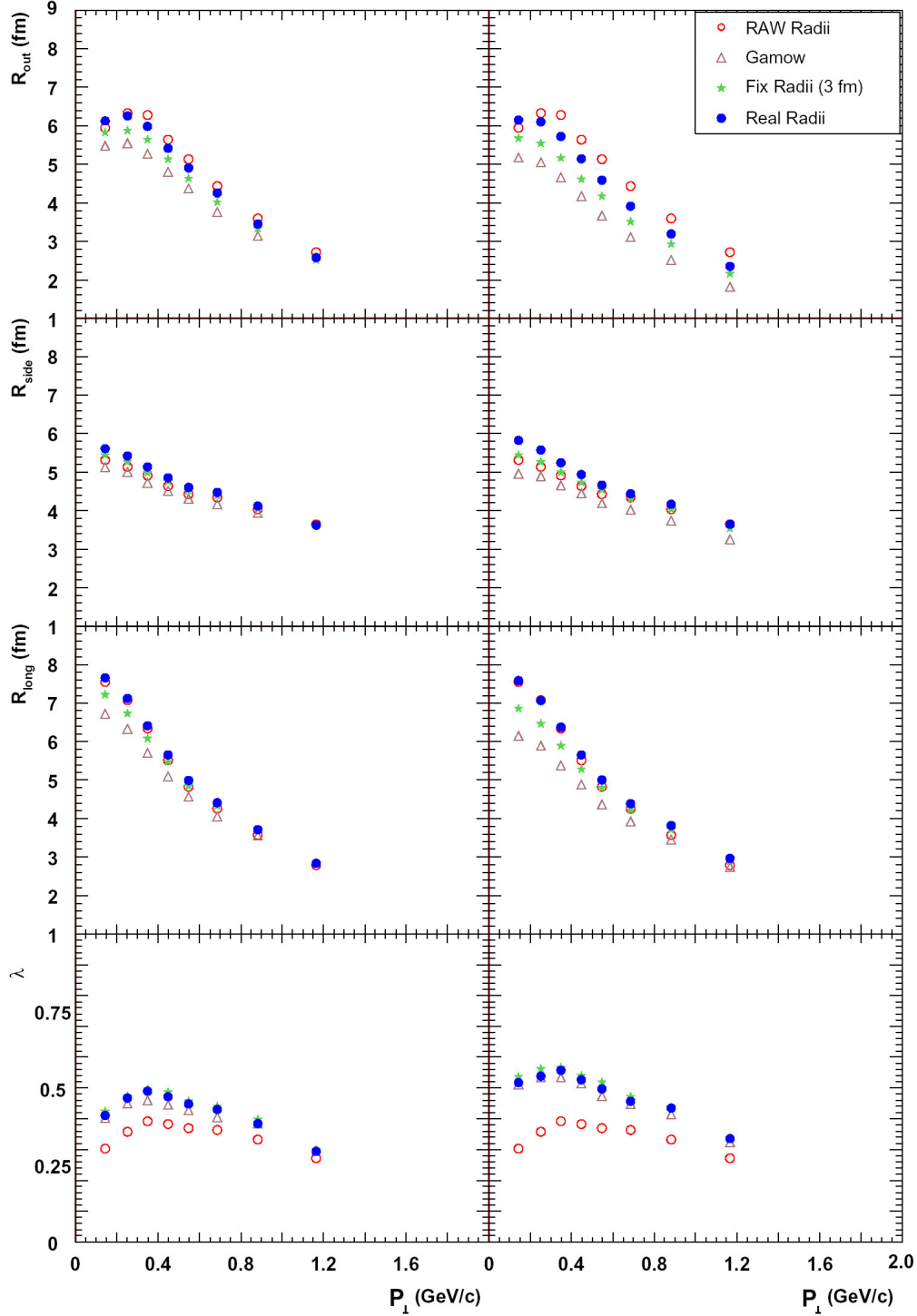


Figure 5.7: The $\pi^-\pi^-$ HBT radii as a function of the pair transverse momentum for different Coulomb correction methods. The HBT radii extracted from the three-dimensional correlation functions by Eq. 5.5 with different Coulomb corrections are shown in the left column. For comparison, the right column presents the HBT radii obtained with the full Coulomb strength. The data were not corrected for the detector resolution. The open red circles represents the uncorrected HBT radii (centrality bin 1-2).

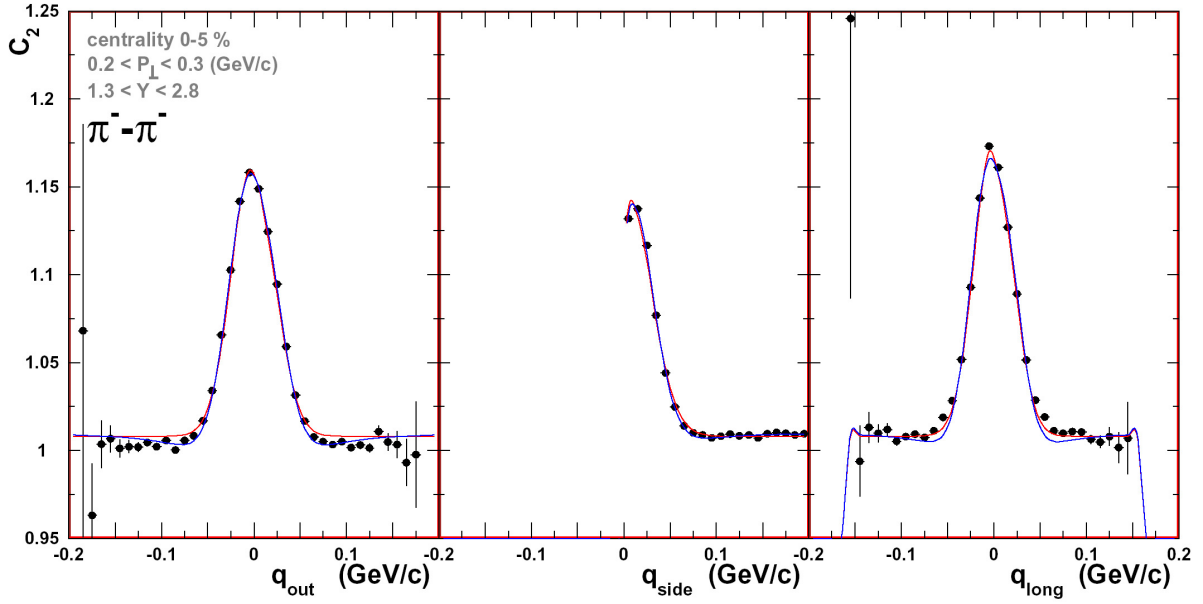


Figure 5.8: Results of the fit by Eq. 5.5 (blue line) with the parameterization of Coulomb interaction between like-sign particles based on the diluted Gamow factor. The red line shows the fit without Coulomb correction.

then used for the three-dimensional fit function. This was the method used to account for the effects of Coulomb interaction in the identical particle correlation functions considered in this dissertation.

A comparison between Figs. 5.6 and 5.8 shows that the phenomenological Coulomb correction can somewhat better describe the tails of $C(q_{out})$; it misses, however, the tails of $C(q_{long})$.

5.6 Transverse Momentum Dependence

In heavy ion collision an assumption of the static emitting source is certainly not an adequate one. The HBT radius parameters measure the size of the regions emitting particles of a given momentum (homogeneity regions) rather than the size of the fireball. The homogeneity radii depend on the velocity gradients and the temperature existing in the emitting source [WSH96, Wie98, TWH00]. This dependence is reflected in the measured correlation radii plotted as a function of the transverse momenta of the pairs of particles [Pra84, MS88] providing information about the dynamics of the matter created during the collision. Additionally to the P_{\perp} dependence of the measured HBT radii the impact parameter significantly influences the extracted parameters. Therefore, a reasonably narrow centrality bins should be used while the

Bose-Einstein correlations are considered. In Fig. 5.9, like-sign pion HBT radii, uncorrected for the Coulomb interaction and detector resolution effects, are shown as a function of the transverse pair momentum for six different classes of centrality.

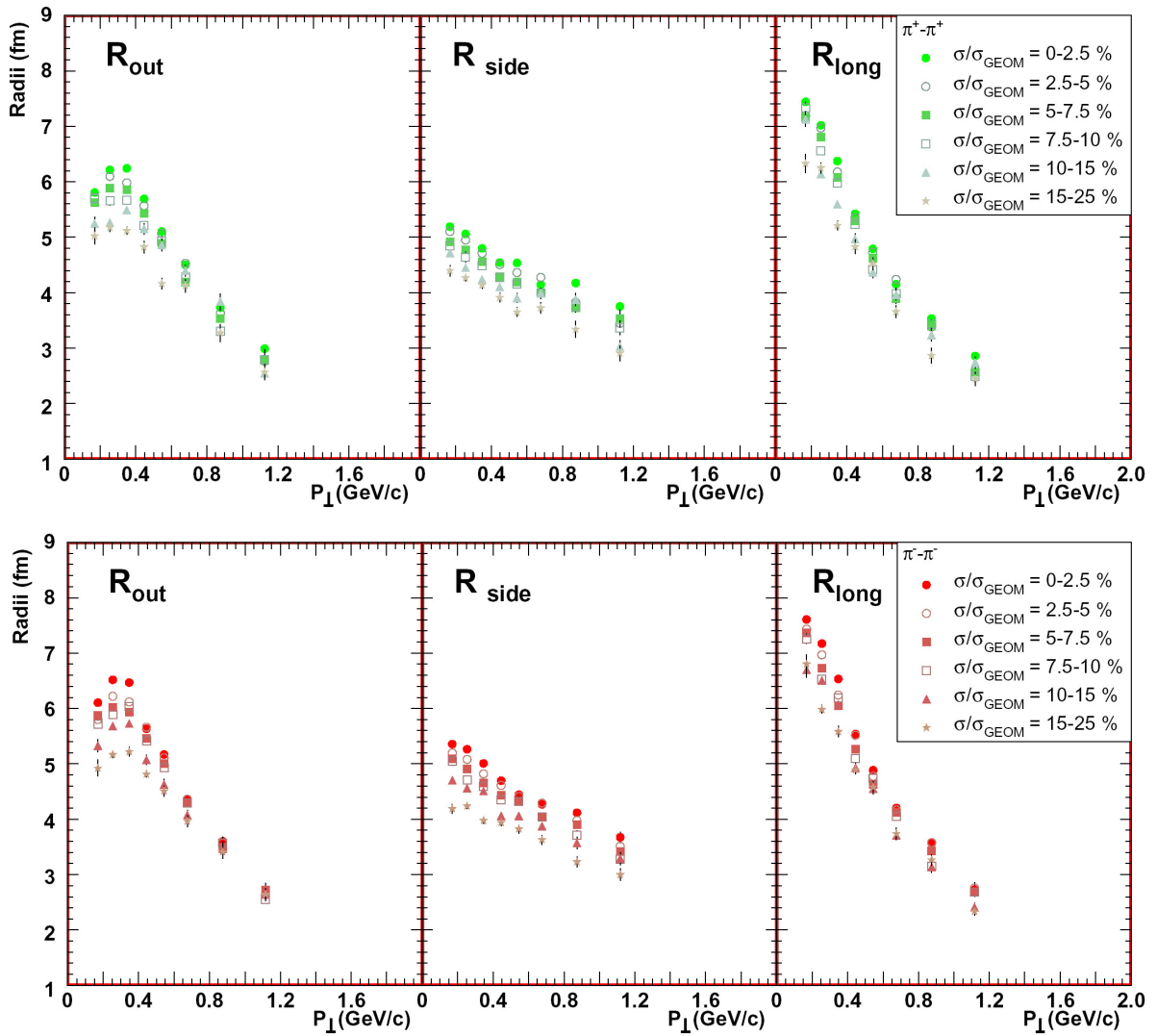


Figure 5.9: The transverse momentum dependence of the raw HBT radii, for $\pi^+\pi^+$ (top) and $\pi^-\pi^-$ (bottom).

5.7 Reaction Plane Orientation Dependence

Additional information concerning the dynamics of the emitting source can be obtained from non-central collisions, where freeze-out collision geometry might reflect the initial anisotropic almond shape, with its longer axis perpendicular to the reaction plane. Existence of the transverse pressure gradients in the reaction plane direction generated in such a colliding system leads to a preferential in-plane expansion [Oll92, KSH00] which diminishes the initial anisotropy as the system evolves. Therefore, the source shape at freeze-out should be sensitive to the evolution of the pressure and the system lifetime. Hydrodynamical calculations [KH03] predict that the source may still be out-of-plane extended after hydrodynamical evolution. However a subsequent rescattering phase tends to make the source in-plane extended [TLS01]. The study of HBT parameters relative to the reaction plane orientation in non-central collisions gives access to the spatial source anisotropy at freeze-out and might shared the light on different scenarios of the system's evolution.

The simple sketch of the method used to analyze the HBT radii relative to the reaction plane is shown in Fig. 5.10. The reaction plane orientation angle Ψ_2 was derived based on the Fourier expansion method explained in Section 4.7. Once the reaction plane is known one can calcu-

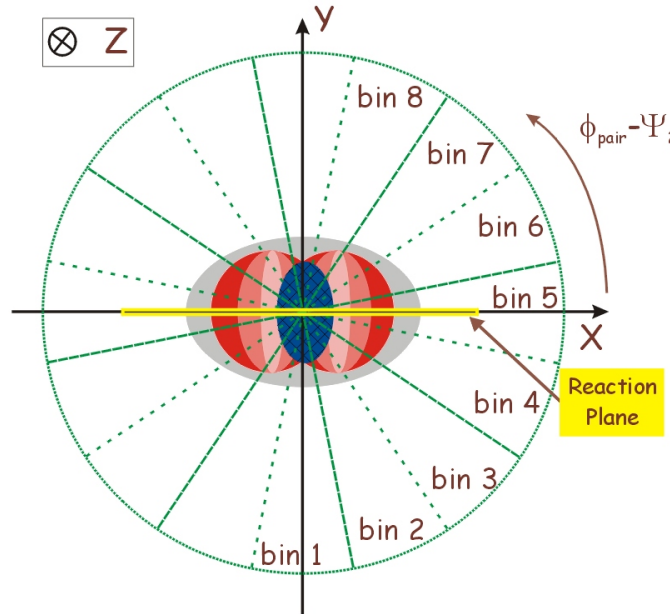


Figure 5.10: Sketch of the analysis method of the reaction plane dependent HBT radii. The space asymmetry in the collision is reflected in the momentum asymmetry of the produced particles depicted as a gray area. Two-pion correlation functions are analyzed separately for 8 bins of the azimuthal angle in respect to the reaction plane.

late the difference between the azimuthal orientation of a pair and the Ψ_2 , $\phi_{pair} - \Psi_2$. Since the orientation of the reaction plane was calculated based on the second Fourier harmonics the information about the sign of the impact parameter vector is lost. In other words, the reaction plane angle is known modulo π . Therefore, due to the mirror symmetry with respect to the reaction plane only those space-time variance will not vanish which do not change the sign under $\Psi \rightarrow \Psi + \pi$ rotation. The analysis was performed in eight bins of the azimuthal angle difference $\phi_{pair} - \Psi_2$ in the transverse plane. For each bin a correlation function was constructed following the description presented in Section 5.2 for eight bins of P_\perp and two bins of Y . Subsequently, the correlation functions were fitted with Eq. 5.5 and the derived HBT parameters were plotted as functions of the azimuthal angle difference. Since the observed anisotropies were hardly significant, and since, based on the blast wave calculations, not much P_\perp was to be expected, all P_\perp and Y bins were merged together before the fit was performed. Fig. 5.11 shows the measured dependence of the HBT radii on the azimuthal emission orientation not corrected for the finite reaction plane resolution and the finite binning in $\phi_{pair} - \Psi_2$. The dash line is a sine (cosine) fit to the HBT radii (cross-terms), comp. Eq. 5.5. The fit results are discussed in Section 8.1. The last point on all plots is identical with the first one and is omitted during the fit. The influence of the finite reaction plane angle resolution has a significant influence on the measured HBT radii. It decreases the measured amplitude of the HBT radii oscillations similarly as in the case of the elliptic flow [Oll98]. The correction for the reaction plane angle resolution will be discussed in Section 7.3.

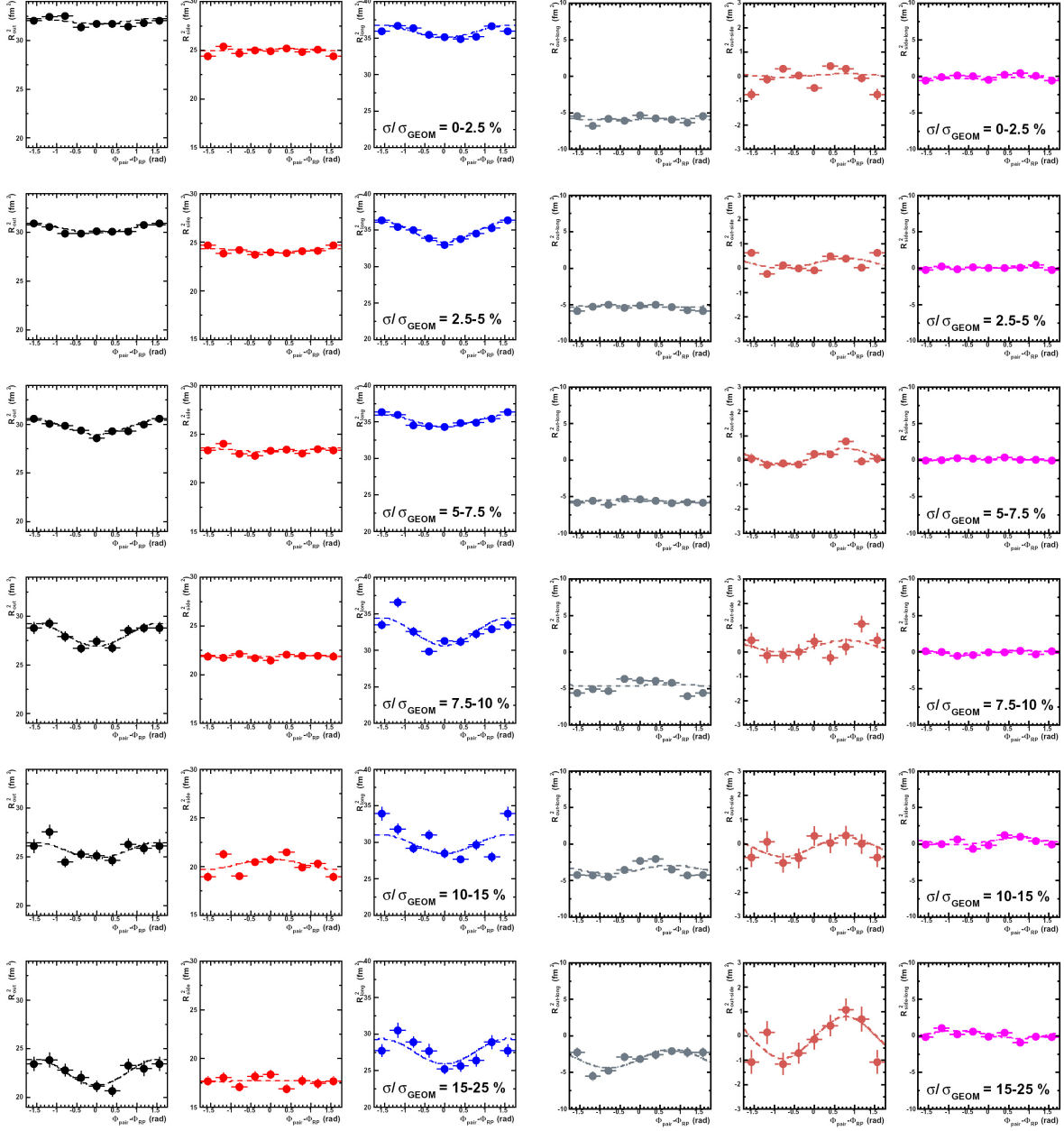


Figure 5.11: The reaction plane dependence of the HBT radii and the cross terms integrated over all bins of the pair P_{\perp} .

Chapter 6

Non-identical Particle Correlation Analysis

The correlations between non-identical same- and opposite-charge particles exhibit a minimum and a peak, respectively, at low relative momentum $\tilde{\mathbf{q}}$ (see Eq. 1.54), caused by the mutual Coulomb and the strong interactions. The small $\tilde{\mathbf{q}}$ implies that the two particles have the same velocity but not necessarily the same momenta. A difference between the average freeze-out position or time of the two particle species reveals itself as an asymmetry of the correlation function $C(\tilde{\mathbf{q}}, \mathbf{P})$ at small \tilde{q} [LLEN96]. The asymmetry in the π -p correlations indicates that the proton source is located at a larger radius than the pion source or that protons are emitted earlier than pions [RftSC03]. This effect was attributed to the collective expansion of the system created during the collision i.e. to the transverse flow. In this chapter an analysis of π -p correlation functions will be presented. The analysis was performed in the Pair Center of Mass System (PCMS) in which the pair momentum vanishes. In this frame the relative momentum difference $\tilde{\mathbf{q}}$ is given by Eq. 1.11.

6.1 Analysis Variables and Frame

Two non-identical particle correlations were studied in the framework of the two-dimensional correlation functions $C(\mathbf{q}, \mathbf{P})$, defined by Eq. 5.2. The ratio of the signal distribution $S(\mathbf{q}, \mathbf{P})$ to the background distribution $B(\mathbf{q}, \mathbf{P})$ was constructed in the same manner as described in Section 5.3. The tracks chosen for the analysis were selected based on the set of cuts presented in Section 5.1, also the two-track resolution effect was treated in the same way as described in the case of the Bose-Einstein correlations. The experimental two-track resolution in general should affect less the non-identical particle correlation since pions and protons emitted with similar velocities have very different momenta in the laboratory frame. The correlation functions were calculated for $\pi^- \pi^+$, $\pi^- p$, and $\pi^+ p$ pairs in five bins of pair transverse momentum. The $\pi^- \pi^+$

correlation functions were calculated in order to cross-check the analysis method, since the correlation function for this combination is expected to be symmetric. The acceptance of the CERES experiment for the pion-proton pairs with the relative momentum below 150 MeV/c is shown in Fig. 6.1, where the horizontal and the vertical lines represent the chosen bins of $P_{\perp \pi-p}$ and $Y_{\pi-p}$, respectively. In order to increase the statistics, the data were integrated over the centrality and the pair rapidity bins. The analysis performed in centrality bins does not exhibit any differences between results obtained for those integrated over all centrality bins within statistical uncertainty. Table 6.1 contains the mean values of the pair transverse momentum in the laboratory frame integrated over rapidity intervals. By convention, \mathbf{q} is calculated as a difference between momentum of the heavier and the momentum of the lighter particle in the laboratory frame. The pairs are boosted to the pair centre of mass frame with $\vec{\beta} = \frac{\vec{P}}{E_{pair}}$. In this reference frame, the q vector is decomposed into the q_{\parallel} , and q_{\perp} defined as

$$\begin{aligned} q_{\parallel} &= q_{out} , \\ q_{\perp} &= \sqrt{q_{side}^2 + q_{long}^2} , \end{aligned} \tag{6.1}$$

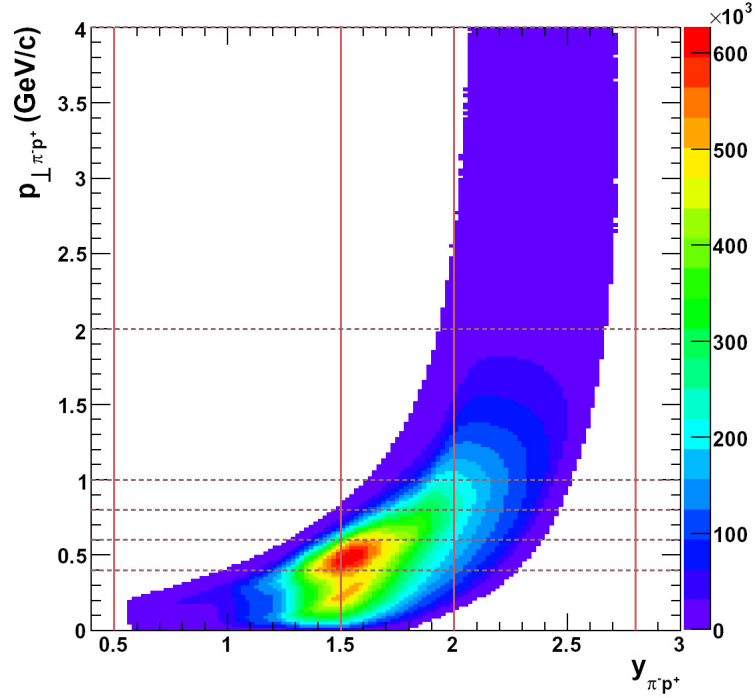


Figure 6.1: CERES acceptance for pion-proton pairs with the relative pair momentum below 150 MeV/c. The vertical and the horizontal lines represent the bins in the pair rapidity and in the pair transverse momentum, respectively.

pair	P_{\perp} bin (GeV/c)	0.0-0.4	0.4-0.6	0.6-0.8	0.8-1.0	1.0-2.0	2.0-4.0
$\pi^- p^+$	$\langle P_{\perp} \rangle$	0.286	0.507	0.685	0.885	1.214	2.185
$\pi^+ p^+$	$\langle P_{\perp} \rangle$	0.287	0.508	0.686	0.884	1.215	2.189

Table 6.1: The different p_{\perp} intervals used in the analysis of the non-identical particle correlation together with their mean p_{\perp} values.

where q_{long} is the component parallel to the beam direction z , q_{side} is perpendicular to the beam direction and to the transverse pair momentum, and q_{out} is perpendicular to q_{long} and q_{side} . The q_{long} , q_{side} , and q_{out} are the well known variables of the Bertsch-Pratt parameterization but calculated in the analysis frame (PCMS). While the q_{out} is parallel to the transverse pair velocity and sensitive to the average separation of particles in the transverse direction, the q_{side} component should not show such effects. A similar analysis can be performed for the longitudinal direction, based on the sign of the q_{long} component as presented in [Miš98]. In Fig. 6.2 (left panel) an example of the two-dimensional correlation function $C(q_{\perp}, q_{\parallel})$ for $\pi^- p$ pairs is shown. The convention chosen in the calculation of the relative pair momentum means that for $q_{\parallel} > 0$ ($q_{\parallel} < 0$) the lighter particle transverse velocity is smaller (larger) than the heavier one's. Therefore, the pion-proton correlations will be stronger when $q_{\parallel} < 0$ than when $q_{\parallel} > 0$, since in the first case pions tend to catch up with protons while in the second case pions tend to move away from protons (see Fig. 1.6).

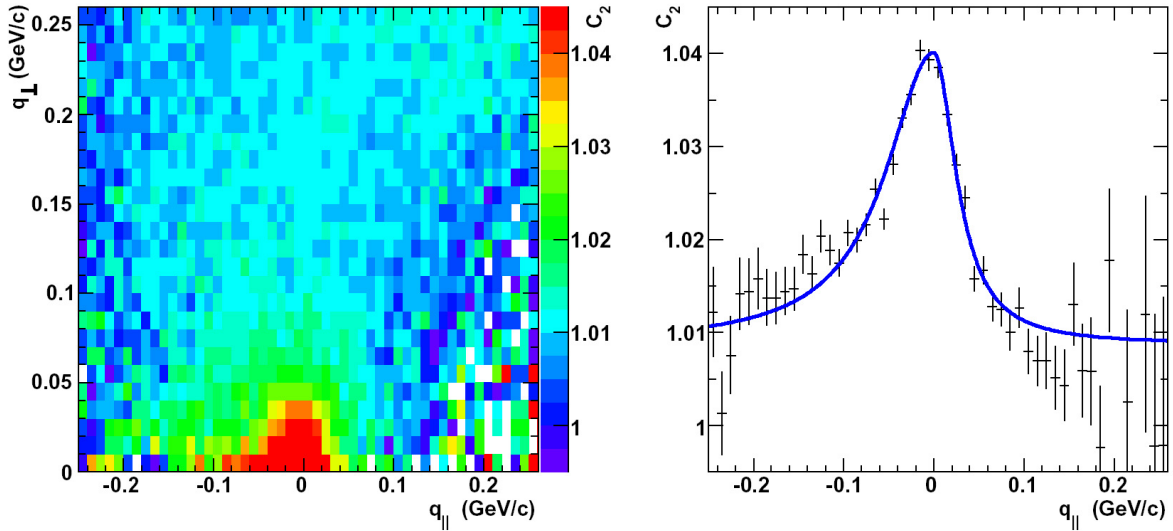


Figure 6.2: An example of the two-dimensional correlation function for $\pi^- p^+$ pairs (left panel). In the right panel the projection on the q_{\parallel} axis with $q_{\perp} \in \{0, 50\}$ MeV/c and the fit by Eq. 8.3 is shown.

6.2 Parameterizing the Asymmetry of the Correlation Peak

The two-particle correlation functions for $\pi^-\pi^+$, π^-p , and π^+p pairs are caused mainly by Coulomb interaction. One should therefore, expect that the correlation effect will be positive for the unlike-sign pairs and negative for the like-sign ones. The derived experimental correlation functions confirm this expected behavior. Moreover, the peak (dip) in the pion-proton correlation function seems to be asymmetric. In order to qualitatively parameterize the asymmetry the signal and the background distributions were projected along q_\perp within $\{0, 50\}$ MeV. Subsequently, the derived projection of the signal was divided by the projection of the background distribution, and a one-dimensional correlation function was obtained. The latter can be reasonably well described by a Lorentz curve with two widths σ_+ and σ_- given by

$$C_2(q_\parallel) = \begin{cases} N \cdot \left(1 + \frac{a}{(q_\parallel/\sigma_-)^2 + 1} \right), & q_\parallel < 0 \\ N \cdot \left(1 + \frac{a}{(q_\parallel/\sigma_+)^2 + 1} \right), & q_\parallel > 0 \end{cases}$$

where N is a normalization factor, and a corresponds to the peak amplitude. The asymmetry is then defined as the ratio between the two obtained widths ($\mathcal{A} = \sigma_-/\sigma_+$). In Fig. 6.2 (right panel) the fit to the one-dimensional correlation function is shown.

Two methods of quantifying the asymmetry are compared in Fig. 6.3. The originally proposed method, based on the one-dimensional correlation functions [LLEN96], is depicted as brown stars while the method proposed in this dissertation is presented by the red circles. The correlation functions were calculated based on the Monte Carlo generator for a constant displacement of 6 fm in the transverse direction between π -p. The detailed description of the methods of constructing correlation functions is presented in Section 7.4. Following the original proposal, the ratio between the one-dimensional correlation functions $C_{2,+}$ and $C_{2,-}$ defines the mean distance between the two particle species at freeze-out. The $C_{2,-}$ and $C_{2,+}$ were obtained using pairs with $q_\parallel < 0$ and $q_\parallel > 0$, respectively. If at any value of q the ratio $C_{2,-}/C_{2,+}$ differs from unity the asymmetry is observed. The sign of the deviation depends on the convention in the calculation of the relative momentum difference between particles as it was already mentioned before. The quality of both methods can be judged by comparing the fit parameter of Eq. 8.3. The fitted curve describes reasonably well the simulated correlation functions. Based on the definition of the \mathcal{A} parameter the significance of a method can be expressed by

$$G_{\mathcal{A}} = \frac{\mathcal{A} - 1}{\delta\mathcal{A}}. \quad (6.2)$$

The ratios of the derived correlation functions are plotted in the left bottom panel of Fig. 6.3. The difference of the two histograms reflects the quality of the analysis method. In the case of the two-dimensional method the deviation from unity is larger, so it, should be more sensitive to the displacement between the sources of the two particle species. On the other hand, taking

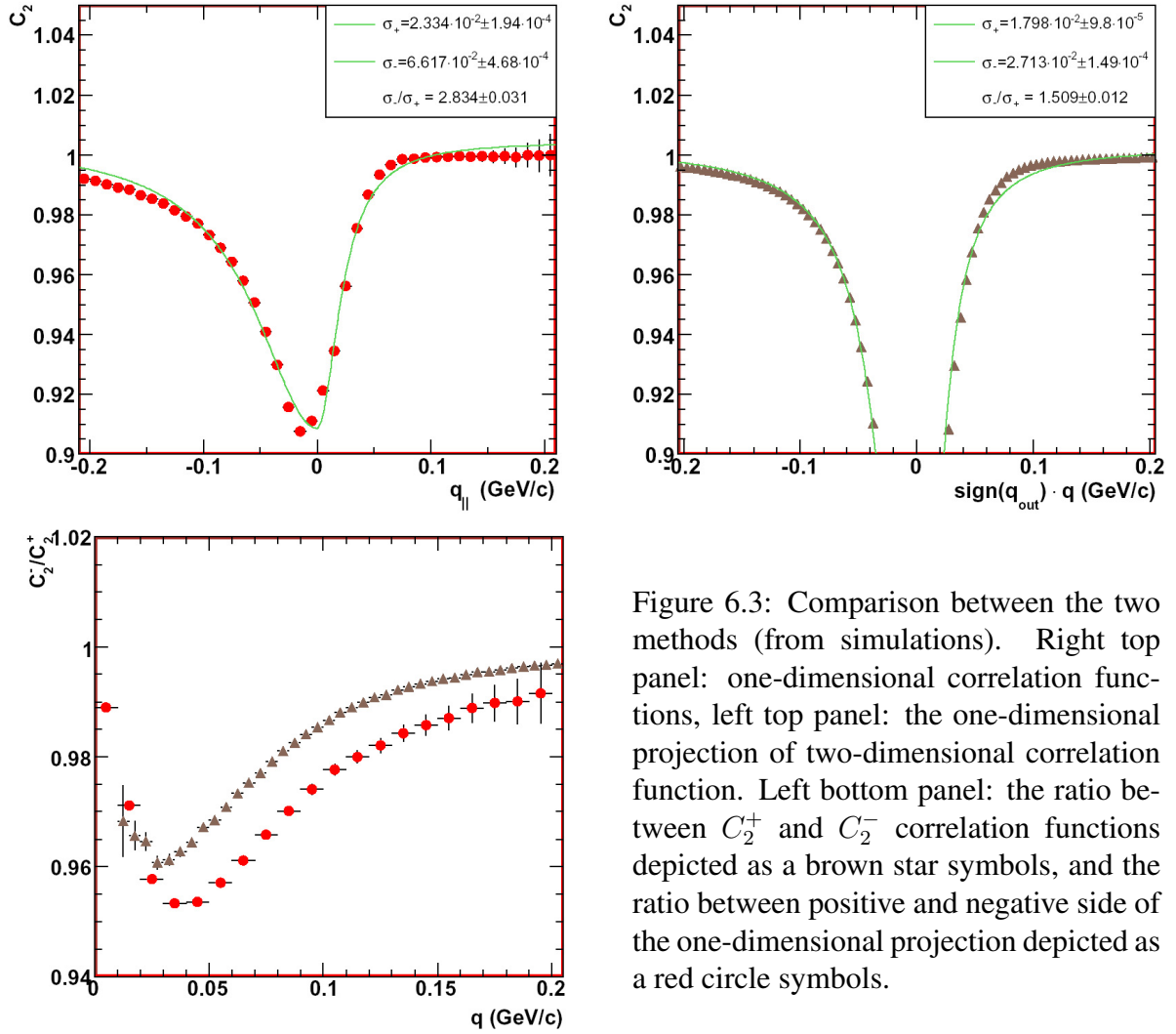


Figure 6.3: Comparison between the two methods (from simulations). Right top panel: one-dimensional correlation functions, left top panel: the one-dimensional projection of two-dimensional correlation function. Left bottom panel: the ratio between C_2^+ and C_2^- correlation functions depicted as a brown star symbols, and the ratio between positive and negative side of the one-dimensional projection depicted as a red circle symbols.

only the $q_{\perp} < 50$ MeV slice rather the entire space leads to larger statistical error bars. The quantitative comparison in terms of significance is presented in Table 6.2. The significance of the two-dimensional method is better by 40%. With the same procedure performed on the experimental correlation functions (see Fig. 6.4) this difference drops to about 8%. Inspecting Fig. 6.3 it can be seen that the fit by Eq. 8.3 did not entirely follow the shape of data points, therefore, it is foreseen to be use a two-dimensional fit instead of.

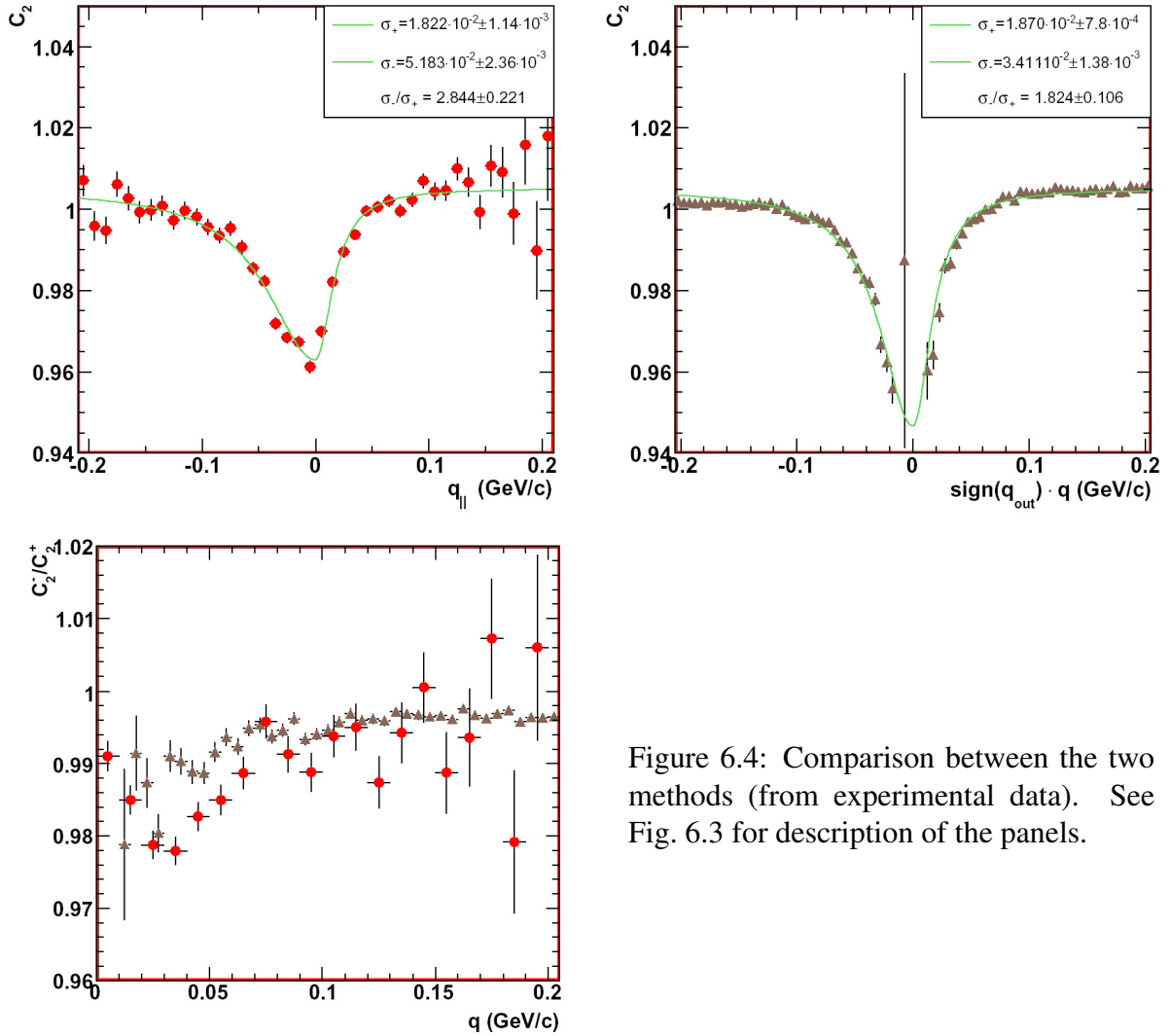


Figure 6.4: Comparison between the two methods (from experimental data). See Fig. 6.3 for description of the panels.

method	1 D	2 D
simulation	42	59
exp. data	8.35	7.77

Table 6.2: The significance of both methods.

6.3 Transverse Momentum Dependence

The displacement between the sources of different particle species from a system with collective expansion will arise naturally due to space-momentum and space-time correlation results in a collective velocity pointing outwards, added to the thermal velocities of the particles. The ve-

locity profile is such that the velocity is zero at the center (as it must be, for symmetry reasons) and maximum at the edge. To form a pion-proton pair with similar velocities a slow pion and a fast proton are needed, the latter coming preferentially from the edge of the fireball and thus profiting from a large velocity boost. This schematic explanation of the origin of the observed pion-proton asymmetry implies that the effect should disappear in the limit of zero pair momentum. The asymmetry as a function of the transverse momentum is shown in Fig. 6.5. The full symbols were obtained from the π^+ - p^+ (square) and from the π^- - p^+ (circle) correlations. The open triangles depicted the results of the unlike pion correlation functions. As expected from the symmetry consideration for the $P_\perp = 0$ the difference between emission time or emission position seems to vanish ($\mathcal{A} \rightarrow 1$). In order to study the asymmetry as a function of the displacement between particle sources a Monte-Carlo generator was used to translate \mathcal{A} values to the displacement expressed in femtometers. The description of the method used to translate between these two different variables and the obtained results are presented in Sections 7.4 and 8.3.

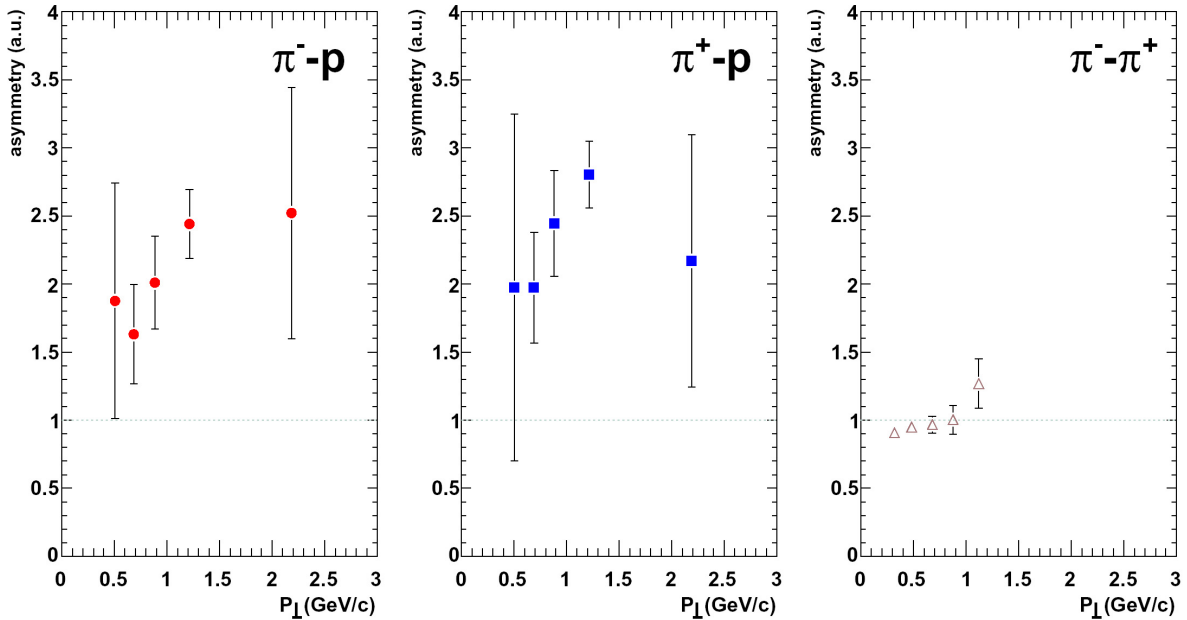


Figure 6.5: The source displacement as a function of the pair transverse momentum represented by the asymmetry variable.

Chapter 7

Monte Carlo

Monte Carlo techniques [RC04] are of great importance for the design and interpretation of experiments in nuclear and particle physics. They offer a possibility to simulate the behavior of physical systems and the response of detectors, and to verify analysis algorithms. In the analysis presented here, Monte Carlo methods were used to determine the Coulomb correction and to understand the impact of the experimental resolution of the HBT radii.

The full CERES Monte Carlo [Sl03, Yur06] is too slow to offer a sufficient statistics in a reasonable time scale for calculation of the two-particle correlation functions discussed in this dissertation. Therefore, a simple fast generator was created, which describes the Bose-Einstein correlations and the Coulomb interactions between particles, was used instead. The generated tracks were described by the four-vectors of the momenta and the positions. The source position of the track was generated according to a three dimensional Gaussian distribution in the rest frame of the pair with the width adjusted to fit the experimental HBT radii. The momentum of the generated track was sampled from a two-dimensional histogram of the experimental momentum vs. the polar angle, reflecting the acceptance of the CERES spectrometer (see Fig. 7.1). The azimuthal angle of the track was generated from an uniform distribution in the range of $(-\pi, \pi)$. In order to minimize the time necessary for accumulation of the required statistics the second track from a pair was generated within ± 0.2 rad of the first one. In contrast to the full CERES Monte Carlo the details of the single track efficiency were ignored; the single track efficiency cancels when normalizing to the event mixing.

In the three dimensional Gaussian, sampled to generate the position, the x , y , and z dimensions were related to R_{out} , R_{side} , and R_{long} , respectively. Therefore, the generated source positions of tracks were rotated according to

$$\begin{aligned} x' &= x \cdot \cos(\phi_{pair}) - y \cdot \sin(\phi_{pair}) , \\ y' &= y \cdot \cos(\phi_{pair}) + x \cdot \sin(\phi_{pair}) , \end{aligned} \tag{7.1}$$

where ϕ_{pair} corresponds to the orientation of the transverse pair momentum vector in the lab-

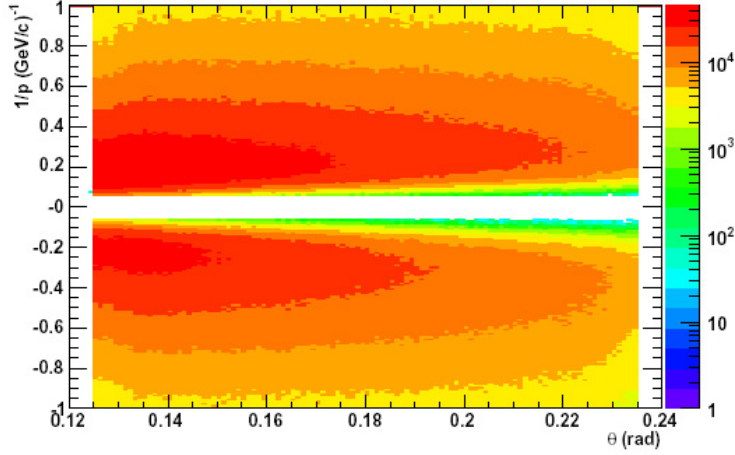


Figure 7.1: The distribution of tracks as a function of the inverse momentum and the θ angle obtained from the simulations.

oratory system. For each generated pair the Coulomb factor was calculated based on the quantum-mechanical description explained in Section 1.3.3. The HBT effect was embedded into the simulated correlation functions through the weight factors

$$C_{HBT} = 1 + \cos \left(\Delta E \cdot \Delta t - \vec{q} \cdot \vec{\Delta r} \right), \quad (7.2)$$

where ΔE , Δt , and $\vec{\Delta r}$ are the differences between the energies, the times, and the positions of the two tracks in a pair, respectively. The histograms for the signal distributions were filled with the weights described by a product of the HBT and the Coulomb correlation functions, and with the Coulomb weight factors for the identical and the non-identical two-particle correlations, respectively. The obtained correlation functions were subject to the analysis chain allowing to test the algorithms used. Moreover, based on the generated correlation functions different corrections to the measured correlation functions were derived as it is described in the following sections.

7.1 Coulomb Correlation Functions

The Coulomb interaction between the like-sign charge particles for small relative momenta significantly influences the Bose-Einstein correlations. The Coulomb correlation functions $C_{2,C}(q_{inv})$ were calculated based on the fast generator by averaging the Coulomb wave function squared over a spherical Gaussian source with $\sigma_t = 0$. This procedure was repeated for different Gaussian source sizes in bins of 0.5 fm. Examples of Coulomb correlation functions are shown in Fig. 7.2. These correlation functions were then used in the fit to the experimental identical pion correlation functions as described in Section 5.5.

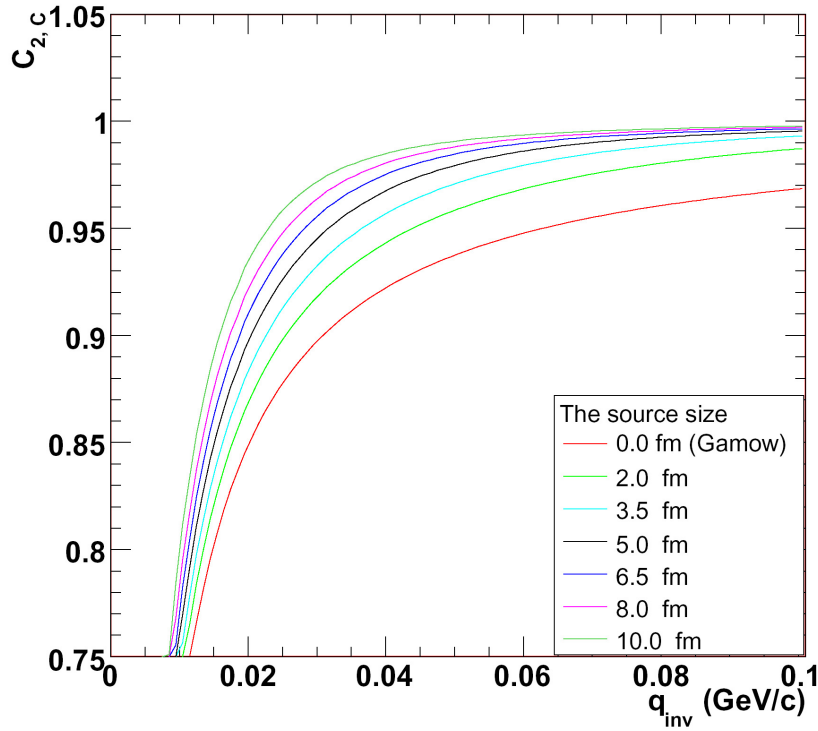


Figure 7.2: Coulomb correlation functions for different source sizes.

7.2 Momentum Resolution Influence on HBT Radii

The limited accuracy of the momentum reconstruction in the TPC, as discussed in Section 4.4, affects the measured correlation functions in the following way. The reconstructed momenta of the particles in a pair will differ from the real momenta of the particles by $\Delta \vec{p}_{1,2}$, where the index corresponds to a given particle in the pair. The peaks in the correlation functions will be lowered and broadened because of that. The broadening will lead to underestimating the HBT radii. The spatial resolution of the track can also significantly influence the measured HBT radii as it enters to calculation of the relative pair momentum via the emission angle. The effect of the finite momentum resolution was studied using the fast generator described above. The reconstructed momenta were smeared according to Eq. 4.2. The simulated angles of tracks were smeared with the momentum dependent widths of the θ and the ϕ angles derived from the matching parameterization described in Section 4.6. In Fig. 7.3 the results of three methods of estimating a correction factor for R_{out} are presented. The simplest one depicted, as a solid brown line, is based on the ratio between the two correlation functions obtained for the case of infinitely good (real) and experimental (meas) momentum resolution, respectively. This method allows to extract a correct factor only if the true HBT radius is known. The second method, depicted as dash curves, assume that the momentum resolution will broaden

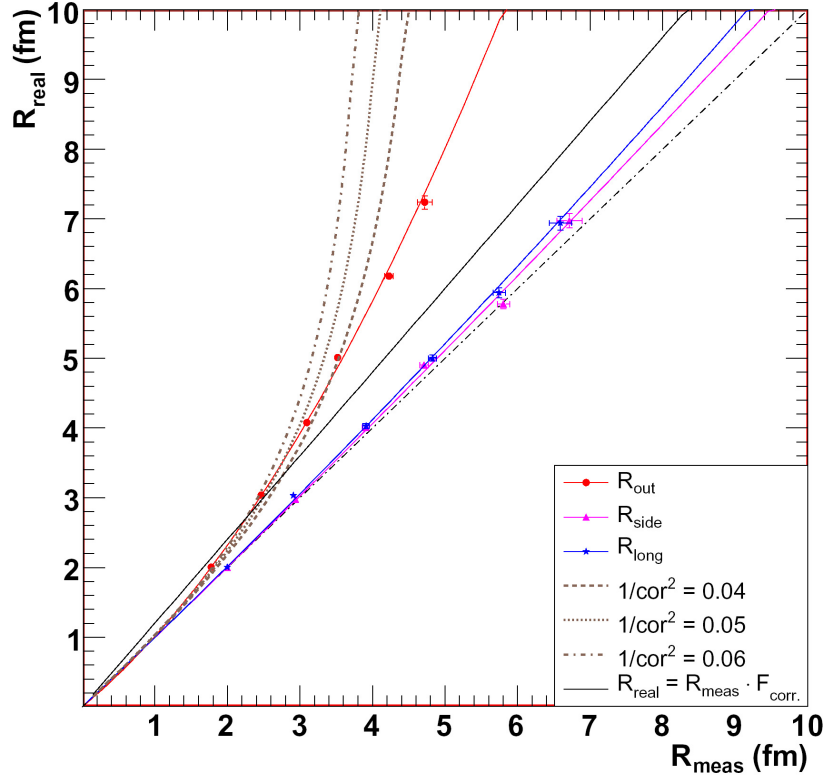


Figure 7.3: Comparison between different ways to remove the effect of the finite momentum resolution of detector on the HBT radii (pair P_{\perp} from 1 to 2 GeV/c).

the measured correlation functions by quadratically adding a constant term to the width. The relation between true radii and measured ones can be expressed by

$$\frac{1}{R_{real}^2} = \frac{1}{R_{meas}^2} + \frac{1}{corr^2}. \quad (7.3)$$

The best method of calculating the correction is based on the simulation of the two-particle correlation functions for real and measured case, respectively, for different source sizes. The dependence of R_{meas} is plotted as a function of R_{real} and then parameterized with a polynomial of second order. The simulated smeared radii R_{meas} as a function of the true radii are shown in Fig. 7.4 for different P_{\perp} bins. The worst resolution is obtained for the R_{out} radii which is dominated by pairs with small opening angle, with q_{out} given by the difference of the length of the momentum vectors. Therefore, the q_{out} component is directly sensitive to the momentum resolution and becomes more affected for increasing P_{\perp} since the momentum resolution is proportional to the p^2 . The influence of the detector resolution on the other two components of \vec{q} is less significant. The q_{side} is mainly determined by the opening angle between the two particles in pair. In the case of q_{long} the effect is reduced by boosting the pair from the

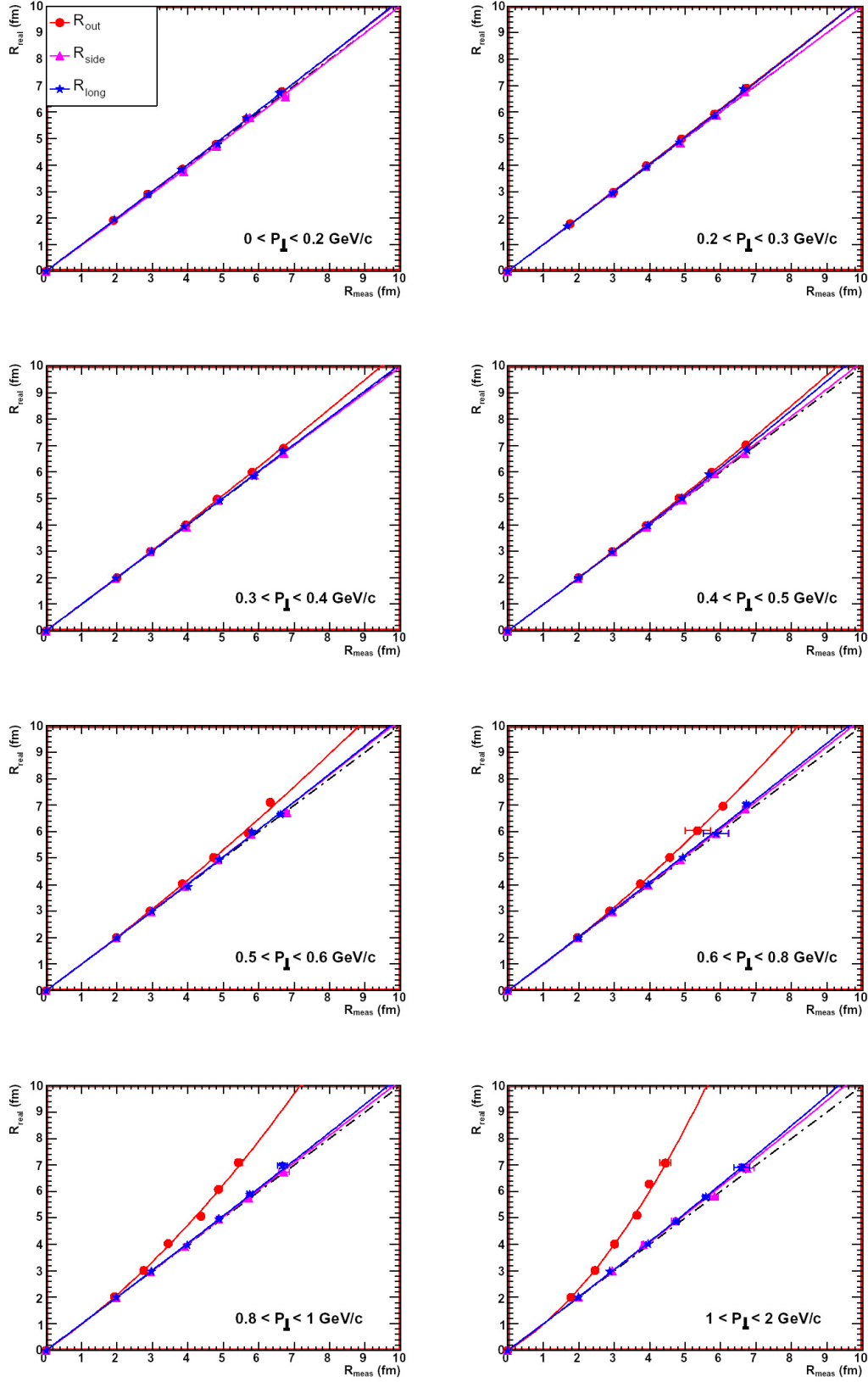


Figure 7.4: The influence of the finite momentum resolution on the measured $\pi^- - \pi^-$ HBT radii.

laboratory to the LCMS reference frame. All three radii were corrected using the polynomial parametrization described above.

7.3 Reaction Plane Resolution Influence on HBT Radii

The influence of the reaction plane resolution on the HBT radii, in the case of the azimuthally sensitive analysis, was studied based on the fast generator. The finite reaction plane resolution and the finite width of the $\phi_{pair} - \Psi_2$ bins reduce the measured oscillation amplitudes of HBT radii. Before these effects can be corrected for the reaction plane resolution must be known. The latter was studied using two methods and the results are presented in Section 4.7.3. In order to better understand the different variables used to present the results of the reaction plane resolution a simple generator of the reaction plane orientation was used. The reaction plane orientation angle was sampled from a uniform distribution within $(-\frac{\pi}{2}, \frac{\pi}{2})$. To simulate the subevent method, the two subevent reaction plane angles were calculated by smearing the original one according to Gaussian distribution with corresponding width, and the $\Psi_{SE2} - \Psi_{SE1}$ difference was calculated. The latter was used to calculate Eq. 4.19; at the same time the $dN/d(\Psi_{SE2} - \Psi_{SE1})$ distribution was filled. From the obtained distribution the $\frac{offset}{peak}$ ratio was calculated. In Fig. 7.5 both variables are plotted as a function of the reaction plane angular resolution expressed in degrees, providing a direct conversion between the variables used. Moreover, results of the experimental reaction plane resolution for different centrality classes are shown as black triangles in both plots. The σ_{RP} values of the points were taken

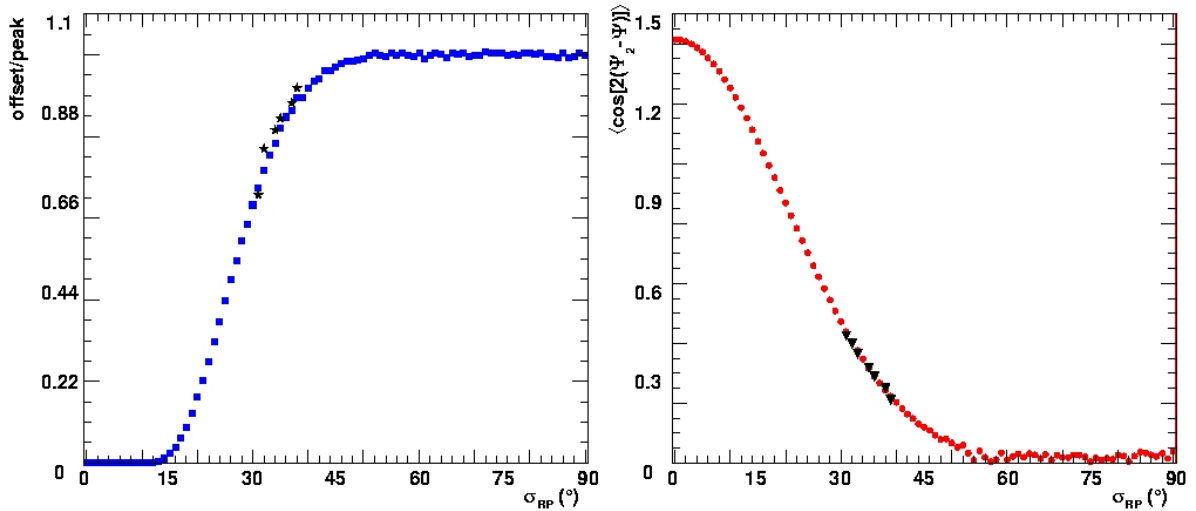


Figure 7.5: The simulation of the reaction plane resolution. The black symbols represent the reaction plane resolution of the CERES experiment.

from the width of Gaussian, fitted to the $dN/d(\Psi_{SE2} - \Psi_{SE1})$ distributions. The obtained angular resolution varies with the centrality between 31-39°.

The azimuthal dependence of the Hanbury-Brown Twiss radii was introduced into the generator based on the tilted source model proposed in [LHW00]. The generated source position of the track was rotated according to

$$\begin{aligned} x'' &= x' \cdot \cos(\Psi'_2) - y' \cdot \sin(\Psi'_2) , \\ y'' &= y' \cdot \cos(\Psi'_2) + x' \cdot \sin(\Psi'_2) , \end{aligned} \quad (7.4)$$

where Ψ'_2 is the generated angle of the reaction plane orientation, and $\langle x'^2 \rangle < \langle y'^2 \rangle$. This introduces a dependence of the generated radii on orientation of pairs with respect to the reaction plane. Within this model a consistent cross-check of the analysis algorithms was performed. Furthermore, the influence of the finite event plane resolution on the HBT radii was studied based on the generated correlation functions. In this method, it is expected that the oscillations of the radii are reduced due to the finite resolution of the event plane and the effect is studied by forming a superposition of sources misaligned to the generated event plane. One should note that this method treats the longitudinal radius as being $\phi_{pair} - \Psi_2$ independent. Moreover, it neglects the finite binning of the data in reaction plane orientation. The effect of such assumption will be discussed in Section 8.2.

The correlation radii generated from the constant source size ($R_x = 4$ fm, $R_y = 5$ fm, and $R_z = 7$ fm) derived for three different values of the reaction plane resolution are shown in Fig. 7.6. The radii unaffected by the event plane resolution ($R_{P_{res}} = 0^\circ$) are depicted as the full circles. The fit to the data is the sine (cosine) in the case of HBT radii (cross-terms). Two extreme cases of the event plane resolution, measured by the CERES experiment, are depicted as the open circles in the case of peripheral collisions ($30 - 40\% \sigma_{GEOM}$) and the full triangles depicted the results obtained for the central collisions ($0 - 2.5\% \sigma_{GEOM}$). From the fits results the correction factor $R_{smear}/R_{perf.}$ can be derived as the amplitude ratio between the HBT radii with and without event plane resolution. In Fig. 7.7 the derived values of the $R_{smear}/R_{perf.}$ ratio as a function of the reaction plane resolution are shown for three component of the Gaussian parametrization. The results obtained for the R_{out} (left panel), the R_{side} (middle panel), and the $R_{out-side}$ (right panel) were parameterized by the first order polynomial as depicted by the green line. While this parameterization does not describe results for $\langle \cos(n\Delta\Psi) \rangle$ larger then 0.8, it still seems to be realistic for the range of the reaction plane resolution measured by the CERES spectrometer. Therefore, the three components of the azimuthally sensitive Bertsch-Pratt parameterization were corrected with the factors derived from such parameterization.

As explained above, such intuitive procedure of the event plane resolution correction neglects all effects connected with the finite bin width used for the two-particle correlations analysis. The smearing of the correlation function by imperfect event plane reconstruction is expected to diminish the amplitudes of the oscillations in the transverse radii but the effect it has on a correlation function is truly present in the individual bins of the separate histograms from

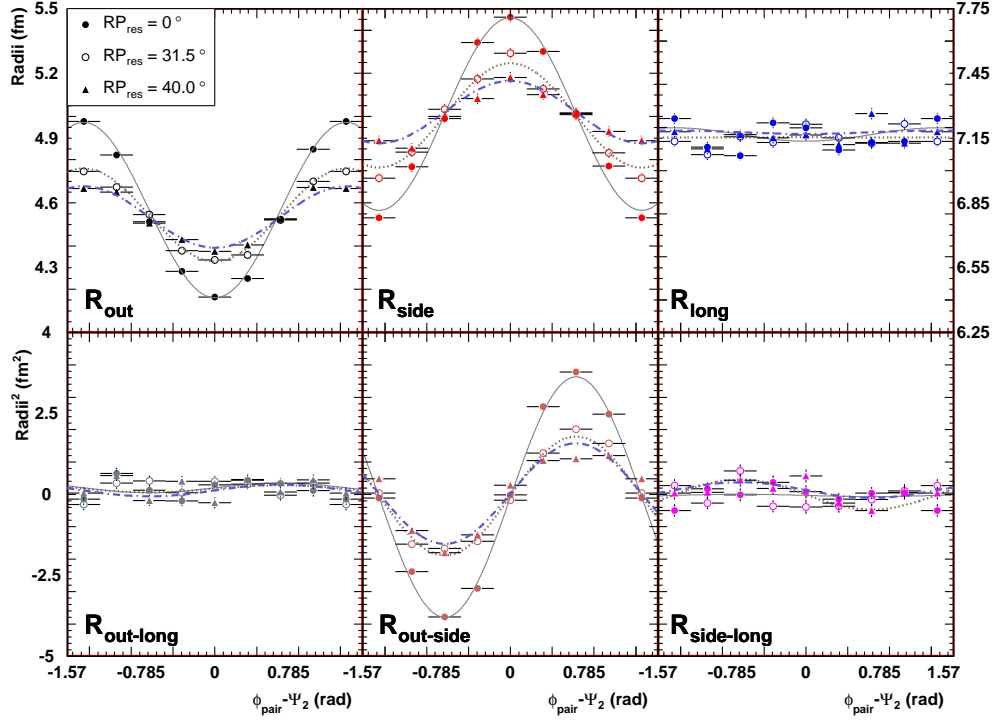


Figure 7.6: The influence of the reaction plane resolution on the HBT radii. The solid, dotted, and dash-dotted lines are fits to the three data sets.

the real and mixed pair distributions. The model-independent correction procedure proposed in [HHLW02] might be more appropriate. The effect of auto-correlation contributions to Ψ_2 was neglected during the analysis presented in this dissertation since this effect was found to be insignificant by the STAR experiment in [Col04].

7.4 Asymmetry of the Correlation and the Source Displacement

The measured non-identical two-particle correlation functions were parameterized using Eq. 8.3. The derived asymmetry parameter \mathcal{A} must be converted to distance before it can be compared to theoretical calculations. The relation between the source displacement and the asymmetry was studied using the fast generator explained at the beginning of this chapter. The shift between the pion and proton source positions was introduced by shifting proton freeze-out points

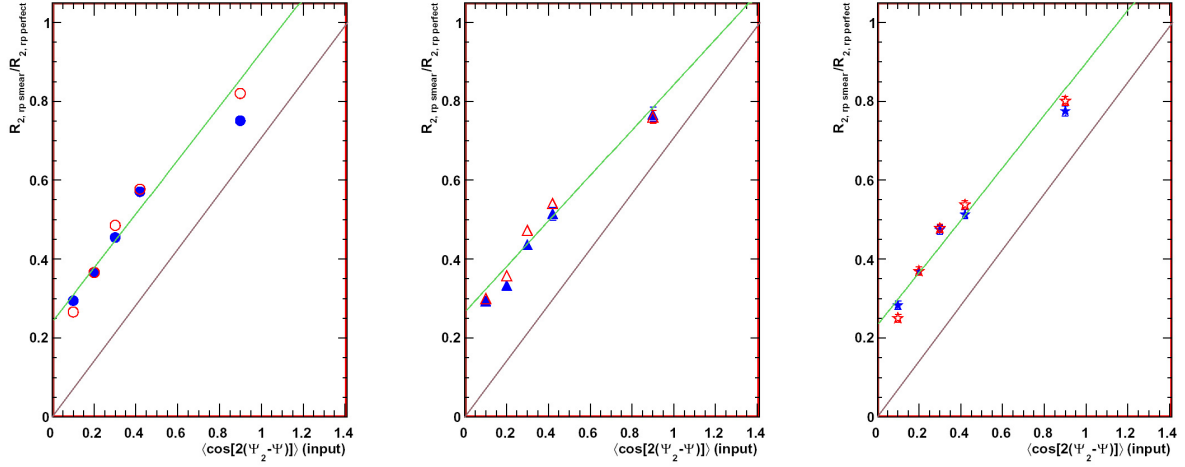


Figure 7.7: Correction factor for the reaction plane angular resolution. The full and the open symbols represent correction factors derived for the $\pi^-\pi^-$ and $\pi^+\pi^+$ correlation functions respectively.

by ΔR in the direction of the transverse pair momentum

$$\begin{aligned} x'' &= x' + \left(\frac{P_x}{P_\perp}\right) \cdot \Delta R, \\ y'' &= y' + \left(\frac{P_y}{P_\perp}\right) \cdot \Delta R, \end{aligned} \quad (7.5)$$

where ΔR is the shift, (P_x, P_y) is the pair transverse momentum, and $P_\perp = \sqrt{P_x^2 + P_y^2}$. Successively, the Coulomb weight factor was calculated and the histograms were filled, one with the Coulomb weight and the other with weight equal to one. The ratio of these two histograms was treated in the same way as the experimental correlation function yielding the asymmetry parameters \mathcal{A} as a function of the transverse pair momentum. At the same time, the influence of the momentum resolution and of the finite source size, as well as of the source rapidity, were studied. In Fig. 7.8 the impact of the momentum resolution on the asymmetry parameter is shown. The momentum of particles was smeared in the same manner as in the case of the identical two-particle correlations analysis. The finite momentum resolution diminishes the asymmetry, especially at a high pair transverse momentum. The influence of the momentum resolution was taken into account during the conversion from the \mathcal{A} parameter to distance. The impact of the source size on the asymmetry parameter for the P_\perp independent 6 fm displacement between pions and protons average source position is shown in Fig. 7.9. The simulated correlation functions had similar source size as the one measured in experiment. Until now, all considerations were based on the assumption of the emission source sitting at midrapidity. This assumption significantly simplifies the analysis but it does not reflect the physical situation during the heavy ion collisions. The influence of the static source hypothesis was studied by

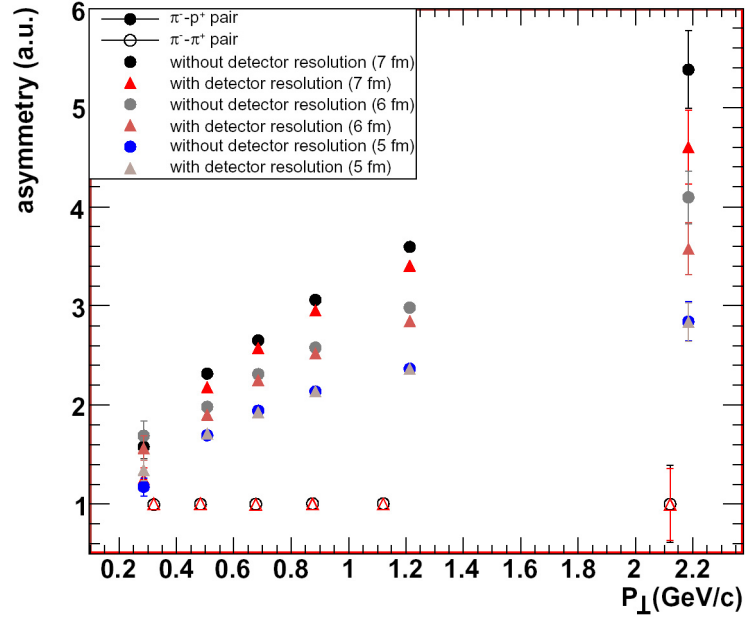


Figure 7.8: The momentum resolution influence on the asymmetry of the unlike particles correlation functions.

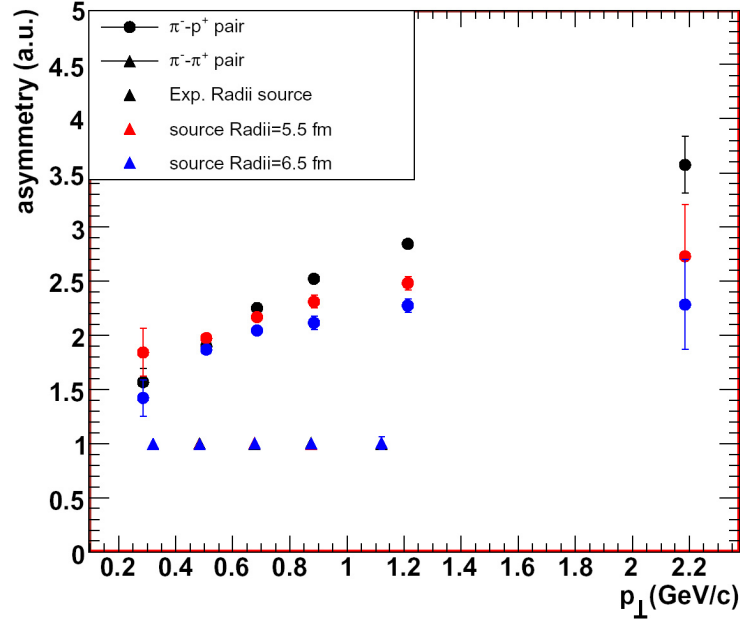


Figure 7.9: The asymmetry parameter dependence on the source radii as a function of P_{\perp} .

boosting the generated positions in the longitudinal and transverse directions (Fig. 7.10). The results were used to estimate the maximum systematic error of the analysis.

In Fig. 7.11 the values of the \mathcal{A} parameters as a function of the displacement in steps of 1 fm are shown for the six bins of P_{\perp} . For symmetry reasons all curves should go through (0,1). However, due to the limited acceptance of the CERES spectrometer, in the case of the pion-proton pairs with the transverse pair momentum between 0-0.4 (GeV/c) the presented parametrization deviates from this point. This uncertainty was included in the systematic error of the measurement for this point. The straight line fit to the points

$$\mathcal{A} = P_0 \cdot \exp(P_1 \cdot \Delta R) \quad (7.6)$$

was used to convert the \mathcal{A} parameter for a given P_{\perp} bin to the pion-proton displacement. The systematic error is calculated assuming no correlations between the two fit parameters. The resulting of displacements are compared to a Blast-Wave model and to hydrodynamical calculations in Sections 8.3.

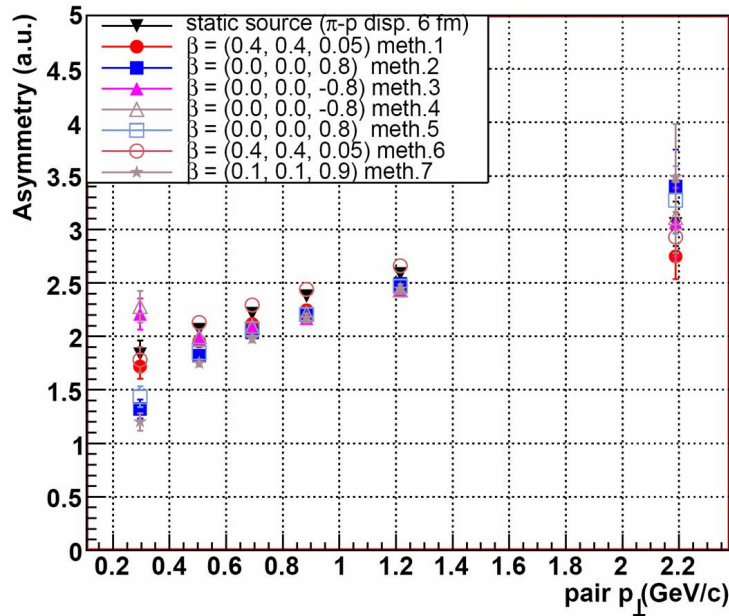


Figure 7.10: The asymmetry parameter deviation for different models of particle source emission.

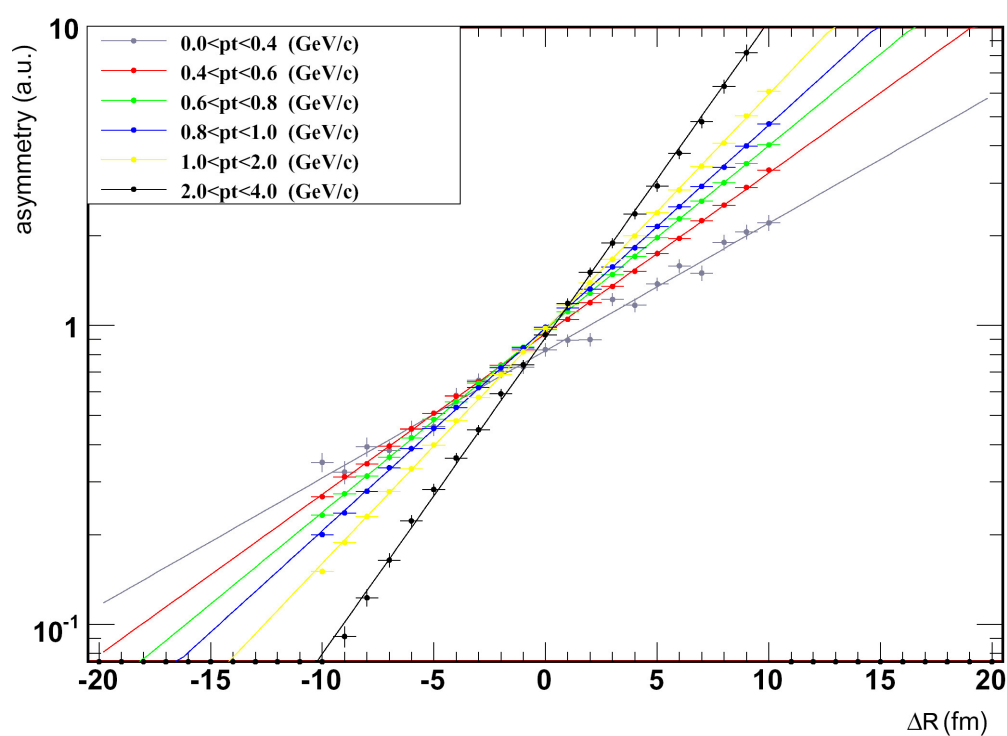


Figure 7.11: The asymmetry-to-displacement calibration.

Chapter 8

Discussion of the Results

In this chapter the results of the two-particle correlation analysis are discussed in the framework of a hydrodynamical model and the blast-wave parameterization. The Bose-Einstein correlations at a beam energy of 158 AGeV were analyzed as a function of centrality and in bins of pair rapidity and transverse momentum, as well as the azimuthal angle with respect to the reaction plane. The obtained results support a collision picture with longitudinal and transverse expansion. The individual dependences are discussed in detail below.

8.1 Transverse Momentum and Centrality Dependence of the HBT Radii

The space-time variances $\langle \tilde{x}_\mu \tilde{x}_\nu \rangle(\mathbf{P})$ depend on the pair momentum P . To understand their physical meaning, one can consider an observer who views a strongly expanding collision region. Some parts of the collision region move towards the observer and the particle spectrum emitted from those parts will appear blue-shifted. Other parts move away from the observer and appear red-shifted. Thus, if the observer looks at the collision system with a wavelength filter of some frequency, he sees only part of the collision region. Adopting a notion coined by Sinyukov, the observer sees a "region of homogeneity". In HBT interferometry, the wavelength filter is the pair momentum \mathbf{P} . The direction of the pair momentum vector corresponds to the direction from which the collision region is viewed, thus inspecting different collision regions. In the Gaussian approximation, the region of the homogeneity is described by a four-dimensional space-time ellipsoid centered around $\langle \tilde{x}_\mu \rangle(\mathbf{P})$ and characterized by the emission function $S(\mathbf{x}, \mathbf{P})$ (see Eq. 1.30). The widths of this regions of homogeneity correspond to the space-time variances $\langle \tilde{x}_\mu \tilde{x}_\nu \rangle(\mathbf{P})$, see Eq. 1.35. Thus, HBT radius parameters give access to the space-time variances $\langle \tilde{x}_\mu \tilde{x}_\nu \rangle(\mathbf{P})$ but they do not depend on the effective source center $\langle \tilde{x}_\mu \rangle$. In the terms of space-time variance with the infinitely long source with boost-invariant longitu-

dinal expansion Makhlin and Sinyukov [MS88] provided a connection between the measured HBT radii and the geometry of the collision region. In this model the R_{long} radii is determined by the inverse of the longitudinal velocity gradient meaning that it rather describes the longitudinal length of homogeneity in the source than the geometrical size. Expanding the exponent of the emission function $S(\mathbf{x}, \mathbf{P})$ presented in [WH99] (Eq.5.1) around $x_{\mu=0}$ and using the saddle point approximation one can parameterizes the transverse dynamical length of homogeneity by

$$\begin{aligned} R_{out}^2(P_{\perp}) &= R_{side}^2(P_{\perp}) + \frac{1}{2} \left(\frac{T}{M_{\perp}} \right)^2 \beta_{\perp}^2 \tau_0^2, \\ R_{side}^2(P_{\perp}) &= \frac{R_{GEOM}^2}{1 + \frac{M_{\perp}}{T} \eta_f^2}, \end{aligned} \quad (8.1)$$

where T is the freeze-out temperature, $M_{\perp} = \sqrt{m_{\pi}^2 + (P_{\perp}/2)^2}$, β_{\perp} is the mean transverse flow, η_f is the transverse flow rapidity of the source, and R_{GEOM} characterized the geometrical transverse size of the fireball freeze-out. This simple expressions illustrate several of the key concepts employed in HBT interferometry, namely, the overall size of the transverse radius parameters is determined by the transverse Gaussian widths of the collision region, and the difference $R_{out}^2 - R_{side}^2$ is proportionally to the emission duration $\beta_{\perp}^2 \langle \hat{t}^2 \rangle$. Moreover, the transverse radii are sensitive to the transverse flow rapidity of the source which imply that the HBT radius shrinks for finite η_f since a dynamically expanding source viewed through a filter of wavelength \mathbf{P} is seen only partial. This shrinking effect increases for larger values of the pair transverse momentum proportionally to the the ratio $\frac{\eta_f^2}{T}$. The P_{\perp} dependence of the R_{side} is a consequence of transverse position-momentum correlations in the source with here originate from the transverse collective flow. Moreover, for the scenario of a boost-invariant expansion in longitudinal direction, based on the saddle point approximation the R_{long} at rapidity $y = 0$ is given by [HB95]

$$R_{long}^2 = \tau_f^2 \frac{T}{M_{\perp}} \frac{K_2 \left(\frac{M_{\perp}}{T} \right)}{K_1 \left(\frac{M_{\perp}}{T} \right)}, \quad (8.2)$$

where τ_f the average freeze-out time, and K_1 and K_2 are the modified Bassel functions of order 1 and 2.

Before proceeding with studding the centrality and transverse momentum dependence, in Fig. 8.1 we compare the radii obtained for central collisions (0-5% of σ_{GEOM}) with those previously published [A⁺03a]. Slight discrepancies visible at the lower and the highest P_{\perp} can be attributed to the improved understanding of the Coulomb influence on the measured correlation functions and the two-track resolution, respectively.

The complete P_{\perp} -dependence of the identical-pion HBT radii for seven classes of centrality and Y range of (1.3-2.8) is shown in Figs.8.1-8.2.

8.1. TRANSVERSE MOMENTUM AND CENTRALITY DEPENDENCE OF THE HBT RADII 127

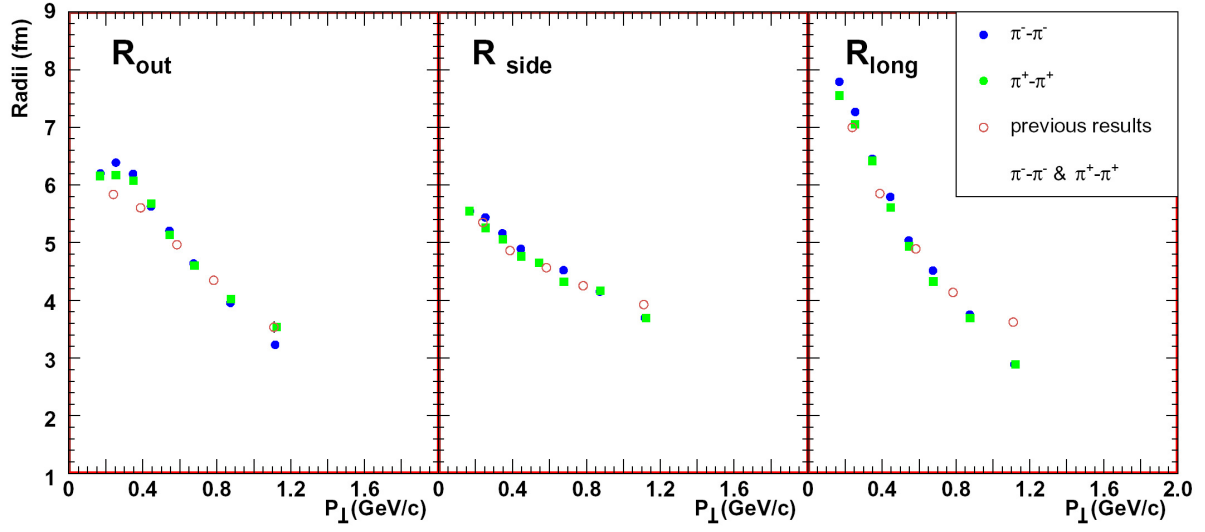


Figure 8.1: Previously obtained HBT radii for the most central events ($<5\%$ $\sigma/\sigma_{\text{GEOM}}$) [A⁺03a] together with the results presented in this work. Both results were corrected for the Coulomb interaction and the detector resolution.

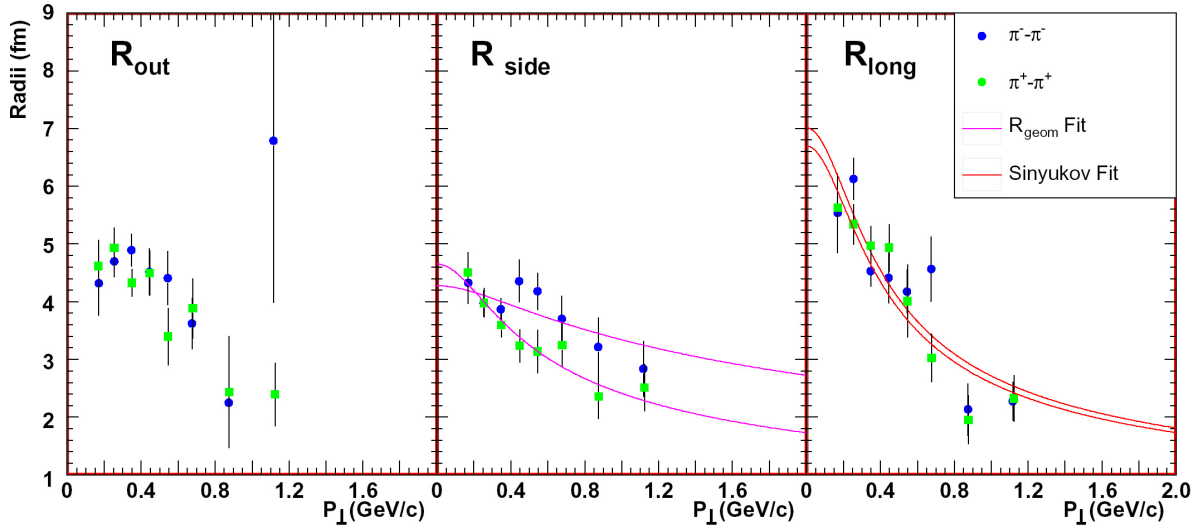


Figure 8.2: Transverse momentum dependence of the HBT radii corrected for the Coulomb interaction and detector resolution for centrality bin 25-35 %.

The R_{side} and R_{long} are fitted with Eq. 8.1 and Eq. 8.2. The results obtained from the hydro-inspired parameterization of the source expansion in the case of the R_{long} confirm the results of the previous CERES HBT analysis. The parameters derived from the fit of the Eq. 8.1 are

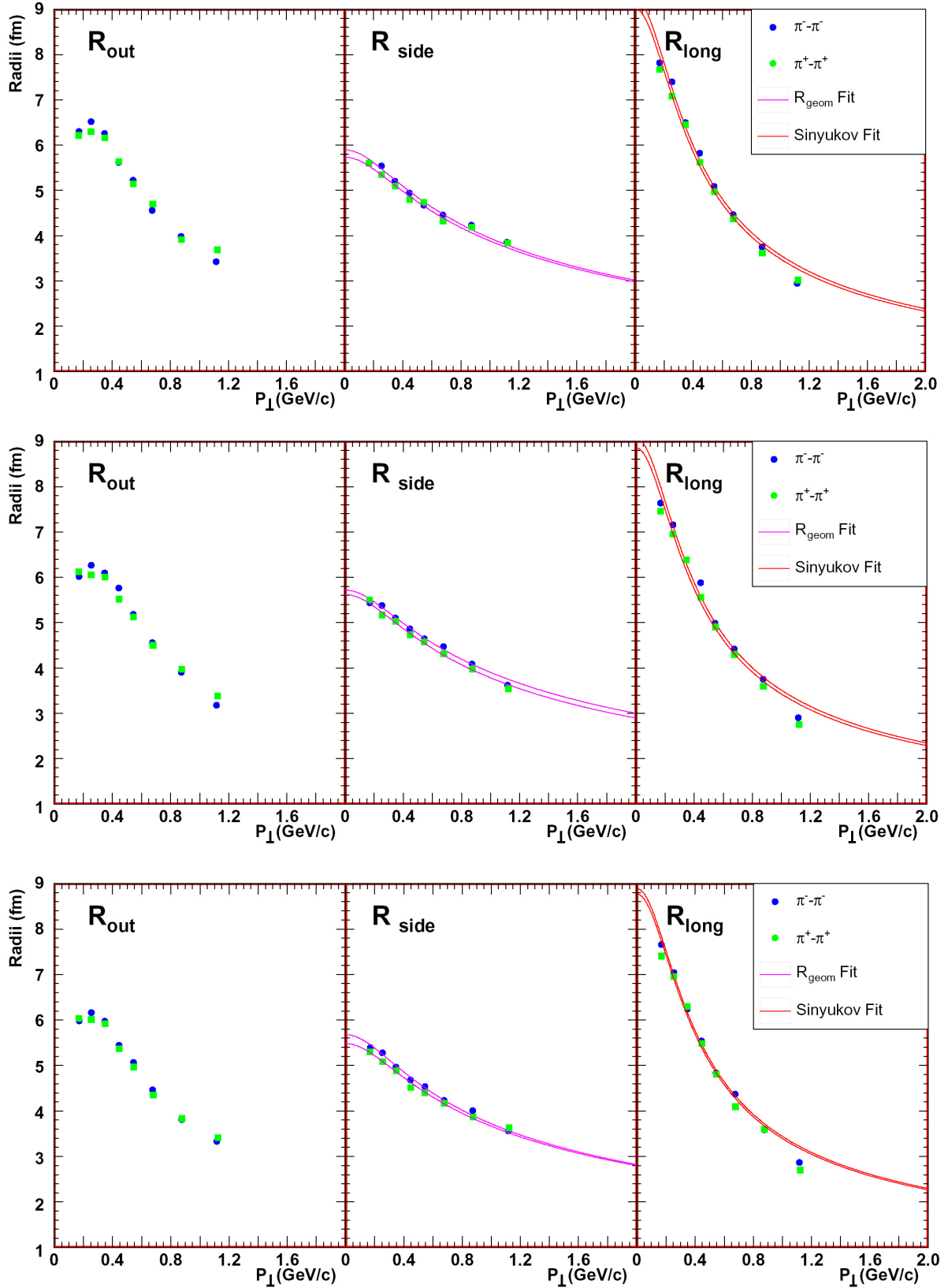


Figure 8.3: Transverse momentum dependence of the HBT radii corrected for the Coulomb interaction and the detector resolution. The top, the middle, and the bottom panel show the radii obtained for the centrality of 0-2.5 %, 2.5-5 %, and 5-7.5 %, respectively.

8.1. TRANSVERSE MOMENTUM AND CENTRALITY DEPENDENCE OF THE HBT RADII 129

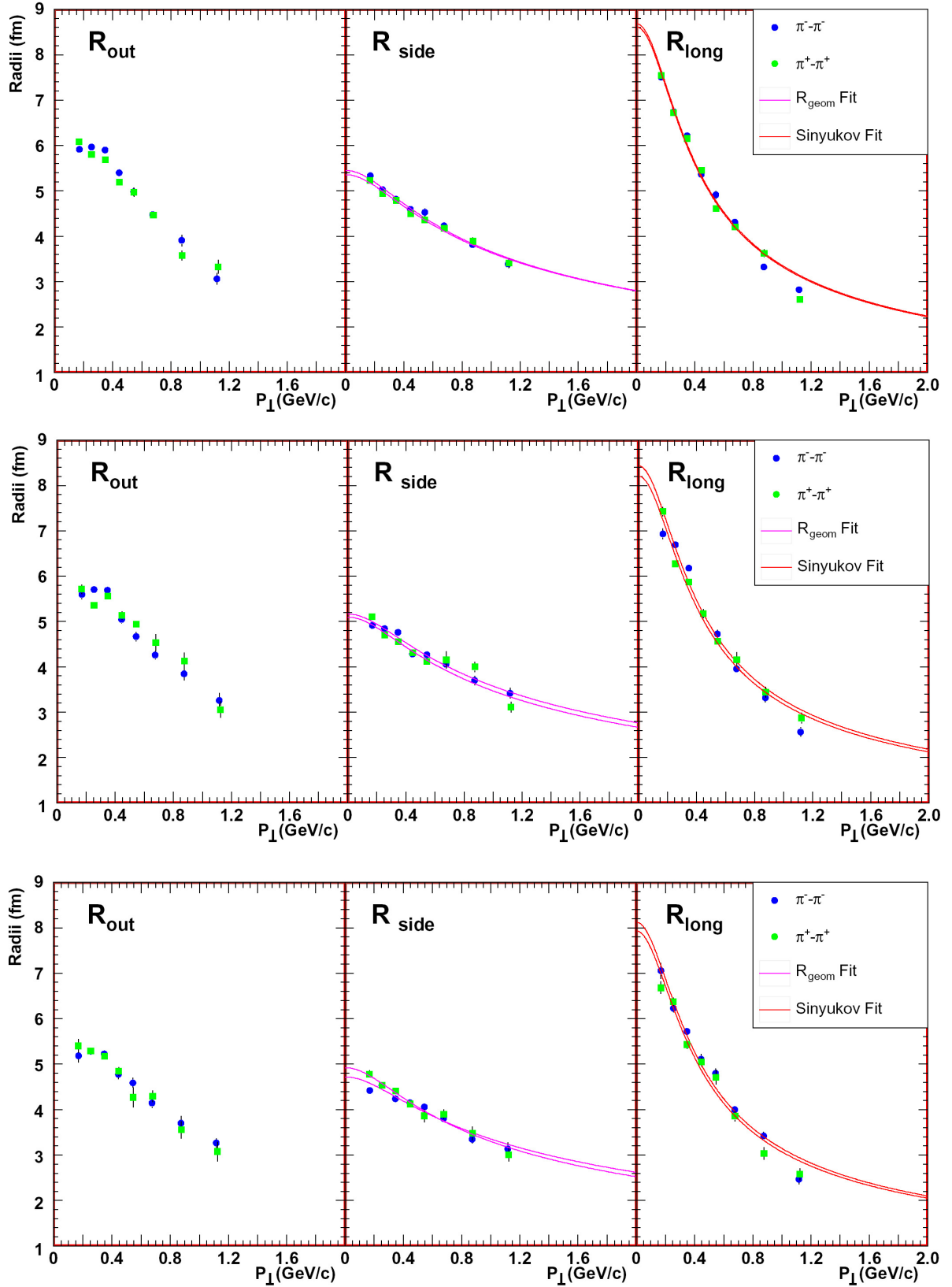


Figure 8.4: Transverse momentum dependence of the HBT radii corrected for the Coulomb interaction and the detector resolution. The top, the middle, and the bottom panel show the radii obtained for the centrality of 7.5-10 %, 10-15 %, and 15-25 %, respectively.

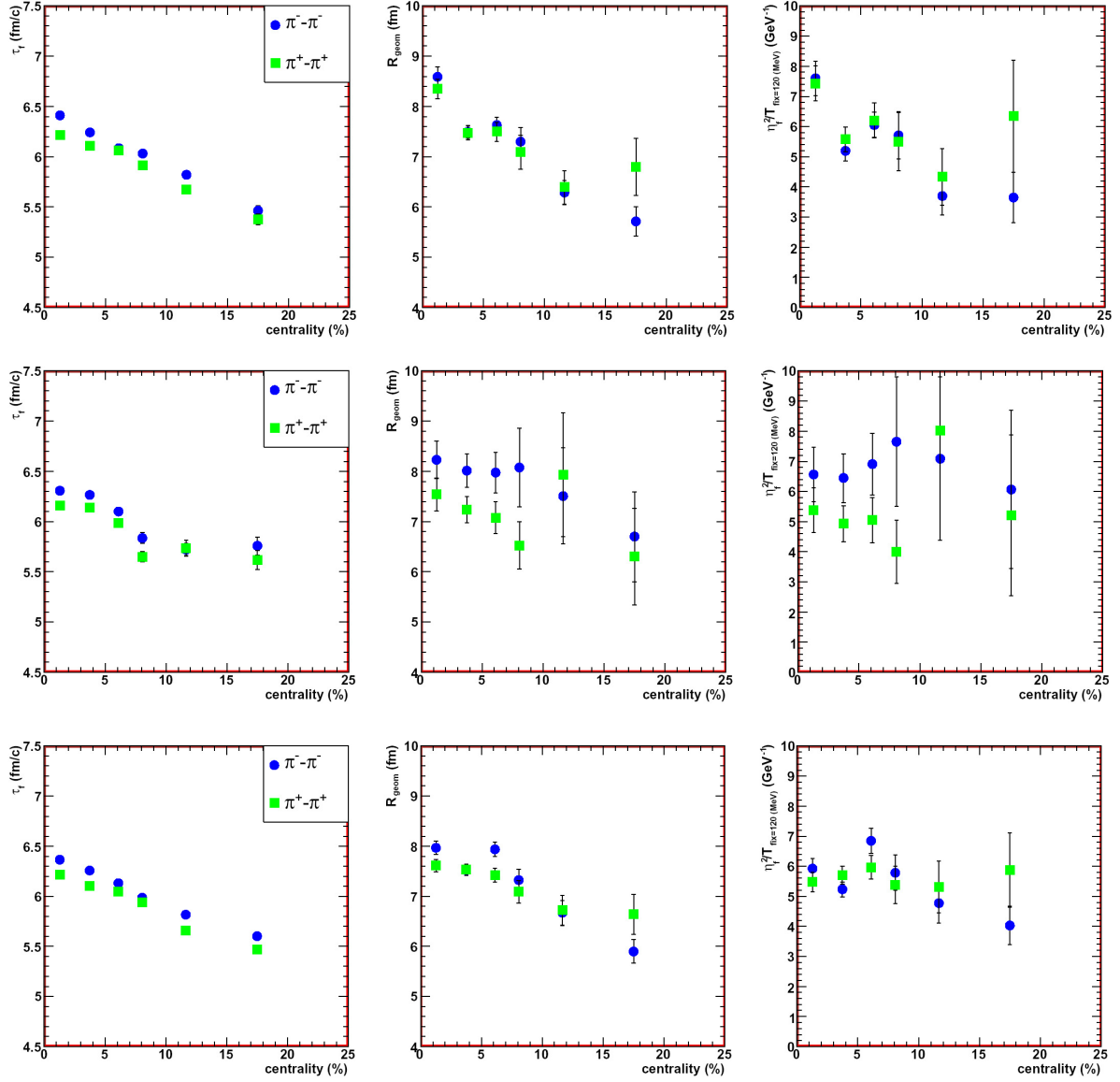


Figure 8.5: The extracted parameters of the emitting source based on the hydrodynamical scenario for three rapidity intervals. All results were obtained for a fixed freeze-out temperature of 120 MeV. Top panel: $Y = 1.3-2.3$. Middle panel: $Y = 2.3-2.8$. Bottom panel: $Y = 1.3-2.8$.

slightly above previous results, however, this can be attributed to the different rapidity selection used in both analysis. The results of the fits are compiled in Fig. 8.5.

8.2 Azimuthally Sensitive HBT Analysis

The dependence of the HBT radius on the azimuthal orientation with respect to the reaction plane $\Phi = \phi_{pair} - \Psi_2$ was fitted by [HHLW02]

$$\begin{aligned}
 R_{out}^2(P_\perp, \Phi) &= R_{out,0}^2(P_\perp) + 2R_{out,2}^2(P_\perp) \cos(2\Phi) \\
 R_{side}^2(P_\perp, \Phi) &= R_{side,0}^2(P_\perp) + 2R_{side,2}^2(P_\perp) \cos(2\Phi) \\
 R_{long}^2(P_\perp, \Phi) &= R_{long,0}^2(P_\perp) + 2R_{long,2}^2(P_\perp) \cos(2\Phi) \\
 R_{out-side}^2(P_\perp, \Phi) &= R_{out-side,0}^2(P_\perp) + 2R_{out-side,2}^2(P_\perp) \sin(2\Phi) \\
 R_{out-long}^2(P_\perp, \Phi) &= R_{out-long,0}^2(P_\perp) + 2R_{out-long,2}^2(P_\perp) \sin(2\Phi) \\
 R_{side-long}^2(P_\perp, \Phi) &= R_{side-long,0}^2(P_\perp) + 2R_{side-long,2}^2(P_\perp) \sin(2\Phi) .
 \end{aligned} \tag{8.3}$$

The 0^{th} -order Fourier coefficient coincides with the HBT radii from an azimuthally-integrated analysis while the 2^{nd} -order Fourier coefficient corresponds to the magnitude of the emission source asymmetry. In Fig. 8.6 the normalized 2^{nd} -order Fourier coefficients are shown as a function of centrality.

If the pion source were to reflect the initial collision geometry (almond shape out-of-plane) a positive $R_{side,2}$ and a negative $R_{out,2}$ should be expected. While $R_{out,2}$ seems to be negative indeed, $R_{side,2}$ is consistent with zero (Fig. 8.6). $R_{long,2}$, for which in first order no effect is expected, behaves similarly to $R_{out,2}$. Systematic checks revealed that the 2^{nd} -order Fourier coefficients are strongly affected by details of the event mixing procedure, particularly by the requirement that the two events should have a similar orientation of the reaction plane. This requirement controls small oscillations in the flat parts of the correlation function, visible in the two-dimensional projections of the correlation functions (Fig. 8.7), and possibly via them the second Fourier component of the correlation radii. Performing the event mixing in bins of 15° rather than 45° makes the small oscillation less dependent on the orientation with respect to the reaction plane and brings the second Fourier component of the R_{out} and R_{side} closer to zero (square in Fig. 8.6) With this, the observed pion source seems to be round in the transverse plane within the measurement errors. This is surprising because both at lower [Col00] and higher [Col04] beam energies asymmetric sources were observed. In Fig. 8.8 the results of the normalized 2^{nd} -order Fourier coefficients derived for different beam energies is shown.

8.3 Pion-Proton Source Displacement

The measured asymmetry of the correlation functions for pion-proton, discussed in Section 6, indicate that the pions and protons are not emitted from the same average space-time point. The unlike-sign pion correlations, on the other hand, do not show significant asymmetry. This

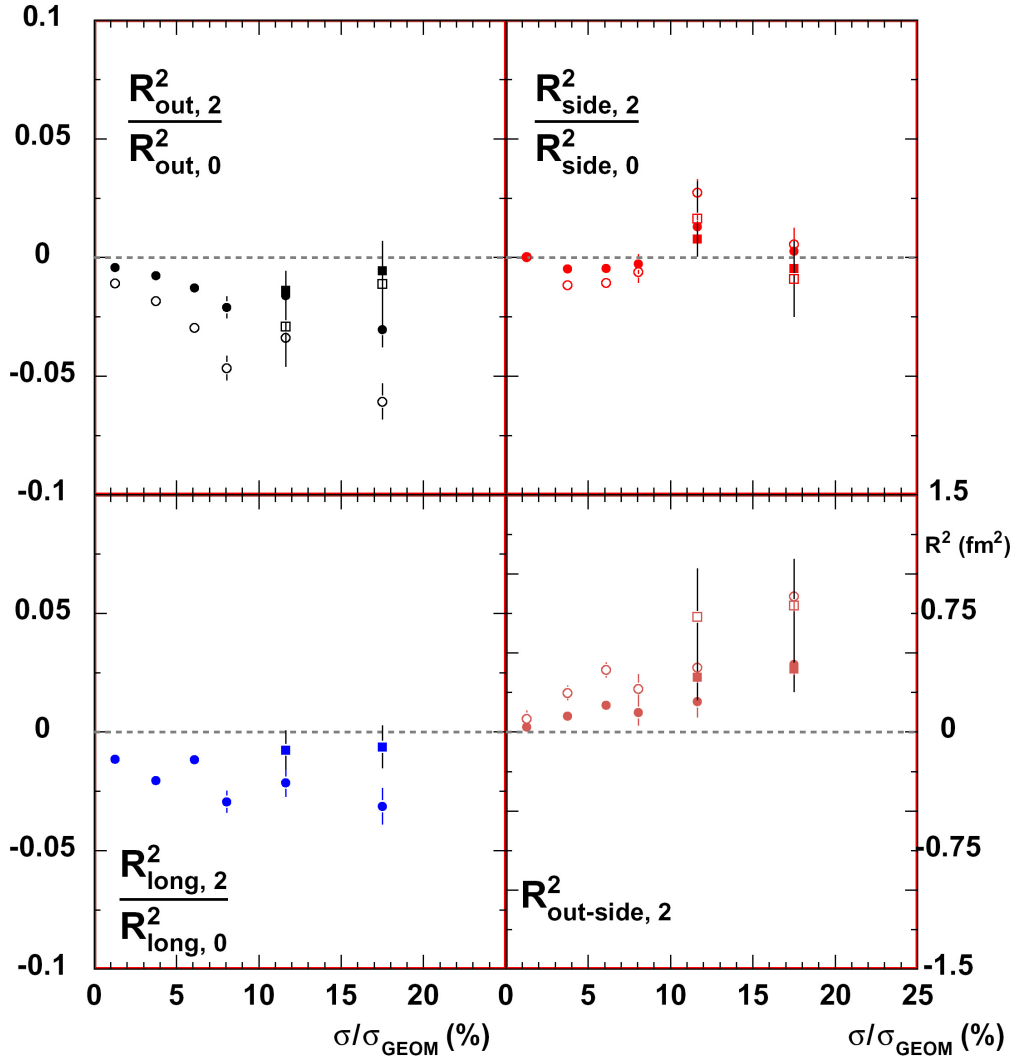


Figure 8.6: Fourier coefficient of azimuthal oscillations of HBT radii as a function of the event centrality for π^+ and π^- pairs combination (0.0-2.0 GeV/c). The close (open) symbols correspond to the uncorrected (corrected) 2^{th} -order Fourier coefficient for influence on finite reaction plane resolution. The squared symbols correspond to the results obtained with the different approach of the event mixing background construction (see text).

indicates that the effect is related to the particle mass. The parameterization presented in Section 7.4 was used to convert the measured asymmetry \mathcal{A} of the correlation functions to the spatial separation between the particles at freeze-out. The conversion was performed assuming similar emitting source size as well as the finite momentum resolution. The assumption of the emission source sitting at midrapidity was included in the systematic error of the measurement.

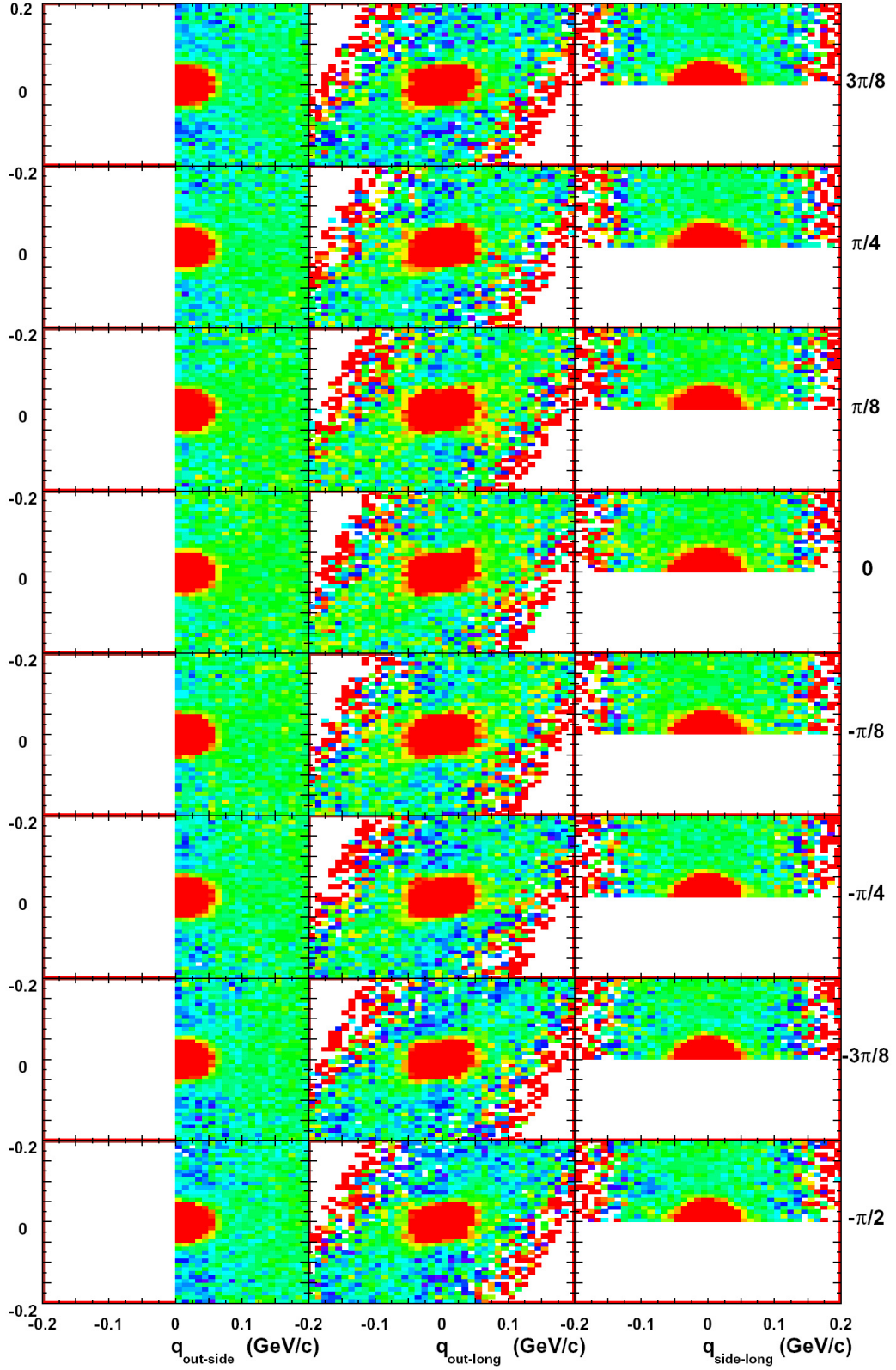


Figure 8.7: The two-dimensional HBT correlation functions as a function of the $\phi_{\text{pair}} - \Psi_2$ angle. The z -axis is set to be constant for all bins of $\phi_{\text{pair}} - \Psi_2$ ($0.985 \geq z \geq 1.035$).

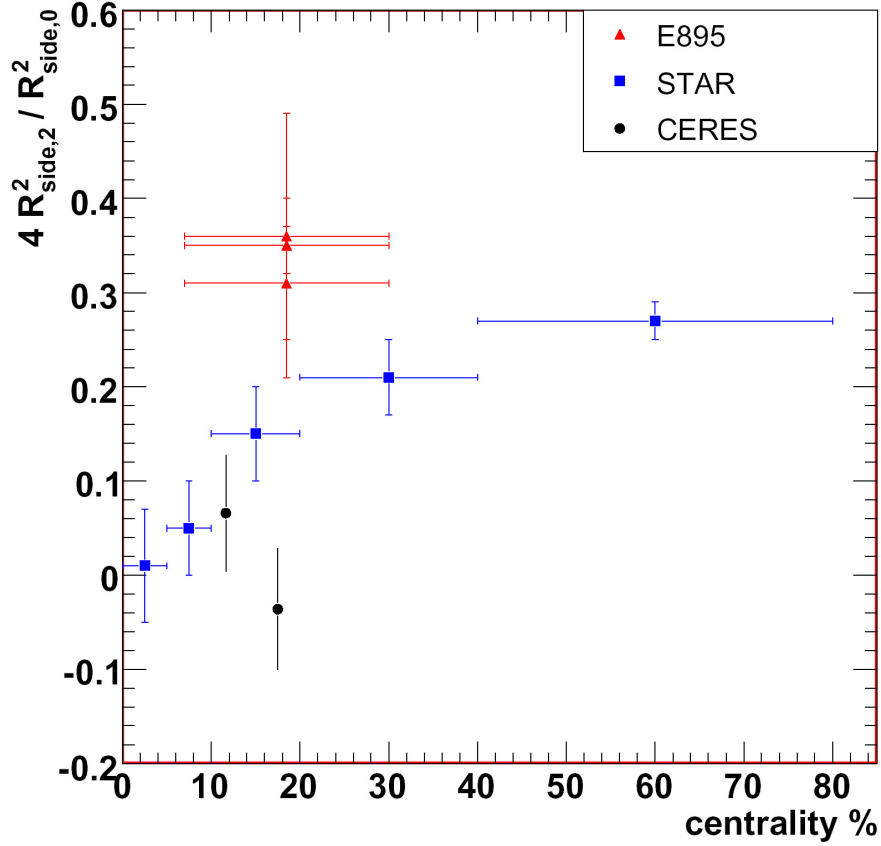


Figure 8.8: The centrality dependence of the source anisotropy measured for different beam energies.

In Fig. 8.9 the source displacement as a function of the pair transverse momentum for three different pair combinations are shown. The similarity between the π^+p and π^-p results indicates that the Coulomb interaction with the positive charged fireball is negligible, consistent with the fact that the spectra of the corresponding particles are in good agreement [AftSC04].

The asymmetry between pion-proton space-time emission, generated by the UrQMD model [BZS⁺99] which produces radial flow through hadronic rescattering, is shown in Fig. 8.9 as green curves. The model predicts the dominance of the spatial part of the asymmetry generated by large transverse flow. Thus, the pion-proton separations were calculated assuming only the displacement in *out* direction. The results of such calculation are in agreement within the results obtained for asymmetry measured by experiment.

The observed increase of \mathcal{A} with the pair transverse momentum ($\beta_\perp = P_\perp/M_\perp$), starting from zero due to symmetry reasons, can be parameterized as proposed by Lendnický and Sinyukov in [Led04, SVA96]. Assuming the longitudinal-boost invariance, a linear non-

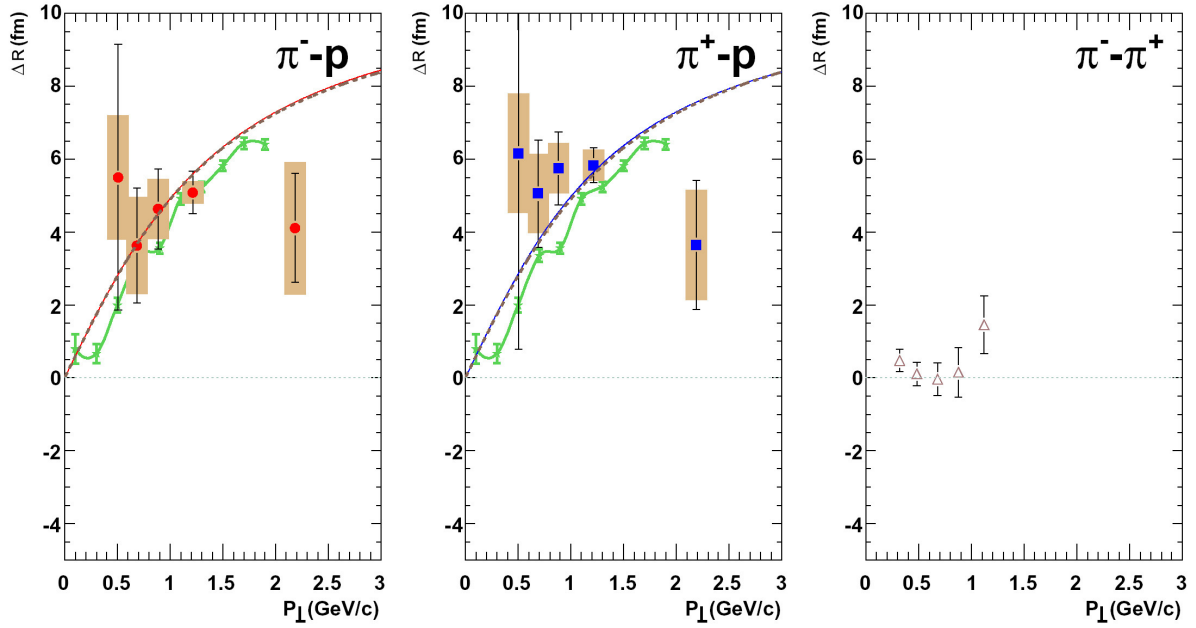


Figure 8.9: The source displacement ΔR as a function of the pair transverse momentum. The full symbols correspond to asymmetry obtained from the $\pi^+ - p^+$ (square) and from the $\pi^- - p^+$ (circle) correlation functions, respectively. The obtained results of the source displacement between $(\pi - p^+)$ from the UrQMD (ver.1.3) are shown as a solid curve (green). The open triangles represent results derived for the unlike pion correlation functions. Fit to the data is based on Eq. 8.4 (see text).

relativistic transversal flow profile $\beta_F = \beta_0 \frac{r_\perp}{R_{GEOM}}$, the local thermal momentum distribution characterized by the kinetic freeze-out temperature T and Gaussian density profile $\exp(-r_\perp^2/(2R_{GEOM}^2))$, one expects a rise of ΔR with the transverse pair velocity

$$\Delta R = \frac{R_{GEOM} \beta_\perp \beta_0}{\beta_0^2 + T/M_\perp}. \quad (8.4)$$

The mean transverse velocity is defined as

$$\beta_\perp = \frac{1}{\sqrt{1 + \left(\frac{m_\pi + m_p}{P_\perp}\right)^2}}, \quad (8.5)$$

and M_\perp is the pair transverse mass, defined as

$$M_\perp = \sqrt{\sqrt{m_\pi^2 + \frac{m_\pi}{m_p + m_\pi} \cdot \left(\frac{P_\perp}{2}\right)^2} \cdot \sqrt{m_p^2 + \frac{m_p}{m_\pi + m_p} \cdot \left(\frac{P_\perp}{2}\right)^2}}, \quad (8.6)$$

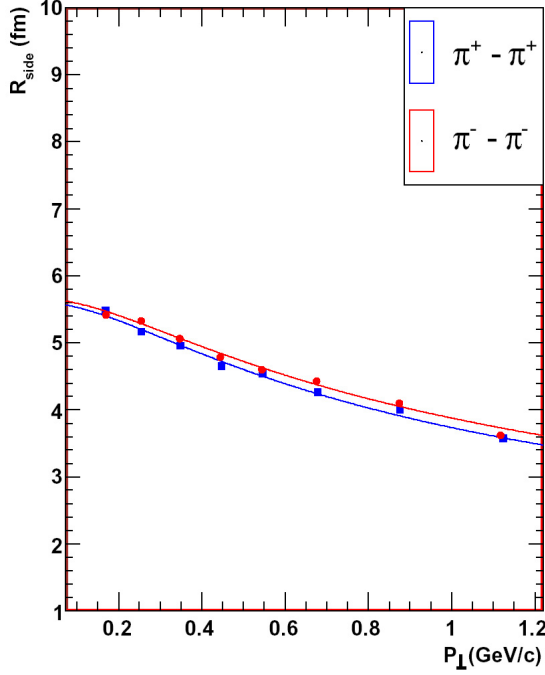


Figure 8.10: The R_{side} fitted by Eq. 8.4 together with ΔR . Presented radii were integrated over the centrality range (0-25%) and the HBT radii were derive.

where m_π and m_p are mass of pion and proton, respectively.

The derived ΔR P_\perp -dependence of the same- and the opposite-sign pion-proton pair correlations were fitted by Eq. 8.4 and the results are shown as the red and blue curves, respectively. Simultaneously the P_\perp -dependence of the HBT radius, R_{side} , derived from the two-particle correlations analysis for $\pi^+\pi^+$ and $\pi^-\pi^-$, were fitted with Eq.8.1 (see Fig 8.3). Assuming a common kinetics freeze-out temperature T , geometric transverse size of the fireball at the freeze-out R_{GEOM} and the transverse flow rapidity η_f

$$\eta_f = \frac{1}{2} \log \frac{1 + \beta_0}{1 - \beta_0} \quad (8.7)$$

it is possible to extract from both measurements all common parameters. The transverse collective flow which causes the P_\perp -dependence of R_{side} is at this same time responsible for the different space-time emission of various particle species. The dash brown curve in Fig. 8.9 represent the simultaneous fit to the all four results (asymmetry and R_{side} dependences) results in the common fit parameters to both charges. In Table 8.1 the collection of the fit parameter derived from presented parameterization are gather. In Fig. 8.11 the contour of χ^2 as a function of the fit parameters R_{GEOM} , β_0 , and T . It is worthy of notice that depending on the charge combination of the two-particles correlations the slightly different fit values are preferred.

The results of the hydro-inspired blast wave parameterization are presented in the next section.

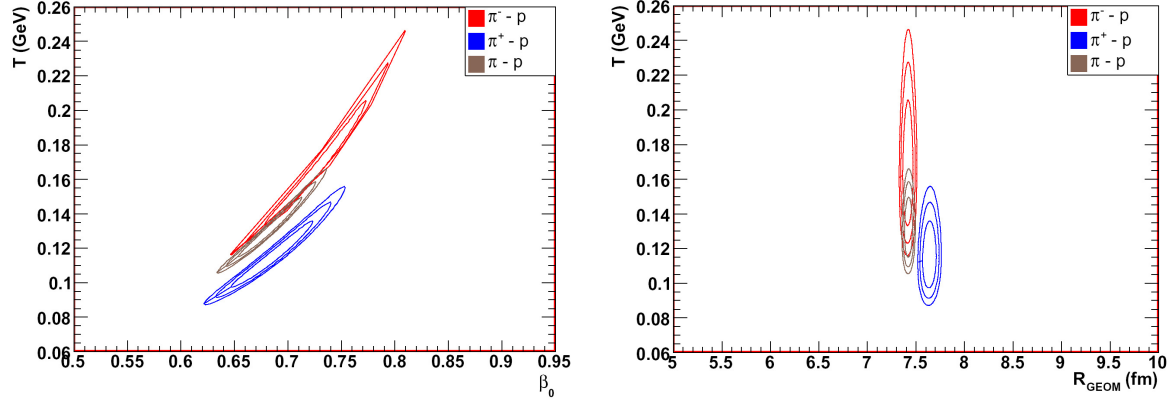


Figure 8.11: The $1\text{-}3\sigma$ contours plots of χ^2 , obtained by simultaneous fit of Eq. 8.4 to ΔR and R_{side} .

Fit par.	$\pi^+ - p$	stat. err.	$\pi^- - p$	stat. err.	$\pi - p$	stat. err.
β_0	0.695	0.007	0.655	0.006	0.663	0.004
$R_{GEOM}(fm)$	7.638	0.07	7.412	0.052	7.421	0.04

Table 8.1: The collection of fit results obtained for $T_f = 120$ MeV.

8.4 Hydrodynamics and Blast Wave Model Parameterization

The hydrodynamical models will describe the evolution of a collision system only when the time scales of the microscopic processes within the system are significantly smaller than the time scale of the macroscopic evolution of the system. In heavy ion collisions this implies that the average time between two successive interactions between partons is much smaller than the life time of the system, and leads to the thermalization of the system. Once the system is in equilibrium the hydrodynamical formalism can be applied.

In this section the CERES results obtained from the hadrons analysis in the top central 7% are presented together with the hydrodynamical calculations performed by P. Huovinen [KHHH01]. The calculations were performed in 2+1 dimensions assuming a boost-invariant longitudinal flow. The initial conditions were fixed via a fit to the p_\perp spectra of negatively charged particles and protons in Pb+Pb collisions at the top SPS energy [KSH99]. The equation of state which is an integral part of hydrodynamical calculations assumed the 1-st order phase transition to the QGP at the critical temperature of $T_c = 165$ MeV. The presented calculations were obtained for the freeze-out temperature of 120 MeV. In Fig. 8.4 the single transverse momentum spectra of all negative hadrons for two bins of rapidity ($Y_1 = \langle 2.1 \rangle$ (black points), $Y_2 = \langle 2.6 \rangle$ (blue points)) and of neutral kaons are shown together with the hydrodynamical calculations (red

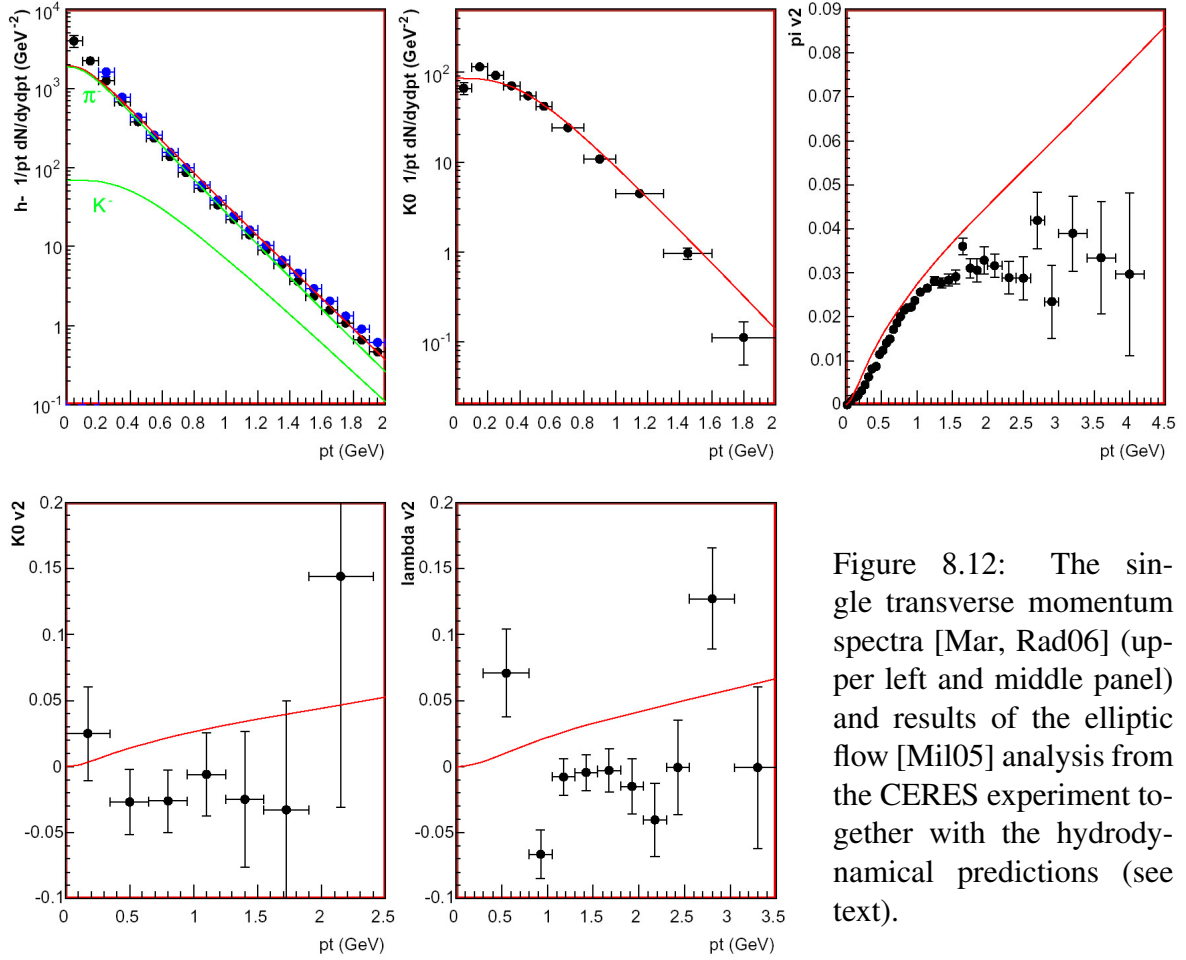


Figure 8.12: The single transverse momentum spectra [Mar, Rad06] (upper left and middle panel) and results of the elliptic flow [Mil05] analysis from the CERES experiment together with the hydrodynamical predictions (see text).

curves). The elliptic flow of charged pions, neutral kaons, and hyperons is presented as well. The comparison between the HBT radii and the hydrodynamical calculations of the source size based on the space-time variances are shown in Fig. 8.4. While the single particle transverse momentum spectra are rather well described the calculation fails in the case of two-particle correlations. The R_{side} parameter is underestimated and R_{out} and R_{long} are overestimated. This kind of discrepancy was observed for the first time at RHIC and for some time it was believed to be specific to this energy range.

The same data sets are reasonably well fitted by the blast wave parameterization [RL04]. In this particular version of the model longitudinal boost invariance is assumed. The azimuthal anisotropies are introduced via the geometrical ellipticity ($R_y > R_x$) and via the azimuthal dependence of the collective transverse rapidity $\rho(r, \phi) = r/R\rho_0 + \rho_2 * \cos(2\phi)$. The fit parameters are

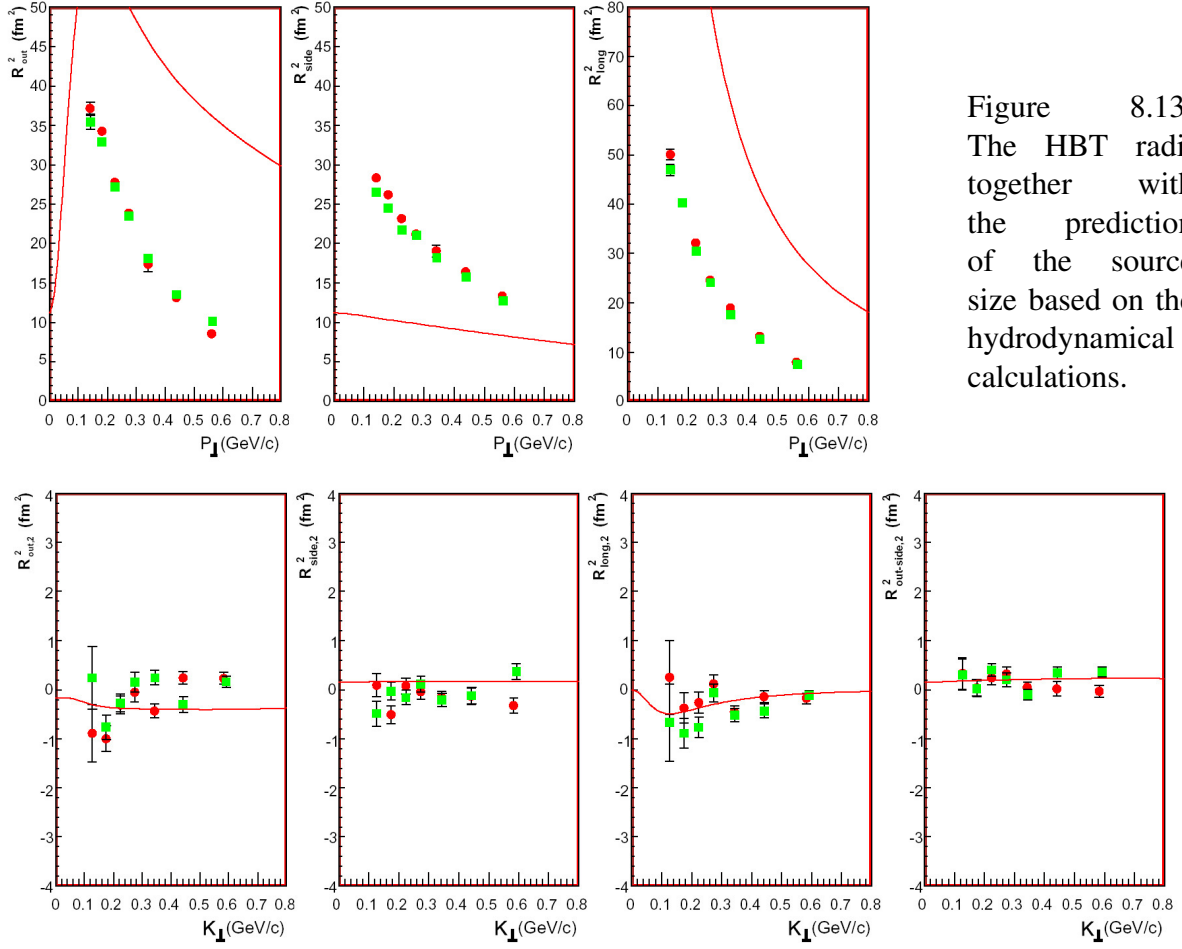


Figure 8.13: The HBT radii together with the prediction of the source size based on the hydrodynamical calculations.

- kinetic freeze-out temperature T ,
- maximum flow rapidity ρ ,
- source radii R_x and R_y ,
- the system longitudinal proper time ($\tau = \sqrt{t^2 - z^2}$),
- the emission duration.

The blast wave fit was performed simultaneously to all the distributions, with a fixed freeze-out temperature $T = 100$ MeV and a sharp sphere profile (relative surface diffuseness of the emission source $a_s = 0.01$). In Table 8.2 the rapidity density of the particle is shown.

$\pi^- dN/dy$	152.7	π^- multiplicity
$K^0 dN/dy$	18.44	K^0 multiplicity
$\phi dN/dy$	1.451	ϕ multiplicity
T	0.100 GeV	temperature (fixed)
ρ_0	0.87	mean transverse rapidity
ρ_2	0.016	second Fourier comp. of transv. rapidity
R_x	11.26 fm	source radius in-plane
R_y	11.42 fm	source radius out-of-plane
a_s	0.01	surface diffuseness (fixed)
τ_0	7.37 fm/c	freeze-out time
$d\tau$	1.55 fm/c	freeze-out duration

Table 8.2: Blast wave fit results.

8.5 Summary

This thesis presents results of a two-particle correlation analysis applied to the central Pb+Au collision data at 158 GeV per nucleon, collected in the final run of the CERES experiment at the CERN SPS. The state-of-the art analysis of identical pion correlations yielded HBT radii which, in their centrality and transverse momentum dependence, are in good agreement with the previous preliminary analysis of a subset of the data and with the results of other experiments. The results support the collision picture with strong longitudinal and transverse expansion.

The high event statistics and the good understanding of the experiment's resolution and of the Coulomb correction allowed to employ two more sophisticated correlation techniques, the reaction plane dependent pion-pion HBT radius analysis and the pion-proton Coulomb correlation analysis. In the first one, the correlation radii were studied as a function of the pion azimuthal emission angle with respect to the reaction plane. The obtained pion source profile in the plane transverse to the beam direction is round within the experimental accuracy, in contrast to the results obtained in similar collision systems (albeit at lower centralities) at the AGS and at RHIC. In the pion-proton analysis, a finite displacement between the sources of pions and protons was derived from the asymmetry of the correlation peak in the pair momentum direction. With the help of a dedicated fast Monte Carlo simulation the displacement was estimated to be around 4-6 fm, with protons being emitted closer to the edge (or earlier) than pions. In a system with transverse expansion such a displacement arises naturally because of the collective transverse velocity added to the thermal velocity of particles with different masses. Since the maximum Coulomb interaction is for pairs in which the pion and the proton move at the same velocity, and since pions on average is much faster than protons, only relatively fast protons and relatively slow pions can contribute to the correlation peak. The fastest protons are the ones which freeze-out close to the edge of the fireball where the collective velocity kick is

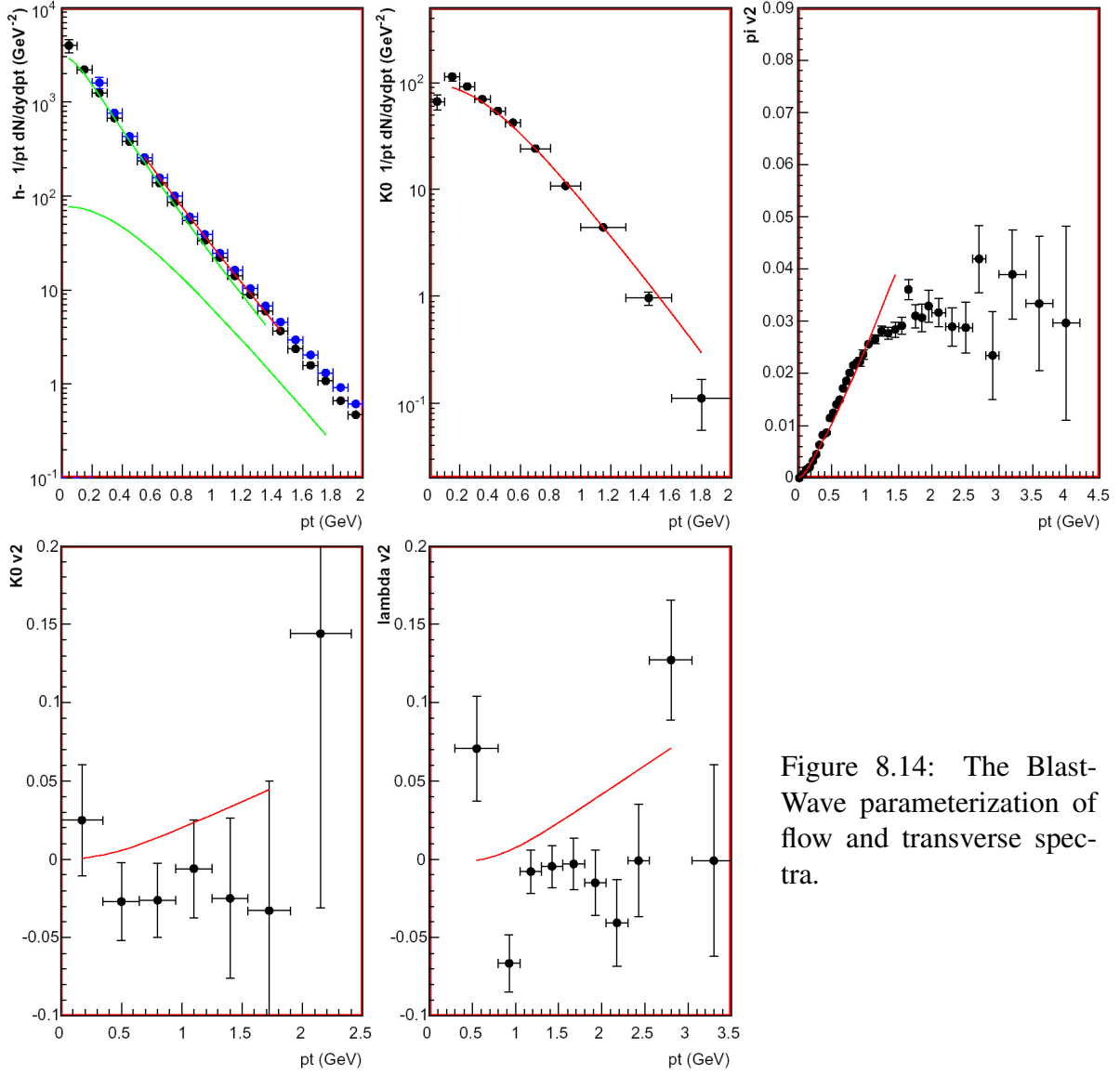


Figure 8.14: The Blast-Wave parameterization of flow and transverse spectra.

the highest; conversely, the slowest pions come from the center of the fireball.

The correlation radii obtained for identical pions and the source displacements deduced from the pion-proton correlations, along with the single transverse momentum spectra and the elliptic flow parameters, were compared to hydrodynamical calculations and to the blast wave model. The hydrodynamics significantly underestimates the R_{side} radius and overestimates R_{out} and R_{long} , similarly as it is the case at the RHIC energies. This indicates that this discrepancy might be caused by non-realistic predictions of the hydrodynamical approach rather than by some unusual reaction mechanism at RHIC, and that calling it "RHIC HBT puzzle" is

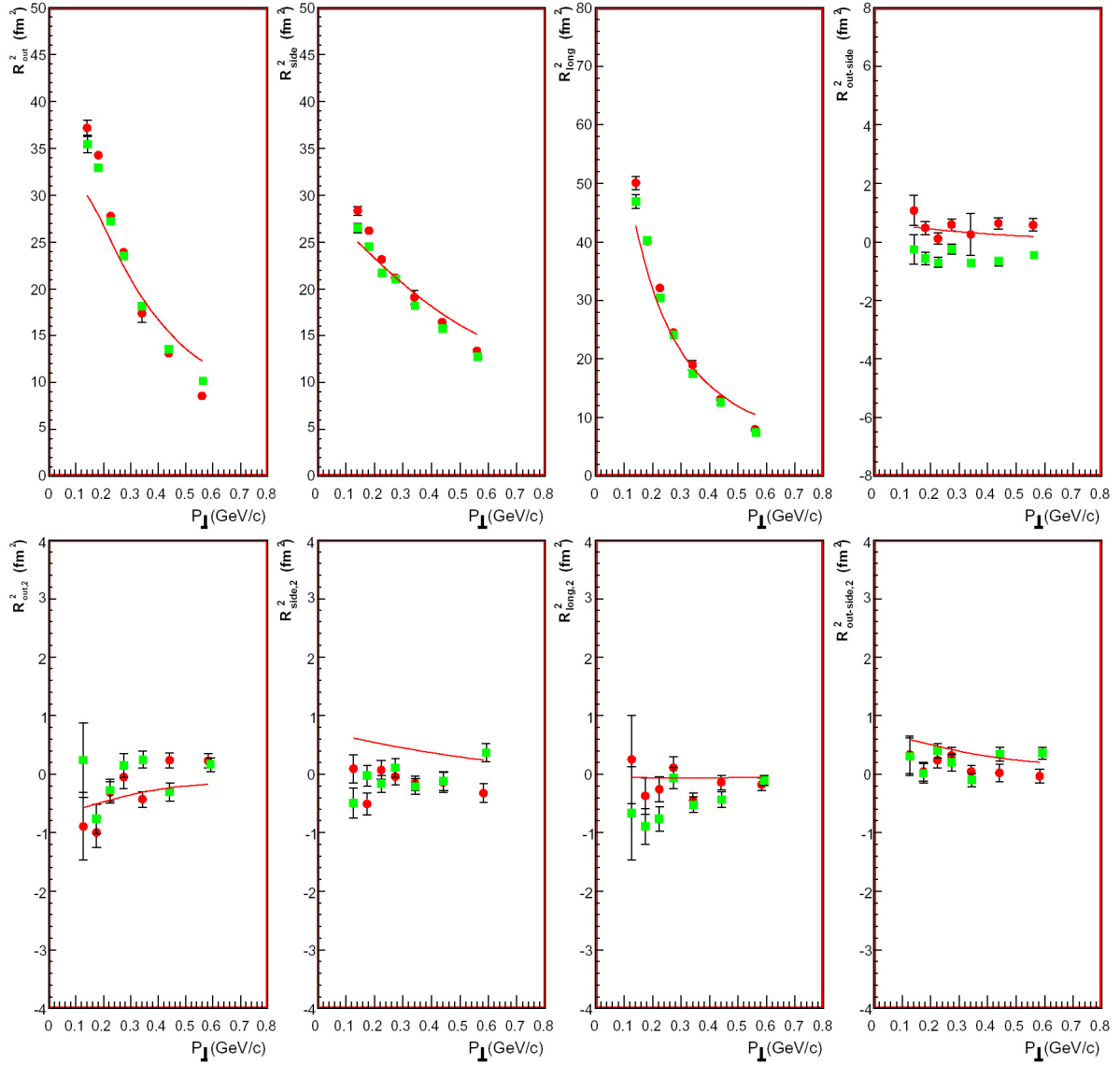


Figure 8.15: The Blast-Wave parameterization of HBT radii.

therefore inappropriate. The blast wave model, on the other hand, fits the data rather well except for the somewhat overestimated second Fourier components of the HBT radii with respect to the reaction plane angle, pion-proton source displacement, and the detailed dependence of R_{side} and R_{out} on the transverse momentum. The latter might be possibly explained by the contribution of soft pions from decays of the short-lived resonances like Δ or ρ which through their finite $c\tau$ increase the effective source size.

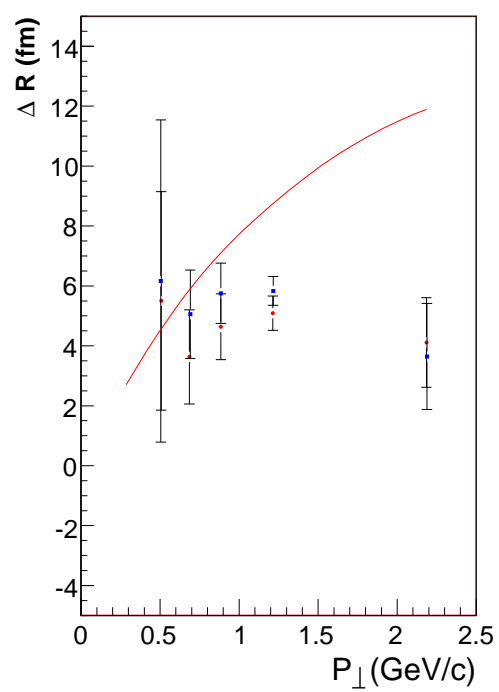


Figure 8.16: The Blast-Wave parameterization of pion-proton displacement.

Appendix A

step3c – Technical Information

The information, stored in the `step3c` ROOT tree format, was organized in two ROOT classes, the event (CSEvent) and the track (CSTrack). List of variables with short description for CSEvent and CSTrack class is presented in the table A.1 and A.2 respectively. The information about non-vertex SDD tracks is stored in the CSTrack, and corresponding sets of variables, as for the SDD vertex tracks, are available by adding the suffix `_s` at the end of the SDD variable name. The access to all variables stored in the ROOT tree is provided by the associate member functions of the ROOT objects. After many calibrations of the `step3c` data set were performed, the collection of the member functions providing access to the fully tuned variables is also available e.g. the reaction plane angle Ψ_n , the centrality of the collision expressed in the percent of the geometrical cross section, the momentum, and the dE/dx of TPC track.

Table A.1: The list of variables stored in the CSEvent class.

variable type	variable name	description
Int_t	run	the run number
Int_t	burst	the burst number
Int_t	evt	the event number
Int_t	time	the production time of event
Int_t	pattern	the trigger pattern (beam=1, minb=2, cent=4, ...)
Int_t	rich1RecoveryTime	the time from last discharge Rich1 (20 ms)
Int_t	rich2RecoveryTime	the time from last discharge Rich2 (20 ms)
Float_t	beamBefore	the preceding beam in ns
Float_t	beamAfter	the following beam in ns
Float_t	BC1Adc	calibrated signal from BC1 beam detector
Continued on next page		

Table A.1 – continued from previous page

variable type	variable name	description
Float_t	BC2Adc	calibrated signal from BC2 beam detector
Int_t	BC3Adc	by mistake this variable correspond to the multiplicity from MC
Float_t	centralityMC	the track multiplicity from MC
Float_t	centralitySD	the track multiplicity from SDD
Float_t	centralityTPC	the track multiplicity from TPC
Float_t	x1eta1SD	the Q_1^X from SDD, $1.7 < \eta < 2.2$
Float_t	y1eta1SD	the Q_1^Y from SDD, $1.7 < \eta < 2.2$
Float_t	x2eta1SD	the Q_2^X from SDD, $1.7 < \eta < 2.2$
Float_t	y2eta1SD	the Q_2^Y from SDD, $1.7 < \eta < 2.2$
Float_t	x1eta2SD	the Q_1^X from SDD, $2.2 < \eta < 2.7$
Float_t	y1eta2SD	the Q_1^Y from SDD, $2.2 < \eta < 2.7$
Float_t	x2eta2SD	the Q_2^X from SDD, $2.2 < \eta < 2.7$
Float_t	y2eta2SD	the Q_2^Y from SDD, $2.2 < \eta < 2.7$
Float_t	x1eta3SD	the Q_1^X from SDD, $2.7 < \eta < 3.2$
Float_t	y1eta3SD	the Q_1^Y from SDD, $2.7 < \eta < 3.2$
Float_t	x2eta3SD	the Q_2^X from SDD, $2.7 < \eta < 3.2$
Float_t	y2eta3SD	the Q_2^Y from SDD, $2.7 < \eta < 3.2$
Float_t	x1TPC	the Q_1^X from TPC
Float_t	y1TPC	the Q_1^Y from TPC
Float_t	x2TPC	the Q_2^X from TPC
Float_t	y2TPC	the Q_2^Y from TPC
Float_t	vertexX	the X position of the vertex in cm
Float_t	vertexY	the Y position of the vertex in cm
Float_t	vertexZ	the Z position of the vertex in cm
Int_t	ntracks	the TPC number of tracks
TClonesArray*	csTracks	the array of the CSTracks

Table A.2: The list of variables stored in the CSTrack class.

variable type	variable name	description
Char_t	SD_shared	the SDD hit shared by several SDD tracks, one can distinguish between no sharing case (=0) and sharing case (!=0)
Char_t	SD1_nanodes	the number of anodes

Continued on next page

Table A.2 – continued from previous page

variable type	variable name	description
Float_t	SD1_theta	the theta angle with respect to the event vertex
Float_t	SD1_phi	the phi angle with respect to the event vertex
Float_t	SD1_dedx	the dE/dx
Float_t	SD1_resum	the dE/dx resumed within 5 (mrad)
Float_t	SD1_dn	opening angle between closest-Hit and next closest-Hit
Char_t	SD2_nanodes	the number of anodes
Float_t	SD2_theta	the theta angle with respect to the event vertex
Float_t	SD2_phi	the phi angle with respect to the event vertex
Float_t	SD2_dedx	the dE/dx
Float_t	SD2_resum	the dE/dx resumed within 5 (mrad)
Float_t	RICH_phi	the phi of the ring
Float_t	RICH_theta	the theta of the ring
Float_t	RICH_radius	the ring radius
Float_t	RICH_nHits	the number of hits on ring for RICH1+2 corrected for background and acceptance
Int_t	RICH_nHits1_NC	the raw number of hits on ring in RICH1
Int_t	RICH_nHits2_NC	the raw number of hits on ring in RICH2
Float_t	RICH_sumAmp	the raw amplitude of hits on ring
Float_t	RICH_sigmaFit	the width of Gauss fit to distribution of hits vs. distance from predictor
Float_t	RICH_nHitsFit	area fit/binWidth
Float_t	RICH_COGshift	the displacement of COG of ring from predictor
Float_t	RICH_OLD_theta	the theta of the ring
Float_t	RICH_OLD_phi	the phi of the ring
Float_t	RICH_OLD_radius	the ring radius
Float_t	RICH_OLD_houghAmp1	the combined hough amplitude
Float_t	RICH1_OLD_sumAmp1	the sum of amplitude in the RICH1
Float_t	RICH2_OLD_sumAmp1	the sum of amplitude in the RICH2
Int_t	RICH_OLD_nHits	the number of hits in RICH1 and 1000*RICH2
Float_t	RICH_OLD_quality	the variance of the combined fit
Int_t	TPC_nHits	the number of fitted hits and 100*hits
Float_t	TPC_chi2rad	the fit quality, χ^2 in r vs. z

Continued on next page

Table A.2 – continued from previous page

variable type	variable name	description
Float_t	TPC_chi2phi	the fit quality, χ^2 in ϕ vs. z
Float_t	TPC_r0	the distance from the vertex in cm
Float_t	TPC_phi0	the phi angle between r0 and vertex in rad
Float_t	TPC_theta	the θ_{R2M} with respect to the event vertex
Float_t	TPC_phi	the ϕ_{R2M} with respect to event vertex
Float_t	TPC_thetaMean	the $\langle \theta \rangle$ positions of all hits on a track
Float_t	TPC_phiMean	the $\langle \phi \rangle$ positions of all hits on a track
		for 0-field and of the first four front hits in case on magnetic field
Float_t	TPC_dedx	the dE/dx
Float_t	TPC_pcor2	the momentum from 2-parameter fit
Float_t	TPC_pcor3	the momentum from 3-parameter fit

The source code and the calibration files were stored in the CERN Andrew File System (AFS). The main directories are listed in the table A.3. The `_coolVersion` correspond to the version of the COOL library used for production of `step3c`, and `_UNITnr_` correspond to the unit number. First three directories correspond to the source code and production chain, and remaining folders contained necessary calibration and configuration files for CERES detector. The table A.4 shows the names of calibration files used for `step3c` production. The unit-by-unit dependent calibration and configuration files were located in `ceres/prod/prod2000/calib/cal_UNITnr_` called `_calib_UbyU/`. The calibration parameters of the vertex refitting procedure were stored for a given unit in the file `vertexfit.dat`, which was located in `_calib_UbyU/` directory. The configuration files required by some COOL objects are listed in the table A.5.

Table A.3: The location of the directories used during production of the `step3c`.

directory name	location path
source	ceres/step3c/source
exec	ceres/step3c/exec
log_files	ceres/step3c/log_files
calib	ceres/sw/00/cool/_coolVersion/example/analyzer/calib/
config	ceres/sw/00/cool/_coolVersion/example/analyzer/config/ ceres/prod/prod2000/calib/cal_UNITnr_
maps	ceres/sw/00/cool/_coolVersion/maps/

Table A.4: The default name of the calibration files was linked with the names described in the column used file. The filed column correspond to the configuration of the magnetic field in TPC.

field	default file	used file
pos	calib/tpc-dphiplmap-frompads.dat	maps/tpc-dphiplmap-pad-u_UNITnr_-cor.dat
neg	calib/dthemap.dat	calib/dthemap-bneg.dat
neg	calib/residuals_frompads_phi.dat	calib/residuals_bypads_bneg_ite0_ite1_phi.dat
neg	calib/residuals_frompads_r.dat	calib/residuals_bypads_bneg_ite0_ite1_r.dat
neg	calib/tpc-dtheplmap.dat	maps/tpc-dtheplmap-u_UNITnr_.dat

Table A.5: The configuration files of the given COOL object used during step3c production.

class name	configuration file
CTPCCalibrationSetup	calib_UbyU/setup.CTPCCalibration
CTPCLookupTable	calib_UbyU/tableBfield.bin
CTPC	config/setup.tpc calib_UbyU/setup.CTPCCalibration
CTPCTrackFitter	config/setup.tpctrackfitter config/track.ref
CSidc1	calib_UbyU/setup.sidc1 calib_UbyU/calibration.sidc1
CSidc1	calib_UbyU/setup.sidc2 calib_UbyU/calibration.sidc2
CRobustVertexFitter	config/setup.vertex
CPionTrackingStrategy	config/setup.pionstrategy

Appendix B

Non-identical Particle Correlation Functions

The non-identical correlation functions have been studied for $\pi^-\pi^+$, π^-p , and π^+p pair combinations. In Fig. B.1 derived projection of correlation functions for equal masses unlike-charge pair is shown. As expected, no significant asymmetry between left and right widths of the correlation functions is observed. The small inefficiency seen for pairs with the transverse momentum larger than 1 GeV/c is attributed to the remaining effects of the two-track resolution. However, as shown in Fig. B.2 and Fig. B.3 no such effects are observed in the case of non-identical particle correlations with different particles species used to construct the pair, as it was explained in chapter 6. The blue solid line is a fit of Eq. 8.3 to the data.

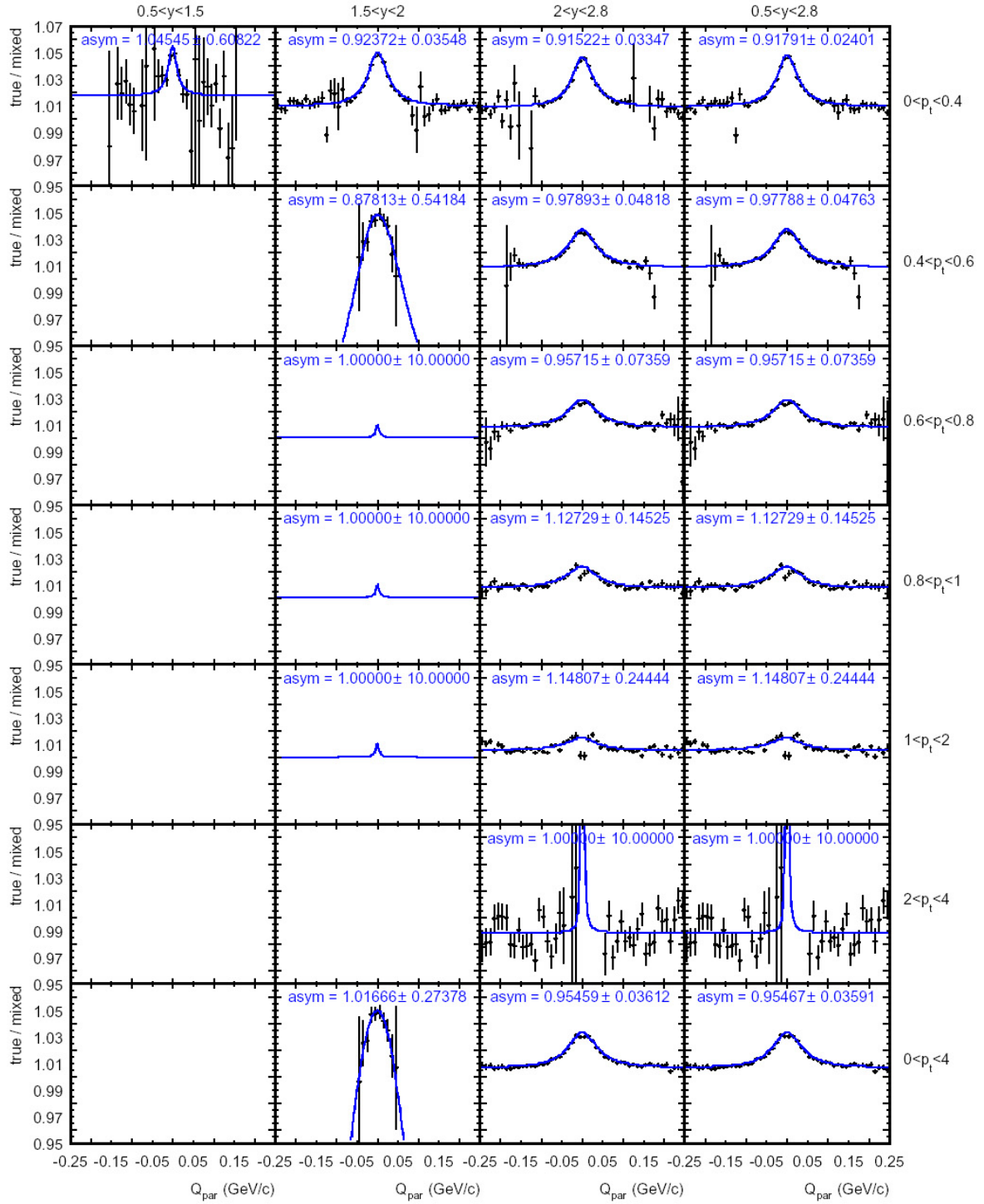
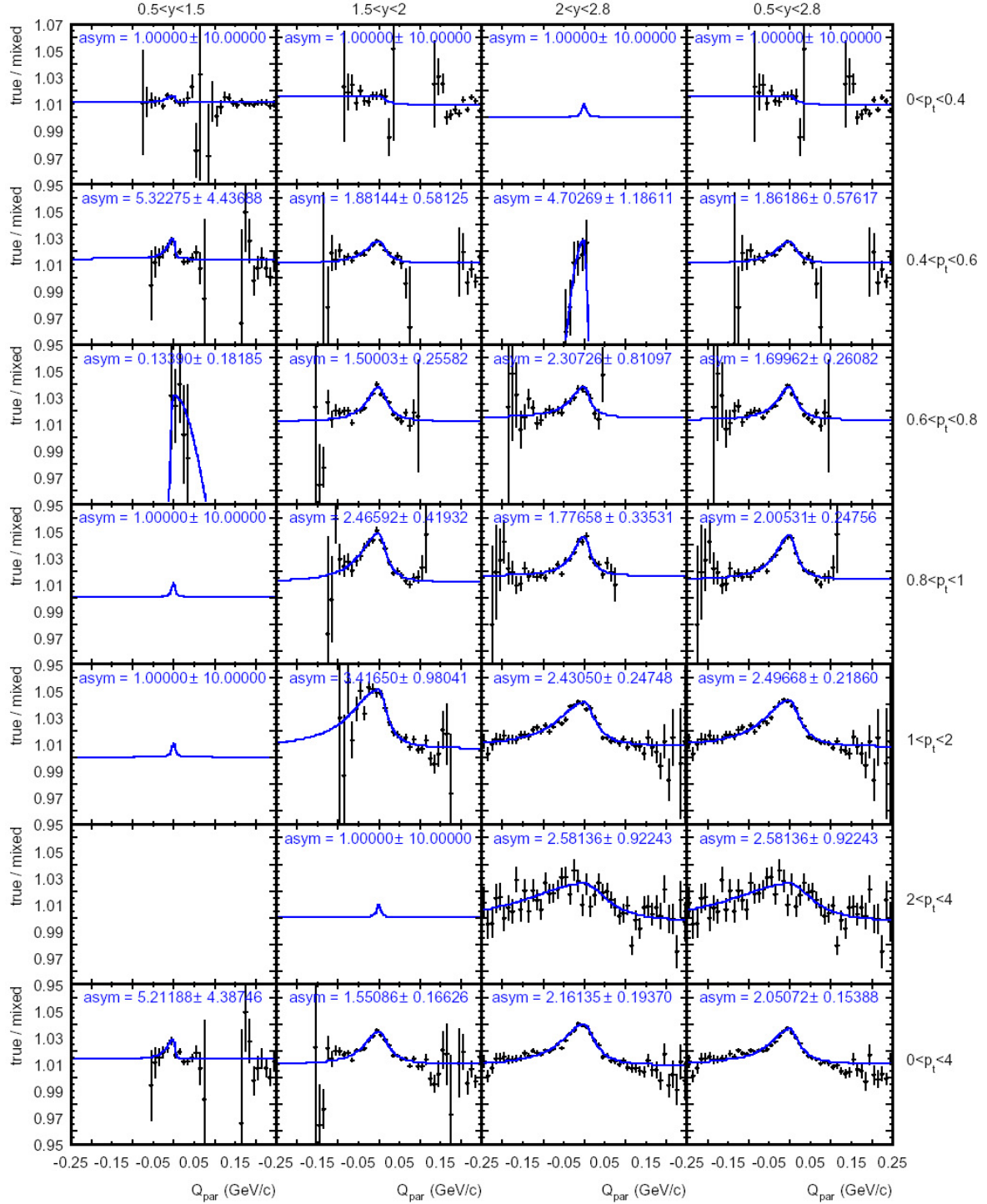
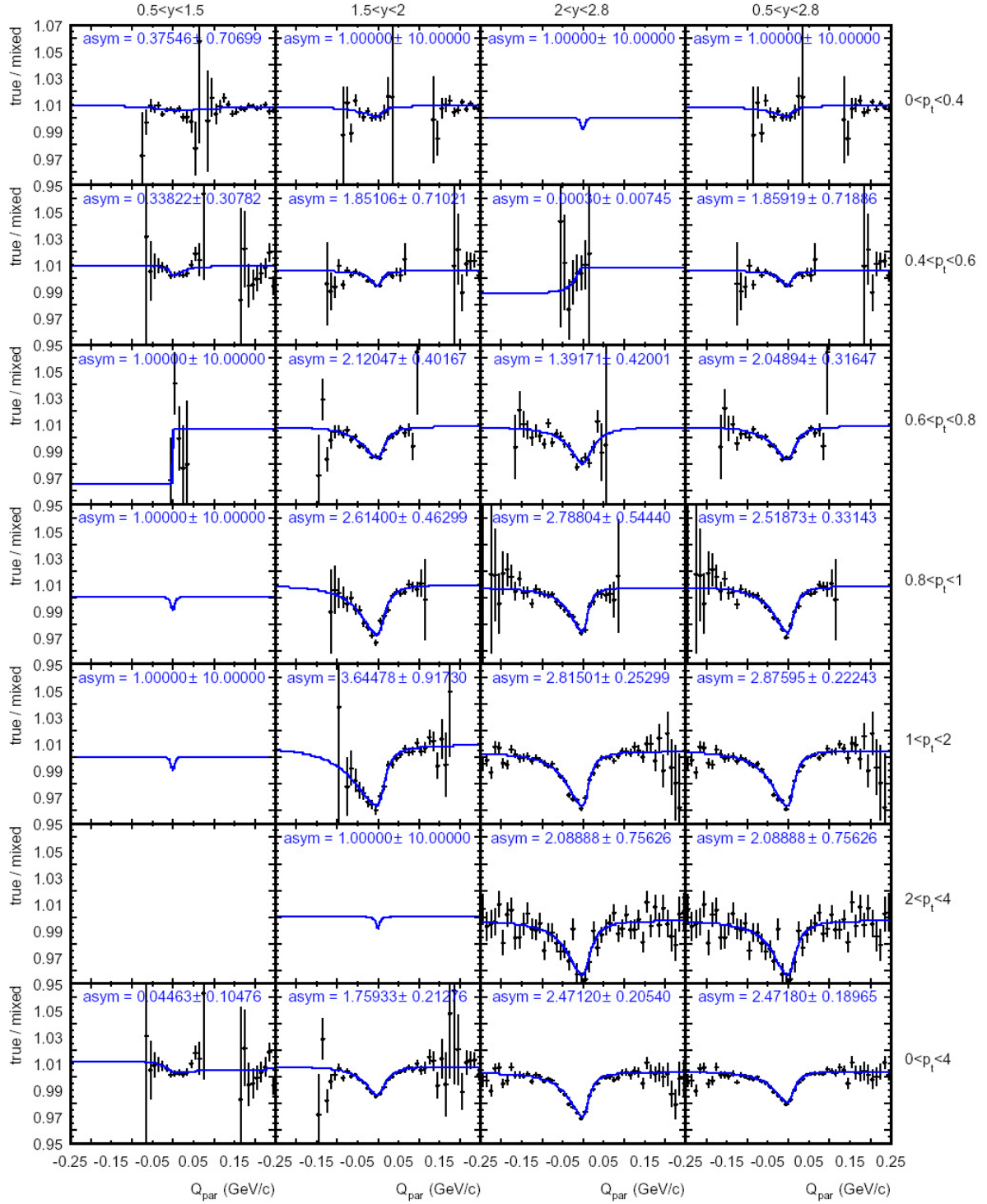


Figure B.1: The unlike-charge pion correlation functions.

Figure B.2: The π^-p^+ correlation functions.

Figure B.3: The π^+ - p^+ correlation functions.

Bibliography

- [A⁺95] G. Agakichiev et al. Enhanced production of low mass electron pairs in 200 GeV/u S-Au collisions at the CERN SPS. *Phys. Rev. Lett.*, 75:1272–1275, 1995. 21
- [A⁺96a] G. Agakichiev et al. Study of electron pair and photon production in Lead+Lead collisions at the CERN SPS; Addendum to proposal SPSLC/P280. Technical report, CERN/SPSLC 96-35, 1996. 30
- [A⁺96b] G. Agakichiev et al. Technical Note on the NA45/CERES Upgrade. Technical report, CERN/SPSLC 96-50, 1996. 30
- [A⁺98a] G. Agakichiev et al. Neutral meson production in p-Be and p-Au collisions at 450 GeV beam energy. *Eur. Phys. J. C*, 4:249, 1998. 21
- [A⁺98b] G. Agakichiev et al. Systematic study of low-mass electron pairs production in p-Be and p-Au collisions at 450 GeV/c. *Eur. Phys. J. C*, 4:231–247, 1998. 21
- [A⁺03a] D. Adamova et al. Beam Energy and Centrality Dependence of Two-Pion Bose-Einstein Correlations at SPS Energies. *Nucl. Phys. A*, 714:124, 2003. xi, 96, 126, 127
- [A⁺03b] A. Andronic et al. Pulse height measurements and electron attachment in drift chambers operated with Xe,CO₂ mixtures. *Nucl. Instr. and Meth. Phys. Res. A*, 498:143, 2003. 40
- [AAA⁺03] D. Adamova, G. Agakichiev, H. Appelshauser, V. Belaga, P. Braun-Munzinger, A. Castillo, A. Cherlin, S. Damjanovic, T. Dietel, L. Dietrich, A. Drees, S. I. Esumi, K. Filimonov, K. Fomenko, Z. Fraenkel, C. Garabatos, P. Glassel, G. Hering, J. Holeczek, V. Kuschpil, B. Lenkeit, W. Ludolphs, A. Maas, A. Marin, J. Milosevic, A. Milov, D. Miskowiec, Yu. Panebrattsev, O. Petchenova, V. Petracek, A. Pfeiffer, J. Rak, I. Ravinovich, P. Rehak, H. Sako, W. Schmitz, J. Schukraft, S. Sedykh, S. Shimansky, J. Slivova, H. J. Specht, J. Stachel, M. Sumbera, H. Tilsner, I. Tserruya, J. P. Wessels, T. Wienold, B. Windelband,

- J. P. Wurm, W. Xie, S. Yurevich, and V. Yurevich CERES Collaboration. Universal Pion Freeze-Out in Heavy-Ion Collisions. *Phys. Rev. Lett.*, 90(2):022301, 2003. 3
- [AftSC04] J. Adams and for the STAR Collaboration. Identified particle distributions in pp and Au+Au collisions at $\sqrt{s_{NN}}=200$ GeV. *Phys. Rev. Lett.*, 92:112301, 2004. 134
- [Ant04a] D. Antończyk. Production and monitoring of step3. <http://www-linux.gsi.de/dantoncz/ceres/step3c/>, 2004. 62
- [Ant04b] D. Antończyk. step2 – data quality monitoring. <http://www-linux.gsi.de/dantoncz/ceres/monitoring/>, 2004. 60
- [AS95] S. V. Akkelin and Yu. M. Sinyukov. The HBT-interferometry of expanding sources. *Phys. Lett. B*, 356(4):525–53, 1995. 13, 14
- [B⁺87] R. Brun et al. GEANT3 – Detector Description and Simulation Tool. Technical report, CERN Report No. DD/EE/84-1, 1987. 59
- [B⁺94] R. Baur et al. The CERES RICH detectors system. *Nucl. Instr. and Meth. Phys. Res. A*, 343:87–98, 1994. 26
- [B⁺95] R. Baur et al. The pad readout of the CERES RICH detectors. *Nucl. Instr. and Meth. Phys. Res. A*, 355:329–341, 1995. 26
- [B⁺97] J. Barrette et al. Proton and Pion Production Relative to the Reaction Plane in Au + Au Collisions at AGS Energies. *Phys. Rev. C*, 56:3254–3264, 1997. 74
- [B⁺05] J. Y. Baud et al. User Guide for CASTOR. <http://it-dep-fio-ds.web.cern.ch/it-dep-fio-ds/Documentation/userguide.html>, 2005. 58
- [Bar99] H. W. Barz. Combined effects of nuclear Coulomb field, radial flow, and opaqueness on two-pion correlations. *Phys. Rev. C*, 59(4):2214–2220, Apr 1999. 19
- [Bay98] G. Baym. The physics of Hanbury Brown–Twiss intensity interferometry: from stars to nuclear collisions. *Acta Phys. Polon. B*, 29:1839, 1998. 18
- [BBM96] G. Baym and P. Braun-Munzinger. Physics of Coulomb Corrections in Hanbury-Brown Twiss Interferometry in Ultrarelativistic Heavy Ion Collisions. *Nucl. Phys. A*, 610:286c, 1996. 17
- [BC74] S. Baker and R. D. Cousins. Clarification of the use of chi-square and likelihood functions in fits to histograms. *Nucl. Instr. and Meth. Phys. Res.*, 221:472–474, 1974. 95

- [Ber89] G. F. Bertsch. Pion interferometry as a probe of the plasma. *Nucl. Phys. A*, 498:173–179, Jul 1989. 15
- [Bia99] S. F. Biagi. Monte Carlo simulation of electron drift and diffusion in counting gases under the influence of electric and magnetic fields. *Nucl. Instr. and Meth. Phys. Res. A*, 421:234–240, 1999. 43
- [Bjo83] J. D. Bjorken. Highly relativistic nucleus-nucleus collisions: The central rapidity region. *Phys. Rev. D*, 27(1):140–151, 1983. 8
- [BM00] P. Braun-Munzinger. Towards the Quark Gluon Plasma. *Nucl. Phys. A*, 663:183, 2000. v, 3, 4
- [BMHS99] P. Braun-Munzinger, I. Heppe, and J. Stachel. Chemical equilibration in Pb+Pb collisions at the SPS. *Phys. Lett. B*, 465:15–20, 1999. 3
- [BMMZ98] P. Braun-Munzinger, D. Miśkowiec, and P. Zimmermann. Laser calibration system for the CERES TPC. Technical report, GSI Scientific Report, 1998. 31
- [BMS02] P. Braun-Munzinger and J. Stachel. Particle Ratios, Equilibration, and the QCD Phase Boundary. *J. Phys. G*, 28:1971, 2002. 3
- [BMSWX96] P. Braun-Munzinger, J. Stachel, J. P. Wessels, and N. Xu. Thermal and hadrochemical equilibration in nucleus-nucleus collisions at the SPS. *Phys. Lett. B*, 365:1–6, 1996. 3
- [Bow88] M. G. Bowler. Extended sources, final state interactions and Bose-Einstein correlations. *Z. Phys. C*, 39:81–88, 1988. 17
- [Bow91] M. G. Bowler. Coulomb corrections to Bose-Einstein corrections have been greatly exaggerated. *Phys. Lett. B*, 270:69–74, 1991. 96
- [BR] R. Brun and F. Rademakers. ROOT - An Object-Oriented Data Analysis Framework. <http://root.cern.ch>. 49
- [BR94] W. Blum and L. Rolandi. *Particle Detection with Drift Chambers*. Springer-Verlag, 2nd edition, 1994. 29
- [BR96] G. E. Brown and M. Rho. Chiral restoration in hot and/or dense matter. *Phys. Rep.*, 269(6):333–380, May 1996. 9
- [BZS⁺99] M. Bleicher, E. Zabrodin, C. Spieles, S. A. Bass, C. Ernst, S. Soff, L. Bravina, M. Belkacem, H. Weber, H. Stocker, and W. Greiner. Relativistic Hadron-Hadron Collisions in the Ultra-Relativistic Quantum Molecular Dynamics Model (UrQMD). *J. PHYS. G*, 25:1859, 1999. 134

- [CE02] CERN-EP/ED. ALICE TPC Readout Chip - User Manual. 2002. 51
- [CL95] T. Csorgo and B. Lorstad. Bose-Einstein Correlations for Expanding Finite Systems. *Nucl. Phys. A*, 590:465c, 1995. 90
- [CNH95] S. Chapman, J. R. Nix, and U. Heinz. Extracting source parameters from Gaussian fits to two-particle correlations. *Phys. Rev. C*, 52(5):2694–2703, 1995. 13
- [Col00] E895 Collaboration. Azimuthal dependence of pion interferometry at the AGS. *Phys. Lett. B*, 496:1–8, 2000. 131
- [Col04] STAR Collaboration. Azimuthally sensitive Hanbury Brown-Twiss interferometry in Au+Au collisions at $\sqrt{s_{NN}}=200$ GeV. *Phys. Rev. Lett.*, 93:012301, 2004. 120, 131
- [CP75] J. C. Collins and M. J. Perry. Superdense Matter: Neutrons or Asymptotically Free Quarks? *Phys. Rev. Lett.*, 34(21):1353–1356, May 1975. 1, 2
- [CSH95] S. Chapman, P. Scotto, and U. Heinz. New Cross Term in the Two-Particle Hanbury-Brown Twiss Correlation Function in Ultrarelativistic Heavy-Ion Collisions. *Phys. Rev. Lett.*, 74(22):4400–4403, May 1995. 14, 15, 16
- [E⁺04] S. Eidelman et al. Review of particle physics. *Phys. Lett.*, B592:1, 2004. 70
- [EKL89] K. J. Eskola, K. Kajantie, and J. Lindfors. Quark and Gluon Production in High Energy Nucleus-Nucleus Collisions. *Nucl. Phys. B*, 323:37–52, 1989. 77
- [EKO91a] J. Ellis, J. I. Kapusta, and K. A. Olive. Phase transition in dense nuclear matter with quark and gluon condensates. *Phys. Lett. B*, 273:123–127, Dec 1991. 1
- [EKO91b] J. Ellis, J. I. Kapusta, and K. A. Olive. Strangeness, glue and quark matter content of neutrons stars. *Nucl. Phys. B*, 348:345–372, Jan 1991. 1
- [G⁺05] C. González Gutiérrez et al. The ALICE TPC Readout Control Unit. In *Proceeding of the 2005 IEEE Nuclear Science Symposium and Medical Imaging Conference*, Puerto Rico, 2005. 53
- [Gar] C. Garabatos. Private communication. 41, 42
- [Gar04] C. Garabatos. The ALICE TPC. *Nucl. Instr. and Meth. Phys. Res. A*, 535:197–200, 2004. vi, 34, 35, 36
- [GGLP60] G. Goldhaber, S. Goldhaber, W. Lee, and A. Pais. Influence of Bose-Einstein Statistics on the Antiproton-Proton Annihilation Process. *Phys. Rev.*, 120(1):300–312, Oct 1960. 10

- [GKW79] M. Gyulassy, S. K. Kauffmann, and L. Wilson. Pion interferometry of nuclear collisions. I. Theory. *Phys. Rev. C*, 20(6):2267–2292, Dec 1979. 18
- [GL79] E. Gatti and A. Longoni. Optimum Geometry for Strip Cathodes or Grids in MWPC for Avalanche Localization Along the Andoe Wires. *Nucl. Instr. and Meth. Phys. Res. A*, 163:83–92, 1979. 41
- [GM64] M. Gell-Mann. A schematic model of baryons and mesons. *Phys. Lett.*, 8:214–215, 1964. 2
- [GM02] C. Garabatos and D. Miśkowiec. Electric field of CERES TPC. Technical report, GSI Scientific Report, 2002. 28
- [GR84] E. Gatti and P. Rehak. Semiconductor Drift Chamber - An Application of a Novel Charge Transport Scheme. *Nucl. Instr. and Meth. Phys. Res. A*, 225:608–614, 1984. 24
- [H⁺96] P. Holl et al. A 55 cm² cylindrical silicon drift detector. *Nucl. Instr. and Meth. Phys. Res. A*, 377:367–374, 1996. 25
- [H⁺ 1] P. Holl et al. Study of Electron Pair and Photon Production in Lead+Lead Collisions at the CERN SPS. Technical report, CERN/SPSLC, 94-1. 21
- [HB95] M. Herrmann and G. F. Bertsch. Source dimensions in ultrarelativistic heavy-ion collisions. *Phys. Rev. C*, 51(1):328–338, Jan 1995. 15, 126
- [HBT56] R. Hanbury-Brown and R. Q. Twiss. Correlation between photons in two coherent beams of light. *Nature*, 177:27–29, 1956. 10
- [Hei96a] U. Heinz. Hanbury-Brown/Twiss interferometry for relativistic heavy-ion collisions: Theoretical aspects. *nucl-th/9609029*, 1996. 12
- [Hei96b] H. Heiselberg. Interferometry with Resonances and Flow in High-Energy Nuclear Collisions. *Phys. Lett. B*, 379:27, 1996. 90
- [Her06] J. Castillo Hernandez. Development of a Ternary Mixture Monitor. Master's thesis, 2006. 54
- [HHLW02] U. Heinz, A. Hummel, M. A. Lisa, and U. A. Wiedemann. Symmetry constraints for the emission angle dependence of Hanbury–Brown–Twiss radii. *Phys. Rev. C*, 66(4):044903, Oct 2002. 120, 131
- [Ins] National Instruments. LabVIEW. <http://www.ni.com/labview>. 49
- [Joo05] M. Joos. Private communication. 2005. 53

- [Jun05] A. Junique. Private communication. 2005. 50
- [Kar02] F. Karsch. Lattice QCD at High Temperature and Density. *Lect. Note Phys.*, 583:209, 2002. 3
- [KH03] P. F. Kolb and U. Heinz. Emission angle dependent HBT at RHIC and beyond. *Nucl. Phys. A*, 715:653–656, March 2003. 101
- [KHHH01] P. F. Kolb, P. Huovinen, U. Heinz, and H. Heiselberg. Elliptic flow at SPS and RHIC: from kinetic transport to hydrodynamics. *Phys. Lett. B*, 500:232–240, 2001. 137
- [KL03] F. Karsch and E. Laermann. Thermodynamics and in-medium hadron properties from lattice QCD. *hep-lat/0305025*, 2003. v, 3
- [Kop74] G. I. Kopylov. Like particle correlations as a tool to study the multiple production mechanism. *Phys. Lett. B*, 50(4):472–474, 1974. 94
- [KP71] G. I. Kopylov and M. I. Podgoretskii. Interference effects in two-resonance system. *Yad. Fiz.*, 14:1081–1090, 1971. 10
- [KSH99] P. F. Kolb, J. Sollfrank, and U. Heinz. Anisotropic flow from AGS to LHC energies. *Phys. Lett. B*, 459:667, 1999. 137
- [KSH00] P. F. Kolb, J. Sollfrank, and U. Heinz. Anisotropic transverse flow and the quark-hadron phase transition. *Phys. Rev. C*, 62(5):054909, Oct 2000. 101
- [Lan53] L. D. Landau. On multiple production of particles during collisions of fast particles, English edition: Collected papers of L.D. Landau, D. Ter Haar ed., Pergamon, Oxford (1965). *Izv. Akad. Nauk. SSSR (Physics Series)*, 17:51, 1953. 7
- [LD91] G. R. Lynch and O. I. Dahl. Approximations to multiple Coulomb scattering. *Nucl. Instr. and Meth. B*, 58:6–10, May 1991. 70
- [Led04] R. Lednicky. Correlation femtoscopy of multiparticle processes. *YAD.FIZ.*, 67:73, 2004. 134
- [Leo94] W. R. Leo. *Techniques for Nuclear and Particle Physics Experiments*. Springer-Verlag, 2nd edition, 1994. 39
- [LHW00] M. A. Lisa, U. Heinz, and U. A. Wiedemann. Tilted pion sources from azimuthally sensitive HBT interferometry. *Phys. Lett. B*, 489:287–292, 2000. 119

- [Lip00] C. Lippmann. Aufbau und Inbetriebnahme eines Gasqualitätsmonitors für die HADES-Driftkammern. Master's thesis, Institut für Kernphysik, Johann Wolfgang Goethe Universität, Frankfurt, 2000. 33
- [LLEN96] R. Lednický, V.L. Lyuboshitz, B. Erasmus, and D. Nouais. How to measure which sort of particles was emitted earlier and which later. *Phys. Lett. B*, 373:30–34, 1996. 19, 105, 108
- [Lud06] W. Ludolphs. *Measurement of Open Charm in 158 AGeV/c Pb-Au Collisions*. PhD thesis, Combined Faculties for the Natural Sciences and for Mathematics of the Ruperto-Carola University of Heidelberg, Germany, 2006. 58, 60
- [LW74] T. D. Lee and G. C. Wick. Vacuum stability and vacuum excitation in a spin-0 field theory. *Phys. Rev. D*, 9(8):2291–2316, Apr 1974. 2
- [Mar] A. Marin. Private communication. xii, 138
- [Mat88] E. Mathieson. Cathode Charge Distributions in Multiwire Chambers: 4. Empirical formula for small anode-cathode separation. *Nucl. Instr. and Meth. Phys. Res. A*, 270:602–603, 1988. 41
- [MAT89] QUARK MATTER. Proceedings of the 7th International Conference on Ultra-Relativistic Nucleus–Nucleus Collisions, Lenox, USA, 26-30 September, 1988. *Nucl. Phys. A*, 498, 1989. 1
- [MAT04] QUARK MATTER. Proceedings of the 17th International Conference on Ultra-Relativistic Nucleus–Nucleus Collisions, Oakland, USA, 11-17 January, 2004. *J. Phys. G: Nucl. Part. Phys*, 30(8), 2004. 1
- [MAT06] QUARK MATTER. Proceedings of the 18th International Conference on Ultra-Relativistic Nucleus–Nucleus Collisions, Budapest, Hungary, 4-9 August, 2005. *Nucl. Phys. A*, 774, August 2006. 1
- [McL86] L. McLerran. The physics of the quark-gluon plasma. *Rev. Mod. Phys.*, 58(4):1021–1064, Oct 1986. 1
- [Mer61] E. Merzbacher. *Quantum Mechanics*. Wiley & Sons, New York, 2nd edition, 1961. 18
- [MftCC06] D. Miśkowiec and for the CERES Collaboration. Collection of CERES Results. *Nucl. Phys. A*, 774:43, 2006. 9
- [Mil05] J. Milošević. *Investigation of Azimuthal Asymmetries in Charged and Strange Particle Distributions from CERES*. PhD thesis, Combined Faculties for the Natural Sciences and for Mathematics of the Ruperto-Carola University of Heidelberg, Germany, 2005. xii, 138

- [MIN] MINUIT. CERN Program Library Long Writeup D506. 96
- [Miś98] D. Miśkowiec. Separation between sources of pions and protons in central Au+Au collisions at the AGS (E877). *nucl-ex/9808003*, 1998. 19, 107
- [Miś99] D. Miśkowiec. New trigger implementation for CERES/NA45 at CERN. Technical report, GSI Scientific Report, 1999. 23
- [Miś00] D. Miśkowiec. Technical information about run 2000. <http://www-linux.gsi.de/misko/ceres/daq/run-history-2000.txt>, 2000. 58
- [Miś04] D. Miśkowiec. *Overlap* computer program. <http://www-linux.gsi.de/misko/overlap>, 2004. 80
- [Mor01] T. Morgan. Construction and Calibration of the STAR FTPC Drift Velocity Monitor. Technical report, Max-Planck-Institut für Physik (Werner-Heisenberg-Institut), 2001. 36
- [MS88] A. N. Makhlin and Yu. M. Sinyukov. The hydrodynamics of hadron matter under a pion interferometric microscope. *Journal Zeitschrift für Physik C Particles and Fields*, 39(1):69–73, March 1988. 99, 126
- [MT87] F. Mosteller and W. Tukey. *Data Analysis and Regression: A Second Course in Statistic*. Addison-Wesley, 1987. 59
- [Mus05] L. Musa. Private communication. 2005. 50
- [Oli91] K. A. Olive. The Quark - hadron transition in cosmology and astrophysics. *Science*, 251:1194–1199, 1991. 1
- [Oll92] J. Y. Ollitrault. Anisotropy as a signature of transverse collective flow. *Phys. Rev. D*, 46(1):229–245, Jul 1992. 101
- [Oll95] J. Y. Ollitrault. Collective flow from azimuthal correlations. *Nucl. Phys. A*, 590:561c–564c, 1995. 72
- [Oll97] J. Y. Ollitrault. Reconstructing azimuthal distributions in nucleus-nucleus collisions. *arXiv:nucl-ex/9711003*, 1997. viii, 74, 75, 79
- [Oll98] J. Y. Ollitrault. Flow systematics from SIS to SPS energies. *Nucl. Phys. A*, 638:c195–c206, August 1998. 102
- [Pol78] A. M. Polyakov. Thermal properties of gauge fields and quark liberation. *Phys. Lett. B*, 72:477–480, 1978. 1, 2

- [Pot96] K. M. Potter. The Large hadron Collider (LHC) project of CERN. Technical report, CERN LHC Project Report 36, 1996. 33
- [Pra84] S. Pratt. Pion Interferometry for Exploding Sources. *Phys. Rev. Lett.*, 53(13):1219–1221, Sep 1984. 99
- [Pra86a] S. Pratt. Coherence and coulomb effects on pion interferometry. *Phys. Rev. D*, 33(1):72–79, Jan 1986. 18
- [Pra86b] S. Pratt. Pion interferometry of quark-gluon plasma. *Phys. Rev. D*, 33(5):1314–1327, Mar 1986. 15
- [PS75] V. Palladino and B. Sadoulet. The ALICE TPC. *Nucl. Instr. and Meth.*, 128:323–335, 1975. 35
- [PV98] A. M. Poskanzer and S. A. Voloshin. Methods for analyzing anisotropic flow in relativistic nuclear collisions. *Phys. Rev. C*, 58:1671–1678, 1998. viii, 74, 76, 79
- [Rad06] S. Radomski. PhD thesis, TECHNISCHE UNIVERSITÄT DARMSTADT, 2006. xii, 138
- [RC04] C. P. Robert and G. Casella. *Monte Carlo Statistical Methods*. Springer-Verlag New York Inc., 2nd edition, 2004. 113
- [RftSC03] F. Retiere and for the STAR Collaboration. Non-identical particle correlation analysis as a probe of transverse flow. *Nucl. Phys. A*, 715:591, 2003. 105
- [RL04] F. Retiere and M. A. Lisa. Observable implications of geometrical and dynamical aspects of freeze-out in heavy ion collisions. *Phys. Rev. C*, 70(4):044907, 2004. 19, 138
- [RW00] R. Rapp and J. Wambach. Chiral symmetry restoration and dileptons in relativistic heavy-ion collisions. *Adv. Nucl. Phys.*, 25:1–205, 2000. 9
- [S⁺98] Yu. M. Sinyukov et al. Coulomb corrections for interferometry analysis of expanding hadron systems. *Phys. Lett. B*, 432:248–257, 1998. 96
- [Sch98] W. Schmitz. Cathode pad design for the CERES-TPC. Technical report, CERES-Note, 1998. 30
- [Shu73] E. V. Shuryak. The correlations of identical pions in multibody production. *Phys. Lett. B*, 44(4):387–389, 1973. 10
- [Shu78] E. V. Shuryak. Quark-gluon plasma and hadronic production of leptons, photons and psions. *Phys. Lett. B*, 78:150–153, 1978. 1

- [Sh03] J. Shrivová. *Azimuthal Correlations of High-pt Pions in 158 AGeV/c Pb-Au Collisions Measured by the CERES Experiment*. PhD thesis, Charles University in Prague, Faculty of Mathematics and Physics, 2003. 25, 113
- [SP71] R. M. Sternheimer and R. F. Peierls. General Expression for the Density Effect for the Ionization Loss of Charged Particles. *Phys. Rev. B*, 3(11):3681–3692, Jun 1971. 66
- [Sta99] J. Stachel. Towards the Quark-Gluon Plasma. *Nucl. Phys. A*, 654:119c, 1999. 3
- [SVA96] Y. M. Sinyukov S. V. Akkelin. The HBT-interferometry of expanding inhomogeneous sources. *Z. Phys. C*, 72:501–507, 1996. 134
- [Til02] H. Tilsner. *Two-Particle Correlations at 40, 80, and 158 AGeV Pb-Au Collisions*. PhD thesis, Combined Faculties for the Sciences and for Mathematics of the Ruperto-Carola University of Heidelberg, Germany, 2002. 31
- [TLS01] D. Teaney, J. Lauret, and E. V. Shuryak. A Hydrodynamic Description of Heavy Ion Collisions at the SPS and RHIC, 2001. 101
- [TPC01] TPC Technical Design Report. Technical report, CERN/LHCC, 2000-001. 33
- [TWH00] B. Tomasik, U. A. Wiedemann, and U. Heinz. Dynamics and Sizes of the Fireball at Freeze-out. *Nucl. Phys. A*, 663:753, 2000. 99
- [VC96] S. A. Voloshin and W. E. Cleland. Hanbury-Brown–Twiss analysis of anisotropic transverse flow. *Phys. Rev. C*, 53(2):896–900, Feb 1996. 16
- [Vee98] R. Veenhof. Garfield, recent developments. *Nucl. Instr. and Meth. Phys. Res. A*, 419:726–730, 1998. 39
- [Vee03] R. Veenhof. Choosing a gas mixture for the ALICE TPC. Technical report, CERN/TPC ALICE-INT-2003-29, 2003. 34
- [VZ96] S. Voloshin and Y. Zhang. Flow Study in Relativistic Nuclear Collisions by Fourier Expansion of Azimuthal Particle Distributions. *Z. Phys. C*, 70:665–671, 1996. 10, 72
- [Wei00] R. M. Weiner. Boson Interferometry in High Energy Physics. *Phys. Rep.*, 327:249, 2000. 17
- [WH97] U. A. Wiedemann and U. Heinz. Resonance contributions to Hanbury-Brown Twiss correlation radii. *Phys. Rev. C*, 56(6):3265–3286, Dec 1997. 90
- [WH99] U. A. Wiedemann and U. Heinz. Particle Interferometry for Relativistic Heavy-Ion Collisions. *Phys. Rep.*, 319:145, 1999. 12, 126

- [Wie98] U. A. Wiedemann. Two-particle interferometry for noncentral heavy-ion collisions. *Phys. Rev. C*, 57(1):266–279, Jan 1998. 16, 99
- [WSH96] U. A. Wiedemann, P. Scotto, and U. Heinz. Transverse momentum dependence of Hanbury-Brown–Twiss correlation radii. *Phys. Rev. C*, 53(2):918–931, Feb 1996. 99
- [WW02] B. A. Weaver and A. J. Westphal. Energy loss of relativistic heavy ions in matter. *Nucl. Instr. and Meth. B*, 187:285–301, 2002. 40, 66
- [Yur06] S. Yurevich. *Electron-Pair Production in 158 AGeV/c Pb-Au Collisions from CERES*. PhD thesis, Combined Faculties for the Natural Sciences and for Mathematics of the Ruperto-Carola University of Heidelberg, Germany, 2006. 58, 59, 62, 67, 113
- [ZBB⁺84] W. A. Zajc, J. A. Bistirlich, R. R. Bossingham, H. R. Bowman, C. W. Clawson, K. M. Crowe, K. A. Frankel, J. G. Ingersoll, J. M. Kurck, C. J. Martoff, D. L. Murphy, J. O. Rasmussen, J. P. Sullivan, E. Yoo, O. Hashimoto, M. Koike, W. J. McDonald, J. P. Miller, and P. Truöl. Two-pion correlations in heavy ion collisions. *Phys. Rev. C*, 29(6):2173–2187, Jun 1984. 19
- [Zie98] J. F. Ziegler. The stopping and range of ions in matter. <http://www.srim.org/>, 1998. 41

Acknowledgements

This work would have not been possible without the effort and involvement of many people to whom I would like to express my gratitude. I am deeply grateful to Prof. Dr. P. Braun-Munzinger for giving me the opportunity to join his research groups and introducing me as a member of the CERES and the ALICE collaborations. For all these years I have learnt much from him. I appreciate his interest of my work as well as many valuable suggestions for improving the work. Dr. D. Miśkowiec deserves a special mention, his enthusiasm and experience helped me to make the research interesting and enjoyable. Since the very beginning he has guided me with patience through the beautiful field of the two-particle correlations. I express also many thanks to Dr. C. Garabatos who introduced me into the physics of gaseous detectors. He give me a unique opportunity to extend my knowledge about the complex systems used for developing modern physics detectors. I am also very grateful to Prof. Dr. J. Stachel for her useful suggestions. I want to show my appreciation of the members of the CERES and the ALICE collaborations, especially to Prof. Dr. Harald Appelshäuser and Dr. A. Marin for their comments and suggestions during all these years. I would like to thanks to Pasi Huovieni for providing me with the hydrodynamical calculation. A special thanks to my office mate Oliver Busch for all discussions about physics and great working atmosphere. There are no words which will express how much I thanks to my girlfriend Katarzyna. Finally, I would like to thank all my friends. Last but not least, not to forget my family for all their support and encouragement they have given me throughout my education.

Curriculum Vitae

Personal Data

Name	Dariusz
Surname	Antończyk
Place of Birth	Kraków
Date of Birth	03 December 1976
Marital Status	single
Nationality	polish

Education

10/2002 - 10/2006	Doctoral fellowship at the Gesellschaft für Schwerionenforschung and preparation of the dissertation
09/1997 - 10/2002	M.Sc. of Physics, Institute of Physics of the Jagiellonian University in Kraków, Poland Main subject: Experimental Particle Physics Thesis: Client/server software for controlling a low voltage power supply in ATLAS TRT

Publications

1. *Latest results on $e^+ e^-$ pair production in CERES*, Nucl. Phys. A749, 160-165 (2005)
2. *Leptonic and Charged Kaon Decay Modes of the ϕ Meson Measured in Heavy-Ion Collisions at the CERN Super Proton Synchrotron*, Phys. Rev. Lett. 96, 152301 (2006)

3. *Performance studies with an ALICE TPC prototype*, Nucl. Inst. Meth. A565, 2, 551-560 (2006)
4. *Non-identical particle correlation in central Pb+Au collisions at 158 A GeV*, Nukleonika 51, Supplement 3, 47-50 (2006)

Presentations

1. *Two-particle correlations in Pb+Au collisions at 158 AGeV*, DPG Tagung, Köln, 2004
2. *Non-identical particle correlations in central Pb+Au collisions at 158 GeV per nucleon*, V-I Workshop on 'Physics of strongly interacting matter at high densities' Bad Liebenzell, 3-5 October 2005
3. *Two-particle correlations in Pb+Au collisions at 158 AGeV*, DPG Tagung, München, 2006

Erklärung

Hiermit erkläre ich an Eides statt, daß ich die vorliegende Dissertation selbständig verfaßt, keine anderen als die angegebenen Hilfsmittel verwendet und noch keinen Promotionsversuch unternommen habe.

Darmstadt, den 15. Okt 2006,

gez. Dariusz Antończyk.

Unterschrift